UNIVERSITY OF SOUTHAMPTON

An investigation into the fine-scale structure of Polar Cap Aurora using ground-based and spacecraft instrumentation

by

Jade Ashley Reidy

A thesis submitted in partial fulfillment for the degree of Doctor of Philosophy

in the

Faculty of Engineering and Physical Sciences

Department of Physics and Astronomy

June 2019

Declaration of Authorship

I, Jade Ashley Reidy, declare that this thesis titled, 'An investigation in to the fine-scale structure of Polar Cap Aurora using ground-based and spacecraft instrumentation' and the work presented in it are my own. I confirm that:

- This work was done wholly or mainly while in candidature for a research degree at this University.
- Where any part of this thesis has previously been submitted for a degree or any other qualification at this University or any other institution, this has been clearly stated.
- Where I have consulted the published work of others, this is always clearly attributed.
- Where I have quoted from the work of others, the source is always given. With the exception of such quotations, this thesis is entirely my own work.
- I have acknowledged all main sources of help.
- Where the thesis is based on work done by myself jointly with others, I have made clear exactly what was done by others and what I have contributed myself.

Signed: _____

Date: _____

"At once she saw something strange was happening in the sky...the sight filled the northern sky; the immensity of it was scarcely conceivable. As if from Heaven itself, great curtains of delicate light hung and trembled. Pale green and rose-pink, and as transparent as the most fragile fabric, and at the bottom edge a profound and fiery crimson like the fires of Hell, they swung and shimmered loosely with more grace than the most skillful dancer."

The Northern lights, Philip Pullman.

UNIVERSITY OF SOUTHAMPTON

Abstract

Faculty of Engineering and Physical Sciences
Department of Physics and Astronomy

Doctor of Philosophy

by Jade Ashley Reidy

This thesis will investigate the formation and structure of polar cap arcs using ground-based and spacecraft instrumentation. In particular, we present polar cap arc substructure down to unprecedented spatial and temporal scales using the Auroral Structure and Kinetics (ASK) instrument. Events are identified using images from Special Sensor Ultra-violet Spectrographic Imager (SSUSI) instruments on board Defence Meteorological Satellite Program (DMSP) F16-F19.

Three studies are presented. First, an event with polar cap arcs occurring on the dawn and duskside of the northern hemisphere on 19 January 2008 was observed by SSUSI instruments on board DMSP F16 and F17. The structure on the duskside occurred over Svalbard and was analysed using a multitude of ground-based instrumentation, including ASK, and was found to be consistent with formation on closed field lines. The arc on the dawnside of the northern hemisphere was found, using in-situ particle data, to be consistent with formation on open field lines. This first study shows that polar cap arcs consistent with different formation mechanisms can occur simultaneously.

The second study surveyed SSUSI and corresponding SSJ/5 data to identify and classify polar cap arc events in December 2015. Further examples of arcs occurring on both magnetic field topologies are found as well as examples that are not, at first sight, consistent with either. The occurrence frequency of polar cap arcs is also investigated and they are found to be present in the SSUSI images at least 20% of the time.

Finally, two events with polar cap arcs consistent with different magnetic field topologies occurring over Svalbard are analysed using ASK data. The first occurred on 4 February 2016 and is consistent with formation on closed field lines; the second occurred on 15 December 2015 and is consistent with open field lines. The small-scale structure within these arcs is found to be quite different and consistent with their occurrence on different magnetic field toplogies. The ground-based observations are then compared to the spacecraft observations to infer more information about the two formation mechanisms.

Acknowledgements

I would firstly like to thank my amazing supervisors Rob, Andrew, Dan and Betty for their support and encouragement throughout the last three and a half years and for helping me get this thesis done. Rob, thank you for all your patience, time and generally being such a great supervisor. Andrew, thanks for letting me come to BAS and for all your support there. Dan, thank you for taking me to Svalbard and the lands of the northern lights. Also thanks to Dan and Noora for inviting me onto your ISSI teams.

Thank you to all the PhD students and postdocs in the SEP and astronomy groups. Specific shout outs to Steve, Andy and Joe, my road trip buddies, its not been the same since you left. David, Josh and James (the Indidanna crew), you guys made the Svalbard trips so wildy successful and fun. John, thanks for all your help and advice over the years. Newbie Dale, thanks for all the gossip and biscuits. Bella, thanks for being the best girlfriend in the department, you rock. Lastly, to the amazing Pete, thank you for being the worlds greatest host and always being there to chat.

Thanks to all the PhD students at BAS who have made me so welcome over the last year, particularly to Hayley, I dont think I would have got through the last three months without our coffee breaks.

I would also like to thank my amazingly supportive friends and family. In particular my Mum, for all the food and comfort, my Gran for always being there for a chat and my sisters, nieces, nephews and Dexter for all the distractions and generally making life worth living. And thanks to my best amigos who got me through to the end of this thesis.

Thanks to my Mum, Amber and Lucia for being proof readers even when you had no clue what this was saying (and who I would like to formally blame for all remaining typos).

Lastly, thanks to Dean for supporting me throughout this PhD, and for all your understanding (and distractions) over the last three and a half years!

Contents

List of Figures

List of Tables

Abbreviations

ACE	**A**dvanced **C**omposition **E**xplorer
ASK	**A**uroral **S**tructure and **K**inetics
AMPERE	**A**ctive **M**agnetosphere and **P**lanetary **E**lectrodynamics **R**espose **E**xperiment
ARTEMIS	**A**cceleration, **R**econnection, **T**urbulence and **E**lectrodynamics of the **M**oons **I**nteraction with the **S**un
DMSP	**D**efense **M**eterological **S**atellite **P**rogramme
EISCAT	**E**uropean **I**ncoherent **SCAT**ter Scientific Association
ESR	**E**iscat **S**valbard **R**adar
EMCCD	**E**lectron **M**ultiplying **C**harge-**C**oupled **D**evice
HiTIES	**Hi**gh-**T**hroughput **I**maging **E**chelle **S**pectrograph
IMAGE	**I**nternational **M**onitor for **A**uroral **G**eomagnetic **E**ffects
IMF	**I**nterplanetary **M**agnetic **F**ield
KHO	**K**jell **H**enriksen **O**bservatory
KTH	Royal Institute of Technology, Stockholm, Sweden
MHD	**M**agneto**h**ydro**d**ynamics
MLT	**M**agnetic **L**ocal **T**ime
MSISE-90	**M**ass **S**pectrometer **I**ncoherent **S**catter thermospheric model
PCA	**P**olar **C**ap **A**rc
$\mathbf{R}_e$	Earth radii
SIF	**S**pectrographic **I**maging **F**acility
SSUSI	**S**pecial **S**ensor **U**ltra-violet **S**pectrographic **I**mager
SuperDARN	**Super D**ual **A**uroral **R**adar **N**etwork
TLC	**T**he **L**ittle **C**amera
TPA	**T**rans**p**olar **arc**
TRINNI	**T**ail **R**econnection during **N**orthward **N**on-substorm **I**nterval

UNIS	University Centre Svalbard
UT	**U**niversal **T**ime
UV	**U**ltra **V**iolet

Chapter 1

Introduction

1.1 General overview

The aurora is a visual representation of the complex interactions between the Earth and the Sun's magnetic fields. These dynamic light displays have fascinated people throughout history, with the first reported auroral observations dating back as far as 2000 BC in ancient Chinese literature. Naturally, many myths and legends exist about the causes of the northern lights, particularly in the Nordic and Canadian regions. According to a Finnish folk tale, the lights are created by an Arctic fox sweeping its tail across the snow which throws the lights into the sky; the Finnish name for the northern lights, 'revontulet', translates literally to fox fires. It was not until the first international polar year (1882 - 1883), that Sophus Tromsholts related the occurrence of the aurora with the occurrence of Sun spots (which are correlated with solar activity). Later, around 1900, Kristian Birkeland used his Terrella experiments to understand why auroral activity occurred in the polar regions. These experiments led to the well accepted theory that the interaction between particles flowing away from the Sun and the Earth's magnetic field ultimately generates the auroras.

This thesis will investigate the fine-scale structure within a mysterious subset of auroral arcs which occur at high latitudes, known as polar cap arcs. These high latitude arcs were first reported by Douglas Mawson, who made detailed logs of the auroral activity over different Antarctic stations during expeditions in 1908 and between 1911-1914 [Mawson, 1916, 1925], shown in Figure 1.1. He found, on average, that the arcs were aligned in a

north-south direction around midnight and an east-west direction in the morning and evening, pointing towards the Sun; this arcs were subsequently termed sun-aligned arcs.

FIGURE 1.1: Mawson's Antarctic expedition. Photo from the National Archives of Australia.

Despite over a century of study, the formation of these arcs is still not well understood. This thesis uses ground-based and spacecraft observations of polar cap arcs to investigate how they are formed and what consequences this has on our near-Earth magnetic environment. In particular, this thesis will look at ground-based observations from Svalbard. Due to its high latitude location, Svalbard spends a lot of time in the typically dim polar cap region (within the auroral oval), especially when on the nightside and is hence ideal for studying these arcs. The University of Southampton has ground-based instrumentation located on Svalbard. Figure 1.2 shows a picture of aurora occurring over Svalbard, although this is main oval aurora rather than the elusive polar cap arcs which are the focus of this thesis.

The interactions between the Earth's magnetosphere (the region of space in which the Earth's magnetic field dominates, described in Section 1.4) and the constant stream of plasma emitted by the Sun, known as the solar wind (Section 1.3), ultimately result in the auroral displays which are of interest to this thesis. Section 1.2 will explain the

fundamental physics which underpins these interactions, before giving a review of polar cap arc studies which have led up to this thesis in Section 1.5. Happy reading!

FIGURE 1.2: Aurora above Svalbard. Photo credit Dan Whiter.

1.2 Plasma physics

A plasma is an ionised gas with approximately equal numbers of positive and negative charged particles (quasi-neutral). It can co-exist with a background of neutral particles, depending on the source of the ionization. It is the fourth state of matter and makes up approximately 99% of the observable universe, for example the Sun is made of plasma (as are all stars). For an ionised gas to be called a plasma it must satisfy three conditions, known as the plasma criteria, which are discussed below.

The first condition relates to Debye shielding, which describes the collective effect in which a 'cloud' of electrons surround ions in a plasma, due to the electrostatic potential. These electrons shield the electric field of the ions and result in the plasma being quasi-neutral. The Debye length (λ_D) is the distance over which Debye shielding occurs; within distances of λ_D particles have to be considered individually, but over larger distances (i.e. $\lambda_D >> 1$), the plasma may be considered as a fluid [Kivelson and Russell, 1995].

Equation 1.1 gives the Debye length where ϵ_0 is the permittivity of free space, k_B is the Boltzman constant, T is the electron temperature, e is the charge of an electron and n_e is the electron density.

$$\lambda_D = \sqrt{\frac{\epsilon_0 k_B T}{e^2 n_e}} \tag{1.1}$$

For a plasma to be quasi neutral, the Debye length must be must smaller than the scale length of the plasma (L) i.e. $\lambda_D << L$. This is the first plasma criterion. This condition can be shown to be equivalent to the free particle criterion that the thermal energy of the particles must be greater than the potential energy due to other particles.

In order for Debye shielding to occur, the number of particles within a sphere of radius λ_D (the Debye sphere), known as the plasma parameter Λ (given by equation 1.2) must be large.

$$\Lambda = n_e \lambda_D \tag{1.2}$$

The second plasma criterion is: $\Lambda >> 1$.

If a plasma is disturbed by an external force, the electrons will be accelerated back by a restoring force to maintain quasi-neutrality. This results in electrons oscillating around the more massive ions at the electron plasma frequency (ω_{pe}) given by equation 1.3, where m_e is the mass of an electron [Kivelson and Russell, 1995].

$$\omega_{pe}^2 = \frac{n_e e^2}{m_e \epsilon_0} \tag{1.3}$$

The third plasma criterion states that the particles must be collisionless on the timescale of the collective processes (i.e. the electron plasma frequency) and hence $\omega_{pe}\tau_n >> 1$ where τ_n is the average time between two electron-neutral collisions. All three plasma criteria must be obeyed in order for a medium to behave as a plasma i.e. it must be quasi-neutral on a large scale, must consist of free particles and must be collisionless on timescales of the collective processes [Baumjohann and Treumann, 1996].

A plasma can be produced by heating a gas to high enough temperatures such that the kinetic energy of the particles is greater than the ionisation energy (the energy required to separate an electron from the nucleus); this is a process that occurs throughout the Sun. Another way to produce a plasma is to irradiate a gas with photons of higher energy than the ionisation energy; this process is called photoionisation and occurs in the upper atmosphere of the Earth due to UV radiation from the Sun (as it does in any planetary atmosphere that is irradiated by UV radiation) [Baumjohann and Treumann, 1996]. The plasma layer at the top of the Earth's atmosphere is called the ionosphere; this is where the auroras occur and will be discussed in more detail in Section 1.4.3.1.

Generally, there are three ways in which a plasma can be described: single particle dynamics, which considers the individual particles within a plasma; magnetohydrodynamics (MHD), which treats all the particles within a plasma as a fluid and kinetic theory which is statistical. The basics of these three approaches are described in Sections 1.2.1-1.2.3 respectively.

1.2.1 Single particle dynamics

Equation 1.4 describes the motion of a charged particle in a magnetic and electric field (where q is the charge of the particle); this is called the Lorentz equation and is fundamental for charged particles in a plasma. All charged particles inherently have an electric field (**E**) and, if moving at velocity (**V**), they also have a magnetic field (**B**) [Baumjohann and Treumann, 1996].

$$\mathbf{F} = q(\mathbf{E} + \mathbf{V} \times \mathbf{B}) \tag{1.4}$$

These electromagnetic fields are fundamentally described by Maxwell's laws which encompass: Gauss's Law, no magnetic monopoles, Faradays Law of Induction and Amperés Law. These are shown in differential form by equations 1.5- 1.8 respectively, where ρ is the charge density and μ_0 is a constant, the magnetic permittivity of free space.

$$\nabla \cdot \mathbf{E} = \frac{\rho}{\epsilon_0} \tag{1.5}$$

$$\nabla \cdot \mathbf{B} = 0 \tag{1.6}$$

$$\nabla \times \mathbf{E} = -\frac{\partial \mathbf{B}}{\partial t} \tag{1.7}$$

$$\nabla \times \mathbf{B} = \mu_0 \mathbf{j} + \mu_0 \epsilon_0 \frac{\partial \mathbf{E}}{\partial t} \tag{1.8}$$

Charged particles in a dipolar magnetic field, such as that of the Earth, experience gyration, bounce and drift as demonstrated in Figure 1.3 which shows particle motion on one magnetic field line. Each of these motions will be described in detail below.

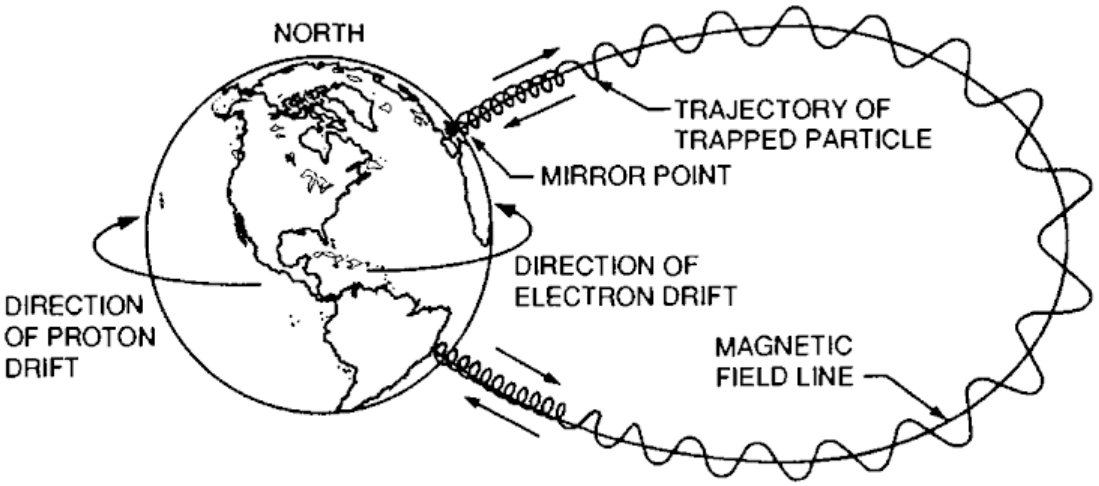

FIGURE 1.3: The trajectory of particles in the Earth's dipolar magnetic field from Walt [2005].

1.2.1.1 Gyromotion of charged particles

If a particle is in a constant magnetic field and the electric field is zero, the equation of motion of the particle (given in equation 1.4) becomes:

$$\mathbf{F} = m\frac{d\mathbf{V}}{dt} = q(\mathbf{V} \times \mathbf{B}) \tag{1.9}$$

This equation demonstrates that a magnetic field results in a force which is perpendicular to the direction of motion and the field itself, this will cause the particle to experience

circular motion and gyrate about the magnetic field line (guiding axis) [Baumjohann and Treumann, 1996]. By equating this force to the centripetal force, the radius of gyration (r_g) and the gyrofrequency, or cyclotron frequency (ω_g) can be expressed in the following way respectively:

$$r_g = \frac{mV_\perp}{qB} \tag{1.10}$$

$$\omega_g = \frac{qB}{m} \tag{1.11}$$

where m is the mass of the particle and $V_\perp$ is the perpendicular component of it's velocity.

Equation 1.9 shows that the force causing the circular motion is dependent on the charge of the particle and therefore, ions and electrons gyrate in opposite directions. If a particle has a component of velocity in the same direction as the magnetic field (i.e. parallel), the path of the particle can be described by a helix. The angle between the perpendicular and parallel velocity components is known as the pitch angle, α.

$$\alpha = arctan(\frac{V_\perp}{V_\parallel}) \tag{1.12}$$

In a uniform magnetic field, with no electric field applied to it, the circular motion of a particle does not change the kinetic energy of the particle.

1.2.1.2 Bounce motion

Figure 1.4 shows the path of a particle in a converging magnetic field. In this situation, the particle will experience a force in the opposite direction to the increasing field strength, known as the mirror force.

This force results in the parallel velocity ($V_\parallel$) decreasing (and hence, due to conservation of energy, $V_\perp$ increasing) as the field strength increases until it reaches zero. At $V_\parallel = 0$, the force will then accelerate the particle in the opposite direction, this is known as

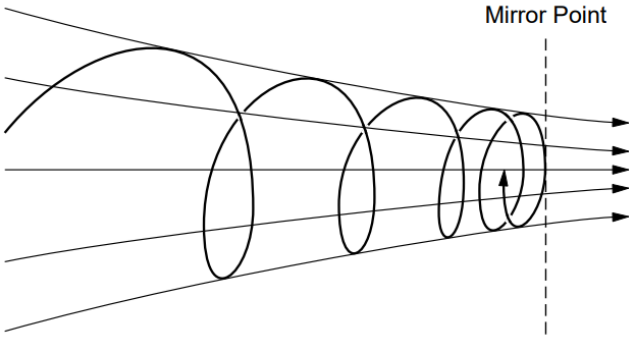

FIGURE 1.4: Particle in a converging magnetic field from Baumjohann and Treumann [1996].

the mirror point (i.e. the point where the particle changes direction) [Baumjohann and Treumann, 1996].

The mirror point can be inferred by using the magnetic moment (μ) of a particle in a magnetic field, given by the ratio of the perpendicular particle energy ($W_\perp = \frac{1}{2}mV_\perp^2$) and the magnetic field strength:

$$\mu = \frac{W_\perp}{B} \tag{1.13}$$

The magnetic moment is a useful parameter for describing a particle in a magnetic field and is the first adiabatic invariant, which means it can be considered 'constant' for perturbations to the system on timescales which are greater than the gyrofrequency. The first adiabatic invariant tells us that, as the magnetic field strength changes, the only quantity that is can change is $V_\perp$ which is dependent on the pitch angle of the particle ($V_\perp = Vsin(\alpha)$). At the mirror point (B_m), the pitch angle is 90° and therefore using equation 1.13:

$$B_m = \frac{B}{sin^2\alpha} \tag{1.14}$$

This shows that the mirror point only depends on the particle's pitch angle (equation 1.12) and relative field strength at a given location, for example at the equator. A particle's pitch angle changes as it moves along a magnetic field line (as the magnetic field strength changes). Therefore, particles of different mass and charge but with the same pitch angle in a given magnetic field configuration, will mirror at the same point.

Particles with $\alpha > sin^{-1}\frac{B_0}{B_m}$ will remain trapped by the converging field whereas particles with $\alpha < sin^{-1}\frac{B_0}{B_m}$ can escape the converging magnetic field [Baumjohann and Treumann, 1996].

In the dipolar magnetic field of the Earth, a population of particles with sufficiently small pitch angles will mirror within the atmosphere. The loss cone is the solid angle containing the particles with $\alpha < \alpha_{LC}$, such that these particles are lost to the system via atmospheric collisions. On field lines which are connected to Earth in both hemispheres, a double loss cone is present. Particles with $\alpha > \alpha_{LC}$ are trapped by the Earth's dipolar magnetic field and bounce between each hemisphere.

1.2.1.3 Drift motion

In general, in a uniform magnetic field ($\mathbf{B}$) that is acted on by external force ($\mathbf{F}$), the resultant motion is helical with a constant drift which is perpendicular to both the external force and the magnetic field. Equation 1.15 gives the general equation for this drift ($\mathbf{V}_F$):

$$\mathbf{V}_F = \frac{\mathbf{F} \times \mathbf{B}}{qB^2} \tag{1.15}$$

In a plasma, electric fields which are parallel to the magnetic fields are quickly cancelled out due to charge separation and subsequently $\mathbf{E}_{\|}$ is usually zero. If there is an electric field acting perpendicular to the magnetic field ($\mathbf{E}_{\perp}$) equation 1.15 becomes:

$$\mathbf{V}_E = \frac{\mathbf{E} \times \mathbf{B}}{B^2} \tag{1.16}$$

Where $\mathbf{F}_E = \mathrm{q}\mathbf{E}$. This drift ($\mathbf{V}_E$) is known as the $\mathbf{E}\times\mathbf{B}$ drift. This drift is independent of particle charge or mass and is therefore the same for all particles [Kivelson and Russell, 1995].

In a magnetic field which is not homogeneous (such as that of the Earth), as particles move into regions of increasing or decreasing field strengths, they will experience gradient drift ($\mathbf{V}_g$) given by:

$$\mathbf{V}_g = \frac{W_\perp \mathbf{B} \times \nabla \mathbf{B}}{qB^3} \tag{1.17}$$

where $W_\perp$ is the perpendicular component of the kinetic energy. This drift is proportional to the charge of the particles and hence electrons and ions experience drifts in opposite directions [Kivelson and Russell, 1995].

In a magnetic field with curved field lines the trajectory of the particles is constantly changing as it experiences centrifugal force ($\mathbf{F}_c = \mathrm{m}\mathbf{V}^2/\mathrm{R}_c$). This external force leads to a curvature drift ($\mathbf{V}_c$) shown by:

$$\mathbf{V}_c = \frac{2W_\parallel^2 \mathbf{R}_c \times \mathbf{B}}{qR_c^2 B^2} \tag{1.18}$$

where $W_\parallel$ is the parallel component of the particles kinetic energy and $\mathbf{R}_c$ is the radial direction of gyration ($\mathbf{R}_c/|\mathrm{R}_c| = 1$). This drift is also dependent on charge, and therefore moves electrons and ions in different directions. It is also proportional to the parallel component of the particles velocity and acts in the same plane as the $\mathbf{E} \times \mathbf{B}$ drift [Kivelson and Russell, 1995].

It can be seen from Equations 1.17 and 1.18 that both of these magnetic drifts are dependant on components of the particles kinetic energy and are therefore dependant on the particles pitch angle. This results in changes in the relative strength of these drifts as particles move along magnetic field lines; the curvature drift is strongest at the equator and the gradient drift is strongest at the poles. Furthermore, it can be seen from Equation 1.16, that the E×B drift is not energy dependent.

1.2.2 Kinetic theory

Another approach at describing a plasma is kinetic theory. Here, instead of treating a plasma as a sum of the individual particles, kinetic theory takes a statistical approach. As discussed above, plasmas are a collection of approximately equal numbers of electrons and ions and some neutral particles. The motion of these different particles is governed by external forces (such as electromagnetic forces for the charged particles) and internal collision processes. The observed macroscopic plasma parameters, such as electron density, temperature and pressure, are averages of these microscopic interactions. Kinetic

theory considers a particle in terms of phase-space in which it can be described by its position vector ($\mathbf{r}$) and velocity vector ($\mathbf{v}$). A multi-particle system, such as a plasma, can be described by distribution functions $f(\mathbf{r}, \mathbf{v}, t)$, which can be used to derive the macroscopic plasma properties, such as those outlined above.

1.2.3 Magnetohydrodynamics

Magnetohydrodynamics (MHD) describes the collective fluid motion of charged particles in a plasma rather than considering the individual particles. The MHD approximation is valid for timescales which are longer than the gyrofrequency and length scales which are large compared with the gyroradius. Maxwell's equations and generalised Ohm's law (equation 1.19) can be used to derive the induction equation (equation 1.20), which is key for describing different MHD regimes:

$$\mathbf{J} = \sigma(\mathbf{E} + \mathbf{V} \times \mathbf{B}) \tag{1.19}$$

$$\frac{\partial \mathbf{B}}{\partial t} = \nabla \times (\mathbf{V} \times \mathbf{B}) + \frac{\nabla^2 \mathbf{B}}{\mu_0 \sigma} \tag{1.20}$$

The ratio between the two different terms on the right hand side in the induction equation gives the magnetic Reynolds number [Baumjohann and Treumann, 1996]:

$$R_m = \frac{\text{convective term}}{\text{diffusive term}} = \frac{\nabla \times (\mathbf{V} \times \mathbf{B})}{\nabla^2 \mathbf{B}/\mu_0 \sigma} \tag{1.21}$$

For most of the plasma in the solar system, $R_m >> 1$, where the convective term dominates. In this region the magnetic field is moving with the plasma. When $R_m << 1$, the diffusive term dominates and the magnetic field can diffuse through the plasma. The consequences from these two different regimes are discussed below.

1.2.3.1 Frozen-in

In the convective limit ($R_m >> 1$), also known as ideal MHD, the particles in the plasma and the magnetic field move together. This is known as the frozen-in flux theorem and

means that the magnetic flux through a surface which is moving with the plasma (i.e. frozen-in), is constant. Plasma elements can be considered to be stuck on the same magnetic field lines and can only move parallel to the magnetic field. The implications of frozen-in depend on the energy densities of different regions of plasmas. The total pressure exerted by a plasma is the sum of the thermal (P_T), dynamic (or ram, P_D) and magnetic (P_B) contributions:

$$P_{tot} = P_T + P_D + P_B = n_i kT + \frac{1}{2} m_i n v^2 + \frac{B^2}{2\mu_0} \tag{1.22}$$

The plasma beta, β, is the ratio of the of thermal to magnetic pressure. When $\beta >> 1$, the particle energy dominates and the particles carry the magnetic field. When $\beta << 1$ the magnetic energy dominates and the plasma is confined by the magnetic field lines [Baumjohann and Treumann, 1996].

1.2.3.2 Magnetic Reconnection

In the diffusive limit ($R_m << 1$), the frozen-in approximation breaks down and particles can diffuse across magnetic field lines. Under these conditions, a process known as magnetic reconnection can occur whereby field lines from different plasma regions 'merge' or become joined, changing the overall topology of the field lines [Kivelson and Russell, 1995]; this is depicted in Figure 1.5.

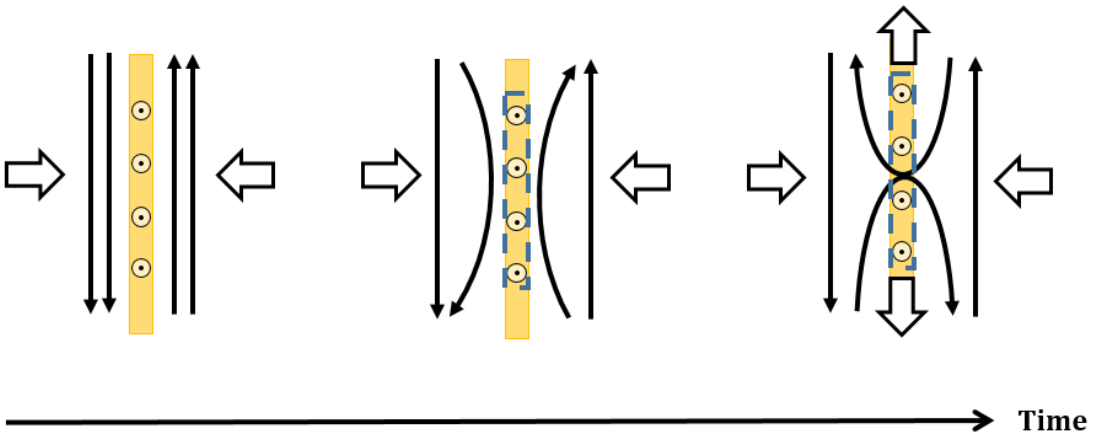

FIGURE 1.5: Evolution of merging magnetic field lines with time. The current sheet in indicated by a yellow shaded region where the current is coming out of the page. The diffusion region (not to scale) is indicated by blue dashed lines.

The image on the left hand side in Fig. 1.5 shows oppositely directed magnetic field lines moving towards each other. In the convective limit, the frozen-in approximation applies and therefore the two different plasmas cannot mix and are separated by a thin current sheet (indicated by the yellow shaded region of Fig. 1.5). However, in the second image depicted in Fig. 1.5, due to external forces pushing these plasmas together and the high magnetic gradient between the opposing field lines, the frozen-in approximation breaks down and diffusion can occur within the blue dotted box; this is known as the diffusion region (not to scale) and is where the magnetic field lines are being reconfigured. The last image on the right of Fig. 1.5 demonstrates the newly orientated field lines. These field lines are then ejected away from the diffusion region, where the frozen-in approximation becomes valid again. Magnetic reconnection results in a transfer of energy and particles between two plasmas [Baumjohann and Treumann, 1996].

Magnetic reconnection is a key process which occurs in the Earth's magnetosphere and results in the acceleration of particles into the ionosphere which in turn generates auroras. The electron diffusion region at the Earth's magnetopause region has recently been observed by the high-resolution data from the Magnetospheric Multiscale (MMS) mission [Burch et al., 2016].

1.3 The Sun's magnetic field and the solar wind

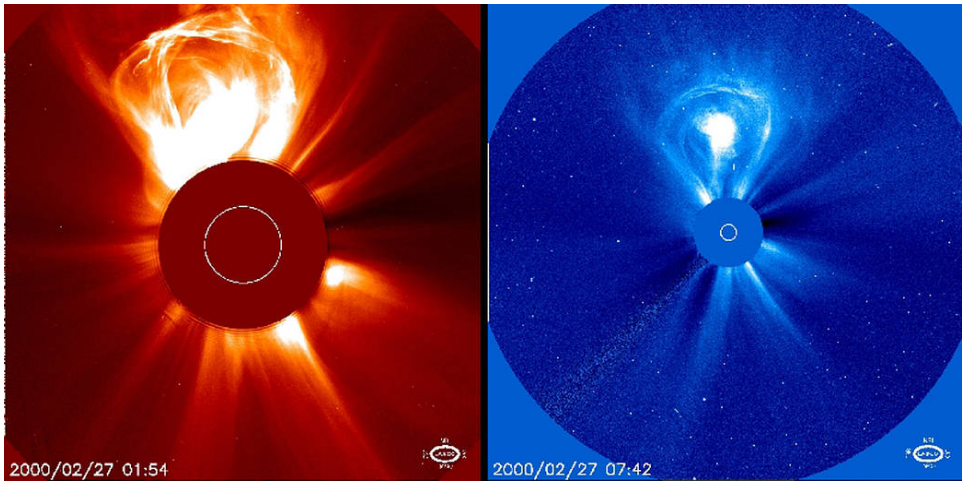

FIGURE 1.6: Images of a coronal mass ejection shown in different wavelengths (credit SOHO ESA and NASA).

The outer layers of the Sun's atmosphere expand out into the solar system, resulting in a constant stream of plasma flowing radially away from the Sun, known as the solar

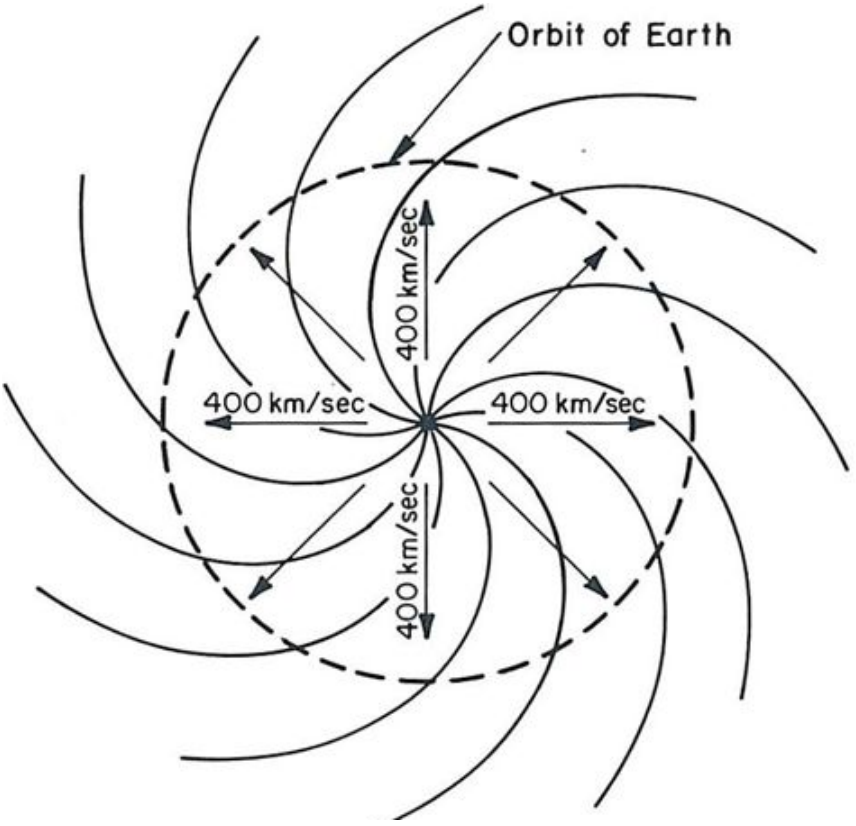

FIGURE 1.7: The structure of the solar wind [Parker, 1963]

wind. This is demonstrated in Figure 1.6 by two images from the Solar and Heliospheric Observatory (SOHO). A large expulsion of plasma, known as a coronal mass ejection, can be seen at the top of each image. Solar wind plasma exists in the convective limit and hence the Sun's magnetic field is frozen into the plasma, such that as the particles leave the Sun they drag the magnetic field out into the solar system. This extension of the solar magnetic field is known as the Interplanetary Magnetic field (IMF). The entire region in which the solar wind has influence is known as the heliosphere. Due to a combination of radial flow and the rotation of the Sun, the solar wind is shaped into a ballerina-like skirt, known as the Parker spiral [Parker, 1958]; a cartoon demonstration of this is given in Figure 1.7. Due to this structuring, as well as other effects from the magnetic conditions on the Sun (such as coronal mass ejections), this solar wind is highly variable by the time it reaches the Earth. This variability plays a huge role in the geomagnetic conditions of the Earth's magnetosphere.

1.4 The Earth's magnetosphere

The Earth's magnetosphere is the region of space that is dominated by the Earth's magnetic field, shown in Figure 1.8. It is shaped by the solar wind, which compresses it on the dayside and drags it out into a long magnetotail on the nightside. The plasma in the Earth's magnetosphere, as in the solar wind, is in the convective limit and therefore obeys the frozen-in approximation. This means that the two plasmas cannot mix and hence the Earth's magnetosphere can be thought of as a cavity within the solar wind; the barrier between the two plasmas is called the magnetopause. As the solar wind is travelling faster than the speed of sound, it is suddenly slowed down when it encounters the Earth's magnetosphere, generating a shock wave known as the bow shock. The region between the bow shock and the magnetopause is known as the magnetosheath; this area contains hot, dense solar wind [Kivelson and Russell, 1995].

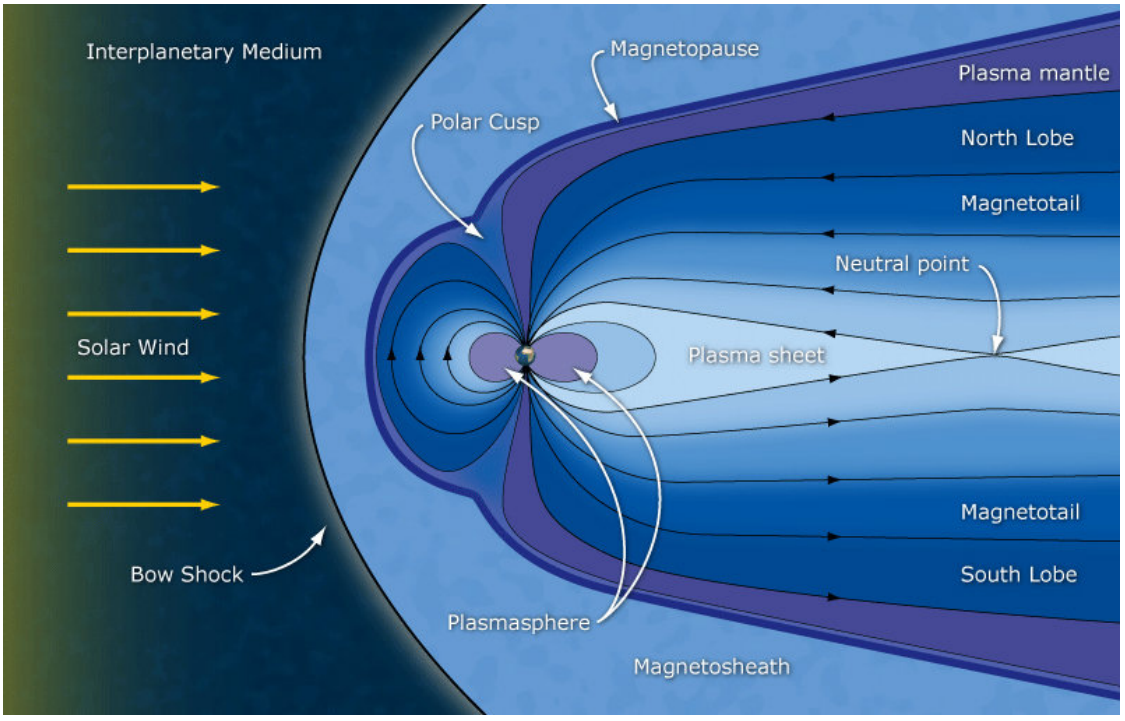

FIGURE 1.8: The different regions of the Earth's magnetosphere (Image credit: ESA/C. T. Russell).

The size of the Earth's magnetosphere is determined by the balance between the magnetic pressure of its magnetic field and the dynamic (or ram) pressure from the flowing solar wind. On the dayside, the distance between the Earth and the nose of the magnetopause is highly variable with a mean value of approximately 10 Earth radii (R_e). The

length of the nightside magnetotail is not known for sure but it is thought to be dragged out to hundreds of R_e [Dungey, 1965].

The magnetotail can be characterised by two regions: the lobes which host the 'open' field lines (field lines which are magnetically connected to the IMF and have a footprint in only one hemisphere), and the plasma sheet which hosts the 'closed' field lines (field lines which simply trace from the ionosphere in one hemisphere to the ionosphere in the other, without passing into the solar wind). The lobes are regions of low density, relatively cold plasma whilst the plasma sheet is a hot, dense region containing all the trapped particles that are bouncing back between the two hemispheres (as discussed in Section 1.2.1.3); these regions are labelled in Fig. 1.8. A closed field line can be identified in particle data by the presence of a double loss cone (e.g. Walsh et al. [2013]).

The interactions between the solar wind and the Earth's magnetosphere (which will be discussed below) generate auroral ovals in both hemispheres which are centered approximately over each of the poles. The typically dim region within the main auroral oval is known as the polar cap (which maps to the magnetotail lobes); this region is of particular interest to this thesis and will be discussed in detail in Sections 1.4.4 and 1.5. The auroral ovals are formed on the closed field lines (which map to the plasma sheet) that surround the open field lines of the polar cap and hence the poleward edge of the auroral oval can be considered to be the border between these two different topologies, known as the open-closed boundary.

1.4.1 Low-latitude reconnection and the Dungey cycle

During periods when the IMF is directed southward (i.e. opposite to the Earth's magnetic field), magnetic reconnection (summarised in Figure 1.5) may occur on the dayside of the Earth's magnetosphere whereby the closed magnetic field lines change topology and become open. This is demonstrated in Figure 1.9 which shows incoming solar wind interacting with the Earth's magnetic field in a similar side-on view of the Earth's magnetosphere as Figure 1.8. The subsequent stages of this convection process are labeled 1-9. Stage 1 shows a southward directed IMF field line interacting with a closed field line on the dayside of the Earth. This field line is opend and then dragged anti-sunward across the polar cap region by the continually flowing solar wind (stages 2 and 3). Between stages 4 and 5 this field line enters the magnetotail and is compressed inwards as

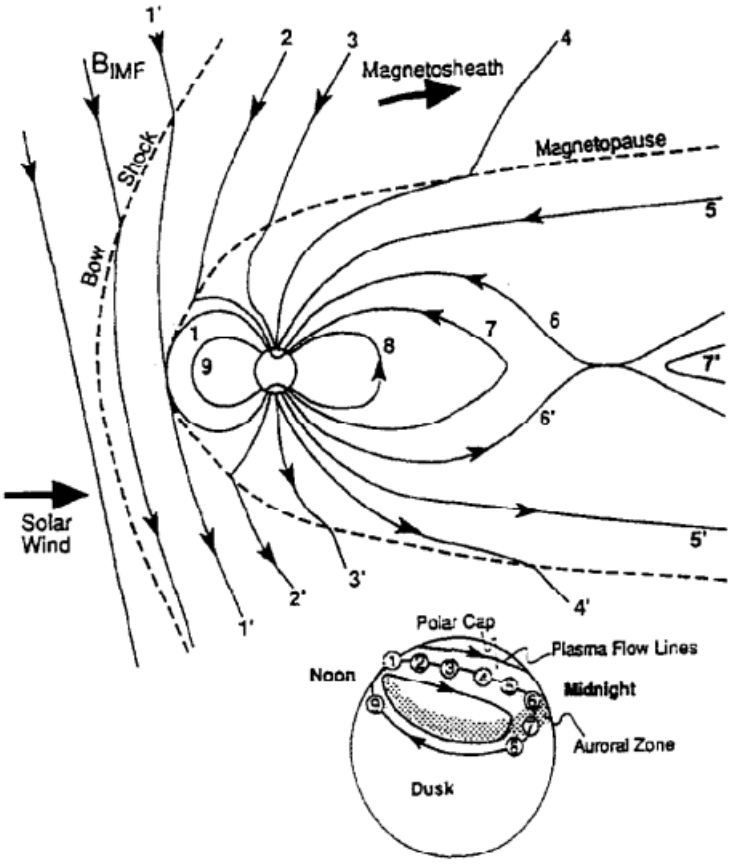

FIGURE 1.9: The Earth's magnetosphere and the stages of the Dungey cycle [Lester, 2003].

a result of the pressure exerted by the solar wind upon the magnetotail. At the center of the magnetotail (stage 6), oppositely directed field lines from each hemisphere meet and undergoes nightside reconnection; this acts to close the open field lines. Once nightside reconnection occurs the field line 'springs' back towards the Earth (stages 7-8), becoming more dipolar; this accelerates particles down into both polar regions where they interact with atmospheric particles and generate auroras (discussed in more detail in Section 1.4.3). Stage 9 represents a closed field line which has convected back round to the dayside, ready to start the cycle again. This is known as the Dungey cycle [Dungey, 1961]. Zhang et al. [2015] measured a full Dungey cycle duration, using spacecraft and ground based instrumentation, to be 3 hours; this observation occurred during relatively slow solar wind speeds varying between 360-420 km^{-1}. In a statistical study, Browett et al. [2016] found the transport of a field line from the dayside to the nightside (and hence not including the return journey) can take between 1-4 hours depending on the IMF conditions.

The ionospheric convection on the duskside of the polar cap during the Dungey cycle is illustrated at the bottom of Figure 1.9; it shows the newly opened field line travel anti-sunward across the polar cap before convecting back to the dayside, equatorward of the auroral oval (same stages 1-9 described above). This pattern is reversed on the dawnside and, as a whole, is known as the twin cell convection pattern.

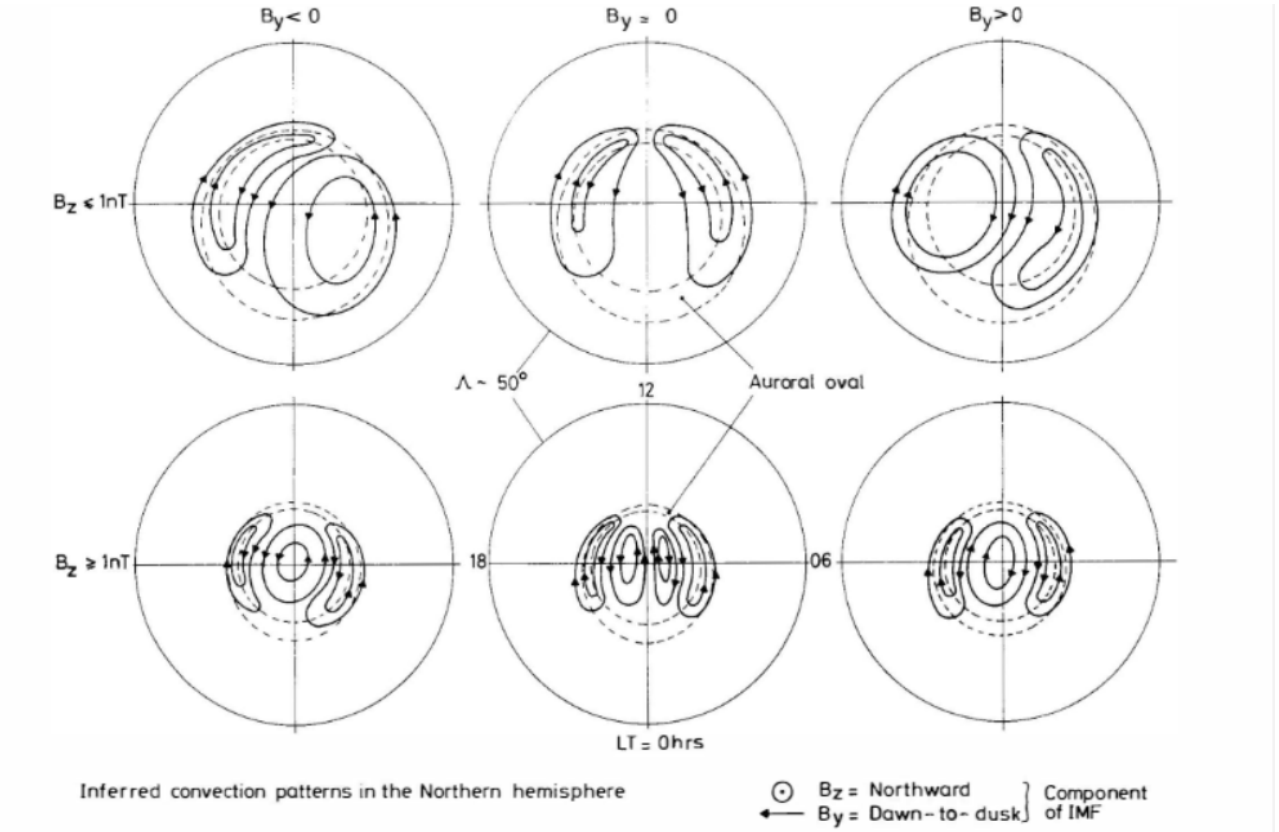

FIGURE 1.10: Ionospheric convection in the polar cap shown for different IMF conditions [Cowley and Lockwood, 1992]. In each image noon is to the top and dawn to the right.

Figure 1.10 shows the average ionospheric flow in the polar cap region for different IMF conditions taken from Cowley and Lockwood [1992]. The top row indicates the average convection patterns during negative IMF B_z conditions, when low-latitude dayside reconnection is occurring, with different IMF B_y components. It can be seen that the presence of the B_y components results in asymmetric ionospheric convection which is skewed depending on the sign of B_y. The ionospheric conditions on the bottom row, where the B_z component is positive are considered in Section 1.4.2.

The area of the polar cap and the location of the main auroral oval depends on the time history of the relative rates of low-latitude dayside reconnection and nightside reconnection; this is known as the expanding-contracting polar cap paradigm [Milan

et al., 2003, 2008]. During periods of dayside reconnection, more open flux is being added to the polar cap and the area of the polar cap increases (expands). This results in the auroral ovals moving to lower latitudes. During nightside reconnection, open flux is closed and hence the polar cap shrinks (contracts) resulting in the auroral oval moving to higher latitudes.

1.4.2 High-latitude reconnection

During northward IMF (i.e. when the IMF B_z component is positive, parallel to the Earth's magnetic field), dayside reconnection can occur at higher latitudes. High-latitude or lobe reconnection was first theorised by Dungey [1963], who suggested that an IMF field line draped over the Earth's magnetosphere could undergo reconnection with lobe field lines in both hemispheres, producing a closed field line on the dayside of the magnetosphere; this is known as dual lobe reconnection. This high latitude reconnection can also occur independently in each hemisphere, known as single lobe reconnection. This kind of lobe reconnection has been reported to occur approximately 90% of the time when the IMF is northward [Twitty et al., 2004]. The occurrence of dual lobe reconnection is somewhat unclear, with some considering it to be a rare phenomena, only occurring during strongly northward IMF conditions (e.g. Imber et al. [2006]), whereas others have found it to occur more frequently (e.g Lavraud et al. [2005, 2006]). Figure 1.11 shows a side of view of the magnetosphere during single lobe reconnection in the northern hemisphere (left) and a view of the ionospheric convection in the polar cap region (right). This high latitude reconnection only acts to reconfigure the open field lines in the polar cap rather than change in the amount of open flux and hence the size of the polar cap does not change (e.g Siscoe and Huang [1985], Cowley and Lockwood [1992] and Milan et al. [2003]). A reverse-cell convection pattern can be seen in the right hand image of Fig. 1.11 during lobe reconnection. This convection is sometimes referred to as a 'stirring' motion and be can be recognized by the sunward flow (opposite to the Dungey-like flow discussed in Section 1.4.1). The bottom row of Fig. 1.10 demonstrates the asymmetric nature of the lobe convection cells which also depend on the IMF B_y component. Lobe reconnection is also thought to have a hemispheric dependence on the IMF B_x component for example, lobe reconnection has been suggested to occur preferentially in the northern hemisphere for IMF $B_x < 0$ and in the southern hemisphere for $B_x > 0$ [Reiff and Burch, 1985] (i.e. it is more common in the hemisphere with

field lines anti-parallel to the direction of the IMF field lines). However, using Cluster data, Lavraud et al. [2005] found a relatively small dependence on the IMF tilt angle (dependant on IMF B_x), and instead found a greater dependence on the dipole tilt of the Earth.

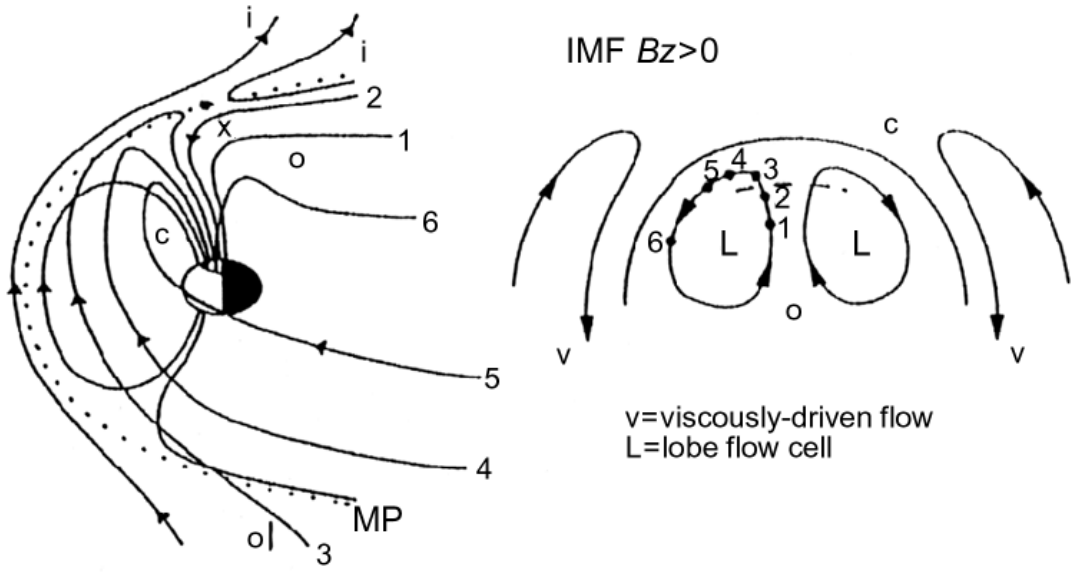

FIGURE 1.11: High latitude magnetopause reconnection [Lockwood, 1998] shown from the side and looking down on the polar cap. The stages of reconnection are indicated by the same numbers in each figure.

1.4.3 Currents

As discussed in Section 1.2.1.3, some magnetic drifts (e.g. curvature and gradient) are charge dependent. This causes charge separation which results in the flow of current. In the Earth's dipolar magnetic field, the trapped particles on closed field lines experience these magnetic drifts and this results in the ions drifting westward and the electrons drifting eastward; the resultant effect is known as the ring current and occurs around the Earth's equator Baumjohann and Treumann [1996]. Furthermore, Amperés Law (given by equation 1.8), tells us that where two different magnetic fields meet, there must be a current sheet. This effect is seen on the magnetopause which is the boundary between the shocked solar wind of the magnetosheath and the magnetosphere. These interactions result in currents flowing along the magnetopause, known as the Chapman and Ferraro currents [Chapman and Ferraro, 1930]. These different currents are closed via field aligned currents in the polar cap regions.

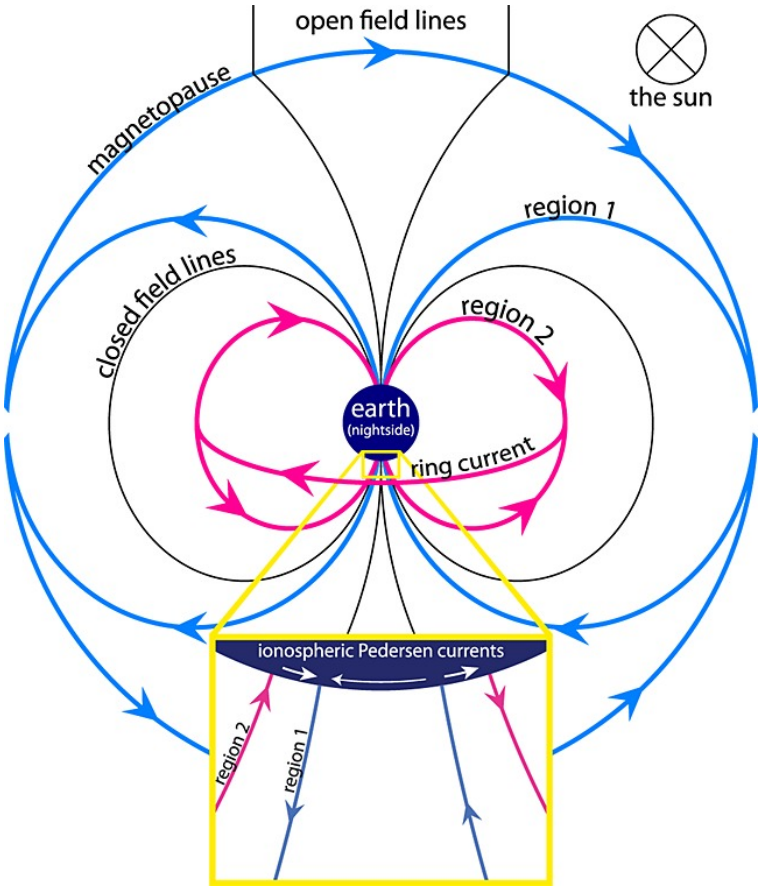

FIGURE 1.12: Cartoon schematic of the global current systems in the Earth's magnetosphere taken from Coxon et al. [2014a]. The region 1 and 2 currents are shown in blue and pink respectively.

Field aligned currents, theorised by Kristian Birkeland in the early 1900's, are known as Birkeland currents [Birkeland, 1908, 1913]. Figure 1.12 is a cartoon schematic of the large scale morphology of these currents, taken from Coxon et al. [2014a]. This configuration was first discovered by using low orbiting satellites [Iijima and Potemra, 1976a,b, 1978]. On average, the field aligned currents form two rings in the polar cap, known as the Region 1 and Region 2 currents. The Region 1 currents (blue lines in Fig. 1.12) occur further poleward and are connected to the Chapman Ferraro currents at the dayside magnetopause. The Region 2 currents (pink lines in Fig. 1.12) are connected to the partial ring current in the nightside inner magnetosphere. Both the Region 1 and 2 currents close in the ionosphere via horizontal Pederson currents [Baumjohann and Treumann, 1996].

These field aligned currents are associated with the Dungey cycle and are hence driven by day and nightside reconnection [Cowley and Lockwood, 1992, Clausen et al., 2012, Coxon et al., 2014a,b]. This is demonstrated in Figure 1.13 which shows a view of the

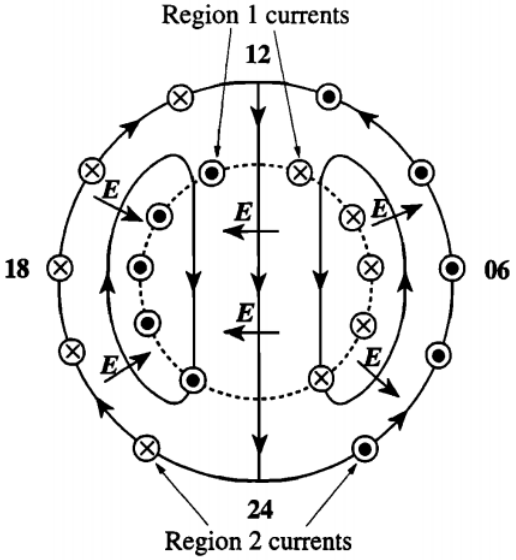

FIGURE 1.13: Field aligned currents in the polar cap taken from Cowley [2000]. The dotted line indicates the edge of the polar cap, marking the boundary between the open and closed field lines.

ionospheric flow convection during Dungey conditions and the Region 1 and 2 currents in and out of the polar cap.

1.4.4 The Aurora

As discussed in the general overview of this chapter, auroras are an integral part of this thesis. The auroras on Earth are driven by complex and dynamic interactions between the solar wind and the Earth's magnetosphere (described in Sections 1.3 and 1.4 respectively); studying auroral images provides insight into these interactions. Some of the key aspects of the aurora on a global scale are demonstrated in Figure 1.14. This figure shows a UV image of the southern hemisphere auroral regions taken from a high altitude spacecraft; this observation were presented by Fear et al. [2015]. The image has been projected onto a magnetic local time/ magnetic latitude grid, with noon at the top and dawn to the right. The colour of the pixels is determined by the intensity of the UV emission (the red area at the top of the image is due to day glow).

As previously discussed, the main auroras occur in ovals in both hemispheres centered approximately over the magnetic poles (indicated in Fig. 1.14). They occur on the closed field lines which encircle the open field lines of the polar cap and some of the most dynamic auroral displays occur within the nightside auroral oval. Poleward of the

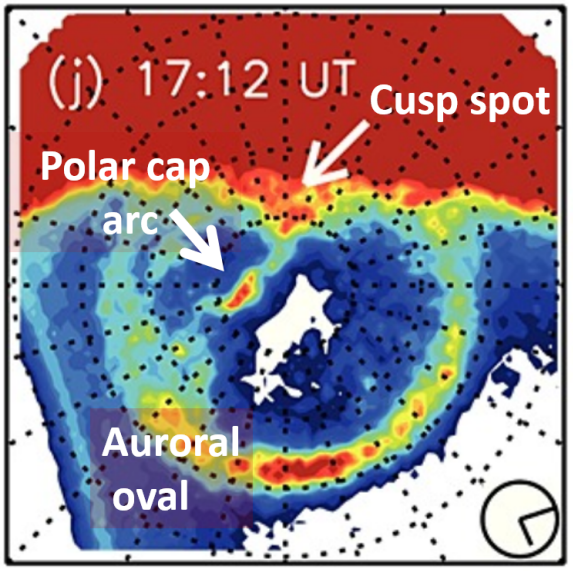

FIGURE 1.14: Global scale features of the aurora from a UV imager on board a high altitude spacecraft adapted from Fear et al. [2015]. Noon is at the top and dawn is to the right.

auroral oval, a thin filament of aurora can be seen connecting the day and nightside oval in Fig. 1.14. This feature has been labelled as a polar cap arc, this kind of auroral phenomena are the focus of this thesis and will be discussed in depth in Section 1.5.

The cusp (labelled as the polar cusp in Fig. 1.8) is the region where solar wind can directly enter the Earth's ionosphere. The auroral signature of dayside reconnection is known as the 'cusp spot' (e.g. Sandholt et al. [1996]). During northward IMF, the cusp spot is driven by lobe reconnection and is located just poleward of the auroral oval [Milan et al., 2000b]; this is indicated in Fig. 1.14 by a white arrow. The position the cusp spots form, and subsequently the location of lobe reconnection, is dependent on the IMF B_Y component (e.g. Sandholt et al. [1996], Milan et al. [2000a]), as discussed in Section 1.4.2.

From the ground, the aurora can generally be classified into two types: diffuse and discrete (for example Akasofu [1974] and references therein). Diffuse aurora is a homogeneous band of luminosity which appears as a singly connected oval, present even during geomagnetically quiet conditions. This kind of aurora is thought to be formed by wave-particle interactions in the plasma sheet where particles are pitch-angle scattered into the loss cone [Ni et al., 2008, Nishimura et al., 2010]. Discrete aurora are bright narrow strips of luminosity known as auroral arcs (e.g. Knudsen et al. [2001], Partamies et al. [2010], Whiter et al. [2013]). Discrete auroras generally occur at the poleward edge

of the main auroral oval and are caused by processes in the magnetotail [Akasofu, 1974]. The famous curtain-like structure of the aurora when seen from the ground is illustrated in Figure 1.15, as an example of discrete aurora.

FIGURE 1.15: Dynamic aurora over Finnish Lapland. Photo credit Maxime Grandin.

1.4.4.1 The Ionosphere and auroral precipitation

Auroras are generated by particles (mostly electrons but some protons and heavier ions) being accelerated down the Earth's magnetic field lines in the polar regions (known as particle precipitation) and colliding with atmospheric particles. These collisions excite the atmospheric particles to higher energy states which then release photons of light as they return to ground state. These interactions occur in the ionised conducting layer of the Earth's upper atmosphere, known as the ionosphere.

The ionosphere is a vast region spanning from approximately 90 km to 1000 km in altitude, where it essentially merges into the plasmasphere in the inner magnetosphere [Baumjohann and Treumann, 1996]. It can be separated out into different layers by considering the electron density. The E-region (between 90-120 km) is dominated by neutral molecules (such as N_2 and O_2). Above this is the F-region, which during the

daytime can be separated into F1 (150-220 km) and F2 (220-600 km). The ionosphere is predominately formed by atmospheric particles being ionised by UV and X-ray radiation from the Sun, known as photoionization [Rees, 1989]. During the night time there is no solar radiation, and the E and F1 regions mostly disappear. However particle precipitation on the nightside, which generates the aurora, also ionises the atmospheric particles. This is known as impact ionisation [Kivelson and Russell, 1995].

The depth at which precipitating particles penetrate into the atmosphere is dependent on their energy, with higher energy particles precipitating deeper into the atmosphere. The classic green aurora (such as in Fig. 1.15) is caused by collision with oxygen atoms between approximately 110-130 km, which results in emission at 557.7 nm. The red aurora sometimes seen at the top of auroral rays (at 630.0 nm), is due to lower energy precipitation ($<$ 1 keV) and is emitted by an atomic oxygen with a peak emission height in the F-region at 250 km [Jones, 1974]. Blue aurora (at 427.8 nm) is a nitrogen emission generated by high energy precipitation ($>$ 10 keV), generally seen at altitudes below 100 km [Kivelson and Russell, 1995]. By measuring different auroral emissions, it is possible to get the characteristics of particle precipitation (e.g Rees [1963], Rees and Luckey [1974]); this technique will be used in this thesis (discussed in Section 2.1.1.1).

1.4.4.2 Auroral Substorm

Auroral substorms describe a sequence of events in which the main auroral ovals are disturbed and large scale reconfiguration of the Earth's magnetosphere occurs. Substorms can generally be thought of in three phases known as growth, expansion and recovery [Akasofu, 1964, McPherron, 1970].

The process begins with 'quiet' arcs which are east-west aligned in the midnight sector of the main auroral oval. During growth phase, dayside reconnection is occurring and open flux is being added into the magnetotail. This results in the polar caps expanding and these quiet arcs moving equatorward to lower latitudes. As dayside reconnection continues, more open flux and hence more energy is stored in the magnetotail until finally there is a big release of energy known as substorm onset. There is some controversy over what causes substorm onset with some arguing that it is tail reconnection at the near Earth neutral line that leads to the explosive substorm release (e.g. Angelopoulos et al. [2008]) while others suggest it is caused by current disruption (e.g. Lui [2009]).

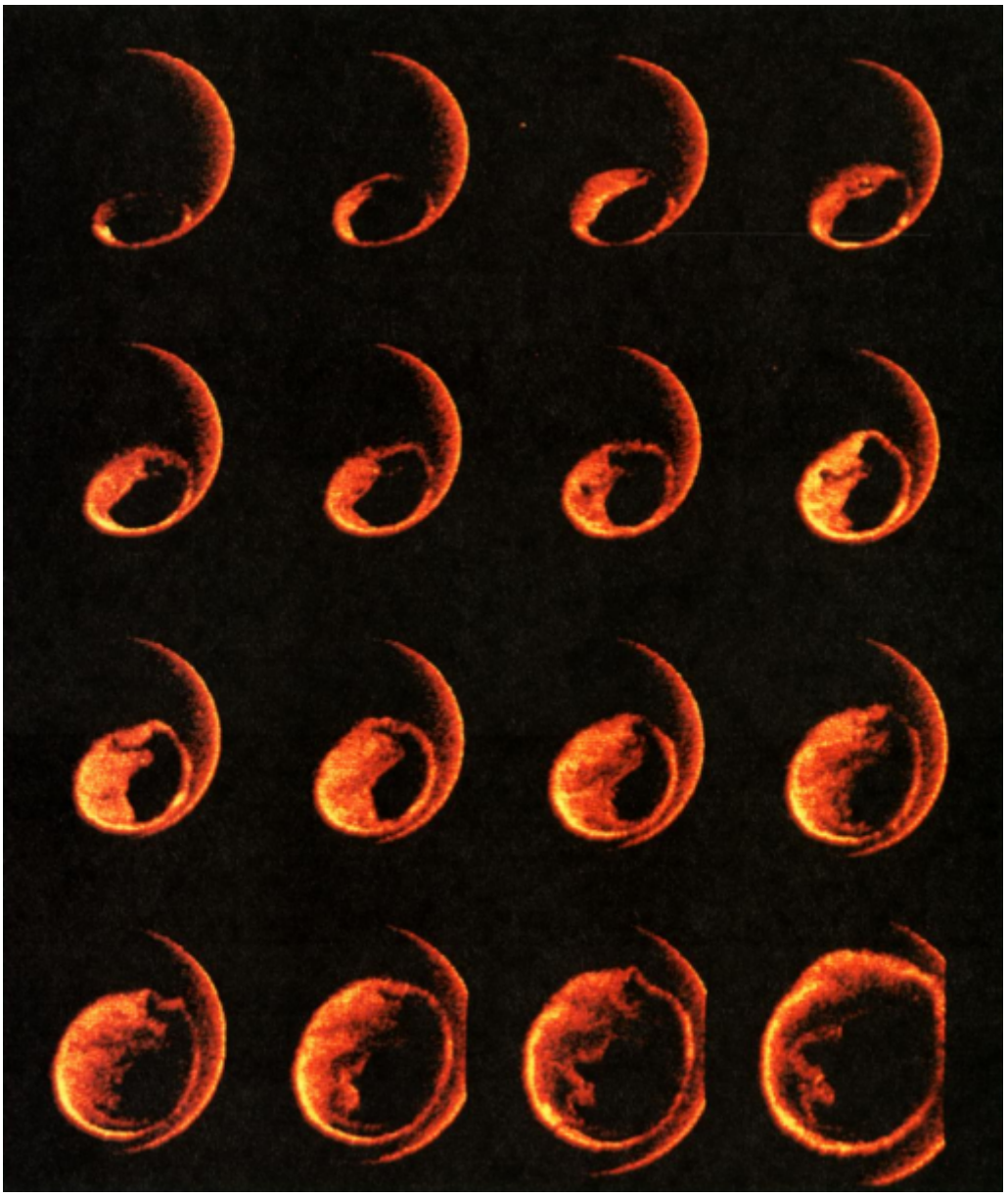

FIGURE 1.16: Observation of an auroral substorm over the Southern hemisphere observed by Dynamics Explorer 1 [Frank and Craven, 1988].

At onset, there is a sudden brightening in the most equatorward arc or the formation of a new arc [Akasofu, S.-I., 1977] followed by a rapid poleward expansion known as the expansion phase. This is demonstrated in Figure 1.16 which shows sequential UV images of the southern hemisphere polar region (similar to Fig. 1.14) taken by a high altitude spacecraft. In the first image a bright spot corresponding to substorm onset can be seen; as the images progress (left to right) bright auroral emission can be seen in the previously dark polar cap region. This is caused by the closure of open flux in the magnetotail. The expansion phase is where the most dynamic discrete aurora occurs and typically lasts between 30-50 minutes.

Lastly, during the recovery phase, the most poleward arc will start to move equatorward as the magnetosphere works to restore its dipolar configuration. The recovery phase can last around two hours.

1.4.4.3 Small-scale aurora

Auroral scales can be of hundreds of kilometres down to tens of metres; higher resolution imaging shows that arcs often contain internal sub-structure [Partamies et al., 2010]. Small scale aurora on scales of tens of metres were first reported by Maggs and Davis [1968] and Davis [1978]. As technology has improved, the ability to measure these small scale auroral features has grown. It is important to understand auroral structure at all scales, particularly as the small scale processes often affect the bulk properties of a plasma.

Quasi-period, small-scale distortions have been observed to develop along auroral arcs (e.g. Hallinan and Davis [1970], Trondsen and Cogger [1998]). Vogt et al. [1999] studied the properties a series of anti-clockwise vortices, known as curls, finding them to have typical wavelengths of 5 km at an assumed auroral altitude of 100 km. Auroral curls are thought to originate from Kevin-helmholtz instabilities [Trondsen and Cogger, 1998]. Larger scale deformations, such as auroral folds have also been observed with a characteristic size of 20 km [Hallinan and Davis, 1970]. More recently, Dahlgren et al. [2010] observed even smaller boundary undulations, or as they term them, auroral 'ruffs'. They observed these features superimposed on top of larger scale deformations and found a peak to peak amplitude in magnetic zenith of less that 800 m (at an assumed auroral height of 100 km).

A lot of small scale structure is thought to be caused by Alfvénic waves; these are low frequency waves in which the ions oscillate perpendicular to the direction of the wave propagation and the magnetic field acts as a restoring force [Stasiewicz et al., 2000, Chaston et al., 2003, 2007]. Recently, Kalmoni et al. [2018] demonstrated that auroral beads during substorm onset are likely the signature of kinetic Alfvén waves driven unstable in the magnetotail. Auroral beads are small scale structures (30-100 km) observed along the substorm onset arc which evolve over time to larger scale sizes.

One of the things this thesis will do is look into the small scale structures within polar cap arcs.

1.4.5 Precipitation in the polar cap

As previously discussed, the polar cap is typically a dim region encircled by the main auroral ova,l however particle precipitation occurs across the entire polar cap and was first classified by Winningham and Heikkila [1974]. Most commonly, weak, uniform, electron precipitation, known as polar rain [Baker et al., 1986], enters the ionosphere via open field lines. These electrons are thought to originate from the field-aligned component of the suprathermal population of the solar wind, known as the 'strahl' [Fairfield and Scudder, 1985]. In order for particles to enter the polar cap from the upstream magnetosheath, they need to have thermal speeds greater than the tailward bulk flow. This results in a noon-midnight gradient in the polar rain across the polar cap, first reported by Torbert et al. [1981], and a lack of ion precipitation (as the larger mass of ions results in lower thermal speeds, and therefore ions typically do not travel fast enough to meet this condition). Furthermore, polar rain shows clear hemispheric preferences depending on the IMF B_x component whereby the hemisphere with field lines in the same direction of as the solar wind experience a higher intensity of polar rain [Yeager and Frank, 1976]. Fairfield and Scudder [1985] suggest that this is due to these field lines pointing more directly towards the solar wind electron flux and hence these particles can more easily enter the Earth's ionosphere in this hemisphere. Figure 1.17 demonstrates an example under negative IMF B_x conditions, where polar rain is more intense in the northern hemisphere. In this figure, an open field line in northern hemisphere lobes is shown doubled back on itself such that the 'end' that is still in the solar wind can be seen to be parallel with the IMF B_x component and therefore the polar rain electrons can enter the magnetotail more readily. The opposite is true for the southern hemisphere when the B_x component is positive. Polar rain has also been found to exhibit dawn-dusk gradients (which are correlated with the IMF B_y component [Meng and Kroehl, 1977]), be more intense during periods of southward IMF (when the merging rate is high) and demonstrate seasonal dependencies. Newell et al. [2009] unified these properties by suggesting that the further down stream a field line crosses the magnetopause (or points less directly towards the solar wind), the weaker the polar rain.

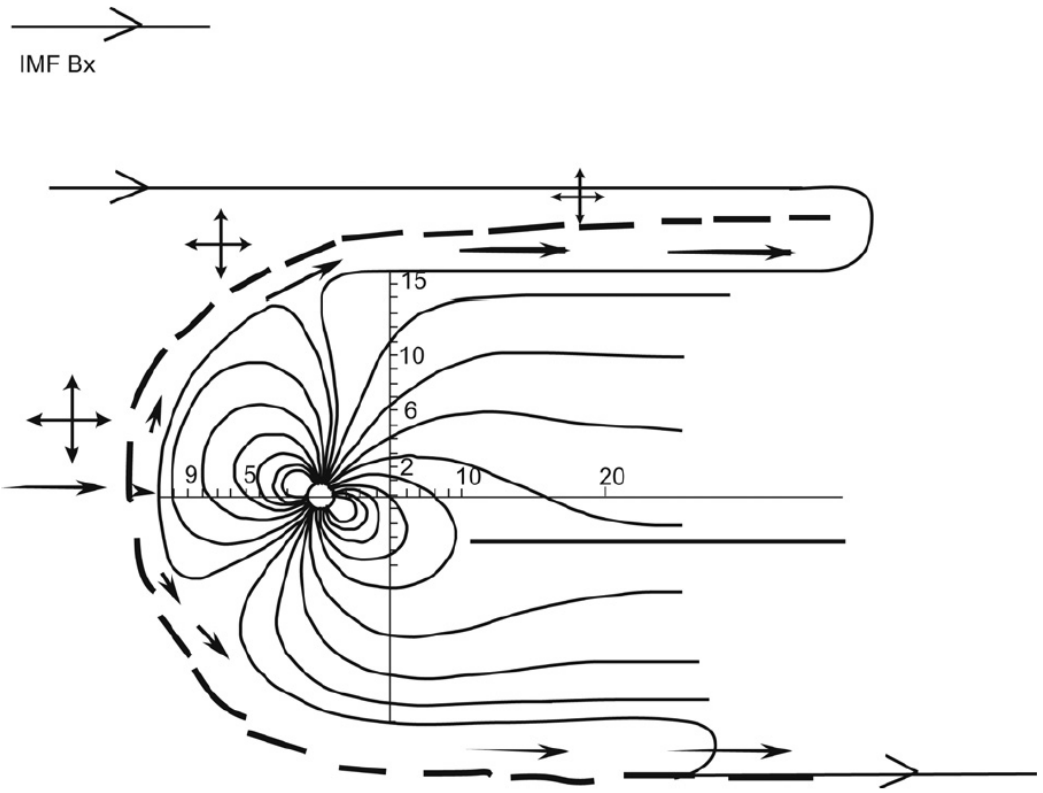

FIGURE 1.17: A schematic of the Earth's magnetosphere during IMF $B_x < 0$ conditions when polar rain is favourable in the northern hemisphere taken from [Newell et al., 2009].

During northward IMF, the otherwise homogeneous polar rain precipitation, has been seen to be interrupted by structured, localised precipitation, known as polar showers [Hardy, 1984, Hardy et al., 1986]. These showers can be classified depending on the presence, or absence, of proton precipitation (known as 'type A' and 'type B' polar showers respectively [Shinohara and Kokubun, 1996]). Type A polar showers, associated with ion precipitation, are generally more intense than type B showers, which are electron-only intensification's. Using one year of particle data from low-latitude spacecraft, Shinohara and Kokubun [1996] found that the type A showers showed no clear dependence on the IMF B_x or B_y components, whereas type B demonstrated a statistically similar dependence on the IMF conditions as polar rain (discussed above). This led Shinohara and Kokubun [1996] to suggest that the properties of the type A polar showers are similar to boundary sheet plasma and are therefore consistent with occurrence on closed field lines, whereas the type B polar showers have similar properties to polar rain and are consistent with open field lines.

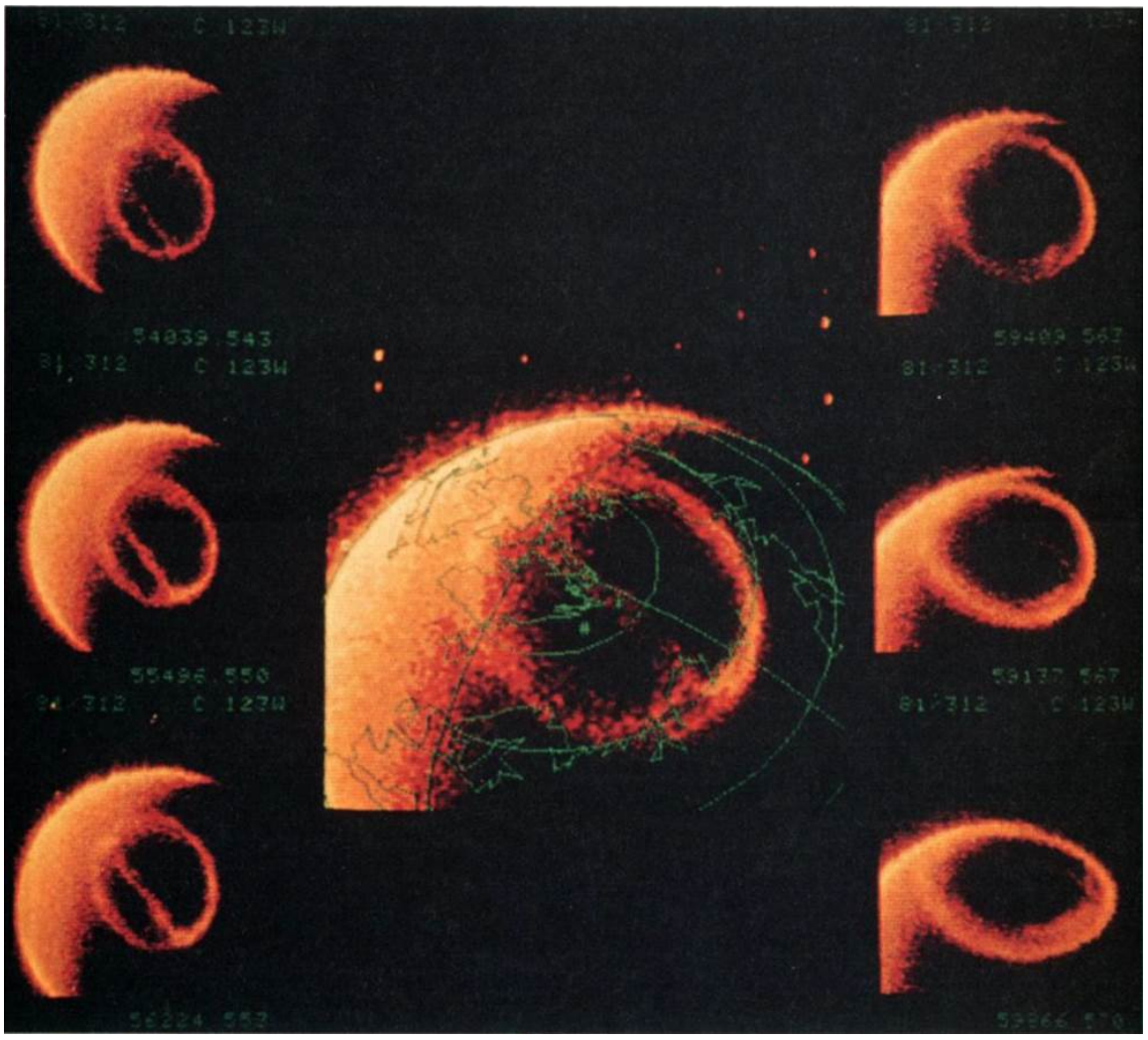

FIGURE 1.18: The theta aurora observed by DE-1 [Frank et al., 1982].

1.5 Polar cap arcs

The main focus of this thesis is investigating the nature of auroras occurring within the typically 'dark' polar cap region, known as polar cap arcs (PCAs). These arcs were first discovered over a century ago by Mawson [1916, 1925] during an Antarctic expedition. Polar cap arcs protrude from the nightside of the auroral oval and are correlated with periods of northward IMF and low magnetospheric activity [Davis, 1963, Berkey et al., 1976, Ismail et al., 1977, Lassen and Danielsen, 1978, Gussenhoven, 1982]. Their location in the polar cap and their motion have been found to be dependent on the IMF B_y component [Frank et al., 1985, Huang et al., 1989, Craven et al., 1991, Valladares et al., 1994, Kullen et al., 2002]; however, there are exceptions to this dependence (e.g. Hosokawa et al. [2011]).

There is some confusion surrounding the terminology associated with polar cap arcs with terms such as high latitude arcs, sun-aligned arcs, theta aurora and transpolar arc, being used interchangeably and without consensus. In this thesis, I adopt the use of polar cap arcs as the general 'umbrella' term for all arcs occurring in the polar cap, similar to the review paper by Zhu et al. [1997]. However, transpolar arcs or theta aurora are considered to be polar cap arcs formed on closed field lines as adopted in a recent review by Fear [2019].

1.5.1 Historical observations

During the International Geographic Year (IGY), 1957-1958, several articles on polar cap arc morphology were published using all sky camera data (for example, Davis [1960, 1962, 1963], Gustafsson [1967]). These studies noted the Sun-Earth orientation of these arcs, with Gustafsson [1967] reporting an angular distribution of 20° relative to the direction of the Sun. However, these studies were typically of isolated arcs and limitations in the field of view meant that a more global picture could not be built. In the 1970's, after the launch of low altitude spacecraft (for example, the Defence Meteorological Satellite Program (DMSP) and International Satellites for Ionospheric Studies (ISIS) missions), studies into the relationship between polar cap arcs and the auroral oval were possible using visible wavelength images of polar cap arcs combined with in-situ particle measurements (e.g. Meng and Akasofu [1976]). However, these studies were restricted to dark region observations due to the limitations of using visible wavelength cameras. Finally in the early 1980's, after the launch of Dynamics Explorer 1, the first satellite UV images of a global polar cap revealed large scale sun-aligned arcs emerging from the nightside oval and joining the dayside oval, forming a Greek letter theta (see Figure 1.18) [Frank et al., 1982, 1986]. This phenomena was termed 'theta aurora' or when considering just the arc, 'transpolar arcs'. The energies of particle precipitation above these arcs were found to be of similar energy to those precipitating above the main auroral oval, suggesting that these arcs are also formed on closed field lines [Frank et al., 1982, Peterson and Shelley, 1984, Menietti and Burch, 1987]. Furthermore, other observations have shown polar rain (precipitation on open field lines described in Section 1.4.4) on either side of a sun-aligned arc [Hoffman et al., 1985]. This suggests that the arc was surrounded by open field lines and that the closed field lines it was formed on were somehow bifurcating the polar caps. These reports were further supported by the launch of other spacecraft

(e.g. the International Sun Earth Explorer, ISEE) and reports of filamentary structures found in the lobes that were similar in origin to boundary sheet plasma [Huang et al., 1987, 1989]. However, at the same time observations suggesting polar cap arcs were formed on open field lines were also being reported: Hardy et al. [1982] presented observations of polar cap arcs embedded within polar rain and Gussenhoven and Mullen [1989] proposed relativistic electrons as the polar cap arc particle source. Therefore, the topological nature of polar cap arcs (i.e. whether they exist on open or closed magnetic field lines) is not clear.

As more spacecraft were launched, observations of simultaneous polar cap arcs in both hemispheres emerged [Mizera et al., 1987, Obara et al., 1988, Craven et al., 1991], which supported the idea that they were formed on closed field lines. However, Østgaard et al. [2003, 2007] presented observations of a 'non-conjugate theta aurora', in which a large-scale theta aurora was seen in one hemisphere, with particle precipitation suggestive of closed field lines, but no arc was observed in the other hemisphere. The so called non-conjugate theta aurora is problematic for both open and closed field line topologies and will be discussed in more detail in Section 1.5.3.3.

Many different mechanisms have been put forward to explain polar cap arcs, some of which predict that the arcs form on open field lines whilst others suggest closed field lines. This is an issue still very much under debate and will be addressed in this thesis. One reason there is so much controversy surrounding polar cap arcs is that there may be more than one type, i.e. there is more than one mechanism forming polar cap arcs during northward IMF. This possibility will be discussed further in 1.5.3.1. However, there are still questions surrounding arcs forming on either topology, such as, if they are formed on closed field lines, how did those closed field lines get into the open polar cap? And if they are formed on open field lines, what is accelerating the particles to high enough energies to generate the auroras? Some possible answers to these questions are discussed below.

1.5.2 Formation mechanisms

As discussed above, there has been a lot of controversy surrounding the formation of polar cap arcs. In a review of polar cap arcs, Zhu et al. [1997] outlined three configurations of the magnetotail that could give rise to these arcs: oval expansion, tail lobe

bifurcation, and open field line. More recently, Newell et al. [2009] and Fear and Milan [2012a] also reviewed several generation mechanisms in the context of more up-to-date observations. A summary of some of these proposed mechanisms is given below.

1.5.2.1 Oval expansion

The oval expansion configuration was first described by Meng [1981a] following observations of continuous soft (<1 keV) electron precipitation extending from the main auroral oval up to high latitudes (> 80°) and simultaneous observations of sun-aligned arcs in the polar cap. Meng [1981a] proposed that, during northward IMF, the central plasma sheet thickens and this leads to the expansion of the poleward portion of the auroral oval. However, in a later paper Meng [1981b] does caution that the soft electron precipitation was not conclusive of closed field lines and could in fact be on open field lines caused by the polar cusp or even plasma from the solar wind (polar rain).

Figure 1.19 shows two possible magnetotail configurations, in line with the oval expansion idea, illustrated by Makita et al. [1991]. On the left hand side a tilted plasma sheet is depicted; this configuration is consistent with observations of polar cap arcs occurring on opposite sides of the polar cap in opposite hemispheres (i.e. Craven et al. [1991]). On the right hand side of Fig. 1.19, an asymmetrically expanded plasma sheet is depicted.

The oval expansion mechanism particularly explains polar cap arcs seen on the dawn and dusk sides of the polar cap that are parallel with the main auroral oval, but it cannot explain arcs occurring in the midnight sector (for example, the theta aurora observed by Frank et al. [1982]). Furthermore, this configuration suggests that the arcs are in fact occurring on the poleward edge of the auroral oval, essentially identifying regular auroral features observed in the main oval as polar cap arcs.

1.5.2.2 Bifurcated magnetotail lobes

One mechanism which tried to explain how plasma sheet plasma could enter the magnetotail lobes was proposed by Rezhenov: [1995]. They suggested that an instability, possibly a ballooning instability acting on the highly curved field lines, in the plasma sheet could result in a 'tongue' of plasma sheet plasma moving tailward to field lines which map further poleward. This mechanism predicts that polar cap arcs emerge near

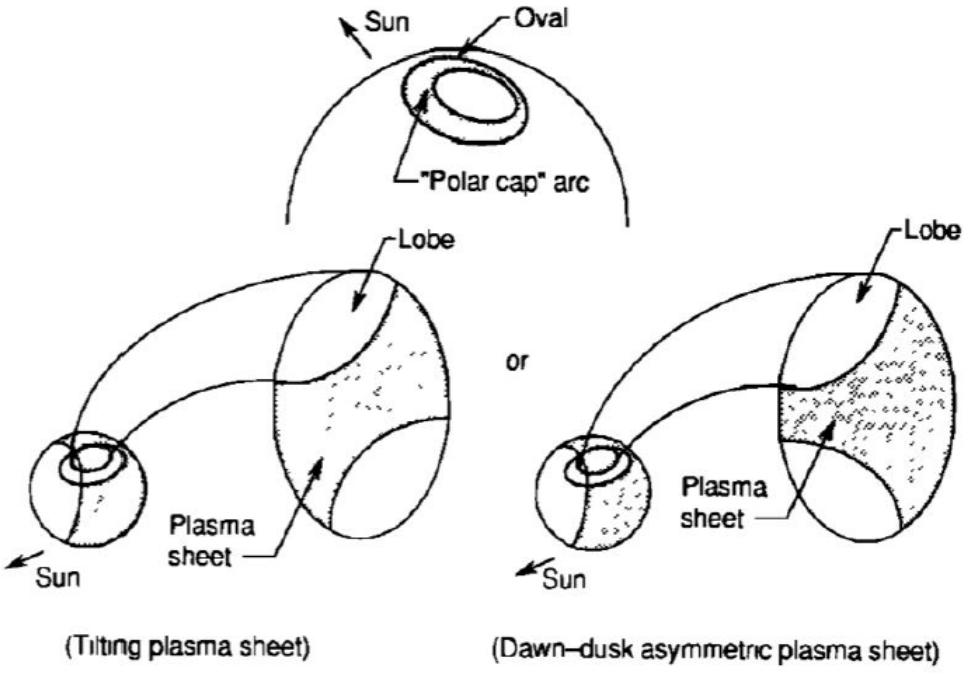

FIGURE 1.19: Possible configurations of the plasma sheet that could result in polar cap arcs, taken from Makita et al. [1991].

midnight and grow sunward and, depending on the IMF B_y, develop towards the dawn/-dusk side of the polar cap. However, Fear and Milan [2012a] suggest that this model is unphysical due to the significant distance between the central plasma sheet and the open closed field line boundary. Furthermore, this mechanism cannot explain the observed dawn-dusk motion of polar cap arcs which has been linked to the IMF B_y component (e.g. Valladares et al. [1994]).

Several mechanisms have been proposed that argue that a change in the IMF B_y component triggers polar cap arc formation. This idea was first introduced by Chang et al. [1998] who suggested an arc formed on the dusk/dawn side of the polar cap could become 'detached' when a change in the IMF B_y or B_x component causes a change in the magnetopause reconnection site, essentially leaving behind a channel of closed field lines within the lobes on which the polar cap arc forms. Kullen [2000] also discuss the idea of an IMF B_y trigger for polar cap arcs using the Tsyganenko 1989 model. Their mechanism follows on from the Meng [1981a] idea of plasma sheet twisting, (depicted by Makita et al. [1991] and shown here in Fig. 1.19), and goes further to suggest that when there is an IMF B_y sign change in an already twisted magnetotail, a channel of closed flux is 'left behind' in the magnetotail lobes. This mechanism, similar to the oval expansion

configuration discussed above, can explain the arcs in the opposite hemispheres being mirrored about the noon-midnight meridian. Furthermore, in several model simulations (e.g. Naehr and Toffoletto [2004], Kullen and Janhunen [2004]), polar cap arcs cannot be generated without an IMF B_y sign change. However, Cumnock [2005] presented observations of 19 polar cap arc events where only three formed following a change in the IMF B_y component. These observations cannot be explained by the mechanisms described by Chang et al. [1998] and Kullen [2000].

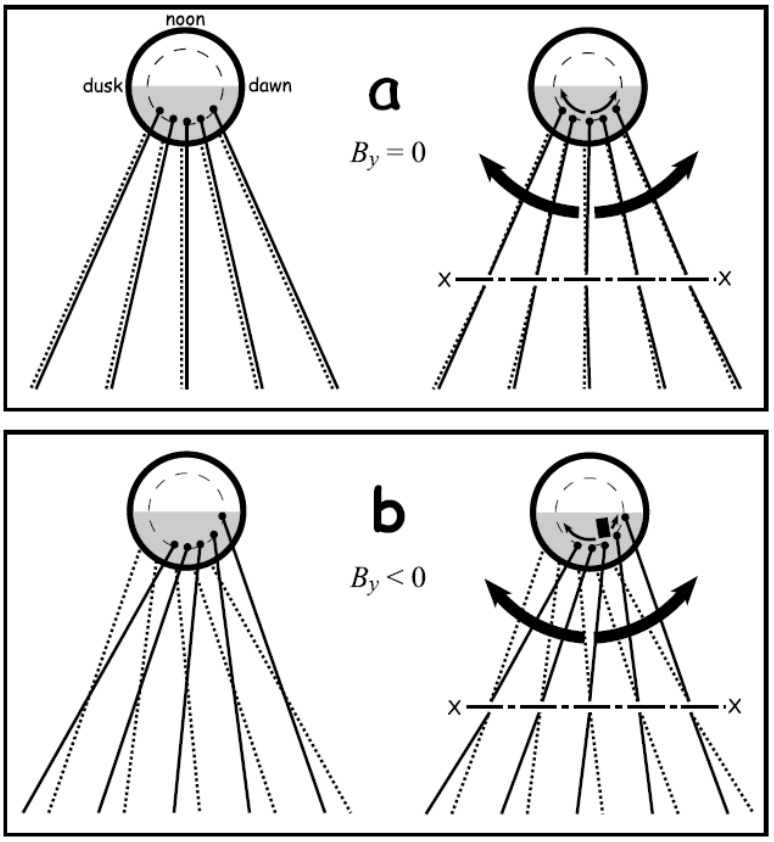

FIGURE 1.20: Cartoon schematics looking down on the polar cap and the magnetotail lobes (the northern hemisphere field lines are indicated by solid lines and the southern hemisphere field lines in the southern hemisphere are indicated by dotted lines) under (a) $B_y = 0$ and (b) $B_y > 0$ conditions taken from Milan et al. [2005]. The figure on the left of each panel indicates the the convection (large black arrows) after nightside reconnection has occurred at the X-line (indicated by horizontal dot-dashed lines). In figure (b) a transpolar arc is formed in the polar cap on the footprints of the field lines which straddle midnight (indicated by a black rectangle).

Milan et al. [2005] proposed a mechanism based on the nightside closure of open magnetotail flux during northward IMF, when dayside reconnection is suppressed and the magnetotail is twisted due to an IMF B_y component. The IMF B_y component is introduced to the tail some hours before during an earlier period of dayside reconnection and

results in the northern and southern hemispheric lobes twisting about the GSE X axis (e.g. Tenfjord et al. [2015], Reistad et al. [2016], Browett et al. [2016]), due to asymmetric addition of flux in the lobes [Cowley, 1981, Grocott et al., 2003, 2007]. Figure 1.20 illustrates what the magnetotail lobes look like from above in the case of (a) $B_y = 0$ and (b) $B_y < 0$; the latter case demonstrates the twisting of the northern and southern lobes. The horizontal dot-dashed line in the right hand image for each scenario shows the reconnection x line with the subsequent return flow of the newly closed field lines indicated by black solid arrows (see Dungey cycle Section 1.4.1). In the case of the $B_y < 0$, the return flow of the newly closed flux can be seen to be asymmetric about magnetic midnight [Grocott et al., 2003, 2007], referred to by Milan et al. [2005] as TRINNIs ("Tail Reconnection during IMF-Northward Non-substorm Intervals"). Milan et al. [2005] suggest that under these conditions, the field line that straddles midnight will become stuck after it undergoes reconnection, due to equal and opposite forces being applied to either end of the field line as it tries to return to the dayside. Furthermore the lack of magnetospheric convection (due to the assumed lack of dayside reconnection) means that there is nothing driving the newly closed field lines back to the dayside. This mechanism predicts that as more field lines are closed at this point, a tongue of closed plasma will protrude into the open magnetotail lobes, growing from the nightside oval across the polar cap, on which the transpolar arc will form (represented by the black square in the polar cap in right hand image for scenario b in Fig. 1.20).

This mechanism was consistent with previous observations, for example that polar cap arcs will form in both hemispheres simultaneously, mirrored about the noon midnight meridian [Gusev and Troshichev, 1986]. Furthermore, the Milan et al. [2005] mechanism predicts that the side of the polar cap the arcs will form will be determined by the IMF B_y component introduced several hours before formation. This relation has subsequently been verified statistically by Fear and Milan [2012a]. In a follow-up paper, Fear and Milan [2012b] also found that TRINNI flows were present in 76% of the events identified in Fear and Milan [2012a] (where supporting ground-based measurements were available). They suggested flows were not observed in the remaining events due to instrumentation limitation. Several different recent case studies have also validated this mechanism, for example Goudarzi et al. [2008], Fear et al. [2014, 2015] and Carter et al. [2017].

Additionally, Milan et al. [2005] suggest that polar cap arc motion is driven by high latitude reconnection (as discussed in Section 1.4.2). Figure 1.21 gives a cartoon schematic

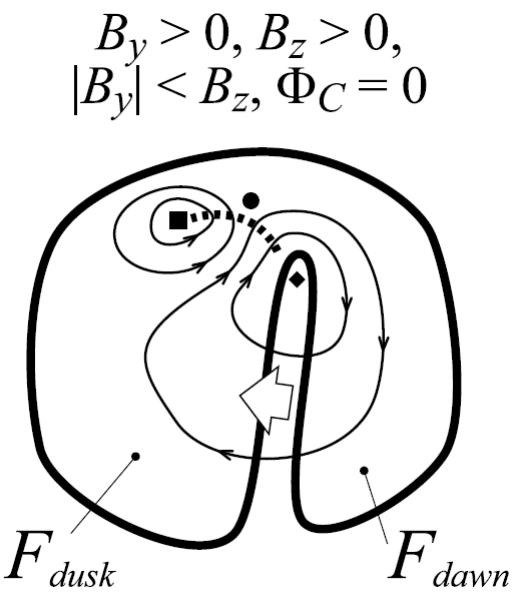

FIGURE 1.21: Cartoon schematic of ionospheric flows associated with a polar cap arc event during high latitude reconnection taken from Milan et al. [2005]. The thick solid black line indicates the open-closed boundary, the thin black lines indicate the direction of ionospheric convection driven by high latitude reconnection and the dotted line shows the footprint of the reconnection site known as the 'merging gap'.

of the ionospheric flow associated with lobe reconnection during IMF $B_y > 0$ conditions when a polar cap arc is present. The solid black line represents the open-closed field line boundary, where the polar cap arc is formed on a 'tongue' of closed flux which is dividing the polar cap into dawn and dusk sectors. The dotted line represents the footprint of the lobe reconnection site, also known as the merging gap. In this scenario, the reverse cell convection pattern can be seen but as the open field lines are 'stirred', flux is transferred from the dusk to the dawn cell across the merging gap. This results in the expansion of the dawn convection cell and contraction of the dusk cell. We know from the frozen-in theorem (Section 1.2.3.1), that two different plasmas cannot mix and hence plasma cannot flow across the open-close boundary where the polar cap arc is situated. This results in polar cap arc moving with the plasma, duskward across the polar cap (indicated by the large arrow), as the dawn cell expands. This mechanism is consistent with the observed correlation between the direction of polar cap arc motion and the IMF B_y component (e.g. Valladares et al. [1994]).

1.5.2.3 Open field lines

Due to their high latitude location, polar cap arcs have often been suggested to be formed on the open field lines that thread the polar cap regions. As discussed in Section 1.4.5, intensification of polar rain, termed polar showers (with and without ion precipitation), have been found to be correlated with northward IMF and are hence naturally associated with polar cap arcs. Furthermore, there have been reports of polar cap arcs embedded within the homogeneous polar rain that is present across the polar cap [Hardy et al., 1982]. Carlson and Cowley [2005] investigated the acceleration mechanism of polar rain by first assuming that the source region of polar cap arcs was polar rain and worked backwards to estimated several electrodynamic parameters using kinetic theory, which could then be compared to observation. Using this approach, they found good agreement between their estimates and observations of polar cap arcs from Carlson et al. [1988]. Their analysis indicates that polar cap arcs can be produced by field-aligned acceleration of polar rain electrons. Carlson and Cowley [2005] state that any modest mechanism that drives shear flows across open field lines could cause this acceleration, for example at the boundaries between the 'lobe' cells and 'merging' cells. The authors state that they expect polar cap aurora caused by accelerated polar rain to be present whenever the IMF is northward, which is approximately half the time.

1.5.3 Remaining Issues

1.5.3.1 Multiple formation mechanisms

Some authors have suggested that multiple mechanisms may be required to explain the discrepancy in the observations of polar cap auroras. A statistical study by Kullen et al. [2002] classified five different types of transpolar arcs depending on their motion, structure and where they formed within the polar cap. The authors, at the time, could not find a mechanism that explained more than one of these types and hence concluded there must be at least five different formation mechanisms. However, Fear and Milan [2012a,b] found that the observed delay in the IMF B_y correlation and the statistical presence of TRINNI flows suggested they could be explained by the Milan et al. [2005] mechanism; this finding was verified by Kullen et al. [2015] across most of the Kullen et al. [2002] categories. One type that did not show these flows were the arcs classified

as 'bending arcs'; these arcs appear to form on the dayside and move poleward (anti-sunward) into the polar cap. Bending arcs have since been identified as a phenomenon of dayside reconnection under IMF B_y dominant conditions and are thought to be an auroral signature of flux transfer events [Carter et al., 2015].

It has also been argued that polar cap arcs are formed by a more complicated process whereby two different mechanisms, one on the dayside and the other on the nightside, occur simultaneously [Eriksson et al., 2005, Mailyan et al., 2015]. However, it is hard to explain why two independent mechanisms would coincide spatially.

In a ground-based statistical study, Hosokawa et al. [2011] argued that the motion of only some arcs was correlated with the sign of IMF B_y while others moved independently from it. They suggested the motion of the B_y dependent arcs is caused by flux transfer due to lobe reconnection, indicating that the plasma source for these arcs is on or adjacent to open field lines. As the B_y independent arcs are seemingly unaffected by lobe reconnection, Hosokawa et al. [2011] suggest they are formed on closed field lines, indicating a different formation mechanism for each type. However another possible explanation for the apparent difference between "B_y-dependent" and "B_y-independent" polar cap arc motion could be that the motion is driven by polar cap convection as outlined by Milan et al. [2005], which would result in the same spatial patterns as reported by Hosokawa et al. [2011] (see Reidy et al. [2017]).

In a review of polar precipitation and aurora, Newell et al. [2009] suggested that three types of polar cap arc could be determined based on their particle data. The first, a common but weak arc caused by an intensification of polar rain that was associated with electron-only precipitation (similar to the type B polar showers discussed in Section 1.4.5). The second, arcs seen adjacent to the auroral oval associated with higher electron flux and an ion signature. Lastly, a rare high energy type consistent with trans-polar arcs that could be identified by ion and electron precipitation surrounded by weak uniform electron precipitation (i.e. formed on closed field lines within the open polar cap), similar to the type A polar showers discussed in Section 1.4.5. These categories correspond approximately to the configurations discussed by Zhu et al. [1997] outlined above. The use of particle data to determine the topology of the field lines on which polar cap arc forms outlined by Newell et al. [2009] will be explored in this thesis.

1.5.3.2 Difference in ground-based vs spacecraft observations

There are several differences between space- and ground-based observations of polar cap arcs, the most prominent being the apparent discrepancy in polar cap arc occurrence frequency. In a ground-based statistical study using one winter season of data from a high latitude all sky camera (located in Qannaaq, Greenland), Valladares et al. [1994] found polar cap arcs to be present at least 40% of the time. Conversely, in a statistical study using UV images from a high altitude spacecraft (Polar UV), Kullen et al. [2002] found polar cap arcs to be present only 10% of the time. Similarly, over a 5 year interval, 743 arcs were identified by Hosokawa et al. [2011] using an all sky imager in Resolute Bay, Canada whereas Fear and Milan [2012a] found only 130 polar cap arcs using images from a different high latitude spacecraft (IMAGE FUV), although these values are not directly comparable due to cloud and spacecraft coverage. Furthermore, Carlson and Cowley [2005] suggest that weaker polar cap arcs, formed by accelerated polar rain, are present in the polar cap whenever the IMF is northward i.e. half the time; this is in line with the occurrence frequencies observed by Valladares et al. [1994]. This discrepancy could perhaps be explained by the weaker arcs, thought to be formed on open field lines, dominating the ground-based studies but being missed by the high latitude spacecrafts which predominately see the more intense but rarer transpolar arc events formed on closed field lines.

This issue will be explored in this thesis by using low altitude UV imagers which are capable of observing finer-scale auroral structure than the higher altitude spacecraft and hence may be able to observe the weaker arcs formed by accelerated polar rain.

1.5.3.3 Non-conjugate theta aurora

One issue surrounding mechanisms that put polar cap arcs on closed field lines is the so-called 'non-conjugate' theta aurora. Any mechanism that puts polar cap arcs on closed field lines predicts that they will occur in both hemispheres simultaneously. The first example of a transpolar arc observed in both hemispheres simultaneously was presented by Craven et al. [1991] using images from the Dynamics Explorer (DE) 1 and Viking satellites. However two events were presented by Østgaard et al. [2003] with simultaneous observations of the auroral regions in both hemispheres with a polar cap arc observed

in only one hemisphere. Simultaneous low-altitude particle data were also available for these events and it was found that both polar cap arcs had an ion signature comparable to the main oval, which the authors suggested was indicative of their occurring on closed field lines; however no ions were detected in the opposite hemispheres. Conversely, Østgaard et al. [2003] interpret these arcs as being formed as a result of lobe reconnection, implicitly suggesting that they are occurring on open field lines. One further observation of a non-conjugate theta aurora was presented in Østgaard et al. [2007]. Østgaard et al. [2003] suggest a possible explanation for the observations is the difference in conductivity between sunlit and non-sunlit hemispheres, which would lead to the suppression of the arc in the summer hemisphere. They also argue that differences in the polarity of the IMF B_x component could be the cause, as lobe reconnection is favoured in one hemisphere depending on the IMF B_x component. This interpretation is based on a model by Chang et al. [1998] who attribute polar cap arcs to a sudden change in the IMF B_y component (described in Section 1.5.2.2). However, Fear and Milan [2012a] argue that this model is unphysical as it requires the magnetopause reconnection site to map equatorward of the open-closed boundary. Therefore, the interpretation of non-conjugate theta auroras, with some plasma aspects indicative of a closed topology, remains very much an open question. Fear and Milan [2012a] briefly discussed a possible interpretation based on the Milan et al. [2005] mechanism, suggesting that the hemisphere without the polar cap arcs may have experienced lobe reconnection (which, in the Milan et al. [2005] mechanism, drives the motion of transpolar arcs) and hence the arc in that hemisphere could have moved and become indistinguishable from the main oval before the first observations in that hemisphere were available. However, this issue is still unresolved and further exploration is warranted.

This thesis will investigate non-conjugate theta aurora using near-simultaneous inter-hemispheric observations of the aurora regions. Observations of both hemispheres are rare due to the limitation of having two spacecraft in the right position at the right time. This thesis uses data from UV imagers on board low altitude spacecraft (detailed in Chapter 2) which provide almost simultaneous measurements of both hemispheres.

1.6 This thesis

This thesis will investigate the remaining questions surrounding polar cap arcs, outlined above. Chapter 2 will introduce the main instrumentation. In particular, this thesis examines the fine-scale structure of polar cap arcs using ground-based small-scale field of view cameras and low altitude satellite-based UV imagers which are capable of observing much finer details than the high altitude cameras used in previous polar cap arc studies. This thesis will seek to draw some consensus between ground-based and spacecraft observations and shed light on the configuration of the magnetosphere during northward IMF.

Chapter 3 will present a case study which uses multiple ground-based and spacecraft instrumentation. These observations show two polar cap arcs that are consistent with different magnetic field topologies occurring simultaneously in the northern hemisphere. One of these polar cap arcs occurred over Svalbard and is hence analysed using ground-based instrumentation, the other is investigated using in-situ particle measurements.

Following on from this study, Chapter 4 will present a survey of polar cap arcs using UV images from low latitude spacecraft with the corresponding particle data. This survey finds further polar cap arcs consistent with both open and closed field lines (similar to that presented in Chapter 3). It also finds events which are not, at first sight, consistent with either an open or a closed field line topology, including an example of a non-conjugate theta aurora.

In Chapter 5, two polar cap arc events that occurred over Svalbard are presented: one containing an arc consistent with formation on open field lines; the other an arc consistent with closed field lines. The structure and characteristic energy of these polar cap arcs are investigated using world leading instrumentation in the study of small scale aurora.

Lastly in Chapter 6, an overall conclusion is given and avenues for further work are discussed.

Chapter 2

Instrumentation

This chapter will outline the main instrumentation used in the analysis presented in this thesis. Of particular interest are ground-based instrumentation on Svalbard; due to its high latitude location, Svalbard is perfectly situated to study polar cap arcs. Global UV images from low-orbiting spacecraft are used to identify polar cap arcs over Svalbard.

2.1 Optical instruments

2.1.1 The Auroral Structure and Kinetics (ASK) Instrument

The Auroral Structure and Kinetics (ASK) instrument is a multi-spectral, high resolution imager which is world leading in the study of small scale aurora [Ashrafi, 2007, Dahlgren et al., 2016]. It has been located on Svalbard since 2005, apart from one winter season (2005/06) where it was moved to Tromsø. It is located on a shelf at the back of the EISCAT Svalbard building, as shown in Figure 2.1. ASK is maintained and operated by the University of Southampton and KTH, Stockholm.

The instrument consists of three narrow view cameras (shown in Figure 2.2) and two photometers. The ASK detectors are three highly sensitive Andor iXon Electron Multiplying Charged Coupled Devices (EMCCDs). It is cooled to -50°C to reduce noise from thermal electrons. The cameras, which are centered on magnetic zenith, can be fitted with a telescope to reduce the field of view and improve the spatial resolution. With the telescopes, the field of view is $3.1° \times 3.1°$ (which corresponding to 5×5 km at an altitude

FIGURE 2.1: The ASK instrument on the shelf behind the EISCAT building on Svalbard. Photo credit: Dan Whiter

of 100 km) and without the telescopes, the field of view is 6.2° × 6.2° (10 × 10 km at 100 km). These cameras are capable of producing between 20-32 images per second.

Each camera (termed ASK1, ASK2 and ASK3) is fitted with a different narrow passband interference filter to select specific auroral emissions. This thesis makes use of data from ASK1 and ASK3 which respond to prompt auroral emissions.

ASK1 images the N_2 1PG (first positive) (4,1) and (5,2) band emission that dominate the auroral spectrum between 640-800 nm [Semeter, 2003]. This emission is caused by high energy electron precipitation and can be accurately modelled [Ashrafi et al., 2009]. The N_2 1PG band emission is produced by transitions between the vibrational states:

$$B^3\Pi_g - A^3\Sigma_u^+ \tag{2.1}$$

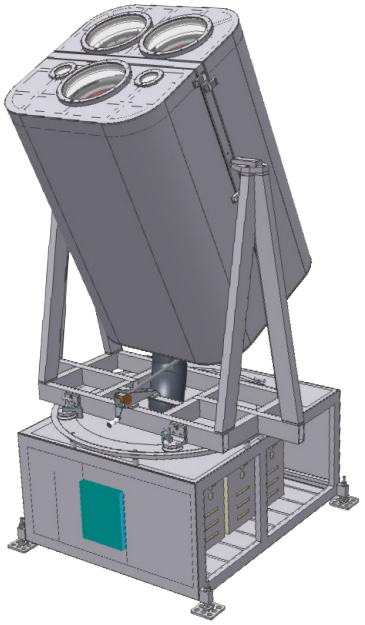

FIGURE 2.2: Schematic of the ASK instrument

where the term symbols Π and Σ give the orbital angular momentum along the internuclear axis of 0 and 1 respectively, the g and u give the parity and the + gives the reflection symmetry. The A and B in front of the term symbols give the electronic state [Banwell, 1994].

ASK3 is sensitive to an atomic oxygen OI emission at 777.4 nm caused by the following atomic transition:

$$3s^5S - 3p^5P \tag{2.2}$$

Here we have used the Russell-Saunders term symbol for atoms: ${}^{2S+1}L_J$, where S is the total spin quantum number, L is the quantum number for the total angular momentum (L =S, P... corresponds to L =0, 1...) and J is the total orbital quantum number [Russell and Saunders, 1925]. If L < S then J = 2L + 1 and hence the 777.4 nm emission line is a multiplet with two weaker emission lines at 777.2 nm and 777.5 nm as there are three possible transitions for J = 1, 2, 3 [Hecht et al., 1985]. The electronic state is given in front of the term symbol.

The emission measured by ASK3 is caused by direct electron impact on oxygen in the F-region ionosphere with an excitation threshold of 10 eV, making this emission a good

measure of low energy precipitation. This emission can also be produced in the lower atmosphere by higher energy precipitation from the dissociative excitation of O_2.

For completeness, the ASK2 camera is sensitive to a long-lived emission from O^+ which emits at 732.0 nm; this can be used to track plasma flows and hence estimate electric fields, although this is beyond the scope of this thesis.

The ASK data is stored in 20 minutes blocks, called megablocks. These data can be preliminary viewed on the ASK website[1] in the form of keograms (vertical cuts down the middle of the images which are stacked in time), demonstrated by Figure 2.3. Once the date and time of interest is located, the data can be read in from tapes (these tapes are located at the University of Southampton and KTH). The images have been binned into 256×256 equally sized pixels, during data acquisition. Once the data are read in, they are then calibrated by subtracting a dark image (which is a combination of dark images taken at the beginning and end of each megablock) and divided by a dark corrected flat image (an image created from cloudy data):

$$\frac{\text{Image - dark}}{\text{Flat - dark}} \tag{2.3}$$

A background image, which is a mean image created from a clear period (stars but no aurora) near to the period of interest, is then subtracted from these images to reduce the noise of the image and make sure the intensity being measured in each pixel is due to the auroral emission. This intensity is then converted into Rayleighs by multiplying by an absolute calibration number and the resolution of the data. The calibration number is found by matching stars in the images to the brightness of stars from a star catalogue [Nagy, 1979]. A value for the emission brightness per image can be obtained by averaging the pixels surrounding magnetic zenith.

The ASK instrument has been used to study auroral features at small spatial scale, for example boundary undulations or 'ruffs' [Dahlgren et al., 2010] (discussed in Section 1.4.4.3) and at high temporal resolution to study flickering aurora [Whiter et al., 2010]. The two main strengths of ASK are the ability to estimate the energy of precipitation and to trace plasma flows, which can in turn be used to estimate electric field strength and direction to very good resolution; these methods are outlined in a review

[1] http://ask1.esr.eiscat.no/keos.html

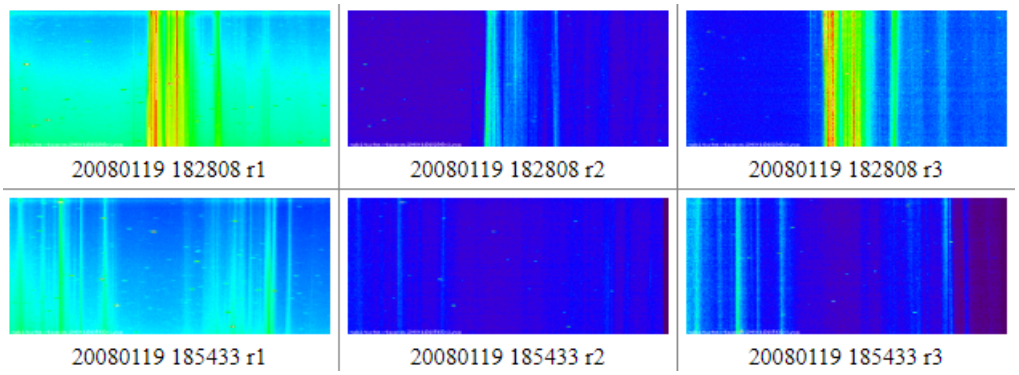

FIGURE 2.3: Examples of ASK keograms located on the website

paper by Dahlgren et al. [2016]. This thesis presents the first small scale observations of polar cap arcs using these capabilities.

2.1.1.1 The Southampton Ionospheric model

The Southampton ionospheric model (described in the appendix of Lanchester et al. [2001]) is used in conjunction with data from the ASK instrument to estimate the energy and energy flux of precipitating particles. The model is a combined electron transport [Lummerzheim, 1987] and ion chemistry model which assumes a neutral atmosphere taken from the MSIS E-90 model thermospheric model [Hedin, 1991]. The ion chemistry part of the model solves the coupled continuity equations for major and some minor atmospheric ion species time dependently. The main input to the model is an electron energy spectrum precipitating at the top of the ionosphere (500 km in the model); in this thesis a Gaussian distribution has been used (this initial condition is verified using radar data in Section 3.2.2.2). The geomagnetic conditions (specifically the AP index and the F10.7 solar radio flux), the time and location are also included as inputs to this model. The AP index is derived from ground based magnetometer data and is used to monitor the geomagnetic activity [Fraser-Smith, 1972]. The F10.7 solar flux is, after sun-spot number, one of the most widely used indices for solar activity; it is a measure of the total emission from the disk of the sun at 10.7 cm, first reported by Southworth [1945] and recently reviewed by Tapping [2013].

The method for combining the model with ASK data was outlined in a paper by Lanchester et al. [2009]. This method compares the ratio of emissions measured by the ASK1 and ASK3 cameras to a modelled relation between the ratio and energy produced by the

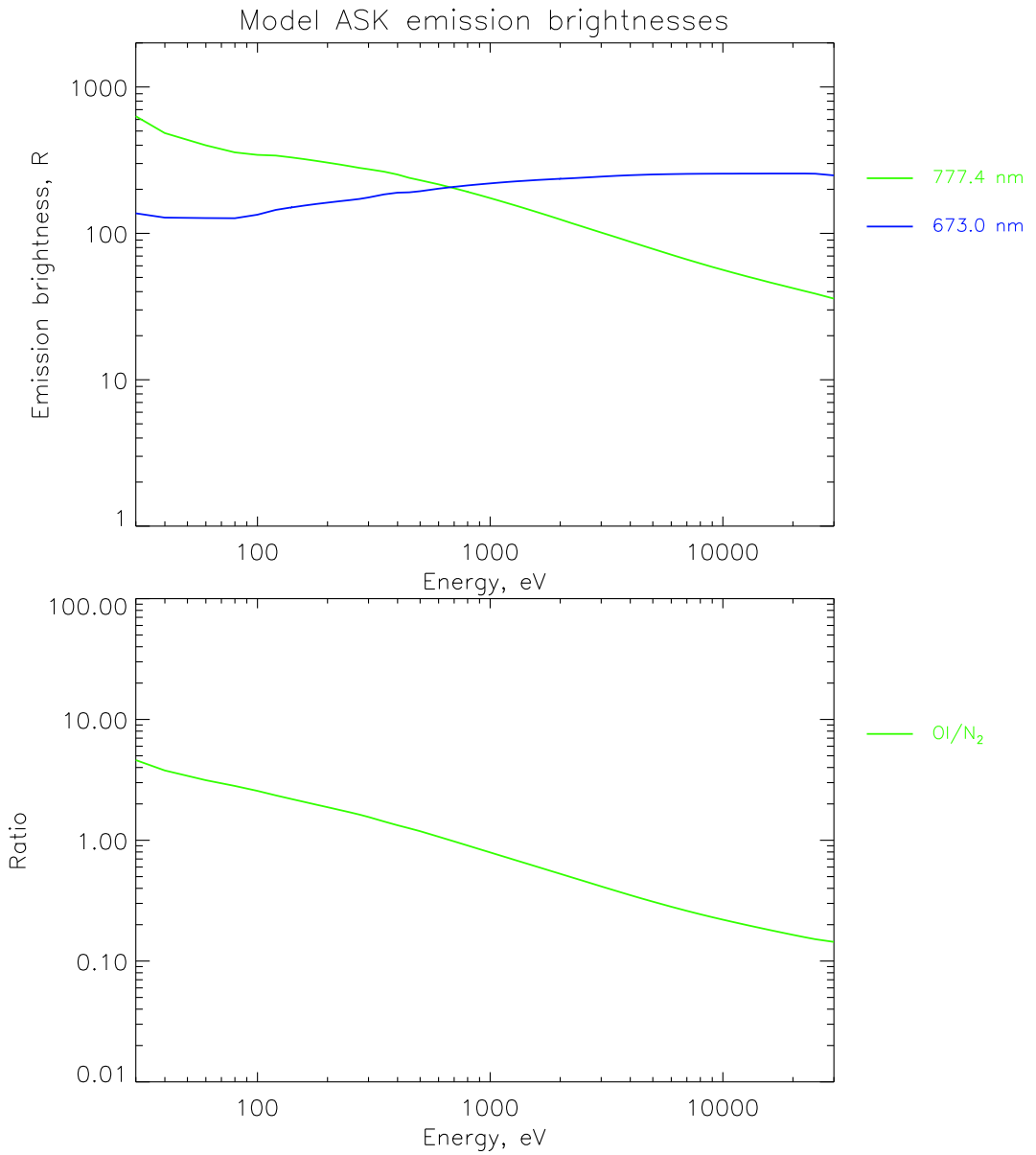

FIGURE 2.4: Emission rates produced by the Ionospheric model for the ASK1 and ASK 3 filters.

ionospheric model. The ASK1 camera has a filter that is sensitive to high energy electron precipitation and the ASK3 camera is sensitive to lower energy precipitation. Hence the ratio of ASK3/ASK1 can provide characteristics of the energy of the precipitating electrons.

Examples of the model production rates, and emission height profiles for the emissions measured by ASK can be found in Whiter et al. [2010], Dahlgren et al. [2011] and Figure 2.4. The height-integrated emissions are used to give a relationship between brightness ratio and peak energy, which is then compared with the measured brightness

ratio to give the peak energy as plotted in the second panel of Fig. 2.4. An estimate of the flux comes from the modelled emission brightness for ASK1 (673.0 nm); Fig. 2.4 shows that above 100 eV, the emission brightness is approximately constant.

This method of estimating the energy and flux of precipitating particle using ASK data and the Southampton Ionospheric model has been used in several studies and has been verified by comparison with other ground based instruments, for example EISCAT, (e.g. Lanchester et al. [2009], Whiter et al. [2010], Dahlgren et al. [2011, 2016]).

2.1.2 The Special Sensor Ultra-violet Spectrographic Imager (SSUSI)

The Special Sensor Ultra-violet Spectrographic Imager (SSUSI) instruments are used to produce maps of the ionosphere and upper atmosphere, and images of the auroral regions [Paxton et al., 1992, 2002]. Four SSUSI instruments have been placed on Defence Meteorological Spacecraft Program (DMSP) spacecraft (DMSP F16-F19). These spacecraft are in polar, sun-synchronous orbits with a period of approximately 90 minutes; this means that SSUSI observes the aurora at approximately the same local time in each orbit. The DMSP satellites orbit in local times of either 18:00-06:00 LT or 21:00-09:00 LT meridians. The SSUSI instruments are similar in design to the Global Ultra-violet Imager (GUVI) instruments on the Thermospheric-Ionospheric-Mesosphere Energy Dynamics (TIMED) satellite [Humm et al., 1998, Christensen et al., 2003].

The SSUSI instruments have two main optical elements: the Scanning Imaging Spectrograph (SIS) and the Nadir Photometer System (NPS) [Paxton et al., 2002]. This thesis makes use of data from the SSUSI SIS which consists of a circular spectrograph and a cross-track scanning mirror at the input telescope (a 75mm focal length off-axis parabola system) with a slit width of 11.84°. The mirror rotates 140° from horizon to horizon, as shown in Figure 2.5. This scan is anti-symmetric about the nadir, with a scan of 80° anti-sunward above the limb and 60° towards the Sun. The scan takes approximately 15 seconds to be produced and builds up brush-stroke like images of the auroral regions over approximately 20 minutes.

These spectrographic measurements are made in the Far Ultra-Violet (FUV) at wavelengths between 115-180 nm. On board processing bins the spectral images into five pre-defined ‘colours’ which are indicated in Figure 2.6 by blue shaded regions. Each

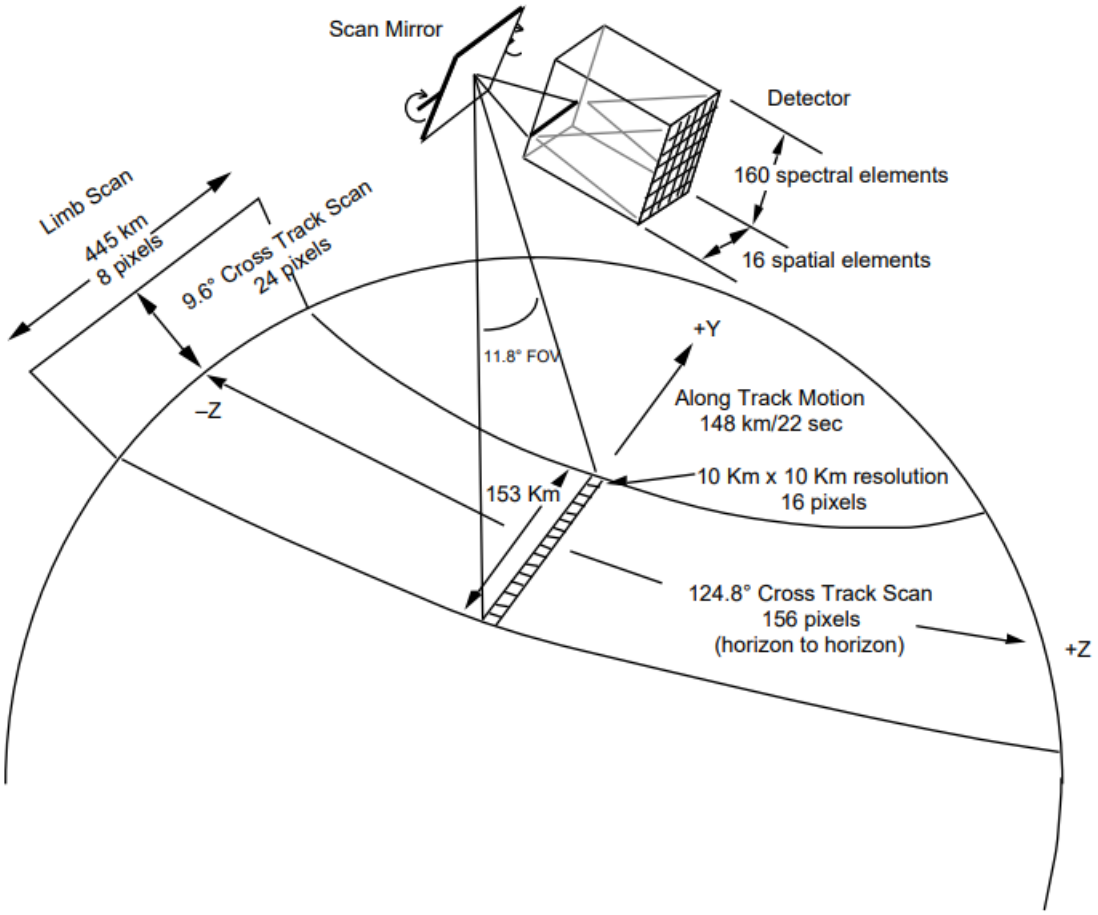

FIGURE 2.5: Cartoon schematic demonstrating the scanning capability of the SSUSI instrument which has a 11.84° field of view and scans 140° along the horizontal axis Paxton et al. [1992].

spectral band was chosen to represent the primary emissions features from Hydrogen, Oxygen and Nitrogen (given in Table 2.1). In this thesis, the Lyman-Birge Hopfield long band is used as these wavelengths show the weak polar cap arc signatures the clearest and are comparable to previous measurements used in polar cap arc studies (such as those from IMAGE WIC, for example in Fear and Milan [2012a]).

Emitting species	Wavelength
HI	121.6 nm
OI	130.4 nm
OI	135.6 nm
N_2 LBH-S	140-150 nm
N_2 LBH-L	165-180 nm

TABLE 2.1: The five SSUSI 'colours'. LBH-S and LBH-L stand for the Lyman-Birge Hopfield short and long bands respectively.

The relatively quick orbit of the DMSP spacecraft means that near simultaneous images

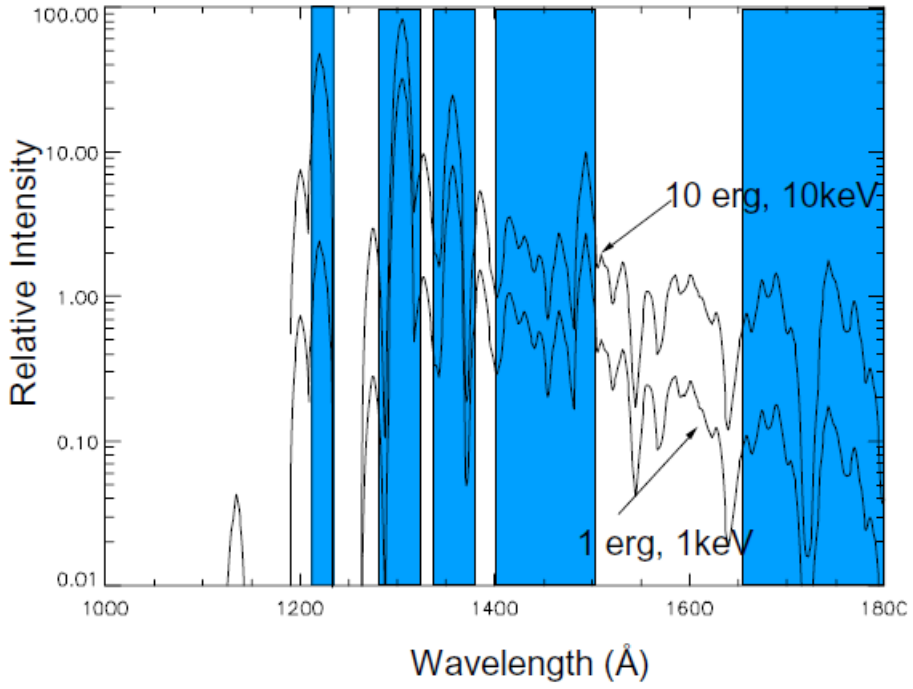

FIGURE 2.6: FUV spectrum with the bands measured by SSUSI indicated in blue [Paxton et al., 2002]

from the northern and southern hemisphere may be obtained from SSUSI up to approximately 45 minutes apart from a single orbit, or more frequently when considering there are up to 4 SSUSI instruments with data available at one time, as indicated in Table 2.2. Furthermore, the DMSP spacecraft are in low-Earth orbit (at around 830 km) and hence allow the SSUSI instruments to observe finer scale auroral structure than previous UV imagers, such as Polar UV and IMAGE WIC. The SSUSI data used in this thesis were downloaded from the SSUSI website[2].

Satellite	Availability
F16	Jan 2005 - Aug 2016
F17	Jan 2007 - present
F18	April 2010 - present
F19	Sept 2014 - Feb 2016

TABLE 2.2: SSUSI data availability from the different DMSP satellites

2.1.3 All sky cameras

Ground-based cameras located on Svalbard with a larger-scale field of view than ASK are used to bridge the gap between these small-scale observations and the global-scale

[2] http://ssusi.jhuapl.edu/

observations from SSUSI. This thesis uses two cameras which are both located in the Kjell Henriksen Observatory (KHO), which is situated near to the ASK instrument.

In Chapter 3, images from The Little Camera (TLC) are used to find an interval when a north-south aligned arc passed through the field of view of the ASK instrument. TLC is part of the Spectrographic Imaging Facility (SIF) maintained by the University of Southampton; images can be obtained directly from the University (via Dan Whiter). This camera has a 645 nm long pass filter on it and a field of view of 80°.

Similarly, in Chapter 5, images from the Sony a7s camera are used to identify periods when auroral arcs passed through the ASK field of view for two separate case studies. This camera has a circular fisheye lens with a field of view of 180° in all directions. These data are obtained directly from the University Centre in Svalbard (UNIS), via Noora Partamies.

2.2 Low-altitude space-based instrumentation

2.2.1 In-situ particle measurements from SSJ/5

In conjunction with the SSUSI images, data are obtained from the SSJ/5 particle detectors, also on board DMSP F16-F19, which provide characteristics of the electron and ion precipitation along the track of the spacecraft. The DMSP particle detectors were designed by D. Hardy of Air Force Research Laboratory, and data were obtained from the Johns Hopkins University Applied Physics Laboratory.

These instruments consist of a pair of electrostatic analyzers coupled with microchannel plates [Hardy et al., 1993, 2008]. The SSJ/5 detectors have a fan field-of-view covering a solid angle of 4° by 90° between zenith and the horizon. This fan is divided into six 15° angular sectors; however, they are currently running in a operational mode similar to the previous model (SSJ/4) in which the counts from all six sectors are combined to give one spectrum every second. The SSJ/5 instrument measures the fluxes of electron and ions in 19 logarithmically spaced energy steps between 30 eV to 30 keV.

Figure 2.7 shows an example spectrogram obtained from the DMSP Java tool which can be downloaded online[3]. This tool allows the user to select the specific spacecraft

[3] http://sd-www.jhuapl.edu/Aurora/spectrogram/index.html

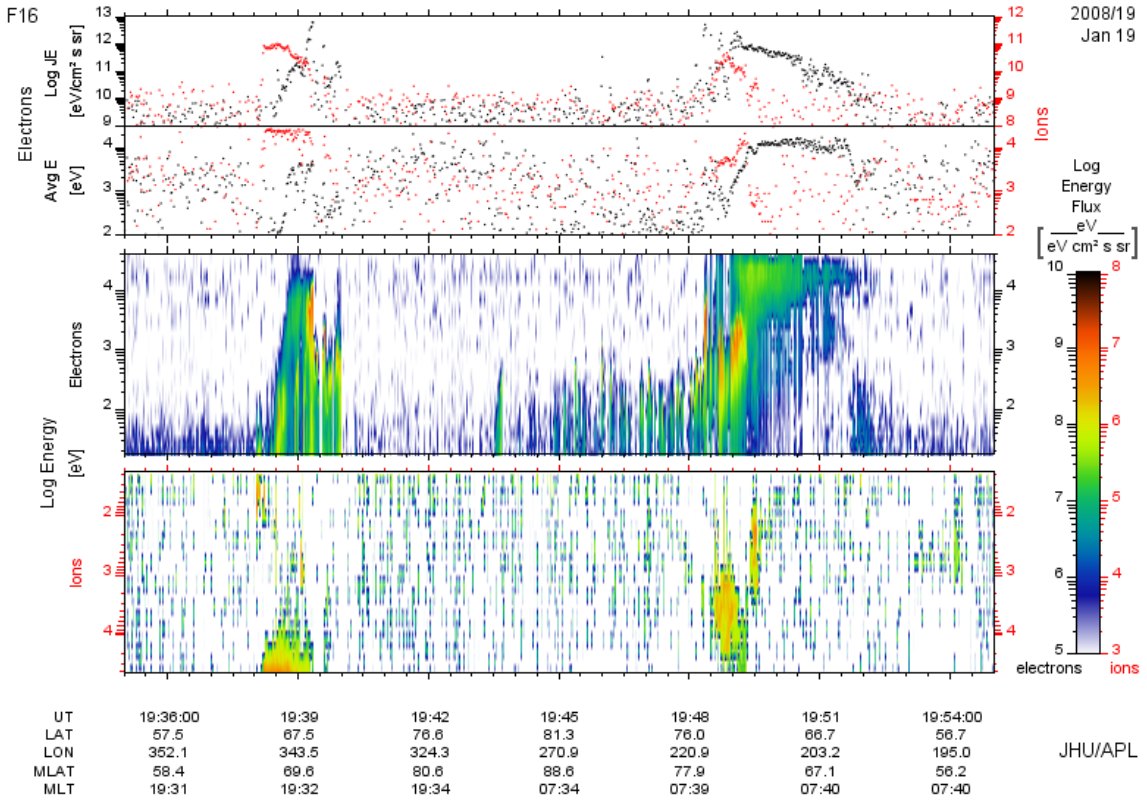

FIGURE 2.7: Example spectrogram downloaded from the DMSP Java script

and period of interest. The top two panels in Fig. 2.7 show the average energy flux and energy for the electrons (black) and ions (red). The bottom two panels show the electron and ion spectrograms respectively, where the colour indicates the energy flux. This particular spectrogram is showing (from left to right) the particle precipitation above the DMSP spacecraft as it passes over: the duskside oval (characterised by high energy electron and ion precipitation), the polar cap (which is characterised by electron-only polar rain precipitation, discussed in Section 1.4.5), and then the dawnside oval (high energy ion and electron precipitation). This example is from a polar cap arc case study which will be presented in Chapter 3 (Fig. 3.13).

The DMSP Java tool also allows for the inclusion of an automated boundary detection routine [Newell et al., 1996a, Redmon et al., 2017]. However, as discussed further in Chapter 4, these boundaries do not work well for northward IMF, where the precipitation in the polar cap can be complex due to the presence of polar cap arcs. In the appendix of Chapter 4, a method for automatically detecting the poleward boundary of the auroral

oval is presented. This is particularly important for polar cap arc studies to make sure the arcs being identified are poleward of the edge of the auroral oval.

2.2.2 AMPERE

Data from AMPERE (the Active Magnetosphere and Planetary Electrodynamics Response Experiment) were used to infer information about the field aligned currents that flow between the Earth's magnetosphere and ionosphere [Anderson et al., 2000, 2014, Waters et al., 2001, Coxon et al., 2014a,b, 2016, 2018]. These data were used as supporting observations in a case study to determine an approximate position of the open-closed field line boundary. The AMPERE data set is derived from magnetometer measurements on board 66 Iridium satellites; these magnetometer measurements are then combined to provide global current maps of the Northern and Southern polar regions. The Iridium satellites are a commercial satellite network owned by the Boeing service company. The Iridium-derived AMPERE data were downloaded from the AMPERE website[4].

2.3 Ground-based radar data

2.3.1 The EISCAT Svalbard Radar (ESR)

The EISCAT (European Incoherent Scatter) Svalbard radar (ESR) is an incoherent scatter radar situated at Longyearbyen in the Svalbard archipelago. It is operated by the European Incoherent Scatter Scientific Association. EISCAT is an international association supported by research organizations in China (CRIRP), Finland (SA), Japan (NIPR and STEL), Norway (NFR), Sweden (VR), and the United Kingdom (NERC).

Incoherent scatter radars transmit radio waves into the ionosphere which are then scattered off electrons and the backscatter spectrum is measured. The shape of the backscatter spectrum can be used to derive key ionospheric parameters, for example, the strength of the backscatter is proportional to the electron density and the width of the return power spectrum is dependent on the ionospheric temperature (which can be separated

[4] http://ampere.jhuapl.edu/

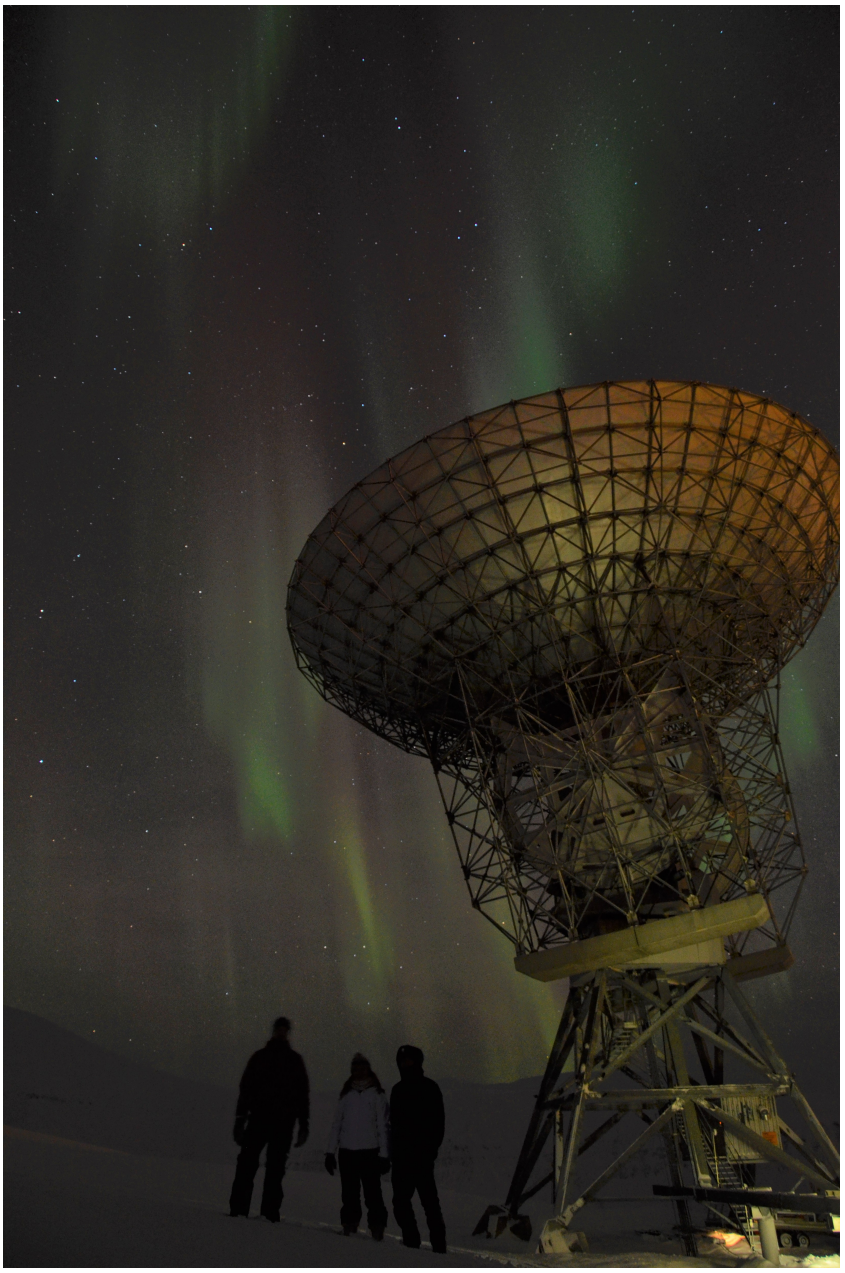

FIGURE 2.8: EISCAT Svalbard radar 32m steerable dish. Photo credit: Dan Whiter.

into electron and ion temperatures). Furthermore, in the ionosphere the motion of electrons is imposed on them by more massive ions and hence by measuring the Doppler shift of the return spectrum, the ion velocity in the ionosphere can be derived.

The ESR consists of a steerable 32 m diameter dish antenna (Figure 2.8) and a co-located 42 m fixed dish antenna (Figure 2.9) that is aligned with the local magnetic zenith [Wannberg et al., 1997]. Data taken during the International Polar Year (IPY) between 2008-2009 has been used in this thesis. This was a period when the ESR operated quasi-continuously taking measurements of ionospheric parameters (such as,

FIGURE 2.9: EISCAT Svalbard radar 42m dish. Photo credit: Dan Whiter.

electron density and temperature and ion temperature) with the 42 m dish at a 6 second resolution.

2.3.2 The Super Dual Auroral Radar Network (SuperDARN)

The Super Dual Auroral Radar Network (SuperDARN) is a network of high frequency coherent scatter radars that measure ionospheric flows in the polar regions of the northern and southern hemispheres [Greenwald et al., 1995, Chisham et al., 2007]. SuperDARN is a collection of over 30 high power, low frequency radars funded by national scientific funding agencies of Australia, Canada, China, France, Japan, South Africa, United Kingdom, and the United States of America. These radars measure the ionospheric convection over mid and high-latitude regions. The radar beam is Bragg scattered from irregularities in the F-region plasma (between 200-400 km), the Doppler shift of the received signal gives the line of site velocity of the plasma.

This thesis uses data from all SuperDARN radars, which are combined with a statistical model to obtain ionospheric flow patterns in the high latitude regions using the map-potential technique [Ruohoniemi and Baker, 1998]. Furthermore, Chapter 3 specifically uses data from the Pykvibaer radar (in Iceland), which has a field of view over Svalbard.

During the period of interest, it was operating in stereo mode, i.e operating quasi-simultaneously on two different frequencies allowing for different spatial and temporal resolutions [Lester et al., 2004]. Data used in this thesis were obtained from the British Antarctic Survey SuperDARN data hub.

2.4 Supporting ground-based instrumentation

2.4.1 The HiTIES instrument

The High Throughput Imaging Echelle Spectrograph (HiTIES) instrument [Chakrabarti et al., 2001] is part of the Spectrographic Imaging Facility (SIF) at KHO, located near the ASK instrument on Svalbard. It is maintained by the University of Southampton and data can be viewed in 20 minute megablocks on the SIF website[5]. The instrument records images at a frequency of 2 Hz (although the spectra are typically post-integrated to between 10 and 120 s depending on the brightness of the emission).

The HiTIES instrument contains a spectrograph with an 8° slit that is centred on the magnetic zenith and an EMCCD detector. Mosaic filters are used to record multiple non-continuous wavelength regions at high resolution; each individual panel of the filters is centred in wavelength on a particular atmospheric emission of interest (although each panel may also contain emissions from multiple other species). Chadney and Whiter [2018] used the 'OH' panel to obtain an estimate of the temperature of the neutral atmosphere by developing a method of fitting different auroral (N_2, O^+ and O_2^+) and airglow (OH) emissions measured by HiTIES.

In this thesis, data from the 'H-α' panel of the three panel mosaic, which observes the wavelength region between 649-663 nm, is of particular interest. This mosaic was installed in December 2015. Doppler shifted hydrogen emissions are a signature of proton precipitation (e.g. Eather [1967]). H-α is the brightest hydrogen emission at 656.3 nm [Galand et al., 2004]. Other emissions such as from airglow (OH) and electron precipitation (N_2 (1PG)) are also present in this wavelength region. These emissions are modelled using methods outlined by Chadney and Whiter [2018] and Price et al. [2019] to obtain the spectra for the 'H-α' emission. Data from the 'H-α' panel is used in this

[5] http://sif.unis.no/

thesis to determine the topology of the field lines on which polar cap aurora is formed by the presence (or lack) of precipitating protons (which are a sign of closed field lines).

2.4.2 Ground-based magnetometers

The study presented in Chapter 3 makes use of data from the Svalbard stations of the International Monitor for Auroral Geomagnetic Effects (IMAGE) network to quantify the disturbance of the Earth's magnetosphere during a polar cap arc event [Tanskanen, 2009]. The entire IMAGE magnetometer chains consists of 41 ground based stations. These stations are a joint European collaboration between Finland, Germany, Poland, Russia and Sweden and cover geographic latitudes from $51° - 79°$. The Svalbard magnetometer data presented in this thesis are provided by the University of Tromsø.

2.5 Up stream solar wind monitors

In order to place the observations into an interplanetary context, we need knowledge of the solar wind behaviour. This is provided by various spacecraft situated in the solar wind.

In this thesis data from the OMNI database [King and Papitashvili, 2005] is used to get the IMF conditions during several polar cap arc events; these data were obtained from the OMNI website[6]. The OMNI database consists of solar wind magnetic field and plasma data sets that have been time-shifted to the nose of the Earth's bow shock and hence give an estimation of the solar wind conditions at the Earth. Most of the magnetic OMNI data used in this thesis came from the magnetometer on board the ACE (Advanced Composition Explorer) spacecraft which is located at the Lagrangian libration point (L1) and is hence upstream from the Earth [Stone et al., 1998, Smith et al., 1998]. OMNI calculates a lag in the solar wind data (ΔT) using the following equation:

$$\Delta T = \frac{n \cdot (\mathbf{R}_d - \mathbf{R}_o)}{\hat{n} \cdot V} \tag{2.4}$$

[6] https://omniweb.gsfc.nasa.gov/

Where $\mathbf{R}_0$ is the spacecraft position, $\mathbf{R}_d$ is the displaced location (i.e. the nose of the Earth's bow shock), V is the velocity of the solar wind and n is the phase front normal (PFN) of the solar wind which is calculated using a combination of minimum variance analysis and cross product methods [Weimer et al., 2003]. This propagation method is based on the assumption that the variations in the solar wind are organised into a series of phase fronts which convect with the solar wind speed (i.e frozen-in, discussed in Section 1.2.3.1). The OMNI propagation method has been verified to be accurate in several studies (e.g. Case and Wild [2012]).

In Chapter 3, data from the Cluster 3 spacecraft was used. During the period of interest Cluster was located just upstream from the bow shock. The Cluster mission consists of four identical satellites that monitor small-scale structures in the magnetosphere by flying in a tetrahedron formation. Observations from the Fluxgate Magnetometer (FGM) [Balogh et al., 2001, Gloag et al., 2010] and the Hot Ion Analyzer on the Cluster Ion Spectrometry (CIS-HIA) [Rème et al., 2001, Dandouras et al., 2010] are used to measure the solar wind speed, density and the direction of the IMF during the event. These data were obtained from the Cluster Science Archive[7]. It was verified that Cluster 3 was in the solar wind during the period of interest by looking at the ion spectrograms in the Cluster Quicklook plots; solar wind can be identified by a high flux of particles in a narrow energy range (around 1 keV).

For some events presented in Chapter 4, where there were data gaps in the OMNI data base, data from the ARTEMIS 1 (Acceleration, Reconnection, Turbulence and Electrodynamics of the Moons Interaction with the Sun) satellite [Auster et al., 2008] has been used. The two ARTEMIS satellites were re-purposed from the THEMIS (Time History of Events and Macroscale Interactions during Substorm) missions and have been in orbit around the Moon since 2010. During periods of interest, it was verified that ARTEMIS 1 was in the solar wind by looking at the ion and electron spectrograms, similarly as with the Cluster 3 spacecraft. These data were accessed online[8].

All the ground-based and spacecraft instrumentation discussed in this chapter will be used in this thesis to investigate the nature of polar cap arcs and, more specifically, they will be used to identify and understand the fine-scale structure of these high latitude arcs.

[7] https://www.cosmos.esa.int/web/csa/access
[8] https://sscweb.gsfc.nasa.gov/

Chapter 3

Multi-instrument observation of simultaneous polar cap auroras on open and closed field lines

This work has been published as:

J. A. Reidy, R. C. Fear, D. K. Whiter, B. S. Lanchester, A. J. Kavanagh, L. J. Paxton, Y. Zhang, and M. Lester. Multi-instrument observation of simultaneous polar cap auroras on open and closed magnetic field lines. *Journal of Geophysical Research (Space Physics)*, 122:4367–4386, 2017. doi: 10.1002/2016JA023718

3.1 Introduction

This chapter presents a case study containing observations of polar cap auroral features which occurred on 19 January 2008. These features were evaluated using multiple ground based and space craft instrumentation.

As outlined in Section 1.5, there is some controversy over the formation mechanism that results in polar cap arcs. Newell et al. [2009] suggest that there are three 'types' of polar cap arc which can be identified by the associated particle precipitation, two of which occur on closed field lines (and can be identified by ion and electron precipitation), and the other occurs on open field lines (and can be identified by electron-only precipitation).

Newell et al. [2009]'s division into two 'closed' field line classifications relates to a distinction between those events which are adjacent to the main auroral oval (discussed in Section 1.5.2.1) and those which are suggested to be formed on closed field lines within the otherwise open polar cap. Milan et al. [2005] put forward a mechanism whereby tail reconnection during northward IMF results in closed flux becoming 'trapped' in the magnetotail and it is on these field lines that the polar cap arc forms, as discussed in Section 1.5.2.2. The third 'type' discussed by Newell et al. [2009], identified by electron only precipitation, is suggested to be formed by accelerated polar rain (discussed in Section 1.5.2.3) on open field lines.

The aim of this thesis chapter is to combine ground based and satellite observations to investigate the formation mechanisms of polar cap arcs. This study considers any high latitude aurora that is distinctly sun-aligned in nature to be a polar cap arc. SSUSI instruments on board DMSP F16 and F17 (introduced in Section 2.1.2) are used to identify an event containing two high latitude structures on opposite sides of the northern hemisphere polar cap and a possible conjugate feature in the southern hemisphere. During the event the two DMSP spacecraft were almost exactly out of phase in their orbits meaning near-simultaneous measurements of each hemisphere were available. The structure on the duskside on the northern hemisphere occurred over Svalbard and was investigated using ground based data from the ASK instrument (Section 2.1.1), the ESR (Section 2.3.1), the IMAGE magnetometer chain (Section 2.4) and the SuperDARN radars (Section 2.3.2). The structure on the dawnside of the northern hemisphere polar cap is investigated using in-situ particle data from the SSJ/5 instrument (Section 2.2.1) on board DMSP F16 and also SuperDARN map potential plots.

The main observations from this event are presented in Section 3.2 which has been separated into the interplanetary conditions and large-scale auroral observations for the overall event (Section 3.2.1) and then the structures on the dusk and dawn sectors of the northern hemisphere are investigated separately in Sections 3.2.2. and 3.2.3 respectively. A discussion is given in Section 3.3 before the main conclusions are presented in Section 3.4.

3.2 Results

3.2.1 Interplanetary conditions and large-scale auroral observations

We present a case study of high latitude aurora on 19th January 2008. Figure 3.1 shows the solar wind conditions between 16:00-21:00 UT on this day provided by the Cluster 3 spacecraft. Figs. 3.1a, b, and c show the IMF components in the Geocentric Solar Magnetospheric (GSM) coordinate system, Fig. 3.1d shows the solar wind speed. The ion and electron spectrograms (not shown) confirm Cluster was in the solar wind during our event, just upstream from the bow shock, at (14, 12, -8) R_e. Our period of interest is between 18:00-21:00 UT. During this time the IMF B_y component was predominately positive with the occasional negative turn. The IMF turned northward at around 18:45 UT and, apart from a few brief southward turns, remained so until around 20:30 UT. Prior to this the IMF alternated between northward and southward. The B_x component was predominately negative throughout the interval. It can be seen in Fig. 3.1d that this is a period of high solar wind speed with a mean value of 610 km s^{-1}.

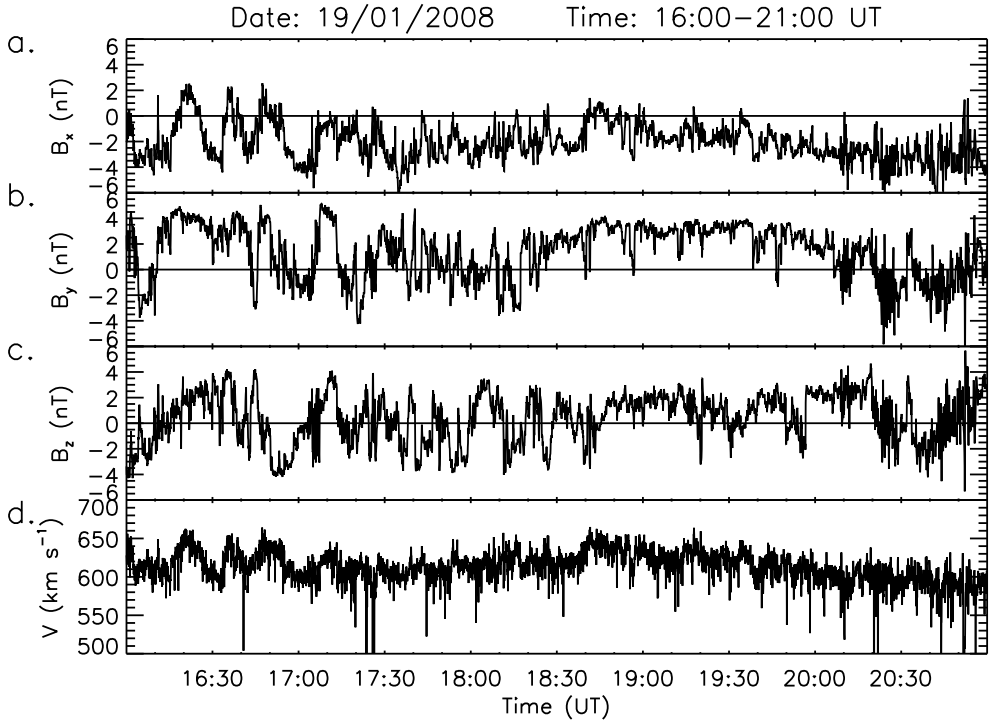

FIGURE 3.1: IMF data from the Cluster spacecraft between 16:00-21:00 UT. The top three panels are the IMF GSM components, B_x, B_y and B_z respectively, at spin resolution. The bottom panel shows the solar wind speed.

Figure 3.2 shows images from the SSUSI instruments on board DMSP F16 and F17 between 17:50 and 19:05 UT. During this interval the spacecraft provide almost simultaneous measurements of the northern and southern hemispheres. Each image has been projected onto an MLT grid with noon at the top and dawn to the right. All of the southern hemisphere images have been reversed about the noon-midnight meridian for ease of comparison, such that dawn is to the right in all figures. Consequently, the spacecraft are travelling in the opposite direction in each hemisphere i.e. left to right in the northern hemisphere image and vice versa in the southern image.

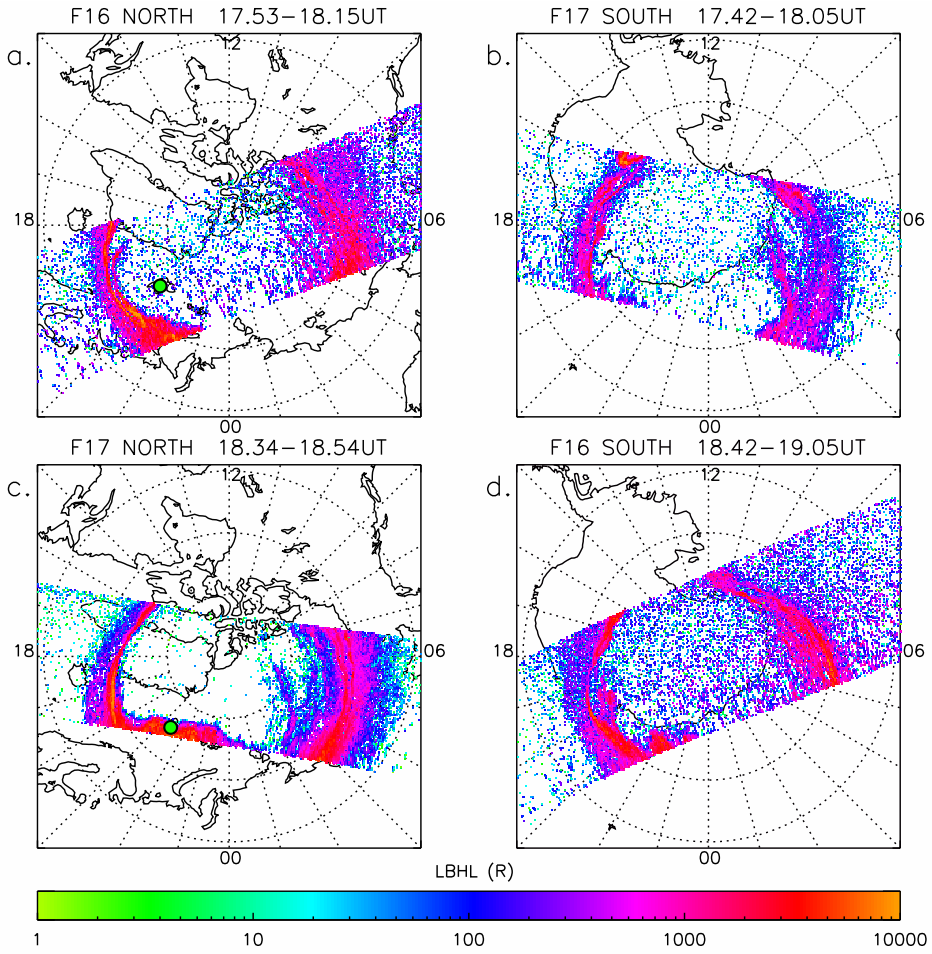

FIGURE 3.2: Images from SSUSI instruments on board DMSP F16 and F17 (LBHL band) between 17:50-19:05 UT with noon at the top and dawn to the right; the southern hemisphere images have been flipped for ease of comparison.

Figs. 3.2 a and b show images of the northern hemisphere between 17:53-18:15 UT and the southern hemisphere between 17:42-18:05 UT respectively. These images coincide with the period when the IMF was alternating between northward and southwards. The green dot in the northern hemisphere images indicates the position of ASK/ESR on Svalbard, which at this time are situated poleward of the auroral oval and are within

the polar cap, looking along open field lines. The southern hemisphere image shows a sun-aligned structure on the dawnside of the polar cap. This structure is not seen in any of the following images and is hence not considered as part of this study. The northern hemisphere between 18:34-18:54 UT and the southern hemisphere between 18:42-19:05 UT are shown in Figs. 3.2 c and d. These images show the auroral regions around the time the IMF turned northward at 18:45 UT. In both hemispheres there is an auroral bulge seen between 21-24 MLT. In the northern hemisphere (Fig. 3.2 c), an approximately sun-aligned arc can also be seen in the dawn side of the polar cap. No obvious counterpart to this structure can be seen in the almost simultaneous southern hemisphere image (Fig. 3.2 d).

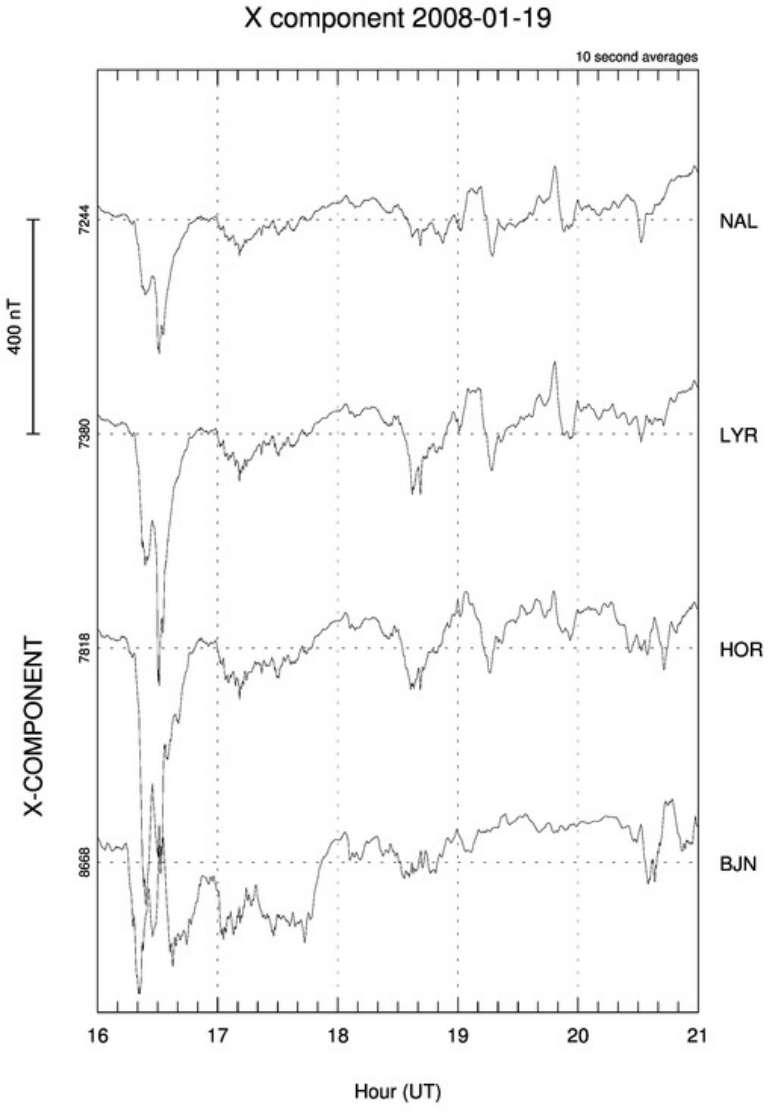

FIGURE 3.3: Magnetic field deflections in the X component (north) obtained from the IMAGE magnetometer Svalbard stations between 16:00-21:00 UT.

Figure 3.3 shows data from the Svalbard magnetometers between 16:00-21:00 UT. A deflection can be seen around 16:30 UT, which likely corresponds to a magnetospheric substorm during the period of southward IMF (e.g. Lühr et al. [1998]). At approximately 18:30 UT smaller deflections are seen, with the weakest deflections shown by the Bear Island magnetometer (BJN) and the strongest at Longyearbyen (LYR). This suggests the activity may be localised to Svalbard, which agrees with the bulges seen in the SSUSI image (Fig. 3.2 c). We hence suggest that the small, localised magnetic deflections are signatures of a poleward boundary intensification [Lyons et al., 1999]. Hence the bulges in the dusk side of the northern and southern hemispheres (Fig. 3.2 c, d) appear to result from flux closure in the tail, most likely at the far neutral line.

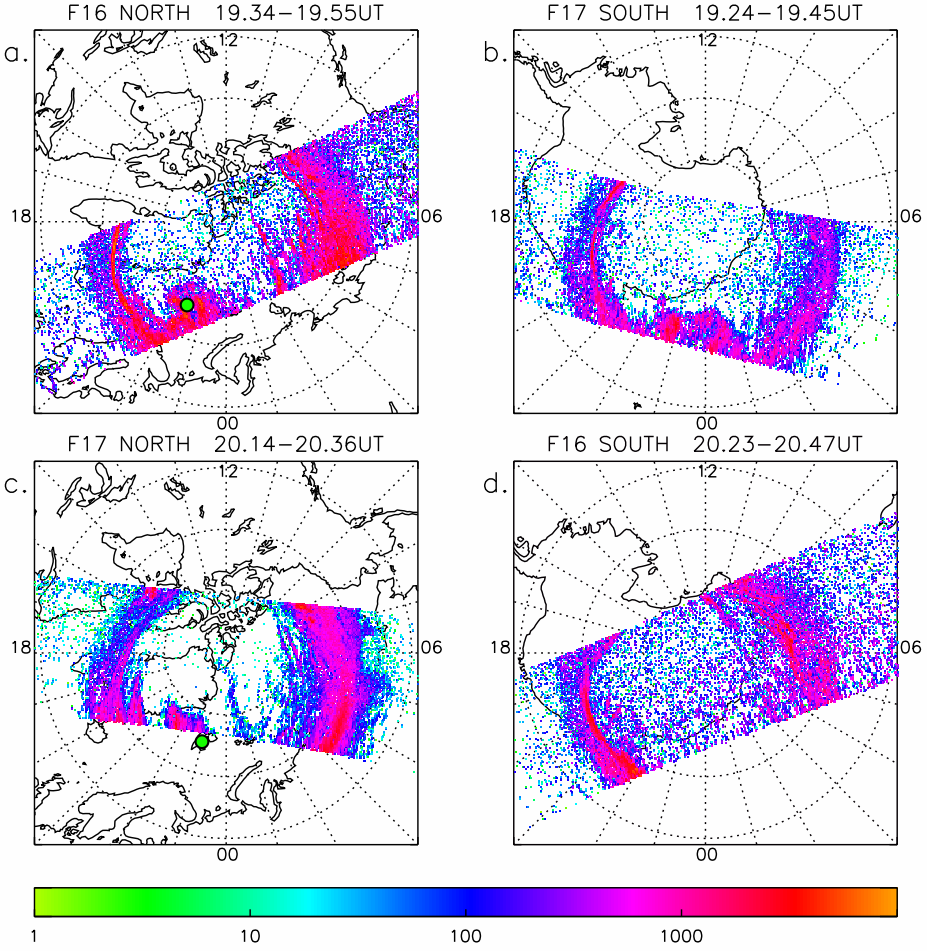

FIGURE 3.4: SSUSI images between 19:25-20:50 UT. Same layout as Fig. 3.2.

SSUSI observations between 19:25-20:50 UT are shown in Figure 3.4 with the same layout as Fig. 3.2. Figs. 3.4 a and b correspond to the intervals between 19:34-19:55 UT for the northern hemisphere image and between 19:24-19:45 UT for the southern hemisphere. By this time the IMF had been generally northward for around an hour. The duskside

bulge in the northern hemisphere (Fig. 3.2c) has protruded further into the polar cap, extending over the field of view of ASK and ESR (green dot) to almost 80° magnetic latitude, becoming distinctly sun-aligned in nature. A conjugate structure can still be seen in the southern hemisphere image, although this structure has not extended as far polewards. There are now also multiple sun-aligned arcs seen in the dawnside of the northern hemisphere image, still with no apparent southern hemisphere counterpart. The last SSUSI images in our period of interest, between 20:14-20:36 UT in the northern hemisphere and 20:23-20:47 UT in southern hemisphere, are shown in Figs. 3.4c and d respectively. The dusk-side protrusion in the northern hemisphere over Svalbard remains after at least 45 minutes but has not grown further into the polar cap. The conjugate form is no longer seen in the southern hemisphere image but this could be a result of the field of view of SSUSI. The sun-aligned structure on the dawn side of the northern hemisphere image has now moved towards the noon-midnight meridian compared to the previous image.

The two structures occurring on either side of the northern hemisphere polar cap will now be discussed separately.

3.2.2 The duskside structure

3.2.2.1 Analysis of optical data

Figure 3.5 shows an image of a north-south aligned arc over Svalbard taken by a 60° field of view camera from the Spectrographic Imaging facility (SIF), also located on Svalbard near the ESR/ASK site. Although this arc is not discernible in the SSUSI images, it likely forms part of the duskside structure observed in Fig. 3.2 c and Figs. 3.4 a and c, due to its sun-algined direction which agrees with the SSUSI observations. The arc entered SIF's field of view around 20:23:23 UT and moved eastwards i.e. dawnward.

Figure 3.6 shows observations from ASK taken during this selected interval (note the 3.1° × 3.1° field of view of ASK is approximately in the center of the SIF image in Fig. 3.5). Fig. 3.6a shows the average intensity measured by ASK1, I_{6370} (black) and ASK3, I_{7774} (red) in the 20×20 pixels surrounding the magnetic zenith between 20:23:25-20:23:40 UT. Snapshots from the ASK1, I_{6370} camera in 1 second intervals between 20:23.29-20:23.36 UT are shown at the bottom of Fig. 3.6. The yellow box indicates

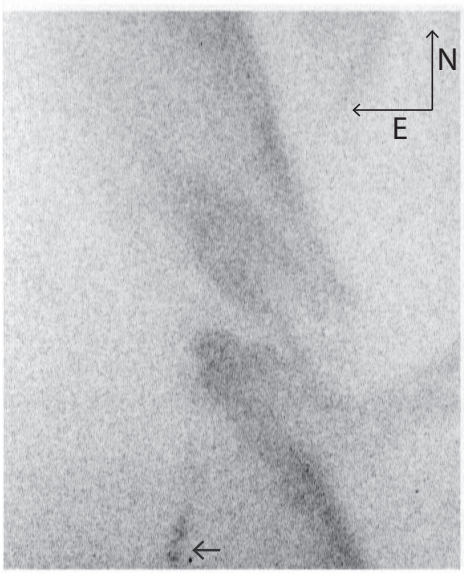

FIGURE 3.5: Image (in negative) obtained from a 60° field of view camera close to ASK at 20:23:23 UT. This camera has a 645 nm long pass filter on it. North is at the top and east is to the left as shown by the arrows. These directions are approximate as the camera is not sensitive enough to see stars and hence more accurate directions cannot be obtained. The arrow at the bottom of the image indicates moonlight.

the pixels averaged around magnetic zenith. The images show a bright curved structure sweeping through the ASK field of view from west to east, followed by a lower intensity more diffuse structure. The rapid changes in these images demonstrate the highly dynamic and small-scale structures within the larger-scale features.

As discussed in Section 2.1.1.1, the Southampton Ionospheric model [Lanchester et al., 2001] can be used to find the changes in energy flux and peak energy from the ratio of different wavelengths observed by the ASK instrument. The input to the model requires an initial shape for the spectrum of the incoming electrons, assumed to be a Gaussian in this study. The modelled production rates were given as an example in the instrumentation section as Figure 2.4. The height-integrated emissions are used to give a relationship between brightness ratio and peak energy, which is then compared with the measured brightness ratio to give the peak energy as plotted in the second panel of Fig. 3.6. The energy flux is found from the brightness of the emission from N_2, which is almost independent of energy. A conversion factor of 240 R/(mW m^{-2}) obtained from the model is used to convert I_{6370} into flux which was then multiplied by the data resolution (20 frames per second in this case).

Fig. 3.6 b shows the precipitation energy varies between 2-11 keV, with a mean value of 5 keV and a mean energy flux of 0.7 mW m^{-2}. This range also agrees with a similar

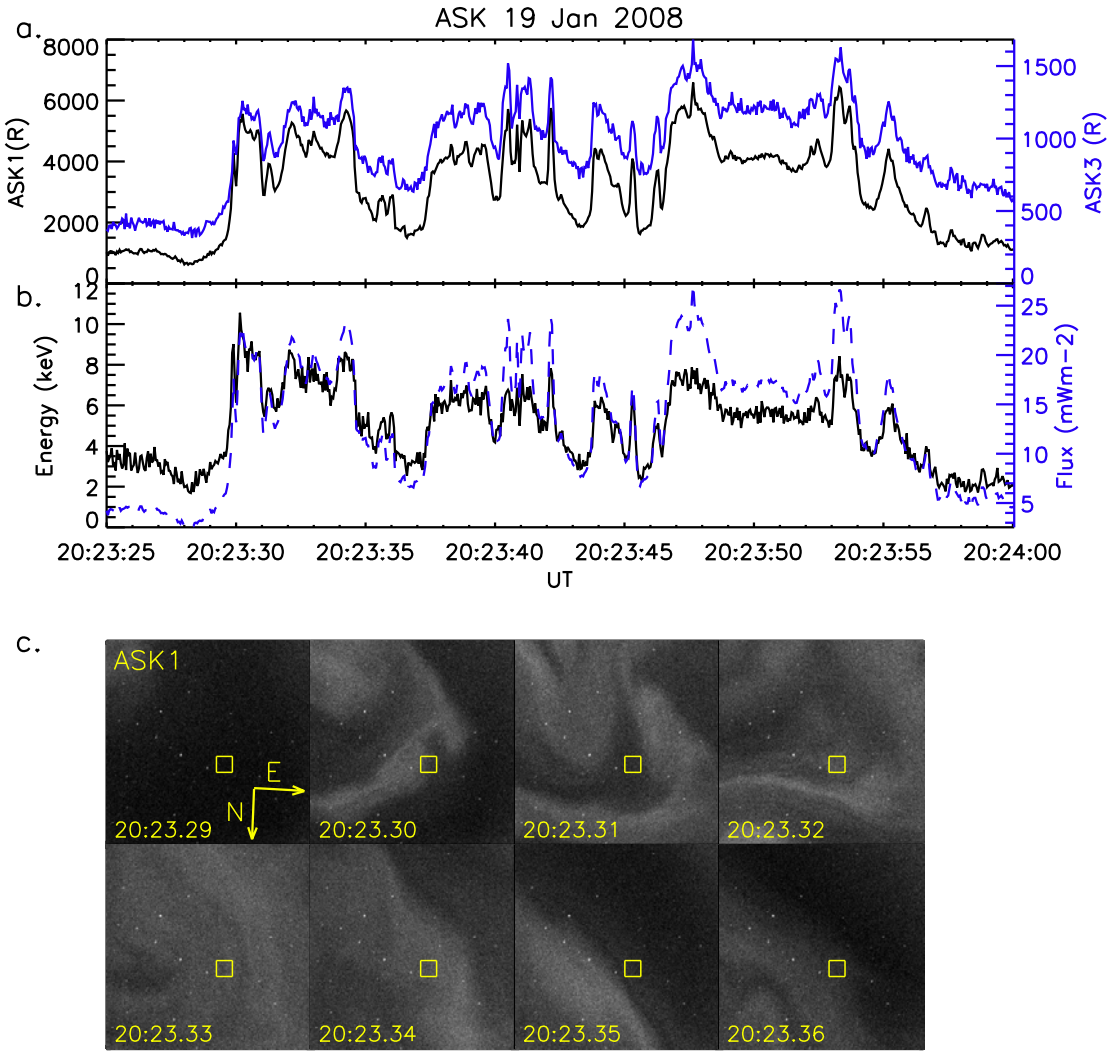

FIGURE 3.6: a. The intensity from ASK1, I_{6370} (black) and ASK3, I_{7774} (blue) between 20:23.25-20:24.00 in the 20 × 20 pixels surrounding magnetic zenith. b. The estimated energy (black) and energy flux (blue) of the precipitating electrons in the interval between 20:23.25-20:24.00 UT. Below are snapshots from ASK1 between 20:23.29-20:23.36 UT in 1 second intervals. The yellow box in each image illustrates the pixels averaged around magnetic zenith. North is approximately at the bottom of the images and East is approximately left.

study carried out by Wu et al. [1991] who observed a polar cap arc associated with precipitation energies between 3-12 keV.

3.2.2.2 Analysis of ESR height profiles

Figure 3.7 shows the electron density (N_e), the electron temperature (T_e) and the ion temperature (T_i) profiles measured by the ESR between 17:00-22:00 UT, plotted at 1

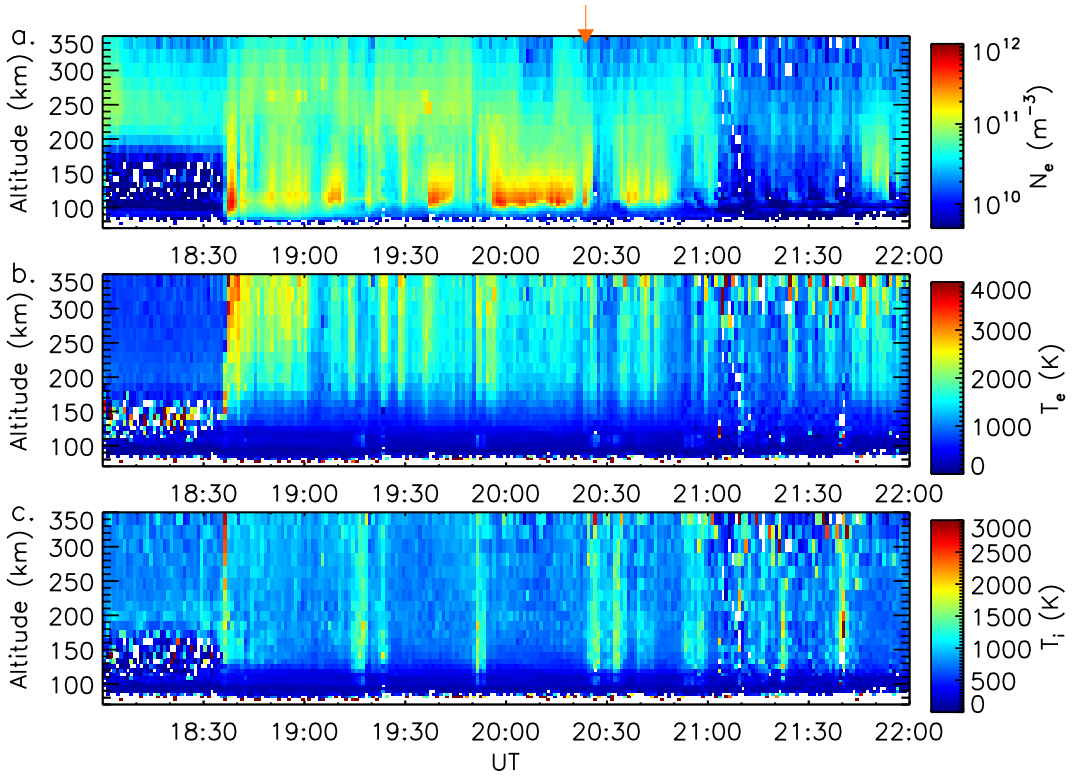

FIGURE 3.7: Electron density, electron and ion temperature profiles between 17:00-22:00 UT from the ESR 42m antenna at 60 second resolution. The orange arrow shows the time of analysis with ASK, ESR and the respective models.

minute resolution. It can be seen that prior to 18:36 UT there is a cool F-region plasma (above 200 km); after this time there is a sudden increase in the E-region N_e down to heights of around 90 km with a corresponding increase in T_e (Fig. 3.7b). These increases occur before the northward turning of the IMF at 18:45 UT and coincide with the start of the interval that SSUSI shows an auroral structure over Svalbard; these features are typical signatures of precipitation on closed field lines. Furthermore, the T_e profiles show very cold plasma before 18:36 UT that is consistent with polar cap electrons, on open field lines. From this dramatic change in T_e, we suggest that the open/closed field line boundary has moved over the field of view of ESR (the open/closed field line boundary has previously been identified using T_e e.g. Aikio et al. [2006]). The optical data from an all-sky camera, not shown, confirms that auroral activity spreads northward across the site during this interval.

The T_i profiles (Fig. 3.7c) show distinct structure during the time of the auroral activity, with increases in T_i corresponding to the gaps in N_e. These increases are consistent with large electric fields and horizontal flows of ions in the region close to auroral brightness

[Lanchester et al., 1996]. This connection between a decrease in N_e and increase in T_i has also been reported and studied by Opgenoorth et al. [1990] and Perry et al. [2015].

The energy of the auroral precipitation can be estimated from the N_e profiles using the Southampton Ionospheric model. The N_e profiles are converted to ionisation rate profiles assuming a recombination rate coefficient, which is an assumption that affects the total flux estimate but does not affect the estimate of the energy of precipitation. The method, described in Lanchester et al. [1998], uses a library of both Gaussian and Maxwellian spectra to find the best fit for peak energy of precipitation. This analysis was applied to the same interval as was chosen in Section 3.4.2.1 to estimate the precipitation energy using the ASK cameras between 20:23:25-20:24:00 UT, shown by an orange arrow above Fig. 3.7a.

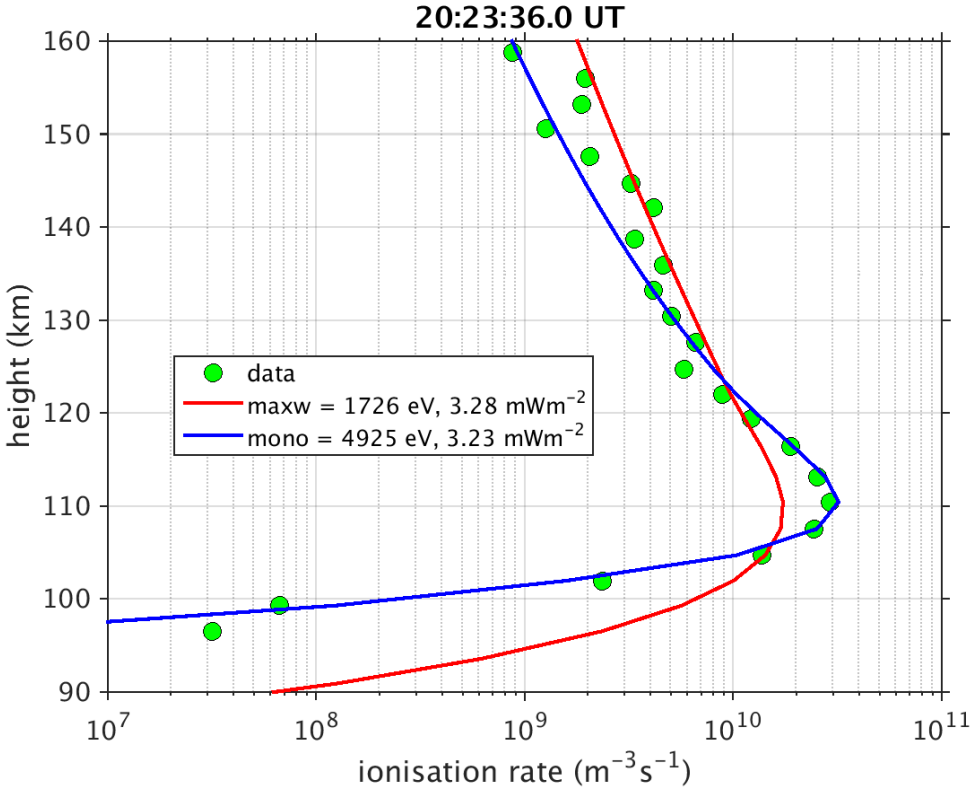

FIGURE 3.8: Ionisation rate profile at 20:23:36 UT. Green dots are measurements at 2 second resolution. Blue line is the best fit to a mono energetic/ Gaussian input, red line is the best fit to a Maxwellian input.

Figure 3.8 shows the results of this fitting process using an N_e profile at 20:23:36 UT. The data are shown in comparison with Maxwellian and mono-energetic (Gaussian) fits at 1.7 keV and 4.9 keV respectively. This clearly shows the data are a better fit to a Gaussian spectral shape. This result agrees with the analysis using the ASK emissions

in Fig. 3.6b which has mean value of 5 keV. The combined ASK and ESR observations and associated modelling show that the energy of the precipitation is consistent with that typically seen on closed field lines.

3.2.2.3 SuperDARN flows

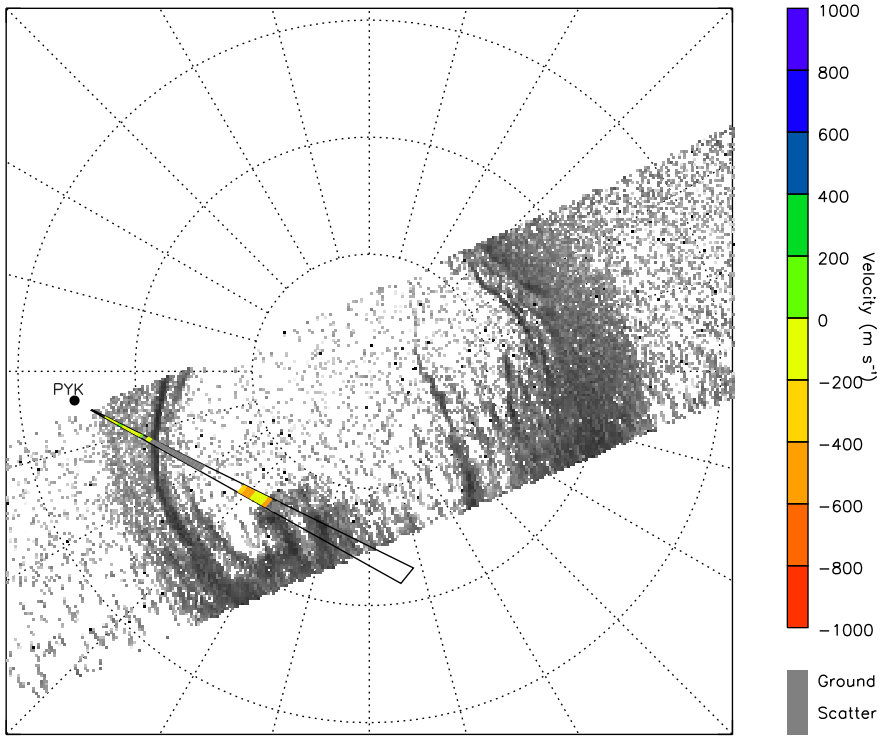

FIGURE 3.9: Velocity flows observed by the Pykkvibaer (PYK) radar from beam 5 at 18:58 UT. This radar is operating in stereo mode. Negative flows (Red/orange) indicates flows away from the radar.

The SuperDARN Pykkvibaer (PYK) radar has a field of view that covers the ASK and ESR site and at the time of interest was operating in 'stereo' mode [Lester et al., 2004], in which two different experimental modes were operating simultaneously on different channels. The primary channel operated at 10.3 MHz in 'common' mode, executing scans of the whole field of view, though no significant scatter was observed. The second channel (10.5 MHz) operated only on one beam (Beam 5) at higher temporal resolution. Figure 3.9 shows the spatial distribution of the data from one scan on this secondary channel at 18:58 UT in context with the northern hemisphere SSUSI image

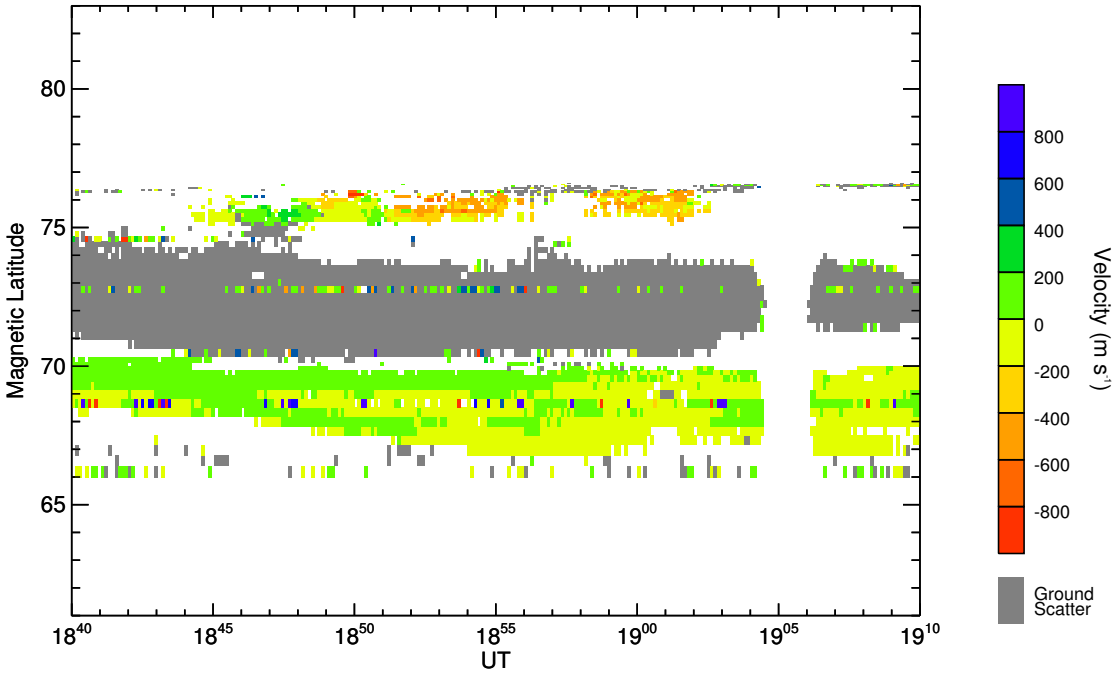

FIGURE 3.10: Time series between 18:40-19:10 UT of the velocity measurements obtained from PYK radar 5 in stereo mode [Lester et al., 2004], again red/orange indicates flow away from the radar.

produced between 18:34-18:54 UT. Although these data appear spatially patchy (since data were only available from the one beam and the scatter is limited in extent along the beam) it can be seen in Figure 3.10, showing the time series of the line of sight velocity measurements observed by the radar between 18:40-19:10 UT, that these flows at 76° are persistent between 18:50-19:03 UT. Fig. 3.9 illustrates that these flows coincide with the poleward edge of the bulge seen in the SSUSI image.

SuperDARN flows in the southern hemisphere were also examined. Figure 3.11 shows a map potential plot at 17:42-18:05 UT in context with the southern hemisphere SSUSI image between 17:58-18:00 UT. The flow is spatially very localised between 20-22 MLT but shows apparent flow out of the polar cap approximately at the location the bulges form in the northern and southern polar caps. Figure 1c in Fear and Milan [2012b], shows a cartoon of nightside flow patterns of a transpolar arc whereby flux is closing in the tail and asymmetric flows are seen either side of the position of the transpolar arc. Hence we suggest these flows are indicative of magnetotail reconnection under the influence of a B_y component, and hence consistent with the mechanism proposed by [Milan et al., 2005] for transpolar arcs. Furthermore, although the data from the single radar beam shown in Fig. 3.9 only tells us that there is ionospheric flow just duskward

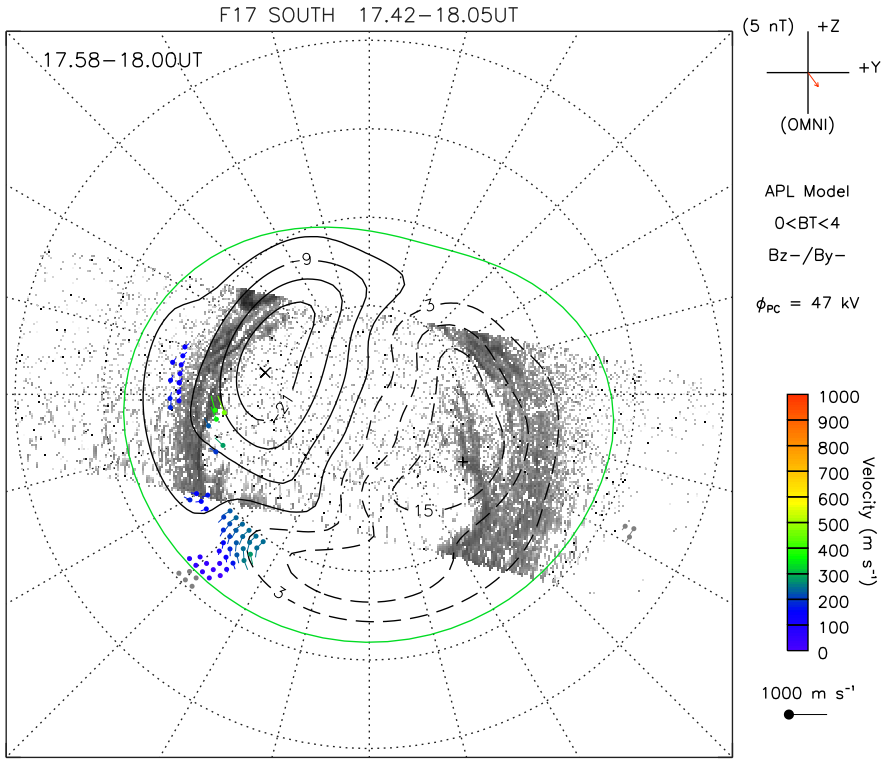

FIGURE 3.11: Map potential plot of southern hemisphere SuperDARN data between 17:58-18:00 UT obtained using the method outlined by Ruohoniemi and Baker [1998]. Data are plotted on top of the corresponding SSUSI image from DMSP F17 between 17:42-18:05 UT. Noon is at the top and dawn to the right.

of the duskside feature that has a component directed away from the radar, we suggest the localised but persistent flows seen at the tip of the duskside structure are at least consistent with the closure and exit of flux from the polar cap adjacent to the arc, and hence consistent with the transpolar arc mechanism.

3.2.3 The Dawnside sun-aligned arcs

3.2.3.1 DMSP

Figure 3.12 shows the footprint of the DMSP spacecraft during the 18:34-18:54 UT pass over the northern polar cap with corresponding SSUSI image. It can be seen that during this pass, DMSP intersected the tip of the furthest extended sun-aligned arc on the dawn side of the polar cap but missed the structure on the duskside. The arrows correspond

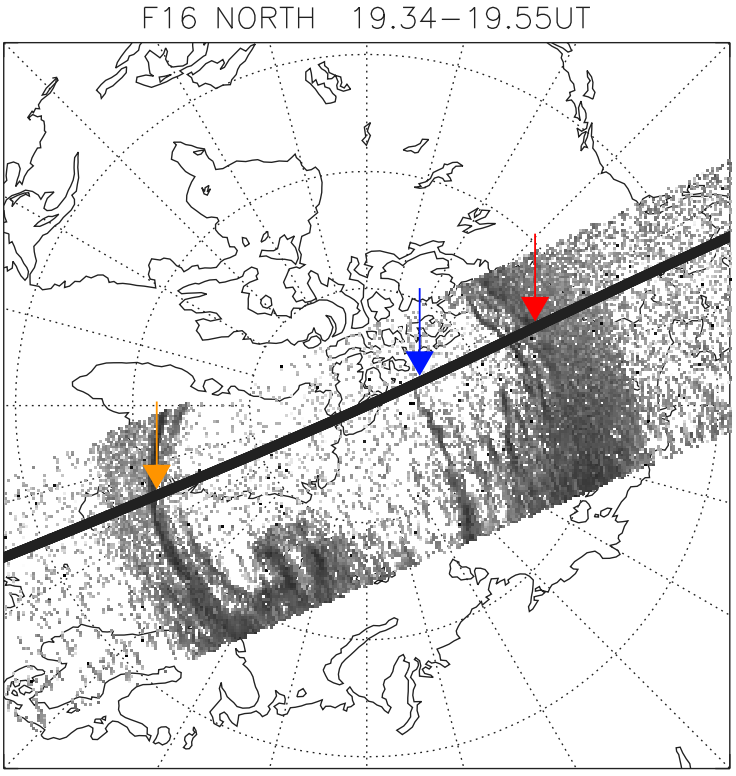

FIGURE 3.12: Footprint of the DMSP F16 spacecraft during the 19:34-19:55 UT pass, overplotted onto the corresponding SSUSI image. The arrows correspond to features in the DMSP particle spectrogram shown in Figure 3.13.

to the spacecraft crossing the duskward edge of the auroral oval (orange), the tip of the dawnside arc (blue) and the dawnside of the auroral oval (red). Fig. 3.13a shows the spectra for each of these features in the corresponding colours. These spectra clearly show that the precipitation causing the dawnside arc is of lower energy than that above the auroral oval.

Figure 3.13b shows the DMSP electron spectrogram with the times of the three spectra indicated again with the orange, blue and red arrows. The black vertical line marks the noon-midnight meridian, hence dividing the dawn and dusk sides of the polar cap. Multiple low energy features can be seen in the dawnside of the polar cap, the highest energy of these corresponds to the furthest protruding arc (blue arrow). Not all of these features can be seen in the corresponding SSUSI image (Fig. 3.12) as they are too low in energy flux to be picked up by the UV imager. The ion spectrogram (Fig. 3.13c) shows two ion signatures corresponding to each side of the auroral oval with no ion signatures

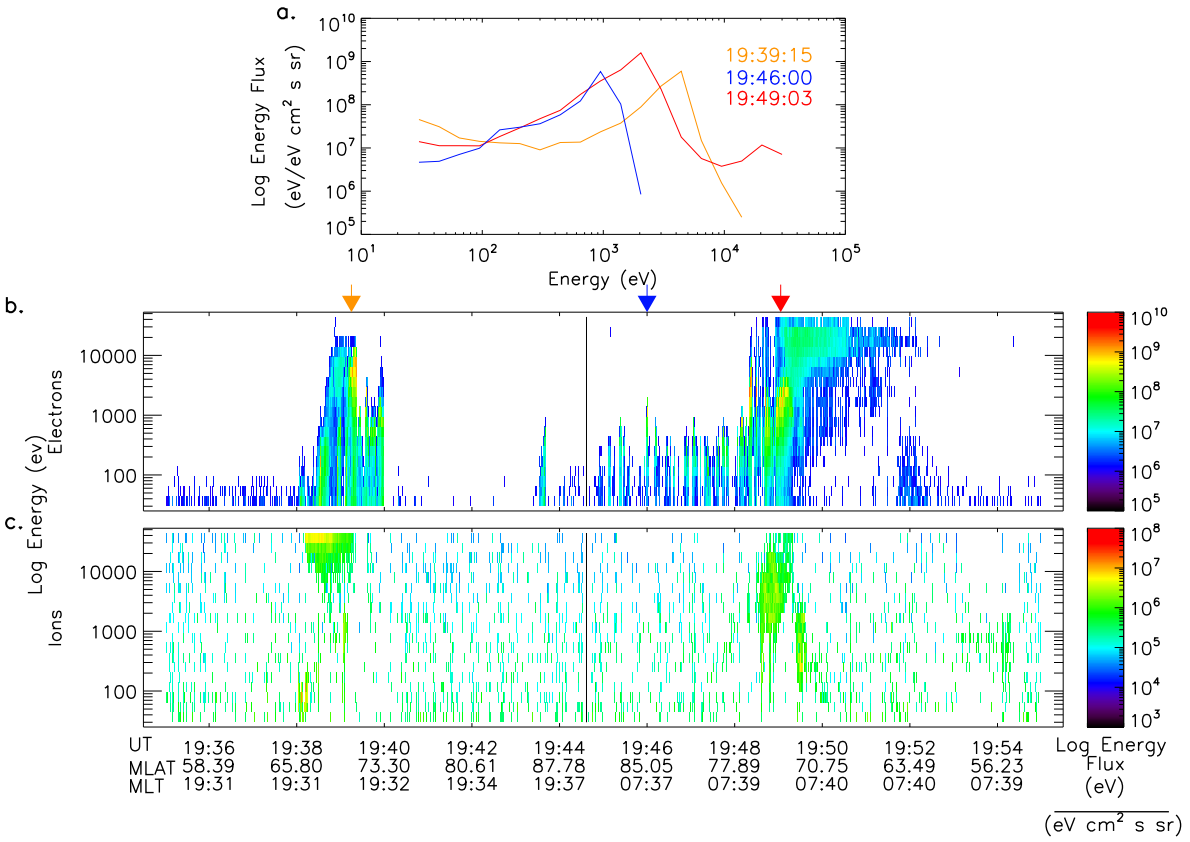

FIGURE 3.13: Data from the particle spectrograph SSJ/5 on-board DMSP F16 between 19:34-19:55 UT. a. Spectra (1 second) from the three times indicated by the arrows on the DMSP pass (Fig. 3.12) at 19:39.15, 19:46.00 and 19:49.03 UT.; b. The electron spectrogram with the time of the above spectra indicated by the corresponding coloured arrows. c. The ion spectrogram. The black line seen in b and c corresponds to the noon/midnight meridian to differentiate the dawn and dusk sides of the polar cap.

within the polar cap between them. Newell et al. [2009] reported a common type of polar cap arc that can be identified by lower energy precipitation with no ion signature. They state this type of arc is consistent with accelerated polar rain, which Carlson and Cowley [2005] suggest can occur from shear flows on open field lines. Furthermore, the IMF conditions of negative B_x and positive B_y favour polar rain in the dawnside of the northern hemisphere polar cap [Meng and Kroehl, 1977, Yeager and Frank, 1976]. We hence suggest the dawnside arc is an example of an arc formed by accelerated polar rain, occurring on open field lines.

As an additional point, Figs. 3.13a and b show the oval electron signatures to have energy of the order of a few keV, with a peak on the dusk side of 5 keV. These energies are very similar to those derived for the duskside structure from the ASK and ESR observations and hence further supports the idea that this feature is formed on closed

field lines.

3.2.3.2 SuperDARN lobe reconnection flows

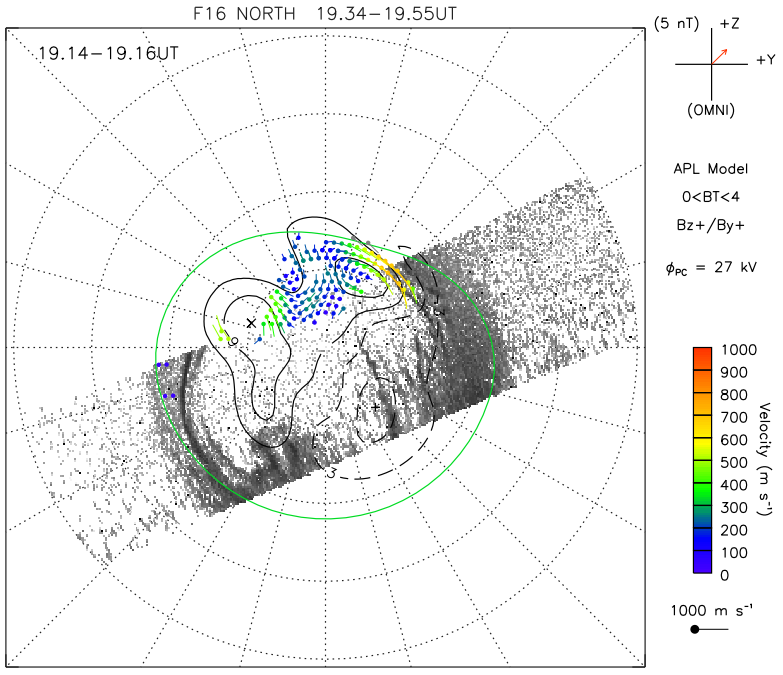

FIGURE 3.14: Map potential plot of SuperDARN data between 19:14-19:16 UT overplotted on the SSUSI image between 19:34-19:55 UT in the northern hemisphere.

Examination of the map potential plots from SuperDARN during our event revealed evidence of lobe reconnection between 19:12-19:30 UT and 20:10-21:00 UT. Examples are shown in Figures 3.14 and 3.15 at 19:14 UT and 20:14 UT, respectively, with the corresponding SSUSI image. Both images show sunward flows on the dayside of the polar cap and what appear to be dawnside lobe reconnection cells. The anti-sunward return flows appear to be poleward of the extension of the main oval from the SSUSI field of view, which is indicative of single lobe reconnection [Milan et al., 2000a].

We previously noted that the furthest extended sun-aligned arc on the dawnside moved duskward between SSUSI images seen in Figs. 3.4a and c, which approximately corresponds to between 19:30 - 20:00 UT. This motion is consistent with what is expected observationally for positive IMF B_y (e.g. Valladares et al. [1994]). It is also consistent with Milan et al. [2005] suggestion that the 'stirring' of flux caused by lobe reconnection

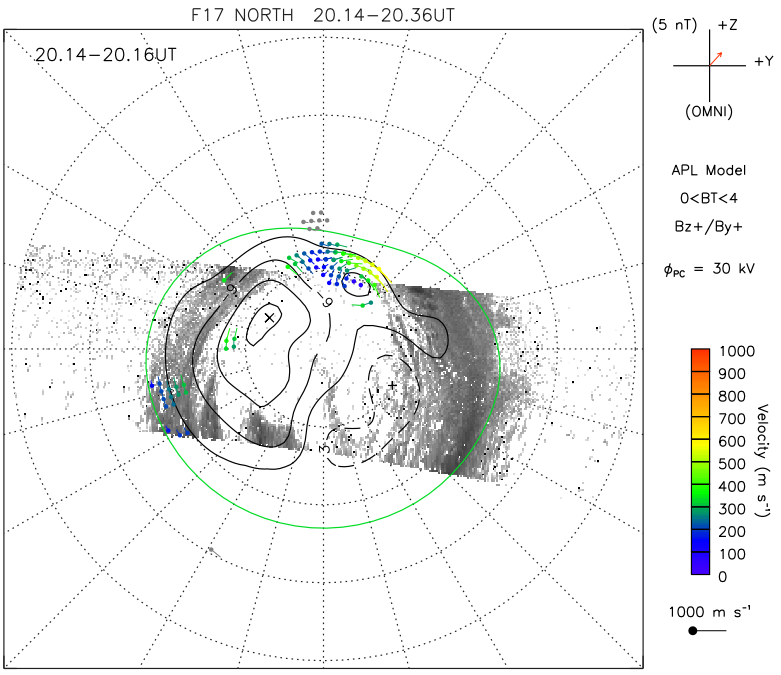

FIGURE 3.15: SuperDARN map potential plot between 20:14-20:16 UT overplotted on the SSUSI image between 20:14-20:36 UT.

in one hemisphere results in flux being transferred between dawn/dusk convection cells depending on the direction of IMF B_y. Milan et al. [2005] argued that this transferal of flux causes the arc, depending on its spatial location relative to the lobe convection, to move in the direction of IMF B_y, which is consistent with our observations.

3.3 Discussion

The structure seen by the SSUSI imager on the duskside of the northern hemisphere was analysed with the ASK instrument and the ESR radar in conjunction the Southampton ionospheric model to estimate the energy of the electron precipitation. This analysis revealed that the structure was associated with high energy precipitation which likely occurred on closed field lines. The structure formed out of an auroral bulge. The small, localised disturbances in the Svalbard magnetometer data (Fig. 3.3) coupled with the location of the bulge at the poleward edge of the oval suggested it is formed by closure of flux at the far Earth neutral line, resulting in a poleward boundary intensification. This is further supported by SuperDARN flows seen in Fig. 3.11, which indicate magnetotail

reconnection was occurring around the position that the bulges formed in the polar cap. Flows measured by SuperDARN in the northern hemisphere (Figs. 3.9 and 3.10) indicated that after the IMF turned northward, flux continued to close in the tail. Hence we suggest, due to an assumed absence of low-latitude dayside reconnection from evidence of lobe reconnection (Figs. 3.14 and 3.15), subsequently closed field lines protruded further into the polar cap instead of convecting back to the day side. Furthermore, the flows in Fig. 3.11 show flows exiting the polar cap at 21 MLT which indicates the IMF B_y was having an effect on reconnection in the tail. These observations are consistent with the mechanism described in Milan et al. [2005] for transpolar arcs. However, as the structure does not cross the entire polar cap, we conclude it is an example of a 'failed' transpolar arc. The transpolar arc most likely failed due to a cessation in nightside reconnection between 19:30-20:30 UT when the structure was seen to stay at the same magnetic latitude in the SSUSI images (i.e. between Figs. 3.2c and 3.4a). This claim is somewhat supported by the fact that we see no evidence of nightside reconnection in the SuperDARN data (such as those seen earlier in Figs. 3.9 and 3.11) during this interval (not shown). Furthermore, the structure is no longer seen by SSUSI after 20:40 UT (also not shown), which coincides with the Southward turning of the IMF (Fig. 3.1).

The Milan et al. [2005] mechanism (described in Section 1.5.2.2) predicts that the transpolar arc would form on the duskside of the northern polar cap for positive IMF B_y, statistically verified by Fear and Milan [2012a], which is consistent with the conditions for this event. However the southern hemisphere counterpart also appears on the duskside which is not consistent with the Milan et al. [2005] mechanism. Grocott [2017] suggests there are two factors which lead to asymmetric flows seen in the polar cap, as seen in the southern hemisphere SuperDARN observations (Fig. 3.11). The first factor is a twist in the magnetotail occurring after a few hours of B_y influence and results in asymmetries between auroral onset location in the northern and southern hemispheres, which is why the Milan et al. [2005] mechanism predicts transpolar arcs on opposite sides of the polar cap in the different hemispheres. A study by Reistad et al. [2016] reported a 3 hour MLT shift in the auroral onset region seen by simultaneous of measurements from the IMAGE FUV-WIC camera in the northern hemisphere and the Polar VIS Earth camera in the southern hemisphere. This shift was seen on the duskside of the auroral oval and was attributed to a persistent positive IMF B_y component which led to asymmetries in the magnetospheric footprints. The second factor is caused by dawn-dusk asymmetries

in the plasma sheet occurring after longer periods of stable B_y which results in a shift in the auroral onset location to earlier MLT for positive B_y and later for negative B_y. The latter mechanism appears to be consistent with our event since the IMF B_y component in the hours before the period of interest (Fig. 3.1) and in the previous 24 hours (not shown) was predominately positive and the structures appear on the same side of the polar cap. Hence our event could be evidence for the two factors being present at the same time, an idea speculated by Grocott [2017], or could suggest that the lack of day-side reconnection rather than the twist in the magnetotail is the key factor in the Milan et al. [2005] mechanism for this case. Furthermore, although our event does not seem to show such a dramatic asymmetry, and is occurring under northward IMF conditions, Figures 3.4a and b do show a shift in the position of the 'failed' transpolar arc, which could be considered consistent with Reistad et al. [2016].

The multiple, sun-aligned arcs seen in the dawn side northern hemisphere polar cap appear to be formed by a different mechanism than the duskside structure. They were only seen in one hemisphere of the SSUSI images (Figs. 3.2 and 3.4) and the DMSP particle data showed the furthest protruding arc to be of lower energy than the oval and duskside structure and not associated with an ion signature (Fig. 3.13). This is different to the DMSP observations of a transpolar arc in a study by Fear et al. [2014] which showed the arc to be associated with high energy electron (up to 10 keV) and ion (greater than 1 keV) signatures. This study also presented observation from Cluster that showed the plasma source for this arc was on closed field lines. They also saw lower energy electron-only signatures, which did not have a counterpart in IMAGE, and suggested these may be associated with fainter polar cap arcs that may be formed on open field lines. These features are more consistent with the DMSP precipitation associated with the dawnside arcs in this study. Similarly, a study by Mailyan et al. [2015] saw a transpolar arc in IMAGE associated with a lower energy plasma signature detected by Cluster than that seen by [Fear et al., 2014]. Mailyan et al. [2015] also presented images from the GUVI (Global Ultra Violet Imager) Instrument (same instrument to SSUSI) on board the TIMED spacecraft, which showed fine structures around the transpolar arc which were associated with low energy electron and no ion signatures in the DMSP particle data. These features are potentially consistent with polar rain signatures, similar to the dawnside arc presented in this study. Additionally, in another polar cap aurora

study using DMSP particle data Cumnock et al. [2009] found examples where a large-scale arc seen by IMAGE was made up of multiple-thin arcs. All of these high latitude arcs were shown to have an ion signature as well as energies comparable to the main oval, and in this respect are different from the dawnside sun-aligned arcs in this study.

Newell et al. [2009] suggest polar cap arcs that do not have an ion signature and are not adjacent to the auroral oval could be produced by enhanced polar rain (discussed in Section 1.5.2.3). It can be seen in Figure 3.13b that the sun-aligned arc on the dawnside of the northern hemisphere polar cap is embedded within similar features of lower energy electron precipitation, which are not seen in the SSUSI image. These features are similar to what Shinohara and Kokubun [1996] classify as type B polar showers, i.e. polar showers without ion fluxes that respond to solar wind conditions (appearing on the dawnside for positive B_y and northern hemisphere for negative B_x) and hence suggested to originate from the solar wind (outlined in Section 1.4.5). Therefore, we conclude that these sun-aligned arcs are consistent with accelerated polar rain and hence formed on open field lines.

We have shown that the dawnside arcs move duskward with the flow in the lobe convection cells. This duskward motion for positive IMF B_y is a consistent with previous studies which observed polar cap arcs to move in the same direction as IMF B_y. Milan et al. [2005] suggest the convection caused by the stirring of the lobes will cause polar cap arcs in the northern hemisphere to convect duskward/dawnward for IMF B_y positive/negative respectively. This pattern is observed during our event. As an additional point, the duskside structure was seen by the SIF ground based camera to move from west to east, i.e. dawnward. This motion also fits with the Milan et al. [2005] mechanism but the arc moves oppositely to the direction of IMF B_y because it is on the other side of the polar cap and hence moving with the dusk cell. However this structure would have been classified by Hosokawa et al. [2011] as a 'B_y-independent' as it is moving poleward irrespective of the direction of IMF B_y. Hence 'B_y dependent' and 'B_y independent' arcs can both be explained by the Milan et al. [2005] mechanism.

3.3.1 Instrumentation contribution

Multiple instrumentation was used in this chapter to study a polar cap arc event.

UV images from the SSUSI instruments on board DMSP F16 and F17 were used to identify polar cap arcs, study their hemispheric nature and determine the lifetime of events and their spatial extents. The SSUSI observations provide a valuable global context, but the relatively low cadence compared with ground-based instrumentation means that it is possible that short-lived events may be missed.

Data from ground-based optical instrumentation on Svalbard (the ASK instrument and the TLC) were used to study the auroral feature on the duskside of the northern hemisphere polar cap at higher spatial and temporal resolution than was possible from the SSUSI images. ASK data were also used to obtain an estimate of the characteristic energy of the precipitation. The method used to estimate the energy method relies on the Southampton Ionospheric model and the calibration and analysis of the ASK data (as described in Section 2.1.1). The mean value of the energies obtained was consistent with the duskside feature being formed on closed field lines and was independently verified using data from the ESR.

Data from the ESR were also used to infer that an open-closed boundary had passed over Svalbard during our period of interest, and measurements from the SuperDARN radars were used to investigate the ionospheric flows around the polar cap arcs. A major limitation in this event was that there was only scatter from one beam of one radar around the 'failed' transpolar arc. Individual radars only provide a line-of-sight component of the ionospheric velocity - in order to obtain a 2D velocity vector, data from multiple radars must be available. Therefore, we can not say for sure what direction the ionospheric flow is in, we can only state that it is away from the radar and that this is consistent with flow out of the polar cap due to nightside reconnection.

The SSJ/5 particle spectrometer on board DMSP F16 was used to analyse the in situ signature of the northern hemisphere dawnside polar cap arc. Multiple peaks in the electron precipitation can be seen on the dawnside of the spectrogram in Fig. 3.13 which are not obviously associated with arcs in the SSUSI image (Fig. 3.12). We suggest this indicates that some arcs fall below the threshold of detection for the SSUSI instruments.

Data from a ground-based magnetometer chain near Svalbard was used to suggest that the magnetic and auroral features observed near to the start of the event were consistent with a polar boundary intensification. This fits with the picture that the duskside auroral feature was formed by closure of open field lines in the magnetotail.

3.4 Conclusion

A case study of polar cap aurora occurring on 19th January 2008 has been presented. Almost simultaneous observations of the northern and southern auroral regions were provided by the SSUSI instruments on-board DMSP F16 and F17. Two different types of high latitude aurora were observed simultaneously in the northern polar cap: a 'failed' transpolar arc on the duskside formed on closed field lines, and sun-aligned arcs on the dawnside which were consistent with precipitation on open field lines.

The duskside structure had a conjugate form in the southern hemisphere which also formed on the duskside on the southern polar cap. The structure started as a bulge, identified in magnetometer data as a polar boundary intensification, which grew into a distinctly sun-aligned structure. The northern hemisphere structure was examined using ground based instruments. Using observations from the ASK instrument in conjunction with the Southampton ionospheric model, the electron precipitation energy above the dusk structure was estimated to be between 2-11 keV and confirmed, by fitting electron density profiles from the ESR, to be monoenergetic in spectral shape. It was shown that these energies are similar to the measurements made by the DMSP particle spectrometer of the auroral oval. Images from the ASK1 camera also revealed highly structured and dynamic small-scale filamentary aurora; these are the first fine-scale observation of polar cap aurora using ASK. It was concluded the duskside structure was consistent with aurora formed on closed field lines. ESR electron temperature profiles showed very cold plasma prior to the onset of the aurora on closed field lines, hence suggesting that these closed field lines were within the open field lines of the polar cap. Coupled with the signatures of nightside reconnection observed in the SuperDARN data, we find this duskside structure to be consistent with the mechanism proposed by Milan et al. [2005] for transpolar arcs. The duskside protrusion was found to be consistent with the mechanism for transpolar arcs but in this case the structure did not cross the entire polar cap and is hence we suggest it is an example of a 'failed' transpolar arc. The arc perhaps failed due to a sudden cessation of nightside reconnection. Furthermore, the fact this feature was shown to form from a polar boundary intensification is consistent with the idea that transpolar arcs (failed or otherwise) are formed from magnetotail reconnection.

The second type of structure was only seen in the northern hemisphere SSUSI images and was analysed using data from the DMSP particle spectrometer. This sun-aligned arc was associated with lower energy electrons than in the oval and no ion signature. It also appeared on the dawnside of the northern hemisphere polar cap which is consistent with statistics for polar rain. Hence this arc is suggested to be an example of the common weaker polar cap arcs described in Newell et al. [2009], consistent with acceleration of polar rain on open field lines.

This chapter adds to the existing knowledge of polar cap arcs in the following ways:

- It presents the first observations of simultaneous polar cap arcs that are consistent with formation on different magnetic field topologies. This observation resolves some of the controversy discussed in Section 1.5.3.1 which has arisen due to conflicting reports of polar cap arcs occurring on open or closed field lines. The fact that these different mechanisms can occur simultaneously is important for the configuration of the Earth's magnetosphere during northward IMF.

- We suggest that the previous discrepancy in observations of polar cap arcs may have have been due to instrumentation limitation whereby ground-based cameras are more sensitive to lower energy polar cap arcs on open field lines whereas the high altitude UV imagers only observe the higher energy events on closed field lines.

- This chapter has also investigated the motion of polar cap arcs using auroral images and measurements of the ionospheric flow from SuperDARN. We discussed the apparent contradictory observations from Hosokawa et al. [2011] and demonstrated that these observations can be explained within the framework of the formation mechanism described by Milan et al. [2005].

- We expand on the understanding of the closed field line formation mechanism suggested by Milan et al. [2005] by relating it to the first observation of a 'failed' transpolar arc and an observation of a conjugate arc that was on the same side of the polar cap in both hemispheres (as opposed to being mirrored about the noon-midnight meridian).

This chapter has demonstrated that the SSUSI instruments are capable of observing polar cap arcs consistent different formation mechanisms, hence suggesting these instruments provide intermediary observations between the ground-based and high altitude instruments. This capability will be further investigated in Chapter 4.

Chapter 4

Inter-hemispheric survey of polar cap auroras

This work has been published as:

J. A. Reidy, R. C. Fear, D. K. Whiter, B. Lanchester, A. J. Kavanagh, S. E. Milan, J. A. Carter, L. J. Paxton, and Y. Zhang. Interhemispheric survey of polar cap aurora. *Journal of Geophysical Research: Space Physics*, 123(9):7283–7306, 2018. doi: 10.1029/2017JA025153

4.1 Introduction

Following the observations presented in Chapter 3, in this chapter we present a survey of SSUSI and SSJ/5 particle data from December 2015. This month was initially chosen in order to identify further conjunctions between polar cap arcs (PCAs) and the ASK instrument. We also investigate the occurrence frequency of polar cap arcs in the SSUSI instruments using three further months of SSUSI data from 2015, including June (southern hemisphere summer), and March and September (the equinox months).

As discussed in Section 1.4, precipitation is present across the entire polar cap known as polar rain. Polar rain originates from the solar wind and enters the Earth's magnetosphere via open field lines. Intensification's in the polar rain, known as polar showers, have been found to be correlated with northward IMF [Hardy et al., 1982]. Shinohara

and Kokubun [1996] classified polar showers depending on whether they contained ion precipitation or not. The type with ion precipitation ('type a') was also found to be associated with high energy electron precipitation and is thought to originate on closed field lines. The type without ion precipitation ('type b') is thought to occur on open field lines due to its similarities in IMF dependence to polar rain (discussed in Section 1.4.5).

New capabilities, including low-altitude auroral imagery (such as that from the SSUSI instruments on board several of the DMSP spacecraft) have led to a renewal of interest in inter-hemispheric observations of polar cap arcs and associated plasma signatures. Carter et al. [2017] reported a simultaneous observation of polar cap arcs occurring in both hemispheres using data from SSUSI and a UV imager on board the IMAGE (Imager for Magnetopause-to-Aurora Global Exploration) satellite. Using the particle data from the DMSP spectrometer SSJ/5 they showed the arcs to be associated with ion precipitation, consistent with formation on closed field lines. Xing et al. [2018] presented a similar observation with a conjugate polar cap arc that was seen to be associated with ion precipitation in the DMSP particle data that was hence also consistent with a closed field line mechanism. DMSP particle data were also published in association with a large-scale polar cap arc in Fear et al. [2014]. Their observations showed an arc associated with an ion signature that was consistent with the closed field line tail reconnection mechanism suggested by Milan et al. [2005]. Conversely, as we presented in the previous chapter, SSUSI observations of a polar cap arc occurring in only one hemisphere were found to be associated with an electron-only signature in the DMSP SSJ/5 particle data. This arc was found to be consistent with formation on open field lines by accelerated polar rain. These different observations appear to be consistent with the type a and b polar showers identified by Shinohara and Kokubun [1996] discussed above and will also be investigated in this chapter.

One problem for either open or closed field lines formation mechanisms, is the so called 'non-conjugate theta aurora' (discussed in Section 1.5.3.2). This kind of aurora will be explored in this chapter by using the near-simultaneous SSUSI observations to investigate the hemispheric nature of polar cap arcs.

This chapter also aims to investigate polar cap arc occurrence by surveying three further months of SSUSI images from 2015. As discussed in Section 1.5.3.3, previous polar cap arc surveys have shown different occurrence rates for polar cap arcs with ground based

surveys finding polar cap arcs to be occurring at least 40% of the time [Valladares et al., 1994], whereas Kullen et al. [2002] found an occurrence of at least 10% of the time using data from Polar UV (a high altitude UV imager). This difference in occurrence rate could be due to the different types of polar cap arcs, with the lower energy arcs dominating the ground based studies and perhaps being missed by the UV imagers that see only the brighter larger scale events. As shown in the previous chapter, SSUSI can observe polar cap arcs occurring on both open and closed field lines and hence this capability will be further investigated in this chapter.

A brief overview of the instrumentation used in this survey is given in Section 4.2. Section 4.3 discusses the polar cap arc events recorded in December 2015 in conjunction with the corresponding particle data. These events are separated depending on whether they were observed in one or both hemispheres. Section 4.4 will present polar cap arc occurrence statistics over four months in 2015. Lastly a discussion and conclusions are given in Sections 4.5 and 4.6 respectively.

4.2 Instrumentation

As previously mentioned, SSUSI images are used to identify polar cap arcs. This survey uses data from the SSUSI instruments on board DMSP F16, F17 and F18 (see Table 2.1), data from the SSUSI instrument on board DMSP F19 are not included in this survey as these data were not publicly available at that time. The corresponding data from the SSJ/5 particle detector (described in Section 2.2.1) on board DMSP F16-F18 are also obtained for events where the spacecraft track intersected a polar cap arc. For one event identified in this suvey, supporting observations of the global field-aligned current systems inferred from the AMPERE data set are provided (described in Section 2.2.2). Data from OMNI [King and Papitashvili, 2005] and ARTEMIS 1 [Auster et al., 2008] are also obtained to evaluate the IMF conditions during the polar cap arc events (discussed in Section 2.5).

4.3 Observations

Data from December 2015 were obtained from the SSUSI instruments on DMSP spacecraft F16, F17 and F18. This was an interval when data from all three spacecraft were available and coincided with an instrument campaign ran by the University of Southampton for the ASK instrument (described in Section 2.1.1). Over that month, 43 polar cap aurora events were identified in the SSUSI data. These events are defined by the presence of polar cap arcs in the SSUSI images; SSUSI images with more than one arc are counted as one event.

Once identified, the events were classified using the SSUSI images in both hemispheres. To be classified as a 'both hemisphere' event, the arc had to be visible in two subsequent images, one from each hemisphere. As discussed later, this classification does not necessarily imply conjugacy, as independent 'open field lines' arcs could form in both hemispheres simultaneously. To be classified as a 'one hemisphere' event, the arc had to appear in one SSUSI image, then be absent in the next available images for all spacecraft in the opposite hemisphere, but then still be visible in the subsequent images of the original hemisphere. If an arc was seen in one image, not in the following hemispheric images and then not in the next images of the original hemisphere, it was left unclassified. This is because the arc was not visible in the SSUSI images long enough for its hemispheric nature to be determined. Events where the SSUSI field of view was obstructed in one hemisphere or where the data quality was not good enough to distinguish the main auroral oval were left unclassified.

Out of the 43 events identified in December 2015, 19 were seen in both hemispheres, 8 in one hemisphere only and 16 were left unclassified. In this chapter, we consider only the events that could be classified as 'one hemisphere' or 'both hemisphere' and that had particle data from the SSJ/5 instruments on board the DMSP spacecraft. All 19 'both hemisphere' and 2 of the 8 'one hemisphere' events had particle data. Figure 4.1 shows the IMF B_y and B_z components averaged over the event duration for these 21 events. The event duration is given by the start and end times of the first and last SSUSI images, respectively, containing polar cap arcs. From Fig. 4.1 it can be seen that most of the events occurred during northward IMF or B_z close to zero and under the influence of a significant IMF B_y component. The color coding is discussed below in

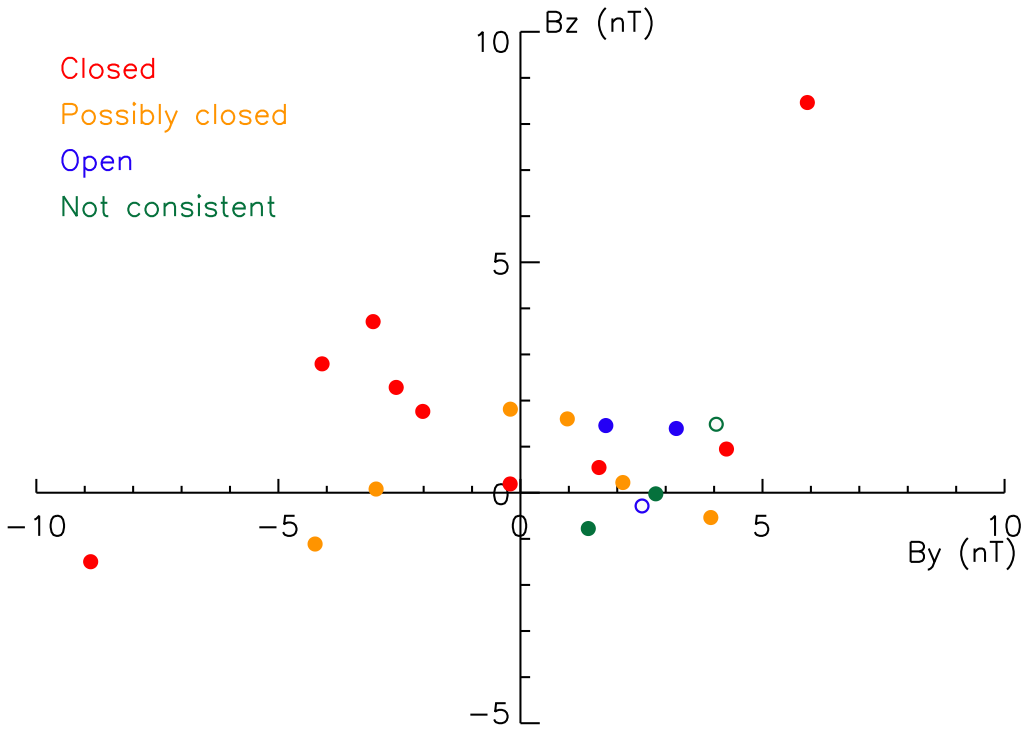

FIGURE 4.1: IMF B_y and B_z components averaged over each of the 22 events identified. The colors denote the possible classifications with filled circles for 'both hemisphere' events and open circles for 'one hemisphere' events.

Sections 4.3.1 and 4.3.2. The filled in circles correspond to 'both hemisphere' events, the open circles represent 'one hemisphere' events.

Data from the particle spectrometer on board the DMSP spacecraft were obtained for events when the spacecraft track crossed the arc, and were used to classify whether each event corresponded to open or closed field lines. If arcs are associated with an ion signature and seen in both hemispheres then they are consistent with a closed field line formation mechanism (e.g. Carter et al. [2017], Xing et al. [2018]). If the arcs are associated with an electron-only signature then they are consistent with an open field line mechanism [Newell et al., 2009, Reidy et al., 2017], whether they are seen in one or both hemispheres. Ion and electron signatures are identified when the summed energy flux of the high energy particles is above a certain threshold. For an arc to be classified as having an ion signature we required both the summed ion and electron fluxes to be above a certain value; this was required in an attempt to avoid associating cusp precipitation (which occurs on open field lines but may contain ions [Frey et al., 2003]) with the polar cap arcs, particularly on DMSP passes which orbit close to the dayside aurora. Hence in this chapter when we refer to an arc having an 'ion signature', we technically mean an ion and an electron signature. For an electron-only signature,

TABLE 4.1: Events identified as occurring in both hemispheres in SSUSI data. Event times are extracted from the SSUSI images whereby the start and end times are recorded when the DMSP spacecraft crosses 70° magnetic latitude. All arcs that intersected the DMSP footprint have an electron signature. The arcs with an accompanying ion signature are marked by 'y', electron-only arcs 'n'. The column is left blank if the DMSP footprint does not intersect the arc. The classification of the arc, i.e. whether it is consistent with an open or closed field line mechanism, is indicated in the last column, with the same categories as in Fig. 4.1.

Event num.	Start Time (UT)	End Time	NH ion sig.	SH ion sig.	Classification
03	2015/12/02 22:21	2015/12/03 01:17	y	y	Closed
04	2015/12/03 14:36	2015/12/03 16:36	y	y	Not consistent
06	2015/12/03 23:59	2015/12/04 01:04		y	Possibly closed
07	2015/12/04 08:36	2015/12/04 13:14	y	y	Closed
08	2015/12/04 16:11	2015/12/04 21:26	y		Possibly closed
10	2015/12/06 13:09	2015/12/06 16:09	y		Possibly closed
11	2015/12/06 17:22	2015/12/06 18:38	n	n	Open
14	2015/12/08 11:06	2015/12/08 12:59	n	y	Not consistent
15	2015/12/08 14:25	2015/12/08 15:18	n	n	Open
22	2015/12/14 17:21	2015/12/14 20:55	y	y	Not PCA
23	2015/12/15 12:55	2015/12/15 14:11	y		Possibly closed
24	2015/12/15 17:08	2015/12/15 20:45	y	y	Both observed simultaneously
26	2015/12/16 18:36	2015/12/16 23:56	y	y	Closed
31	2015/12/22 13:04	2015/12/22 18:16	y	y	Closed
35	2015/12/25 18:18	2015/12/25 22:09	y	y	Closed
38	2015/12/27 01:02	2015/12/27 01:20		y	Possibly closed
39	2015/12/27 14:28	2015/12/27 18:18	y	y	Closed
40	2015/12/27 22:01	2015/12/28 00:49		y	Possibly closed
43	2015/12/31 16:06	2015/12/31 18:15	n	y	Closed

we required the summed electron flux to be above a certain threshold and the summed ion flux to be below a threshold. We found it was not possible to set a single threshold that could be used uniformly for all events, which would identify all plasma signatures in all events without also identifying 'noise' in the spectrograms of some other events. Therefore, the threshold was adjusted in some cases based on a manual examination of the spectrograms, the auroral images and the summed flux time series. Full details of the method used to identify the particle signatures are given in Appendix A.

4.3.1 Events occurring in both hemispheres

Table 2.1 lists the 19 events identified as occurring in the polar caps of both hemispheres simultaneously. In all 19 cases there was a pass by a DMSP satellite over the polar cap arc in at least one hemisphere on at least one orbit and hence particle data for these arcs

have been obtained. As these arcs are seen to be occurring in both hemispheres, our initial expectation would be for them to be consistent with a closed field line formation mechanism and hence we expect to see an electron and an ion signature associated with these arcs. The fourth and fifth columns of Table 2.1 list which arcs had an ion signature in either or both hemispheres. These columns are left blank for events when the arc does not intersect the DMSP track. All arcs were associated with an electron signature on the passes which intersected the arc. It can be seen that: (a) 9 of the events contain arcs with an ion signature in both hemispheres, (b) 2 have electron-only signatures in both hemispheres, (c) 2 have an ion signature in one hemisphere and an electron-only signature in the other and (d) 6 have an ion signature in one hemisphere but the arc in the opposite hemisphere did not intersect the DMSP footprint and hence no particle data could be obtained for those arcs. We discuss each of these groups below by classification, which is indicated in the last column of Table 2.1 and also indicated in Figure 4.1, but at this point note that (a) and possibly (d) are consistent with our expectations (i.e. with closed field lines, given that they are present in both hemispheres) whereas (b) and (c) are not. Events in group (b) are potentially consistent with independent simultaneous open field line arcs in the two hemispheres. NB Events 22 and 24 contain auroral structures initially identified as polar cap arcs, associated with ion signatures in both hemispheres and are hence included in group (a) but are classified differently as 'Not PCA' and 'Both observed simultaneously' which will be addressed in Sections 4.3.1.1 and 4.3.1.2 respectively.

4.3.1.1 (a) Consistent with a closed field line mechanism

Figure 4.2 shows summary images for all the events with a polar cap arc associated with ion precipitation in both hemispheres. Each row consists of four figures corresponding to a single event. For each event, the clearest SSUSI images (i.e. the images where the polar cap arc is most visible) and the corresponding SSJ/5 spectrograms are chosen from each hemisphere. As presented in Chapter 3, the SSUSI images are projected onto magnetic local time grids and the southern hemisphere images have been flipped across the noon-midnight meridian for ease of comparison with the northern hemisphere, such that noon is to the top of each image and dawn is always to the right. This means the DMSP track on the southern hemisphere SSUSI images is in the opposite direction (i.e. from right to left) to the northern hemisphere passes and hence features are mirrored in the southern

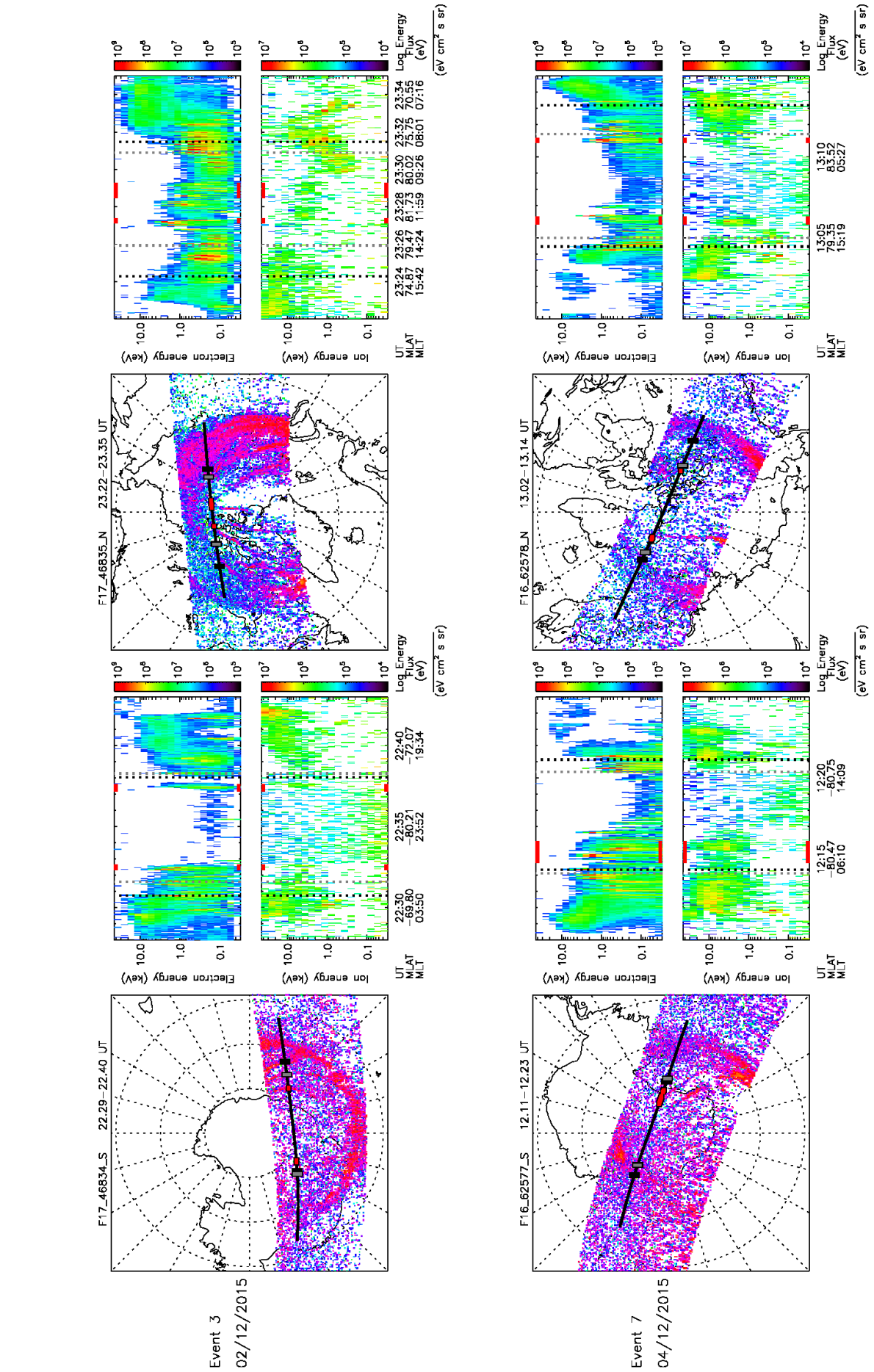

FIGURE 4.2: Summary images for arcs with polar cap arcs in both hemispheres associated with ion signatures. Each row represents an event with a summary SSUSI image from each hemisphere during the event and the corresponding DMSP SSJ/5 particle data. The black line on the SSUSI data is the footprint of the DMSP spacecraft. Ion signatures are indicated in red, electron-only signatures are indicated in orange - Continued overleaf.

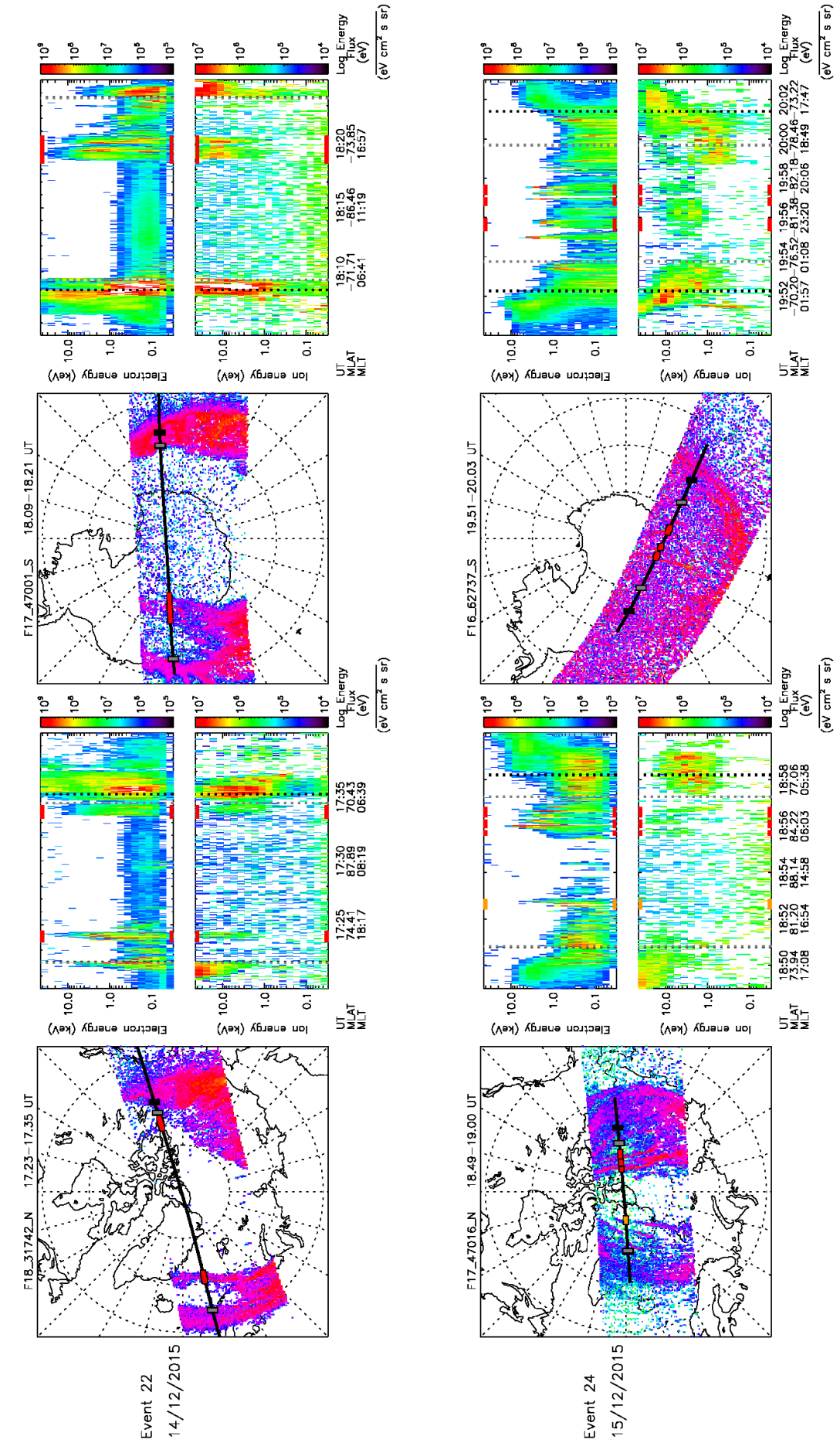

FIGURE 4.2: Continued

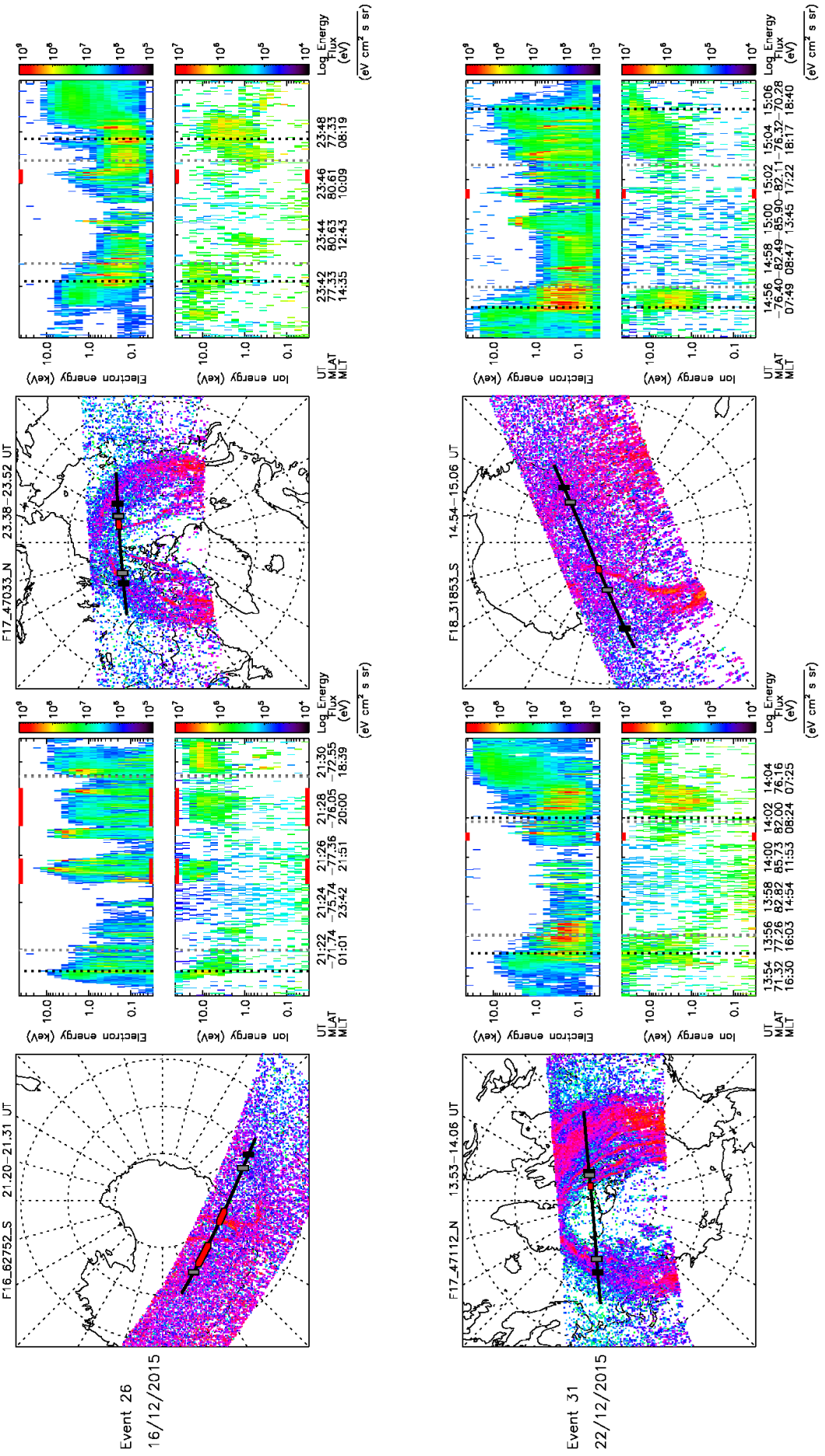

FIGURE 4.2: Continued

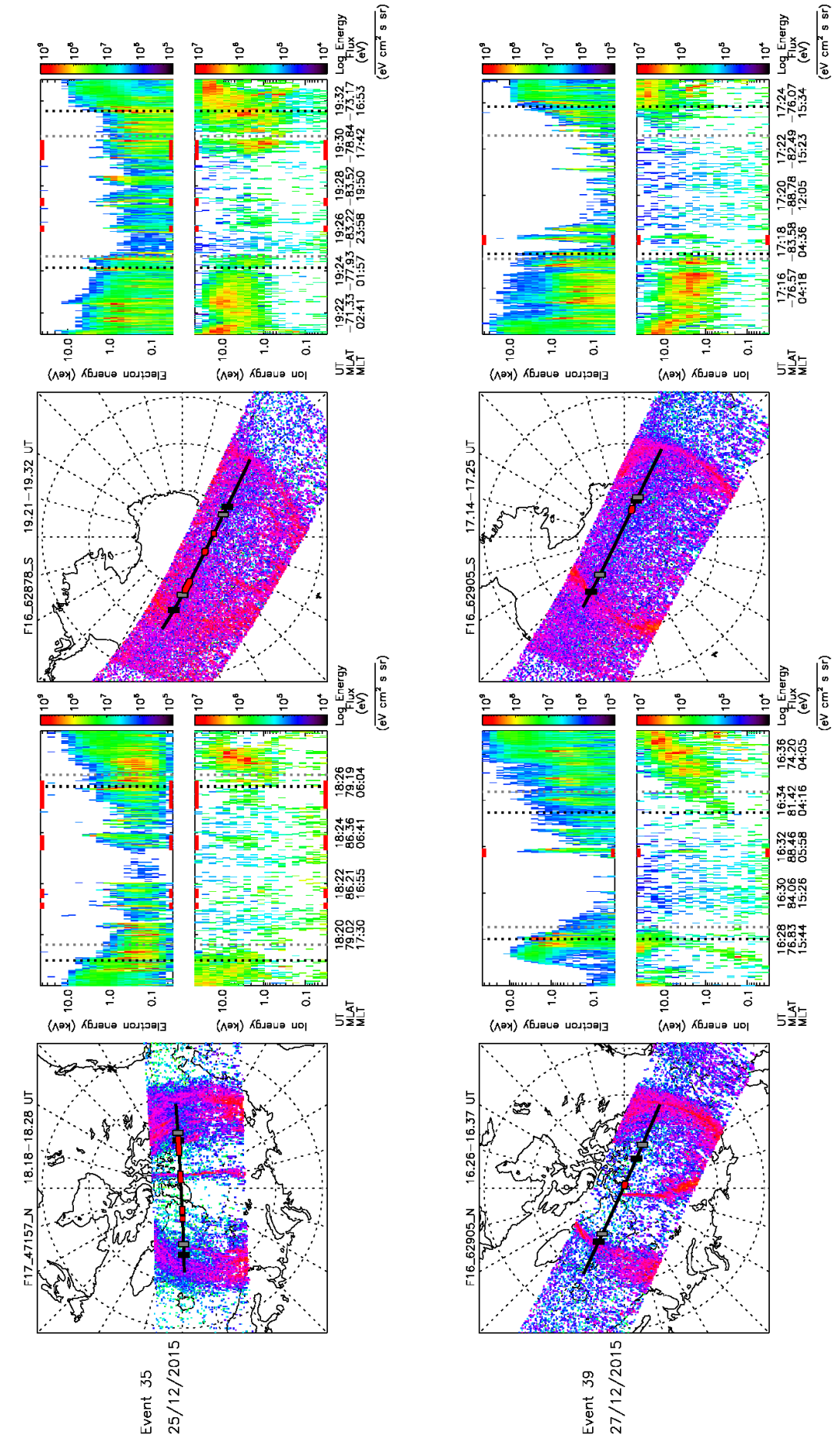

FIGURE 4.2: Continued

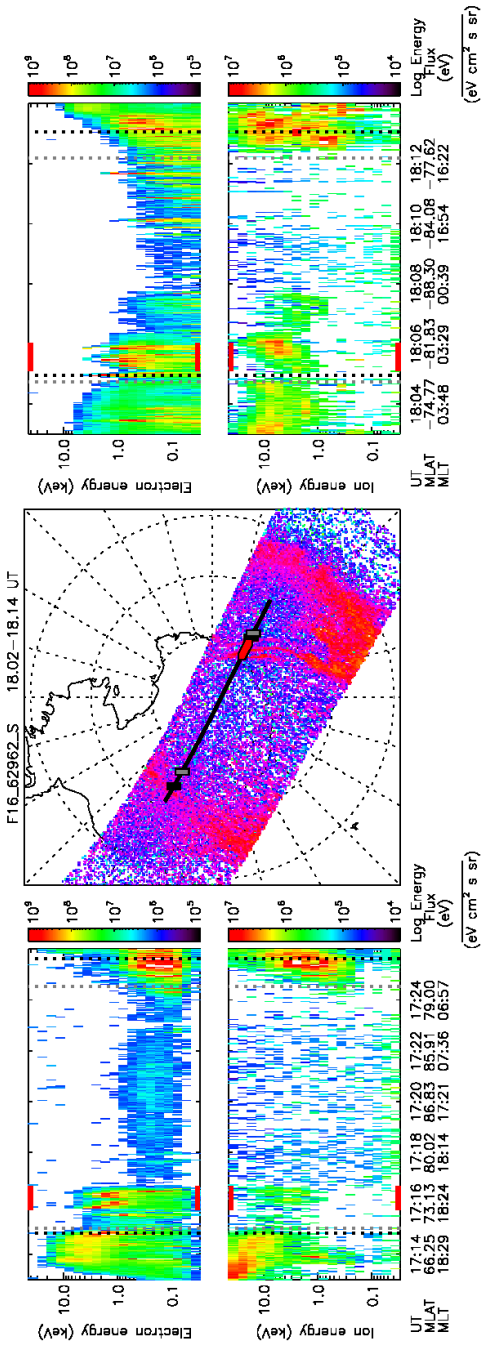

FIGURE 4.2: Continued

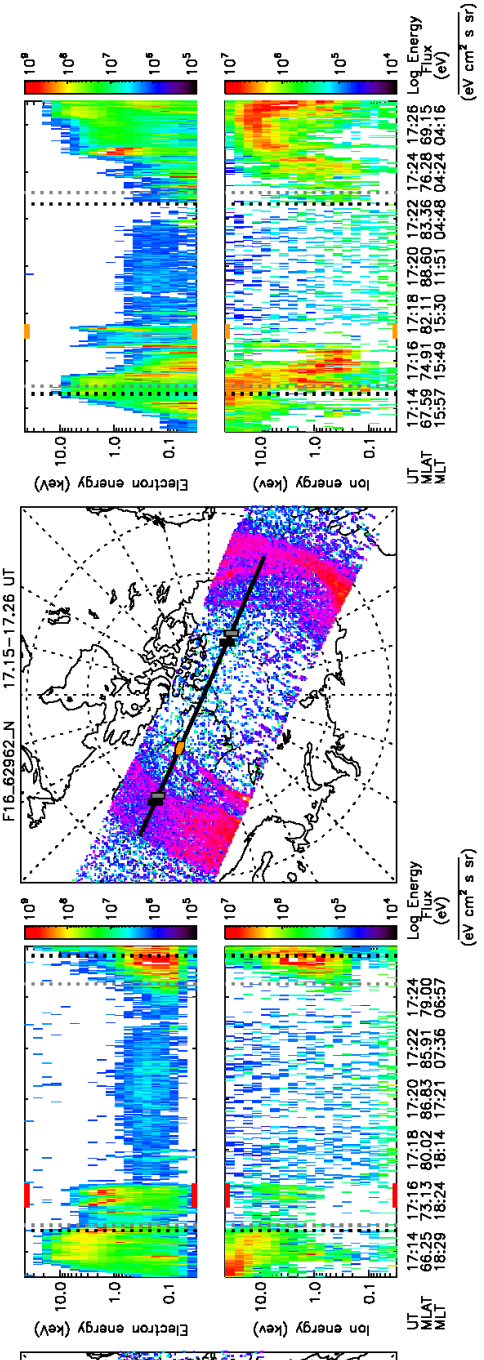

FIGURE 4.3: The SSUSI and corresponding SSJ/5 data for both northern hemisphere passes shown in Fig. 4.2 for Event 43

hemisphere SSUSI and SSJ/5 images. Ion and electron-only signatures, meaning the presence of electron and ion fluxes with energies greater than approximately 1 keV, are identified from the DMSP SSJ/5 data. These are shown on the ion and electron spectrograms and on the track of the DMSP spacecraft (black line) in the SSUSI images in red, for arcs associated with ion precipitation, and orange, for arcs associated with electron-only precipitation (e.g. Event 24, row 4, shows an example of both). An estimated position for the poleward boundary of the auroral oval is also indicated for each event (dashed vertical lines on the particle spectrograms and small vertical lines on the DMSP track on the SSUSI images - grey for the ion boundary, black for the electrons). These boundaries are defined as where there is a significant drop in the high energy particle fluxes poleward of the auroral oval [Newell et al., 1996b]. Full details of the method used to define these boundaries are given in Appendix A.

All of the events shown in Fig. 4.2 contain arcs associated with an ion signature in both hemispheres and are hence consistent with formation on closed field lines. These arcs are represented in Fig. 4.1 by the red filled circles. In each of the particle spectrograms in Fig. 4.2, energetic signatures in both the electrons and ions can be seen corresponding to the polar cap arcs, indicated in red. High energy electron and ion precipitation is detected either side of the polar cap arc as the spacecraft passes through the main auroral oval (e.g. Event 3, top row of Fig. 4.2). In some spectrograms, low energy 'uniform' precipitation can be seen between the oval signatures in the electron spectrograms (e.g. Event 22, third row of Fig. 4.2); this type of signature is typical for what is expected for polar rain (e.g. Gussenhoven et al. [1984]). As a side point, we note that the DMSP spacecraft passes close to the dayside in the northern hemisphere in Events 3 and 26 (first and fifth row of Fig. 4.2). As cusp precipitation (on open field lines) can include ions, the SSUSI images were also examined in the Lyman-alpha channel (not shown). No obvious evidence of a cusp spot could be seen for either event, although it is possible the particle flux was not high enough to generate an auroral signature for the cusp.

The northern hemisphere summary image for Event 43 (bottom row of Fig. 4.2) consists of two SSUSI images overlaid. The main image (and the electron and ion spectrograms shown) are taken from the DMSP F18 spacecraft; the pass occurred between 17:15-17:26 UT and the corresponding footprint is indicated in the SSUSI images by the solid black line. The background image is from the DMSP F16 spacecraft, between 17:15-17:25 UT, and is indicated by the dashed DMSP footprint. It can be seen that

despite the simultaneity of the two passes, the two DMSP SSJ/5 instruments detect different signatures associated with the same arc, with an ion signature observed by the F18 instrument (red), and an electron-only signature by F16 (orange). Figure 4.3 shows the SSUSI image and DMSP particle data from both spacecraft passes separately. This observation presents some interesting issues and will be examined further in the discussion section.

Figure 4.4 shows the IMF conditions for all the events shown in Fig. 4.2, from two hours before the start time of the event. Each row corresponds to an event from Figure 4.2. The SSUSI passes in each hemisphere are indicated throughout the event with boxes; passes where a polar cap arc was observed are shown as solid boxes. Passes where no polar cap arc was observed are shown by a dashed box, in these cases it is likely that the polar cap arc was not observed due to issues with the SSUSI field of view or noise in the image such that no arc could easily be discerned. In some cases the sensitivities of the spacecraft differed and hence polar cap arcs were not observed in all three DMSP passes; this issue will be discussed further in Section 4.4. From Fig. 4.4 it can be seen that most of the events occurred during northward IMF or B_z close to zero, consistent with expectations for polar cap aurora (e.g. Berkey et al. [1976]). Event 22 (third row of Fig. 4.4), however, occurred during strongly southward IMF, with brief northward turnings at around 19:15 and 19:45 UT. The corresponding SSUSI images show that the auroral oval is expanded to approximately 70° magnetic latitude meaning the arcs identified are in Event 22 are at a lower latitude than the other events.

Figure 4.5 shows current density plots from AMPERE [Anderson et al., 2000, Waters et al., 2001, Anderson et al., 2014], solar wind data and the AL, AU and SYM-H parameters for the day of Event 22 (14^{th} December 2015). The two panels at the top of Fig. 4.5 show the field aligned currents from AMPERE at 17:30 UT, around the time of the SSUSI observations shown in Fig. 4.2, in the northern and southern hemispheres. In these panels, the currents are plotted on a magnetic local time grid in a similar manner to the SSUSI images in Fig. 4.2. Red and blue correspond to the upward and downward currents respectively. The next four panels show midnight/noon and dawn/dusk slices of the field aligned currents in the northern and southern hemispheres, as a function of time. The bottom four panels show the IMF B_y and B_z components, the solar wind dynamic pressure, the AU and AL indices and the SYM-H index. It can be seen that an increase in the solar wind pressure (panel 6) is followed by an enhancement in the

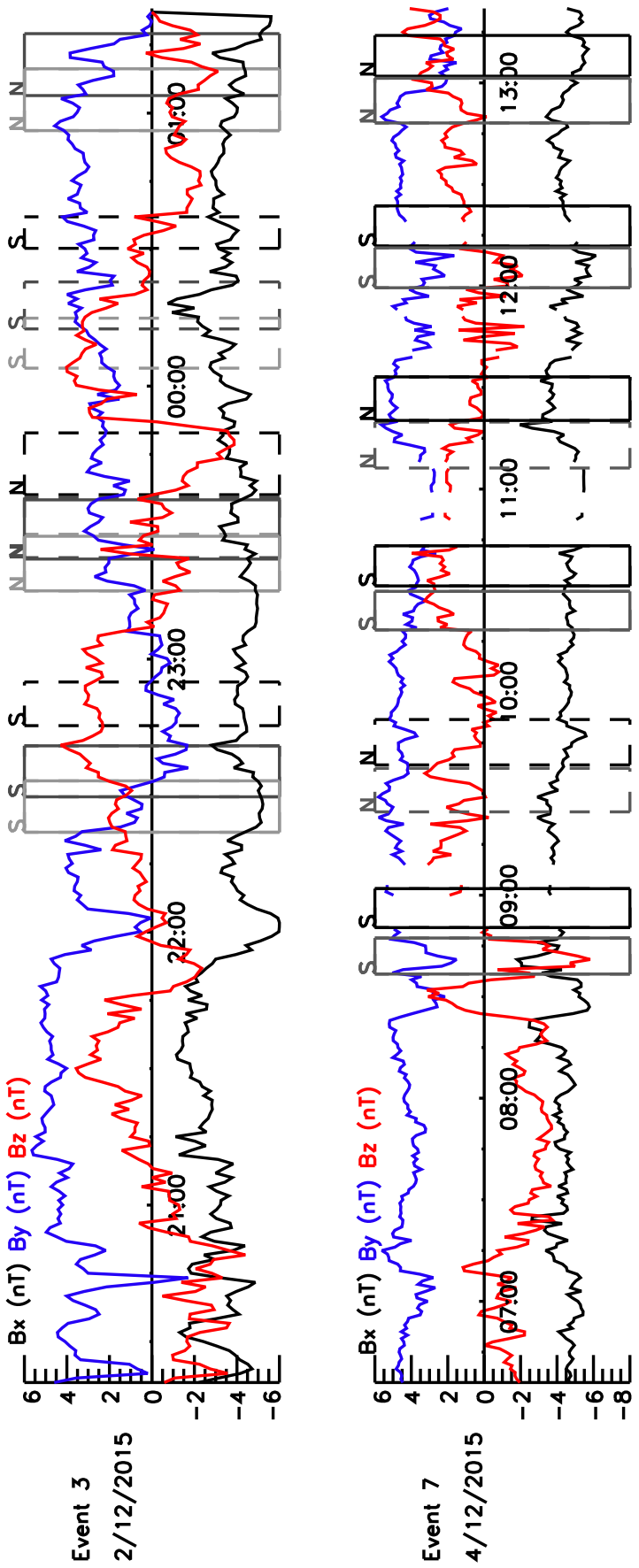

FIGURE 4.4: IMF for events where a PCA was seen in both hemispheres, associated with an ion signature. The boxes (as for all these images) show the times of the two SSUSI passes. B_x is shown in black, B_y in blue and B_z in red. The IMF data for Event 3 comes from Artemis with a negligible time lag applied. The rest of the IMF data is from OMNI. Continued overleaf.

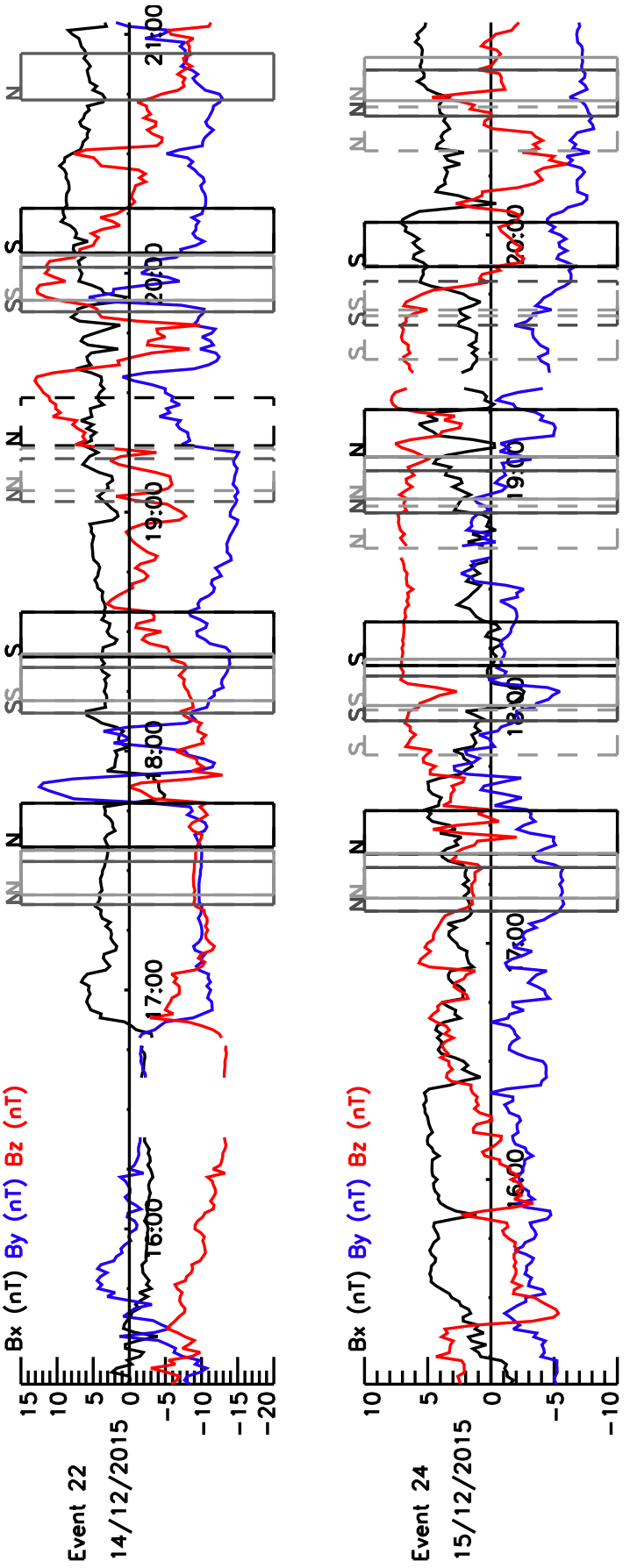

FIGURE 4.4: Continued.

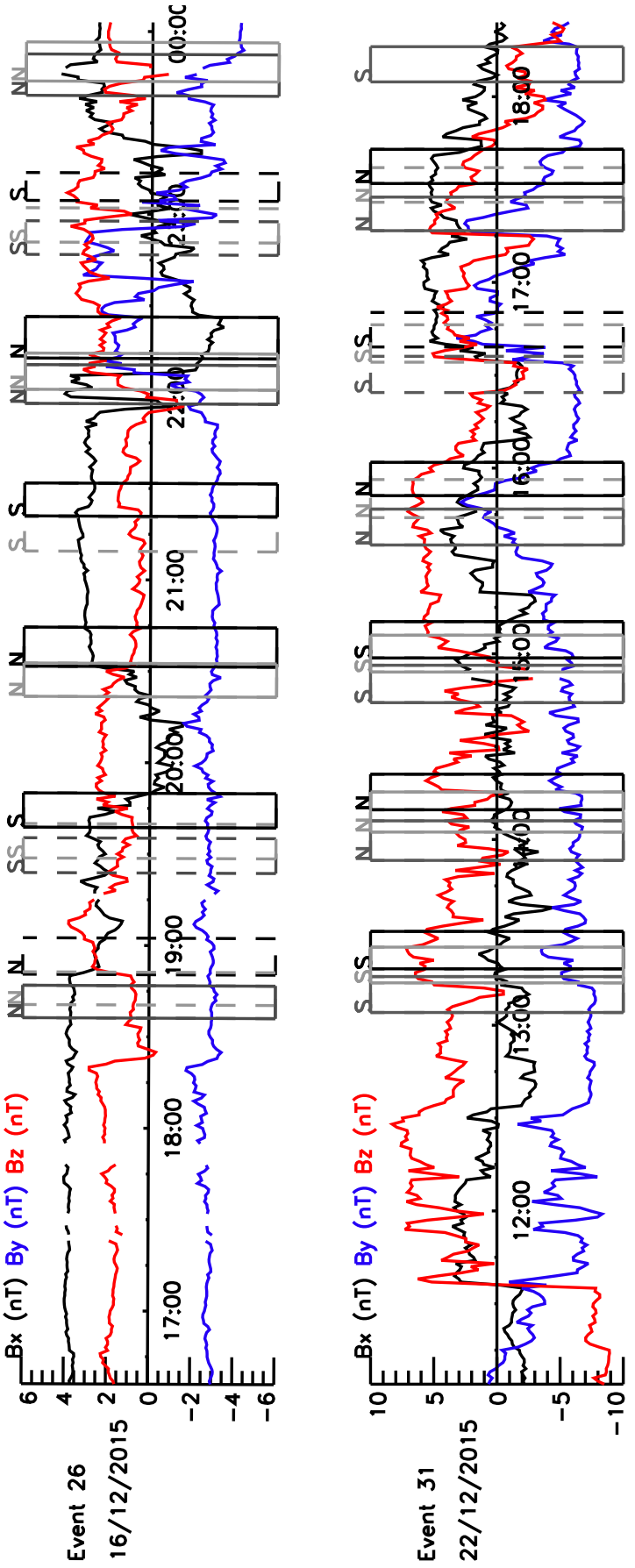

FIGURE 4.4: Continued.

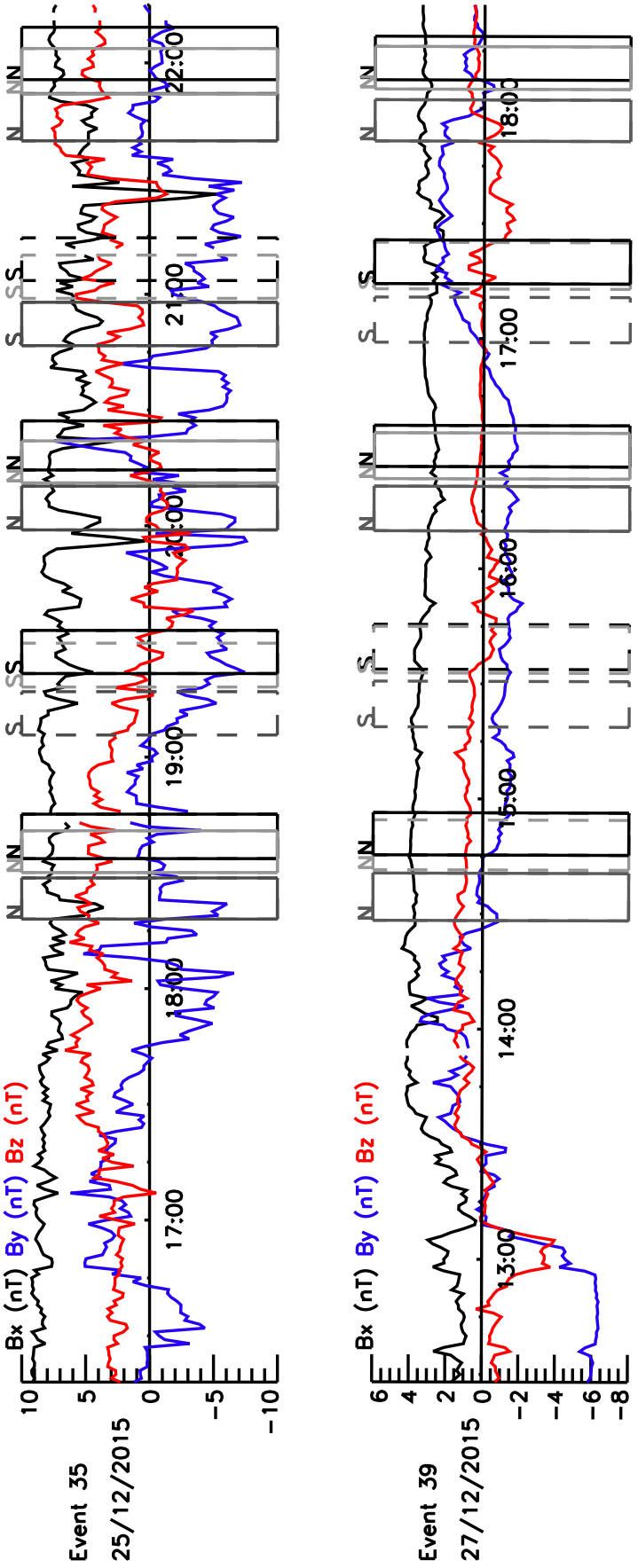

FIGURE 4.4: Continued.

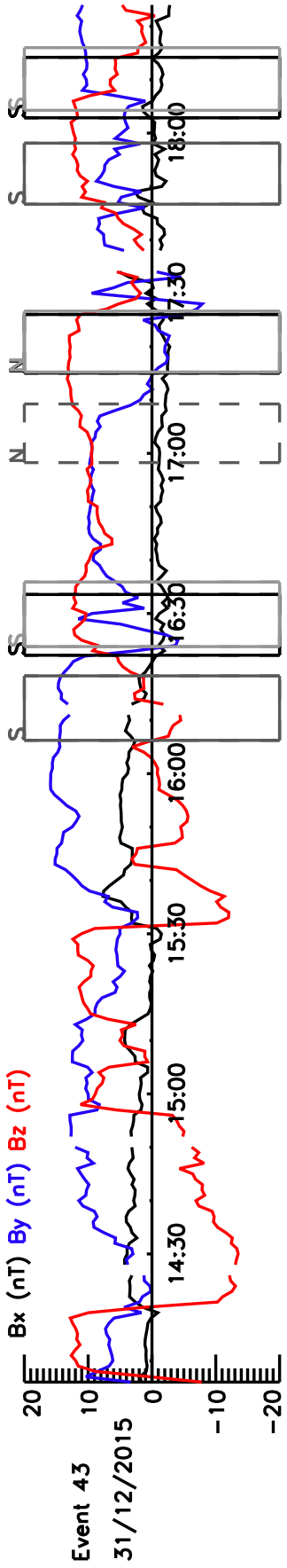

FIGURE 4.4: Continued.

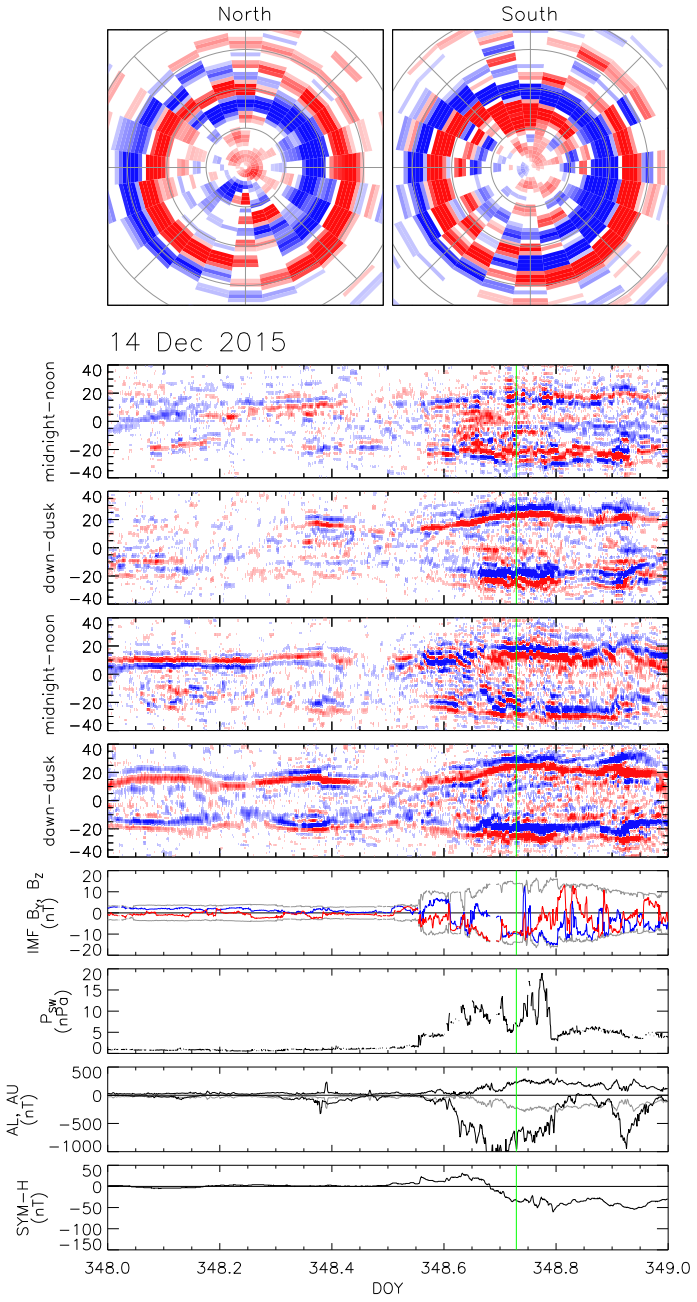

FIGURE 4.5: AMPERE, solar wind and index data for 14th December. The top images show the upward (red) and downward (blue) currents from AMPERE over the northern and southern polar regions at 17:30 UT. This time is indicated in the subsequent plot by the green line. The top four panels of this plot show keograms in the noon-midnight and dawn-dusk meridians of the AMPERE data throughout the day in the northern and southern hemispheres respectively. The fifth panel shows the IMF data with the B_z component shown in red and the B_{total} for positive and negative in grey. The next panel shows the solar wind speed in green and the density in pink (between 0-20 cm^{-3}). The AL, AU indices are shown in the 7th panel and lastly the SYM-H index in the bottom panel. It can be seen from approximately 14 UT a geomagnetic storm took place.

ring current (indicated by the SYM-H value in the bottom panel of Fig. 4.5). An enhancement in the field aligned currents measured by AMPERE can also be seen around this time, with an expansion of the auroral oval consistent with the SSUSI images from Fig. 4.2. Furthermore, the 'arcs' identified in the SSUSI images are co-located with the dusk-side R1 current sheet, meaning they are not consistent with being in the polar cap. Therefore these supporting data show that the 'arcs' identified in the SSUSI images, although they look similar to polar cap arcs and have similar particle precipitation to other polar cap arc observations, are not polar cap arcs but instead an emission phenomenon associated with a geomagnetic storm.

4.3.1.2 (b) Consistent with an open field line mechanism

Figure 4.6 shows the summary images for Event 11, occurring on 6th December 2015 between 08:17-11:41 UT, and Event 15, 8th December 2015 between 14:25-15:18 UT, in the same format as Fig. 4.2. Both of these events have an arc in both hemispheres, each of which is associated with an electron-only signature. In the DMSP SSJ/5 spectrograms a 'spike' in the electrons that is distinct from the main oval signature is indicated by orange lines; no clear ion signature corresponding to these spikes can be discerned from the ion spectrograms during these events. It can be seen in the SSUSI images that each of these electron-only signatures corresponds to a sun-aligned arc within the polar cap. These features are consistent with what is expected for an open field line mechanism i.e. accelerated polar rain or 'polar showers' (e.g. Newell et al. [2009]). However as these arcs are occurring in both hemispheres at the same time, they are not consistent with polar rain IMF statistics which have a clear hemisphere preference controlled by the IMF B_x component, which in both cases is strongly negative (shown in Figure 4.7). These events are represented as blue filled circles in Fig. 4.1.

Event 24 (fourth row of Fig. 4.2) shows an example where, as well as the arcs associated with ion signatures observed in both hemispheres, there is an arc in the northern hemisphere pass with an electron-only signature. This event is classified in Table 2.1 as 'both occurring simultaneously' as arcs with different plasma signatures are observed in the same pass. This observation is comparable to Reidy et al. [2017] (Chapter 3) who found arcs consistent with formation on different magnetic topologies occurring simultaneously.

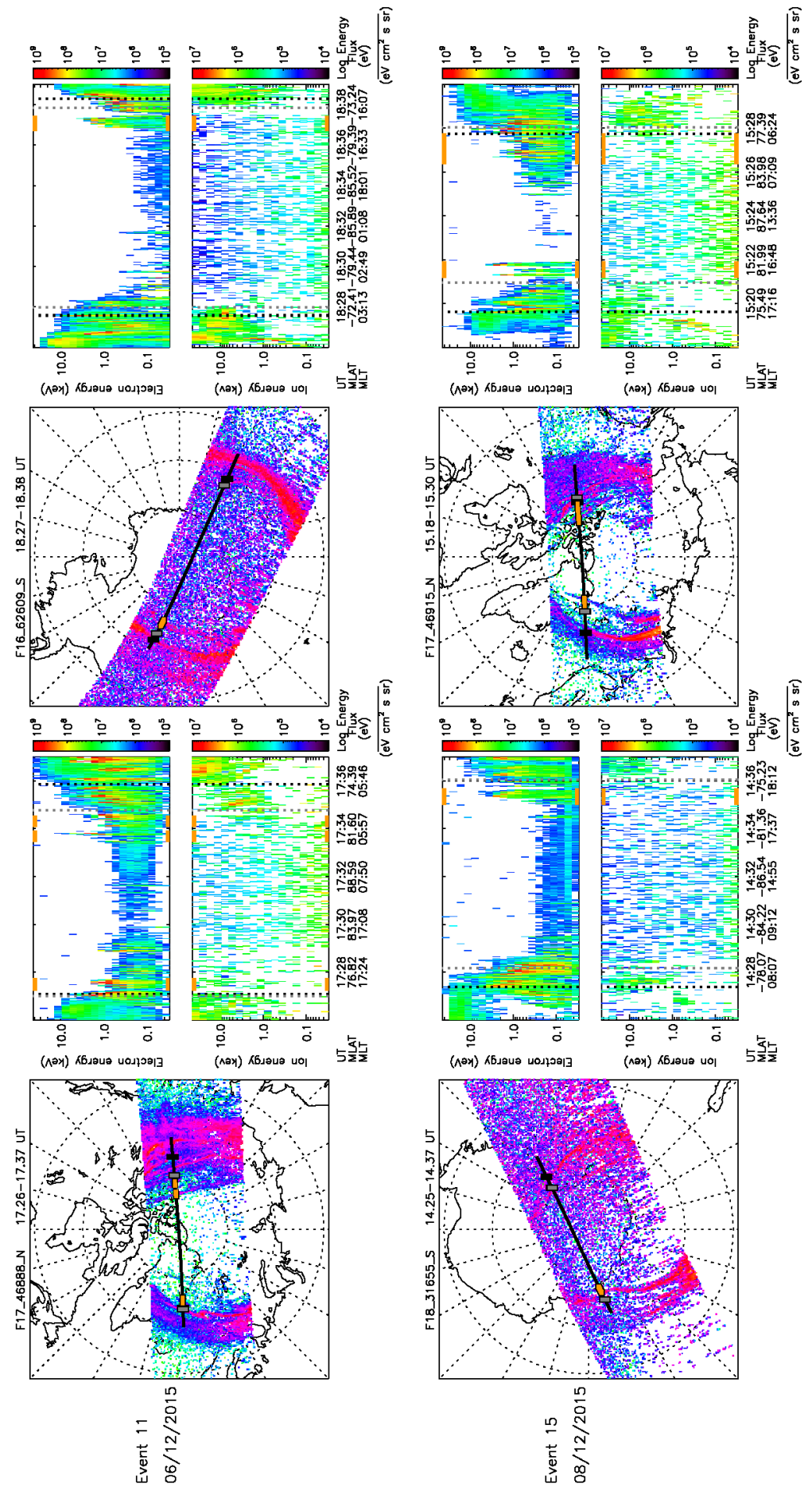

FIGURE 4.6: Summary images for events with arcs in both hemispheres associated with electron-only signatures in the same format as Fig. 4.2.

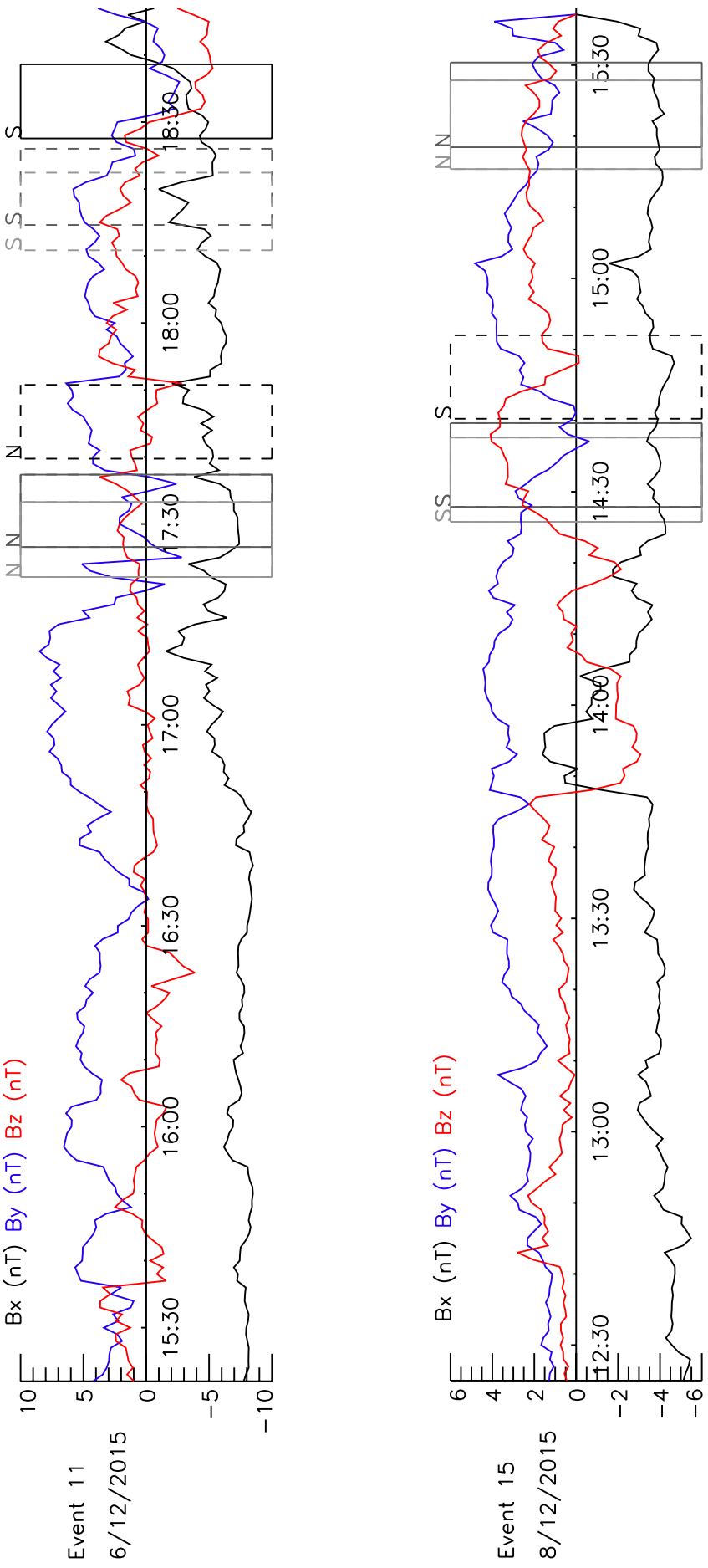

FIGURE 4.7: IMF for events with electron-only signatures in both hemispheres. The IMF data for event 15 comes from Artemis 1 and a time lag of approximately 11 minutes has been applied.

4.3.1.3 (c) Not consistent: Electron-only signature in one hemisphere and an ion signature in the other

Figure 4.8 shows the summary images for Events 4 and 14 (in the same format as Fig. 4.2) which both have an arc associated with ion precipitation in one hemisphere and an arc associated electron-only signature in the other. The IMF conditions for these events are given in Figure 4.9. These events are problematic for both closed field line and open field line formation mechanisms and are hence classified as 'not consistent' and shown as green solid circles in Fig. 4.1.

The arcs may be completely unrelated and coincidentally occurring at the same time in opposite hemispheres. The arcs with an electron-only signature, seen in the northern hemisphere for both events, are potentially consistent with an accelerated polar rain formation mechanism. The arcs in the southern hemisphere of both events are associated with ion signatures but do not fit expectations for a closed field line mechanism because they are seen in only one hemisphere. These arcs are possibly examples of 'non-conjugate' theta aurora, which will be discussed further in Section 3.2.2, but cannot formally be classified as such as they did not persist for more than one orbit i.e. the arcs were short lived. It could also be the case that the arc giving the ion signature was too short lived to be observed in both hemispheres.

It is possible that these arcs are related, but in that case it is unclear why the particle precipitation would be different in opposite hemispheres. It could be that the energy flux of the ions in the northern hemisphere are just below detection and hence we note that there is some uncertainty in the electron-only detections. However, by eye and by applying the semi-automatic method to detect particle signatures described in Appendix A, no clear ion signature corresponding to any of arcs seen in the northern hemisphere SSUSI images can be discerned. Hence we treat these events as if the arcs are occurring independently but simultaneously in opposite hemispheres.

4.3.1.4 (d) Potentially consistent with closed field lines: Particle data only available for an arc in one of the hemispheres

The events where the arc intersects a DMSP track in only one hemisphere are shown in Figure 4.10. As before, the clearest SSUSI image from each hemisphere is shown, with

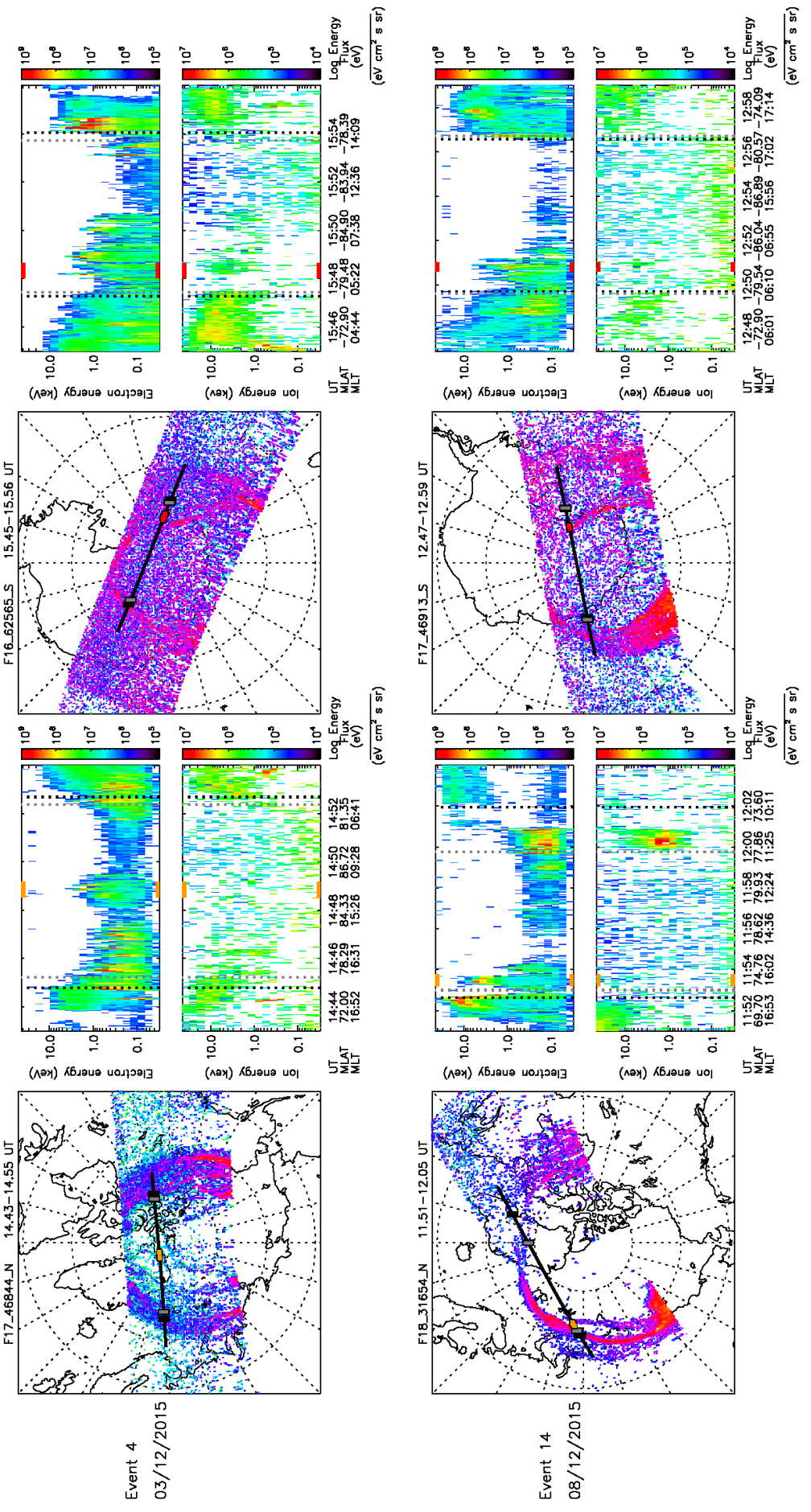

FIGURE 4.8: Summary images for events with different particle signatures in each hemisphere in the same format as Fig. 4.2. The northern hemisphere arc in both of these cases has an electron-only arc and the southern hemisphere contains an arc associated with ion precipitation.

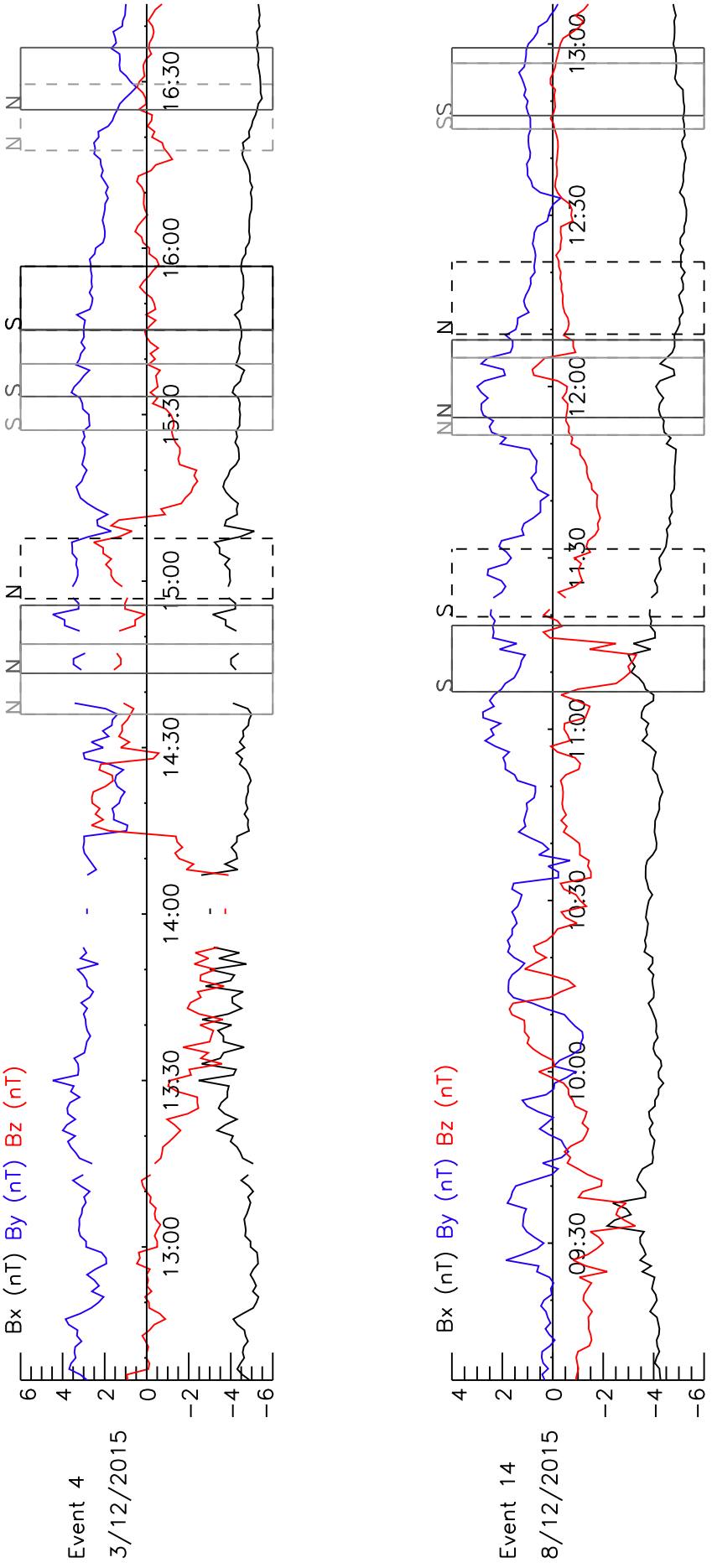

FIGURE 4.9: IMF conditions for the event with different particle signatures associated with the arcs in each hemisphere.

the footprint of the DMSP spacecraft indicated in black. The particle data are shown only for the hemisphere where the arc intersects the DMSP footprint. Figure 4.11 shows the IMF conditions for each event in the same way as for the other groups. All of the events shown in Fig. 4.10 have an arc associated with an ion signature, and the arc is observed in both hemispheres. Therefore, these events are potentially consistent with a closed field line mechanism (represented as orange filled circles in Fig. 4.1). However, we have seen from Events 4 and 14 (group (c)) that there are cases where the particle signatures are different in the different hemispheres and hence we cannot determine the nature of these arcs with complete certainty.

4.3.2 Events occurring in only one hemisphere

From surveying SSUSI data from December 2015, eight events were found where a polar cap arc was observed in only one hemisphere. As above, these arcs are analysed using particle data where the arc intersected the footprint of a DMSP spacecraft. Table 2.2 lists the date and duration of each event and indicates whether particle data could be obtained for each arc. It can be seen that of these 8 events, only 2 had corresponding particle data. As discussed above, polar cap arcs occurring in only one hemisphere are indicative of an open field line mechanism and hence electron-only signatures are expected in the particle data, although this is not what we see, as is evident from the final column of Table 2.2 and discussed below.

TABLE 4.2: Events identified in SSUSI as occurring in only one hemisphere, marked with 'N' for North or 'S' for South. If the arc intersects the DMSP track, the occurrence of an ion signature is marked with either 'y' or 'n'. The classification of these events is indicated for the arcs with particle data.

Event num.	Start Time (UT)	End Time	Hem	Ion sig.	Classification
12	2015/12/07 17:09	2015/12/07 19:05	N	n	Open
16	2015/12/09 08:17	2015/12/09 11:54	N		
19	2015/12/11 10:40	2015/12/11 12:19	S		
25	2015/12/16 11:49	2015/12/16 13:44	N		
30	2015/12/22 07:05	2015/12/22 10:42	N	y	Not consistent
33	2015/12/24 10:03	2015/12/24 13:39	N		
34	2015/12/24 16:50	2015/12/24 18:58	N		
36	2015/12/26 06:29	2015/12/26 08:24	N		

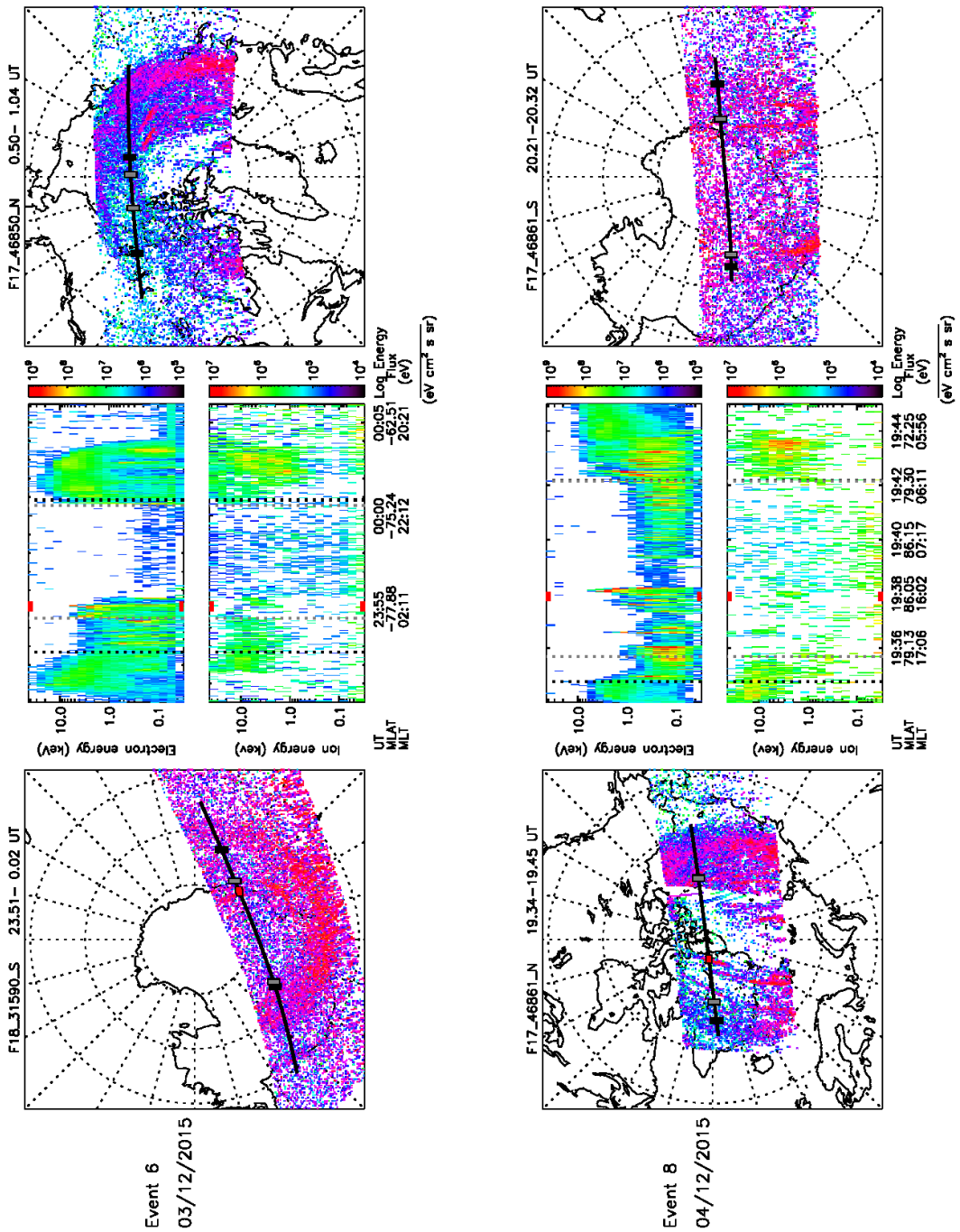

FIGURE 4.10: Summary images for events with DMSP SSJ/5 particle data for an arc in only one hemisphere because the footprint misses the arc in the opposite hemisphere. Continued overleaf.

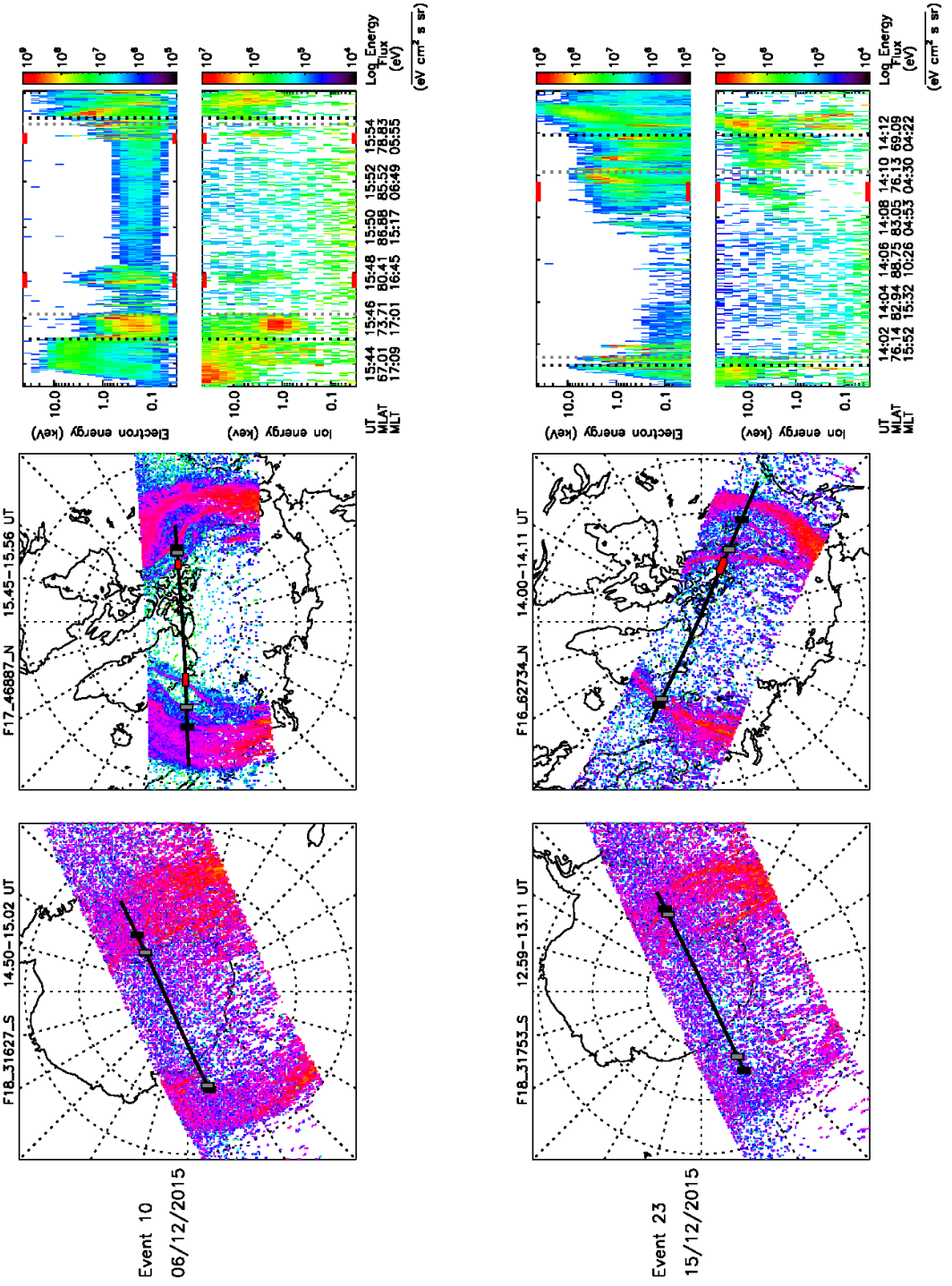

FIGURE 4.10: Continued.

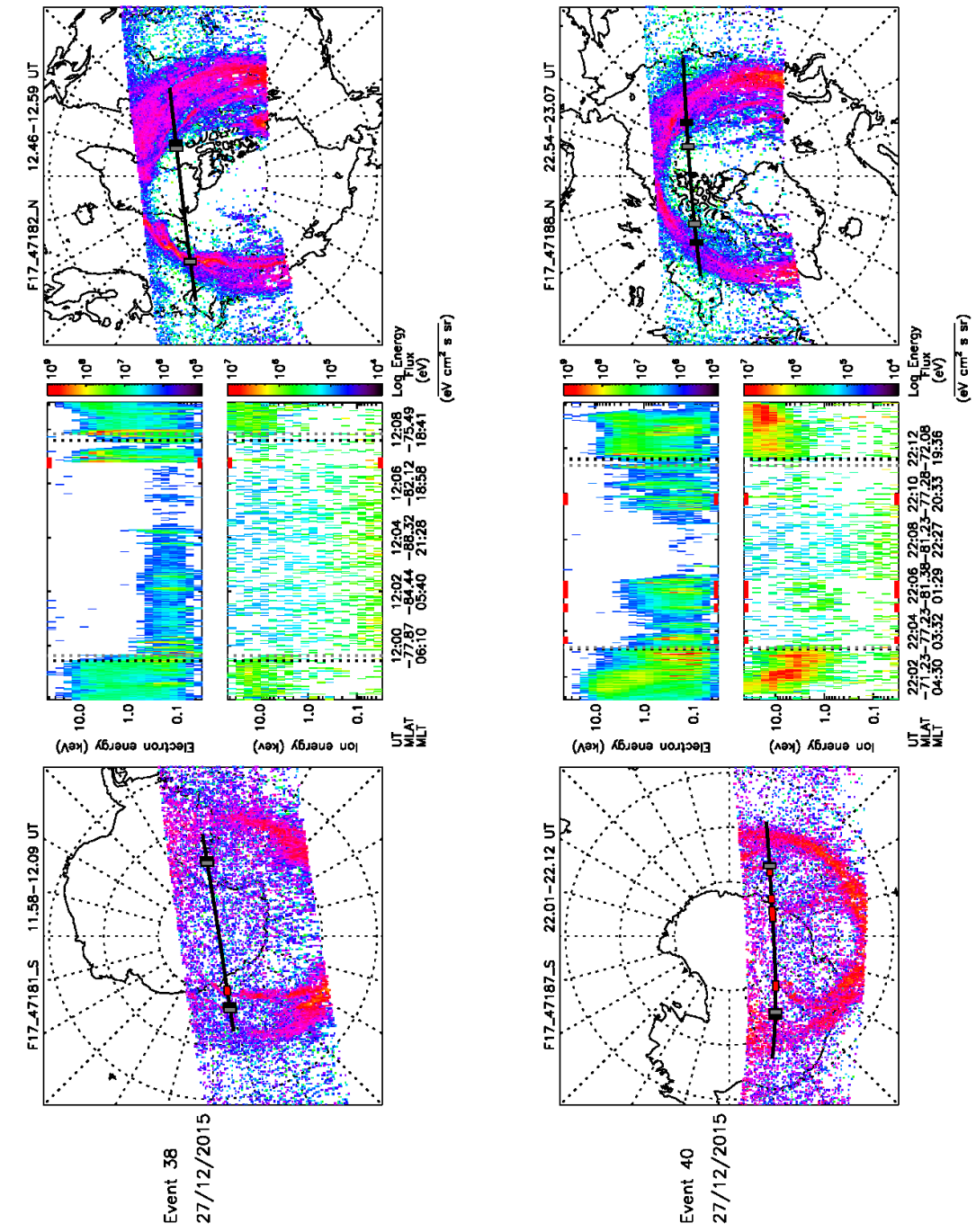

FIGURE 4.10: Continued.

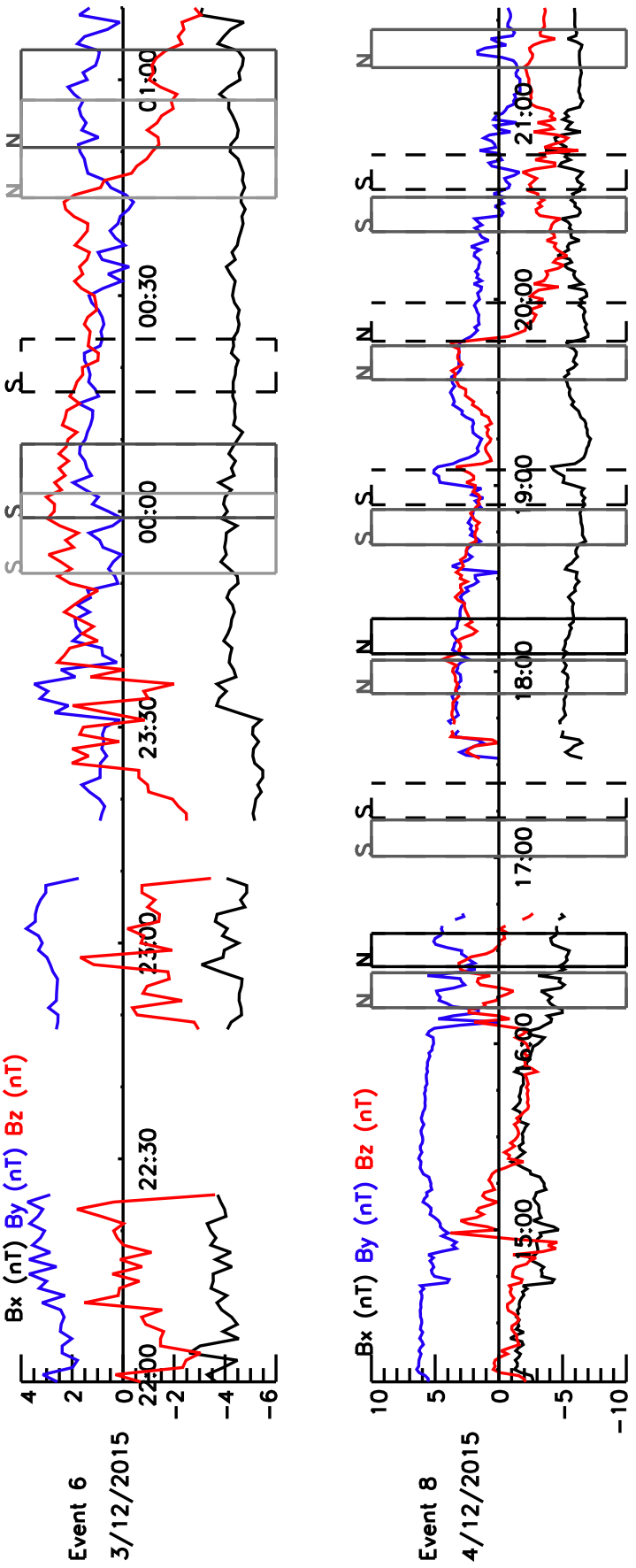

FIGURE 4.11: IMF plots for events with DMSP data only for arc in one hemisphere. The IMF data for event 10 comes from Artemis and a time lag of approximately 8 minutes has been applied. Continued overleaf.

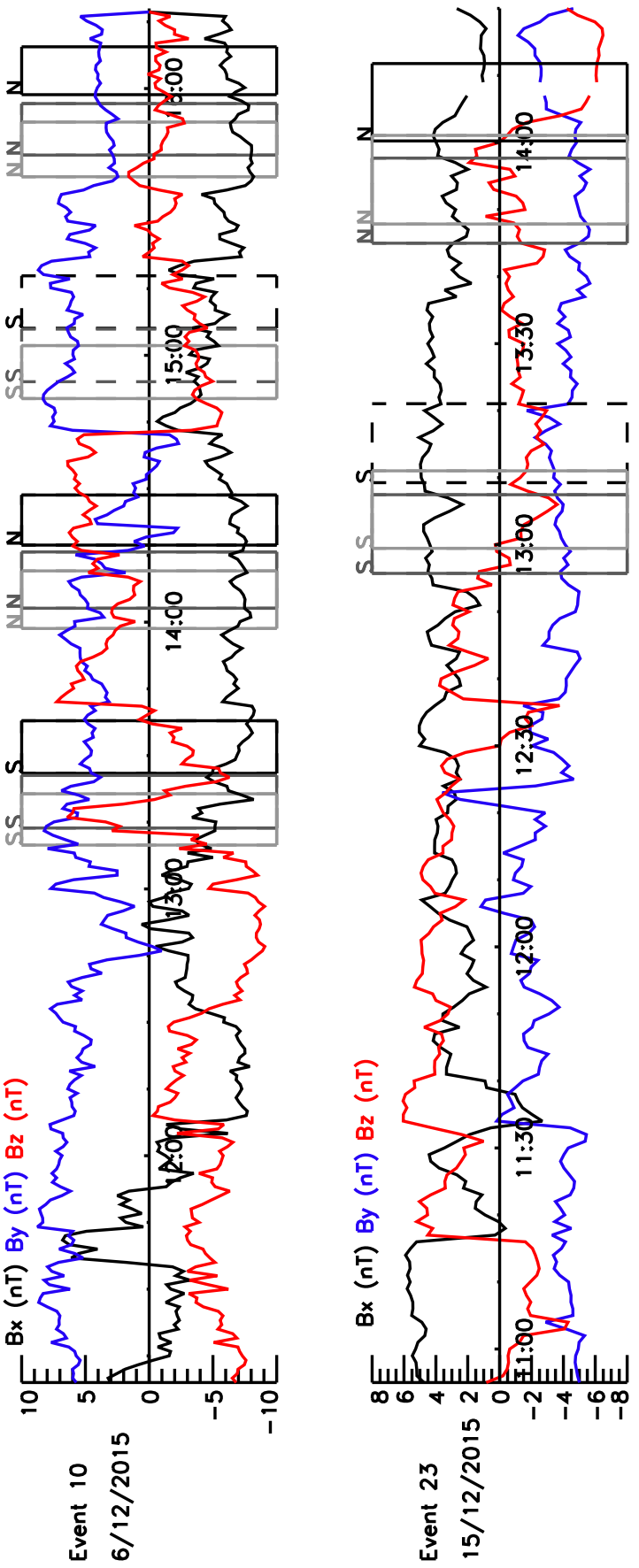

FIGURE 4.11: Continued.

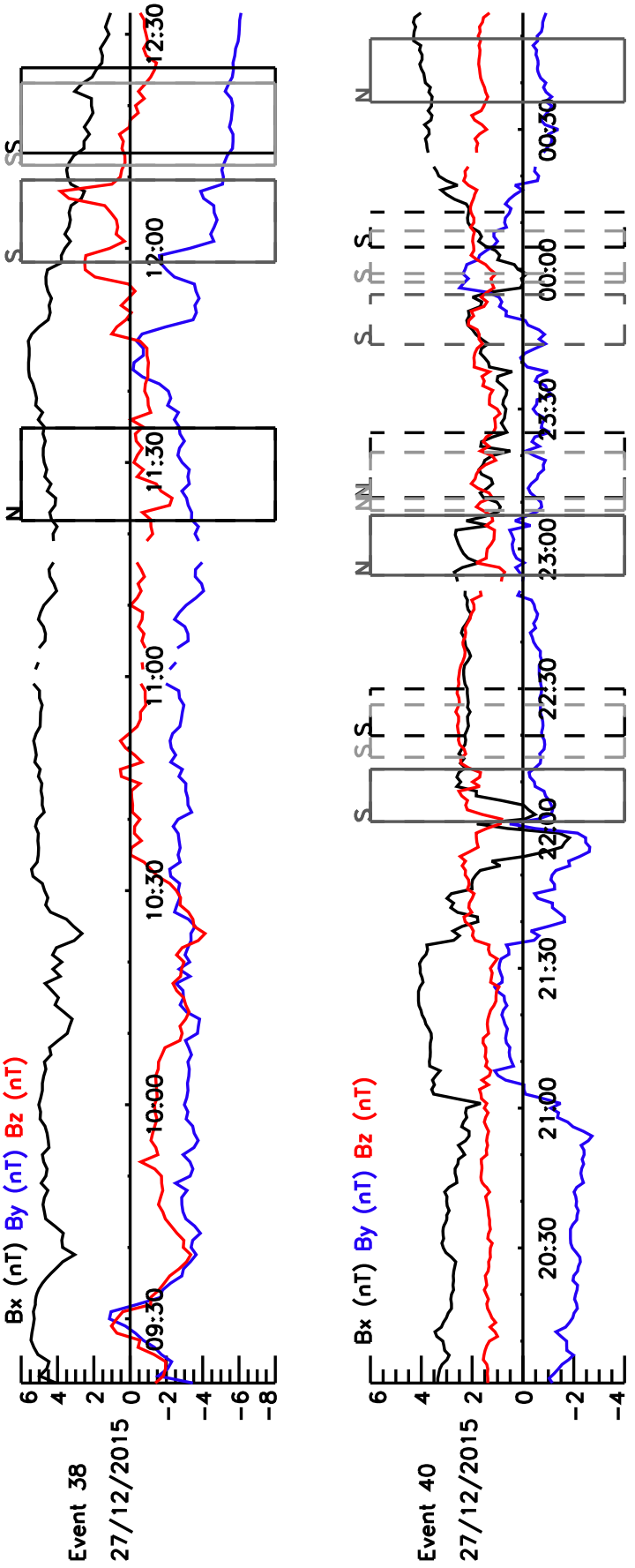

FIGURE 4.11: Continued.

4.3.2.1 Consistent with an open field line mechanism

Figure 4.12 shows the 'one-hemisphere' event (Event 12) which was associated with an electron-only signature in the northern hemisphere and an 'empty' polar cap, i.e. no polar cap arc, in the southern hemisphere, although we note that the field of view in the southern hemisphere does not completely show the dawnside of the southern polar cap. This event is represented in Fig. 4.1 as an unfilled blue circle. The algorithm for detecting the plasma signatures has detected three distinct electron-only signatures in the northern hemisphere, two of which, however, are occurring adjacent to the auroral oval and hence when talking about the electron-only arc for Event 12 we are referring to the arc on the dawn side that is clearly distinct from the main auroral oval. The electron signature for this arc is similar to those discussed in Sections 4.3.1.2 and 4.3.1.3 and by Reidy et al. [2017] (Chapter 3). The IMF conditions for this event (Figure 4.13) are consistent with polar rain statistics [Yeager and Frank, 1976] i.e. the IMF B_x is negative, favouring polar rain in the northern hemisphere, and the IMF B_y is positive which favours polar rain on the dawn side of the northern hemisphere.

4.3.2.2 Not consistent: 'non-conjugate' theta auroras

Fig. 4.14 shows the summary image for Event 30 which occurred on 22^{nd} December 2015. A polar cap arc can be seen in the northern hemisphere SSUSI image (between 9:04-9:17 UT) that is associated with an ion signature in the corresponding particle data. We note that the DMSP spacecraft passes quite close to the dayside oval, and hence there is a chance that the ion precipitation may be associated with lobe reconnection; however, the SSUSI image was also examined in the Lyman-alpha channel (not shown) and no obvious sign of a cusp spot was observed. No polar cap arcs are observed in the southern hemisphere SSUSI images and no high energy particle signatures are seen in the corresponding particle data poleward of the auroral oval. A polar cap arc was observed in the subsequent images of the northern hemisphere (not shown), as per the conditions for being classified as 'one hemisphere' event. The combination of an ion signature but presence in only one hemisphere is not consistent with our expectations for either an open field or a closed field line mechanism and hence this event is represented as an unfilled green circle in Fig. 4.1. This observation is similar to that presented by Østgaard et al. [2003] of 'non-conjugate' theta aurora. (The open field line arcs are also strictly

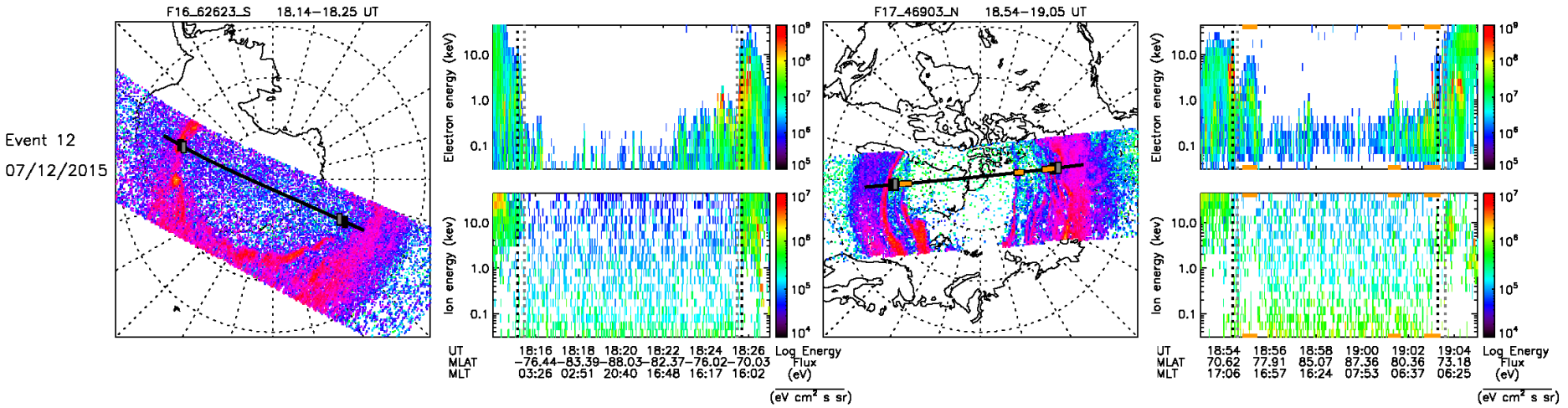

FIGURE 4.12: Summary image for event with a PCA in only one hemisphere, associated with an electron-only signature in the same format as Fig. 4.2.

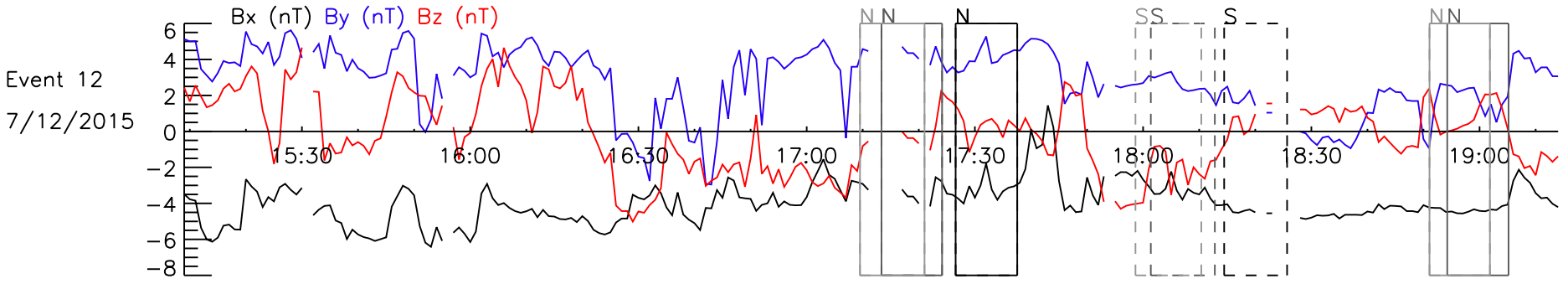

FIGURE 4.13: IMF for one hemisphere electron-only event.

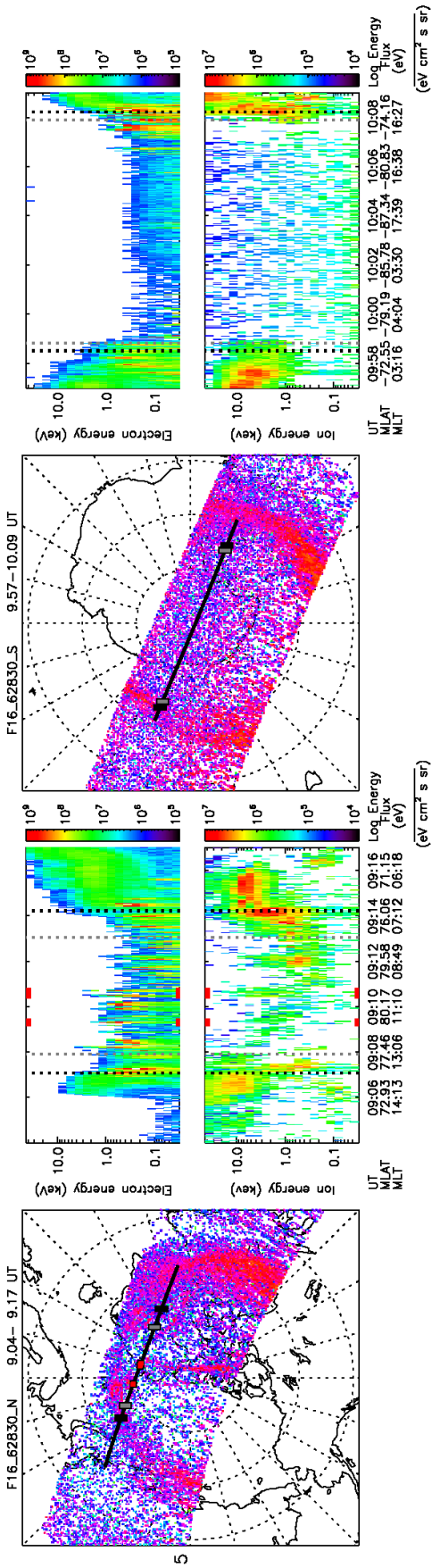

FIGURE 4.14: Summary figure for an event containing an arc that appear to be a 'non-conjugate' theta aurora, in the same format as Fig. 4.2.

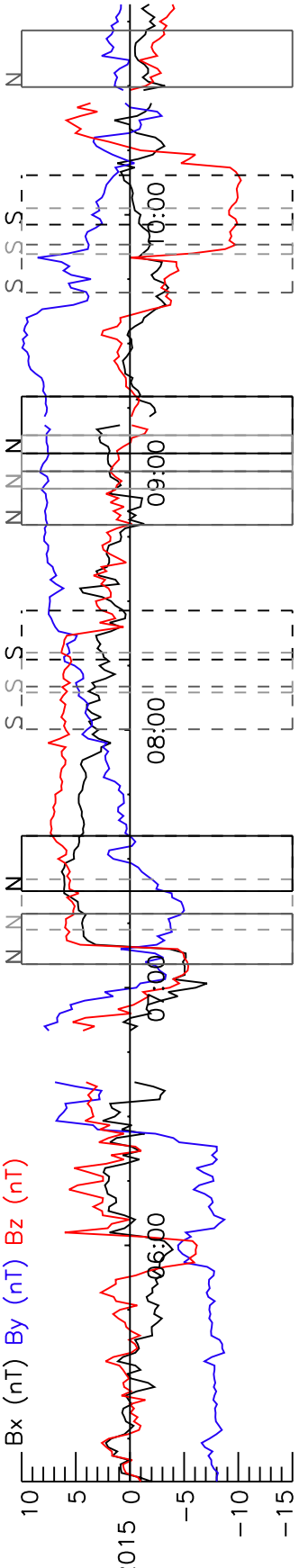

FIGURE 4.15: Corresponding IMF conditions for the 'non-conjugate' theta aurora.

'non-conjugate' but in this chapter we take the term to refer specifically to the type of observation reported by Østgaard et al. [2003] in which an ion signature is present or expected to be present, which therefore suggests closed field lines, but which are only seen in one hemisphere).

As a point of interest, we note that in the northern hemisphere SSUSI image (Fig. 4.14), an example of a poleward moving auroral form can be seen between approximately 6 and 10 MLT, which is the auroral signature of a flux transfer event [Fasel, 1995, Milan et al., 2000b, Sandholt and Farrugia, 2007]. Phenomenologically, this example is typical of a feature that has been identified as a 'bending arc' in some surveys (e.g. Kullen et al. [2002, 2015]), but which has been shown to be a signature of dayside reconnection [Carter et al., 2015], as is the case for flux transfer events. Furthermore, this feature is occurring under B_y dominated conditions, which can be seen in Fig. 4.15 around 09:00 UT, consistent with that found by Kullen et al. [2002, 2015] and Carter et al. [2015].

4.4 Polar cap arc occurrence statistics and seasonal effects

During this study it was noted, and is evident from the summary images discussed above, that the visibility of polar cap arcs in the southern hemisphere SSUSI images was generally poorer than in the northern hemisphere (e.g. Event 24, fourth row of Fig. 4.2). Furthermore, only one of the 8 'one hemisphere' events occurred in the southern hemisphere. Hence we have investigated the seasonal and hemispheric dependence of polar cap arcs, and the effect of inter-spacecraft sensitivity on our observations. Statistics relating to the events discussed above in December 2015, including a percentage of how many polar cap arcs occurred in each hemisphere, are reported in the right hand column of Table 2.3. It can be seen that more arcs were recorded in the northern hemisphere than the southern hemisphere, which is expected as a result of the noisier images from the southern hemisphere. To explore this effect further, we examined the SSUSI data from March, June and September 2015, i.e. the equinox months and a month in northern hemisphere summer, and identified polar cap arcs in these months. These results are also presented in Table 2.3.

It can be seen in Table 2.3 that the percentages of polar cap arcs recorded in each hemisphere during the equinox months are similar, i.e approximately 40% of the arcs were recorded in the northern hemisphere and approximately 60% in the southern hemisphere for both March and September. The percentage of polar cap arcs seen in each hemisphere for June and December is almost opposite, i.e. the hemisphere experiencing summer (South for December and North for June) sees approximately half as many polar cap arcs as in the winter hemisphere. These observations can be explained by sunlight contamination preventing the identification of some features in the summer hemisphere, notwithstanding the attempt to correct for dayglow in the SSUSI data which is undertaken by the SSUSI instrument teams. This observation is consistent with fewer arcs being recorded in the summer hemispheres of June and December. Furthermore, the orbits of the DMSP spacecraft generally occur such that they pass closer to the dayside in the northern hemisphere and closer to the nightside in the southern hemisphere. This means that the northern hemisphere images will generally suffer more from dayglow contamination than the southern hemisphere images, which is hence consistent with the higher number of polar cap arcs observed in the southern hemisphere during the equinox months. (As an additional note: the SSUSI field of view is not equal about the nadir, with more of the swath covering the nightside than the dayside as demonstrated in Fig. 2.5).

Also in Table 2.3, the percentage of the number of images containing polar cap arcs and the percentage of orbits containing polar cap arcs for each spacecraft is given. It can be seen that, consistently, across all four months, more polar cap arcs are observed by the SSUSI imager on board DMSP F17. Fewer polar cap arcs are recorded from the SSUSI imager on board DMSP F18, particularly in March, June and September; this difference is less obvious in December. One potential reason for this difference is that the SSUSI instrument on board DMSP F17 is more sensitive than the other two, according to the latest SSUSI calibrations (Brian Wolven, personal communication), and hence the weaker polar cap arc events are measured more clearly.

Overall, these surveys show polar cap arcs are seen by the SSUSI instruments at least 20% of the time. We are likely missing some polar cap arc events due to the effects of the sunlit hemisphere and the field of view of SSUSI due to the DMSP spacecraft orbits.

TABLE 4.3: Statistics from March, June, September and December 2015. For each month, the total number of polar cap arc events, the total number of images with polar cap arcs and the percentage of polar cap arcs in each hemisphere are recorded. The percentage of images from each spacecraft which contain polar cap arcs are given in rows 5-7 with a total percentage for all three spacecraft in row 8. The percentage of orbits containing polar cap arcs for each spacecraft, and then as a total of all three are given in rows 9-12.

	March	June	September	December
No. PCA Events	50	42	41	43
No. Images with PCA	333	228	327	204
North (%)	41.7	30.7	39.4	67.2
South (%)	58.3	69.3	60.6	32.8
F16 images (%)	11.8	8.0	13.2	7.1
F17 images (%)	20.0	12.0	18.3	11.8
F18 images (%)	7.7	6.4	9.3	6.6
Total images(%)	13.3	8.9	13.5	8.4
F16 orbit (%)	18.9	13.6	21.0	12.0
F17 orbit (%)	29.1	21.7	28.4	21.1
F18 orbit (%)	12.6	11.4	15.2	11.9
Total orbits(%)	20.3	15.5	21.3	14.8

4.5 Discussion

In this chapter we have examined the particle precipitation associated with polar cap auroras and used the ion signature, or lack thereof, to infer the magnetic field topology of these arcs. We have classified the polar cap arc events depending on their hemispheric nature, i.e. whether the arcs were seen in one or both hemispheres, using data from the SSUSI instruments on board three of the DMSP spacecraft. These spacecraft are in 90 minute sun-synchronous orbits and hence provide reasonable time resolution for inter-hemispheric study. From previous polar cap arc studies and proposed mechanisms, arcs occurring in both hemispheres are consistent with a closed field line mechanism and therefore an ion and and electron signature is expected in the particle data (e.g. Carter et al. [2017]). Arcs seen in only one hemisphere are consistent with an open field line mechanism and an electron-only signature is expected in the particle data (e.g. Newell et al. [2009]). In this study, we have defined events as a period of time when polar cap arcs were visible in the SSUSI images rather than by individual polar cap arcs and hence images containing multiple arcs are classified as one event.

64% of the events were found to contain arcs consistent with a closed field line mechanism (14 events), whereby arcs were seen in both hemispheres and were associated with an

ion signature in at least one hemisphere. This percentage includes 8 of the 9 events from group (a) where an ion signature was detected in both hemispheres (Section 4.3.1.1), also counting Event 24 (fourth row of Fig. 4.2) which also had a separate electron-only arc that was observed to occur simultaneously in the northern hemisphere, and the 6 events from group (d) where a polar cap arc intersected the footprint of a DMSP spacecraft in only one hemisphere (Section 4.3.1.4). Not included in this statistic from group (a) is Event 22 (third row of Fig. 4.2) which was found to be a misidentified polar cap arc occurring during a geomagnetic storm. As a separate point, it can be seen in Fig. 4.2 that the polar cap arcs identified are (mostly) mirrored about the noon-midnight meridian in the opposite hemispheres. This asymmetry is consistent with previous observations (e.g Craven et al. [1991]) and also consistent with predictions from several mechanisms which place polar cap arcs on closed field lines (e.g. Kullen [2000], Milan et al. [2005]). It can be seen that in the case of Event 22, the arcs are occurring on the same side of the polar cap in both hemispheres and hence this event does not fit the pattern discussed above.

One of the events identified as being consistent with closed field lines (Event 43, bottom row of Fig. 4.2) was seen to have an arc in the northern hemisphere with an ion signature detected by one spacecraft orbiting closer to the nightside and an electron-only signature detected by another spacecraft, around the same time, orbiting further sunward (shown in Fig. 4.3). We suggest three possible explanations for this observation. The first is that there is a sensitivity issue with some of the DMSP SSJ/5 instruments (or the ion signatures are sometimes weak) such that ions are not always detected. Secondly, it could be a spatial feature; the field lines which map further sunward on the arc are those that have most recently been closed; in the Milan et al. [2005] mechanism, after closure, the field lines will seek to contract, but the field lines which map closer to the dayside will contract least. Therefore it is possible that the precipitating ion signature is less developed. This explanation would imply that an electron-only signature is not a guarantee that the observation occurred on open field lines, which potentially complicates the interpretation of arcs identified as forming by accelerated polar rain. A third explanation for this observation is that the arc may be formed by two independent mechanisms, one on open and the other on closed field lines, each occurring at the same time. Such ideas have been discussed by Eriksson et al. [2005] who suggest polar cap arcs may be formed by two separate dayside and nightside mechanisms. However, it is

hard to explain why two independent mechanisms would coincide spatially. A possible explanation may be based on the arguments of Fear et al. [2015], who noted that if a polar cap arc is frozen to a set of magnetic field lines, the flow pattern excited by lobe reconnection will draw the polar cap arc into the cusp. If this applied to both independent mechanisms, it could potentially cause the two elements to align. However, this suggestion is highly speculative, and we reserve further analysis of this to future studies.

27% of the events were seen to contain arcs with an electron-only signature in the DMSP SSJ/5 particle spectrometer (6 events): two events with an electron-only arc in both hemispheres (Fig. 4.6), two events with an electron-only arc in one hemisphere and an ion signature arc in the other (Fig. 4.8), one event with an electron-only arc in one hemisphere and nothing in the other (Fig. 4.12) and lastly one event with an electron-only arc occurring simultaneously with an ion signature arc in the northern hemisphere of Event 24 (fourth row of Fig. 4.2). (It is important to note that this percentage and the percentage quoted above for arcs consistent with closed field lines are not additive as both include Event 24).

Polar cap arcs associated with an electron-only signature are consistent with an open field line mechanism. Carlson and Cowley [2005] argued that shear flows across open field lines in the magnetotail could accelerate the polar rain enough to generate polar cap arcs. Polar rain favours a hemisphere depending on the IMF B_x component [Yeager and Frank, 1976] (demonstrated in Fig. 1.17). Excluding the two events with electron-only arcs in both hemispheres (Events 11 and 15), all of the electron-only arcs identified above occurred in the northern hemisphere and hence, the polar rain statistics would predict the IMF B_x component to be negative during these events. Using IMF data from OMNI, we found that three of the four electron-only arcs observed in only one hemisphere occurred during negative IMF B_x as expected (Event 4, Fig. 4.9, Event 12, Fig. 4.11 and Event 14, Fig. 4.9). However, Event 24 (fourth row of Fig. 4.4) occurred under positive IMF B_x conditions, which is inconsistent with the overall polar rain dependence. Shinohara and Kokubun [1996] found that the occurrence frequency of 'polar showers' without an ion signature (accelerated polar rain) is increased in the northern hemisphere for negative IMF B_x and in the southern hemisphere for positive IMF B_x, but there was a minority of events which did not conform to this trend. Therefore, although the sign of the IMF B_x component makes accelerated polar rain more likely in one hemisphere,

it is not impossible in the other. Events 11 and 15 are not included in this discussion as the arcs with electron-only signatures occurred in both hemispheres simultaneously (Fig. 4.6) and hence cannot fit this pattern. It has been reported that an exception to the IMF B_x hemisphere control occurs when there is a closed-loop-flux event in the solar wind [Makita and Meng, 1987]. These rare events mean that polar rain will be equally likely in both hemispheres. However no evidence for this type of event can be seen in the IMF data for Events 11 and 15 (Fig. 4.7). Three out of the six electron-only arcs occurred at the same time as an arc associated with an ion signature; Event 24 where this ion signature arc was seen to occur in both hemisphere and was hence consistent with closed field lines and Events 4 and 14 where the ion signature arc was too short lived to determine its hemispheric nature. These observations are therefore potentially consistent with Reidy et al. [2017] (Chapter 3) who showed that arcs formed on different topologies could occur at the same time.

An example of a 'non-conjugate' theta aurora, whereby a polar cap arc associated with ion precipitation was observed in only one hemisphere, was given in Section 4.3.2.2. Event 30 (Fig. 4.14) consists of a northern hemisphere arc associated with an ion signature, which by itself would be suggestive of closed field lines, but observations in the southern hemisphere showed no counterpart in the SSUSI or DMSP particle data. As discussed in Section 1.5.3.3, This type of event is problematic for either an open or a closed field line mechanism and is consistent with that presented by Østgaard et al. [2003, 2007]. (NB. The arcs in the southern hemisphere of Events 4 and 14 (Fig. 4.8) are not considered 'non-conjugate' as the arc does not fit the criteria to be classed as a 'one hemisphere' event as it was short lived). One of the possible explanations given by Østgaard et al. [2003] for the absence of the polar cap arc in the 'empty' hemisphere was due to conductivity differences in the summer hemisphere. There have been reports of suppression of discrete aurorae in the main oval in the sunlit (summer) hemisphere by Newell et al. [1996b]; they attributed these observations to the ionospheric feedback mechanism whereby the ionospheric conductance of the sunlit hemisphere was sufficient to carry the field aligned current hence resulting in a weaker parallel electric field and no discrete auroral arcs in that hemisphere (e.g. Liou et al. [1997], Shue et al. [2001]). Another explanation for our observations could be the poor data quality in the southern (summer) hemisphere due to the effect of dayglow. The statistical study of data from different seasons (Section 4.4) showed that more arcs were seen in the winter hemispheres

than the summer.

By surveying four months of SSUSI data, it was found that polar cap arcs are seen by SSUSI at least 20% of the time. More events or images with polar cap arcs are recorded during the equinox months; we attribute this observation to arcs being missed in the summer hemispheres of the other two months. Polar cap arc events were seen nearly every day during the survey, evenly spread throughout each month. This occurrence frequency is double what was reported by Kullen et al. [2002], indicating that SSUSI is more sensitive to the lower energy arcs, perhaps those on open field lines, than Polar UV used by Kullen et al. [2002]. However our value is less than the 40% recorded by Valladares et al. [1994] using ground based instruments, suggesting SSUSI is not measuring all of the small scale features observed from the ground.

4.5.1 Instrumentation contribution

In this chapter, similar to Chapter 3, the SSUSI observations are used to identify polar cap arc events and determine the hemispheric nature of the arcs. Events where both hemispheres are not clearly visible, either due to the field of view of the spacecraft or noise in the image, are not included in the survey. In Section 4.4 we showed that the SSUSI images are sensitive to the hemisphere, season and spacecraft (with the SSUSI instrument on DMSP F17 being the most sensitive). These differences cannot be fully accounted for, but allow us to give a minimum boundary on the number of polar cap arcs events observed by the SSUSI instruments.

Data from the SSJ/5 instrument on board DMSP were used to investigated the in-situ particle data associated with the polar cap arcs. These data were also used to develop a semi-automatic method of identifying the poleward boundary of the auroral oval and the particle precipitation associated with arcs features within the polar cap. This method requires modification in some cases to capture all the features seen by eye, as discussed in Appendix A. Thus, a limitation of this data set is that it was not found possible to fully automate the boundary detection, and hence an element of subjectivity remains.

Data from OMNI and ARTEMIS were used to determine the IMF conditions for each event. AMPERE data, along with geomagnetic indices (AL, AU and SYM-H), are

presented for one event (Event 22) which despite appearances in the SSUSI images, was not a polar cap arc and in fact occurred during a geomagnetic storm.

4.6 Conclusions

This chapter has used SSUSI and DMSP SSJ/5 particle data to investigate the formation of polar cap arcs. One month of SSUSI data was surveyed (December 2015) to find polar cap arc events and determine if they were occurring in one or both hemispheres. Particle data from the spectrometer on board the DMSP spacecraft were obtained for the arcs that crossed the spacecraft track to analyse the particle precipitation associated with the arcs and to determine whether they were consistent with an open or closed field line mechanism and hence to further investigate the multiple polar cap arc formation mechanism issue discussed in Section 1.5.3.1.

Nine events were found to contain arcs in both hemispheres which were associated with ion precipitation; these arcs are consistent with a closed field line formation mechanism. Six more events were seen to have arcs in both hemispheres but only particle data for an arc in one hemisphere as the arc in the other hemisphere did not cross the footprint of the DMSP spacecraft. These arcs are potentially consistent with a closed field line mechanism, but as some of our 'both hemisphere' events show, we cannot definitively state that there would have been an ion signature if the spacecraft had crossed the arc in the other hemisphere.

Six events were recorded with arcs associated with electron-only precipitation and hence consistent with an open field line mechanism. One of these arcs occurred at the same time (i.e. in the same auroral image) as a closed field line arc and two further events occurred in the opposite hemisphere to a short lived arc associated with an ion signature potentially on closed field lines. These observations suggests that two mechanisms, one on open and the other on closed field lines, can occur simultaneously consistent with Reidy et al. [2017] and that presented in Chapter 3.

An event containing so called 'non-conjugate' theta aurora, whereby an arc associated with an ion signature (which is indicative of closed field lines), was seen in only one hemisphere (which is not indicative of closed field lines) was discussed. These observations are similar to those presented by Østgaard et al. [2003, 2007], discussed in Section 1.5.3.3.

Several suggestions are put forward to explain these observations, including that the SSUSI images in the summer hemisphere are complicated by the effects of daylight. Statistics presented over four months during 2015 are supportive of this interpretation. Additionally it was found that more arcs were detected in the southern hemisphere than the northern hemisphere over the four months surveyed in 2015. We suggest that this trend could be due to the orbits of the DMSP spacecraft, which pass closer to the dayside in the northern hemisphere and closer to the nightside in the southern hemisphere, meaning more of the northern hemisphere images suffer the effects of dayglow.

Lastly the seasonal effect on the occurrence of polar cap aurora was explored using survey results from March, June, September and December 2015. As discussed above, more arcs were seen in the winter hemisphere of December and June and more polar cap arcs were observed overall during the equinox months, March and September. This observation is attributed to the effects of dayglow on the SSUSI data and hence we conclude polar cap arcs occur at least 20% of the time which is approximately midway between the previous observations from Valladares et al. [1994] and Kullen et al. [2002] discussed in Section 1.5.3.2.

Key points:

- This chapter has built on the work presented in Chapter 3 by finding more events consistent with different magnetic field toplogies, showing that the event in Chapter 3 was not an isolated occurrence.
- We have developed a set of criteria, based on previous work (e.g. Craven et al. [1991] and Newell et al. [2009]) which can be used to determine if an arc is occurring on open or closed field lines based on their hemispheric nature and associated particle precipitation.
- Cases which did not fit the aforementioned criteria were explored, including an observation of a 'non-conjugate theta' aurora. This observation furthers the work presented by Østgaard et al. [2003, 2007] by showing the phenomenon in a different data set. Possible explanations for this controversial observation are discussed, although its exact nature still remains an open questions.
- Polar cap arcs events were found occur every day and are observed by the SSUSI instruments at least 20% of the time.

One of the events identified in this survey (Event 24) contained a polar cap arc occurring over Svalbard. The fine-scale structure of this arc, as well as an arc from other event, will be investigated in Chapter 5 using ground based instrumentation.

Chapter 5

Multi-scale observation of two polar cap arcs occurring on different magnetic field topologies

5.1 Introduction

This chapter will present two multi-scale observations of polar cap arcs that are consistent with different magnetic field topologies; one of which was identified as part of the survey in Chapter 4 (Event 23, Figure 4.2). This event was classified as 'both observed simultaneously' meaning arcs consistent with different magnetic field lines were observed at the same time, this chapter is concerned with the arc occurring above Svalbard that was consistent with open field lines. A separate event is presented in this chapter that was not part of the survey (which occurred on 4 February 2016). This event contained arcs consistent with closed field lines occurring over Svalbard. SSUSI and SSJ/5 data from DMSP F19 are used in this chapter which were not publicly available at the time of the survey discussed in Chapter 4.

Following on from the previous two chapters, the fine-scale structure of polar cap arcs from these two events are explored using the ASK instrument located on Svalbard. The ASK instrument, discussed in Section 2.1.1, is world leading in the study of small scale aurora with a 6° field of view (corresponding to 10 km × 10 km at 100 km altitude) and capabilities of measuring up to 32 images per second. Different terminology surrounding

small scale structure was introduced in Section 1.4.4.3. Previous studies using the ASK instrument have predominately been of small scale aurora within the main auroral oval (e.g. Dahlgren et al. [2010]) and hence the chapter will present the first ASK observations of polar cap arcs consistent with different topologies.

This chapter will build on the ASK observations of a 'failed' transpolar arc presented in Chapter 3, by investigating a more traditional transpolar arc consistent with closed field lines and a separate polar cap arc consistent with formation on open field lines. These two events will initially be discussed separately in Sections 5.2 and 5.3 respectively. As in Chapter 3, the ASK data presented in these chapters will be compared to the Southampton Ionospheric model (Section 2.1.1.1) to estimate the energy and energy flux of the precipitation associated with these arcs using the same methods as described in Sections 2.1.1.1 and 3.2.2.1. HiTIES data from the H-α panel (described in Section 2.4.1) is presented for both events to investigate the presence of proton precipitation measured from the ground. SuperDARN map potential plots (Section 2.3.2) are also presented for the 'open' event to investigate the nature of the ionospheric flows in the polar cap, which could have given rise to accelerated polar rain. The observations from each event are compared to one another and then to spacecraft observations from the DMSP SSJ/5 in Section 5.4. A conclusion is then given in Section 5.5 which describes how the small-scale structure of polar cap arcs occurring on different magnetic field topologies is different (as expected).

5.2 Observations

5.2.1 Closed field line observation

Figure 5.1 gives a summary of the auroral and IMF conditions for a polar cap arc event which occurred on 4 February 2016. Fig 5.1a and b demonstrate SSUSI observations from the event of each hemisphere (south and north respectively) with the corresponding DMSP particle data to the right; these images were chosen to give an overview of the event (similar to those presented in Chapter 4). We have also used the same semi-automated detection method to identify the poleward edge of the auroral oval as in Chapter 4 and described in Appendix A, shown in black for electrons and grey for ions as before. These observations show polar cap arcs occurring on the dawnside of the

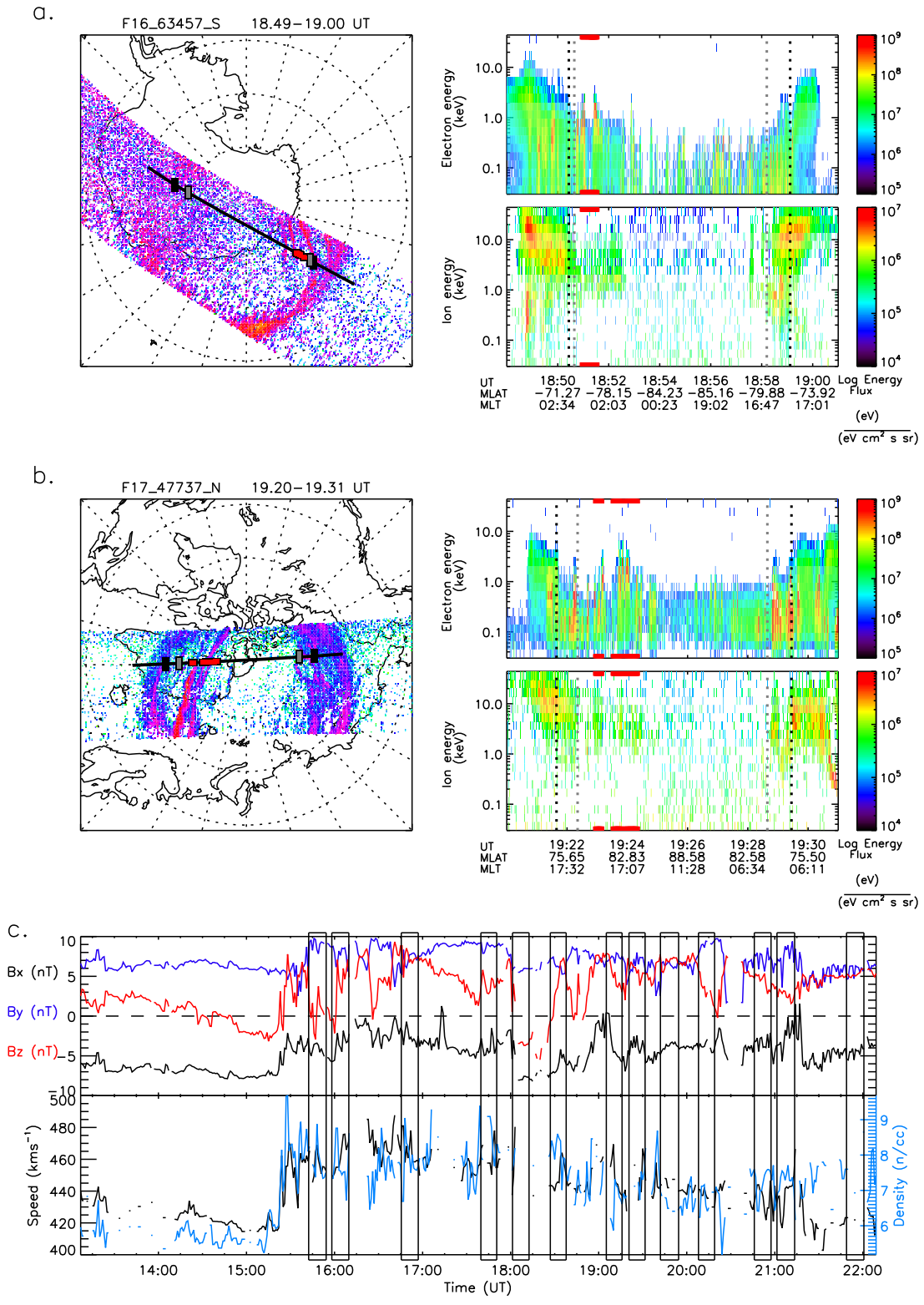

FIGURE 5.1: Overview of the 4th February 2016 polar cap arc event. Summary SSUSI and the corresponding SSJ/5 data for the southern hemisphere (a) and the northern hemisphere (b). The top panel of (c) gives the IMF magnetic field Bx, B$_y$, B$_z$ components in black, blue and red respectively. The bottom panel of (c) give solar wind speed (black) and density (blue). The times of all the northern hemisphere SSUSI images where a polar cap arc was observed indicated by boxes.

southern hemisphere and on the duskside of the northern hemisphere associated with both ion and electron signatures (indicated by red lines). Using the same criteria as the survey presented in Chapter 4, this event would have been classified as consistent with formation on closed field lines. Furthermore, these arcs are occurring on opposite sides of the polar cap in each hemisphere consistent with Craven et al. [1991] and Milan et al. [2005]. This chapter will now only consider the northern hemisphere SSUSI observations which show polar cap arcs over Svalbard during this event.

Fig 5.1c shows the magnetic field components (top panel) and the speed and density of the solar wind (bottom panel) during the event. The times of all the northern hemisphere SSUSI images where a polar cap arc was identified during this event are indicated by boxes in these bottom three panels. The first polar cap arc observations in the northern hemisphere SSUSI images occurred around 15:45 UT. This is shortly after a clear change in the solar wind conditions, around 15:30 UT, where the solar wind speed and density increased and the IMF became strongly northward. During the event the IMF remained predominately northward, with a few short southward turnings, and had negative B_x and positive B_y components. A minimum event duration of 6 hours can be inferred from the times of the SSUSI images plotted, where an arc was observed, between approximately 16:00-22:00 UT. Using the times of the SSUSI images before and after this interval (where no arc could be discerned), an upper life time of 7 hours can be determined.

Figure 5.2 shows all the northern hemisphere SSUSI observations where a polar cap arc was identified during this event (the times of which correspond to the boxes indicated in Fig. 5.1c). Each of the images corresponds to a 20 minute window but the times at the top of all the SSUSI images indicate when the DMSP spacecraft was poleward of 70 degrees magnetic latitude (the spacecraft name, orbit number and hemisphere of observation are also indicated at the top of each image). The location of Svalbard is indicated in each SSUSI image by a green circle. An arc can be seen on the duskside of the polar cap, near Svalbard, throughout this event. As discussed in Chapter 4 (Section 4.4), the SSUSI instruments on board the different DMSP spacecraft have different sensitivities; here the polar cap arcs are generally clearest in the DMSP F17 and F19 images (e.g. Figs. 5.2a and b) and weakest in the DMSP F18 images (e.g. Fig. 5.2c). Furthermore, the DMSP F16 images (Figs. 5.2e and i) are generally 'noiser' than the other SSUSI observations.

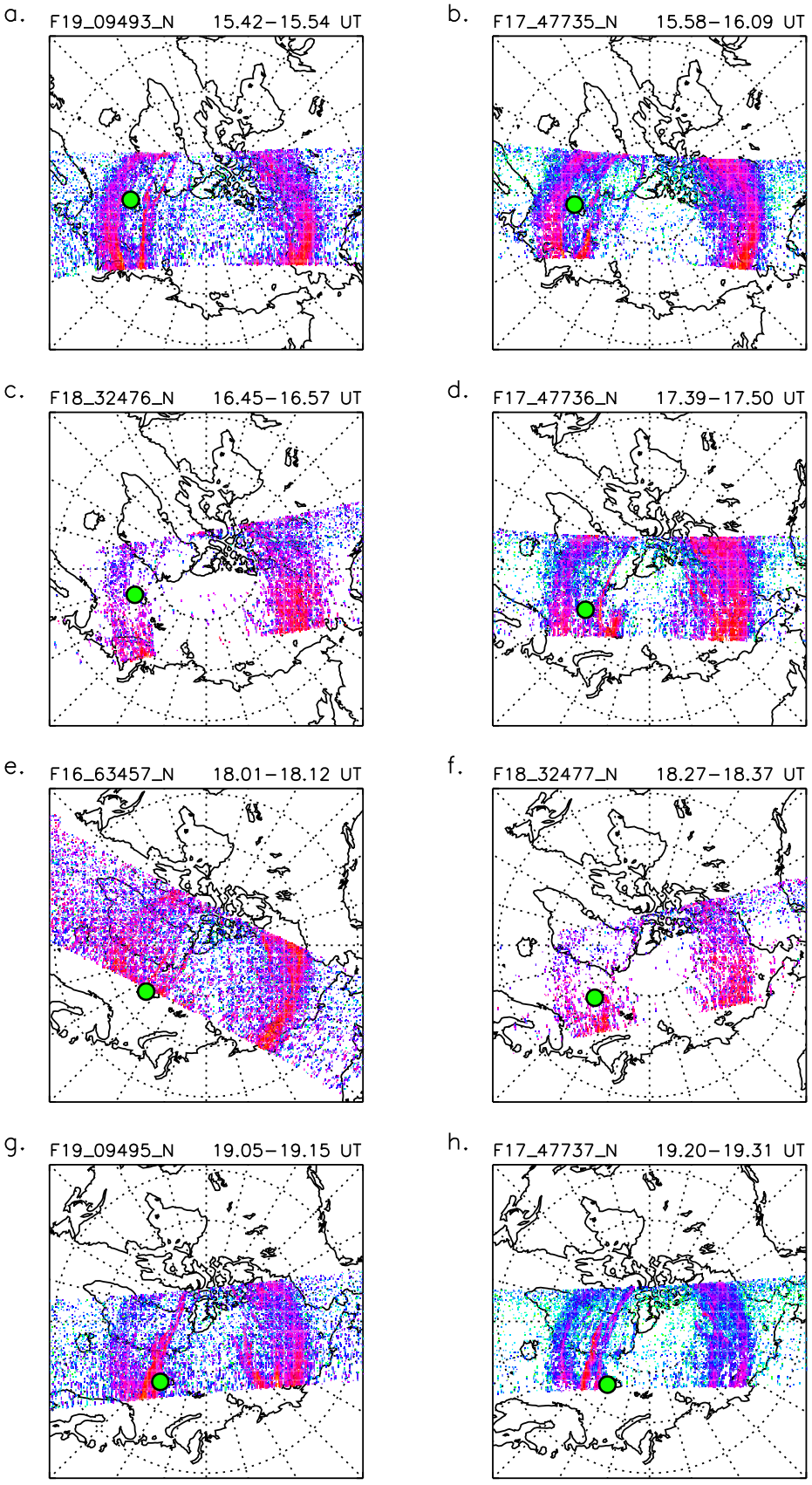

FIGURE 5.2: Figure showing all the northern hemisphere SSUSI observations where a polar cap arc was identified. The times of these are also indicated in Fig. 5.1c. Svalbard is indicated by a green dot in each of these images. Continued overleaf.

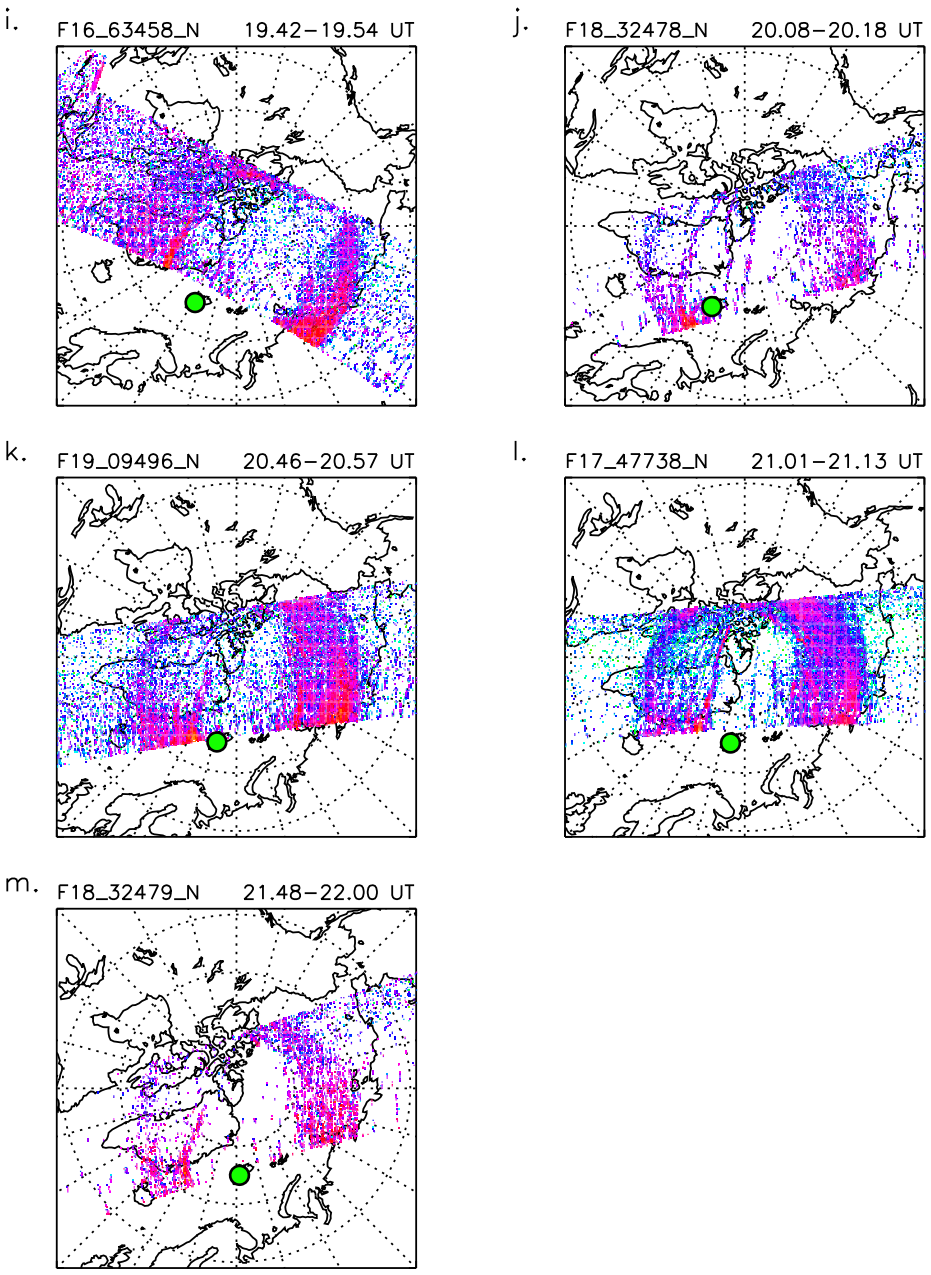

FIGURE 5.2: Continued.

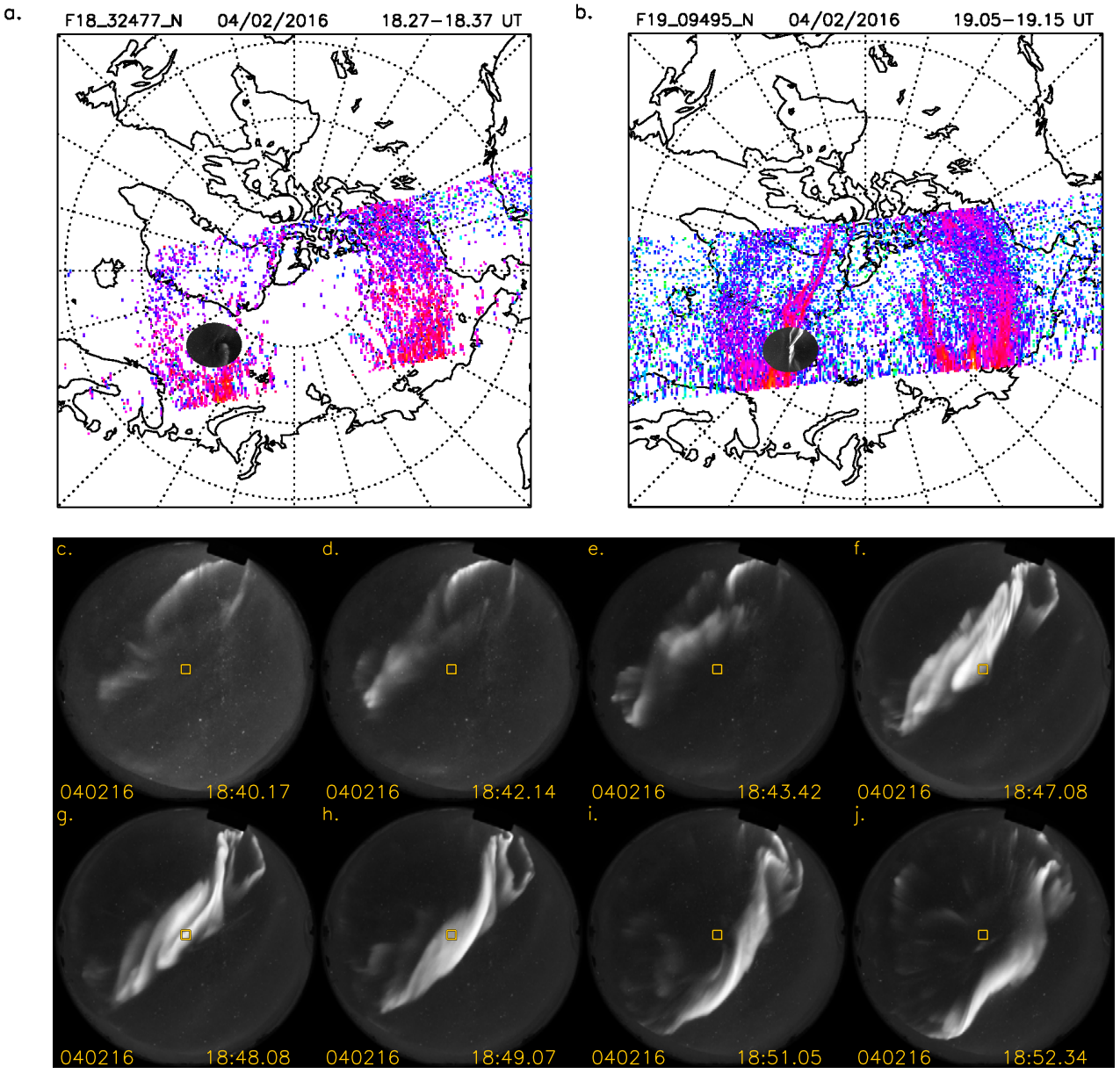

FIGURE 5.3: a. A northern hemisphere SSUSI DMSP F18 image between 18:27-18:37 UT. b. A northern hemisphere SSUSI DMSP F19 image between 19:05-19:15 UT. c-j: Images from the Sony all sky camera between 18:40-19:52:30 UT in approximately 2 minute intervals. The yellow box in each image shows the approximate field of view of the ASK instrument. An extra image at 18:48:08 UT is included to demonstrate the time when the arc was in the ASK field of view. All sky images at 18:32:56 UT and 18:48:08 UT projected onto the SSUSI images in a and b respectively.

The polar cap arc passes over Svalbard between the DMSP F18 observation at 18:27-18:57 UT (Fig. 5.2f) and the DMSP F19 observation at 19:05-19:15 UT (Fig. 5.2g). Before these images there is some ambiguity in whether Svalbard is under the polar cap arc or in the polar cap itself. To explore the issue further the two aforementioned SSUSI plots are re-produced in Figures 5.3a and b respectively. Figs. 5.3c-j show images from the Sony all sky camera (described in Section 2.1.3) between 18:40-18:52 UT in approximately 2 minute intervals. The yellow squares in each of the all sky images indicates the approximate field of view of the ASK instrument (which is aligned with magnetic zenith). In these images north is at the top and east is to the left. A bright, approximately north-south aligned arc can be seen passing from East to West (duskward) over magnetic zenith during this interval. An additional image at 18:48:08 UT (Fig. 5.3g), is included to show the exact time when the arc crossed magnetic zenith. This image has been projected onto the SSUSI image in Fig. 5.3b to show that the two observations are almost perfectly aligned (even though they are occurring at different times). An all sky image at 18:32:56 UT has also been plotted on the SSUSI image in Fig. 5.3a to demonstrate the arc has moved duskward over Svalbard.

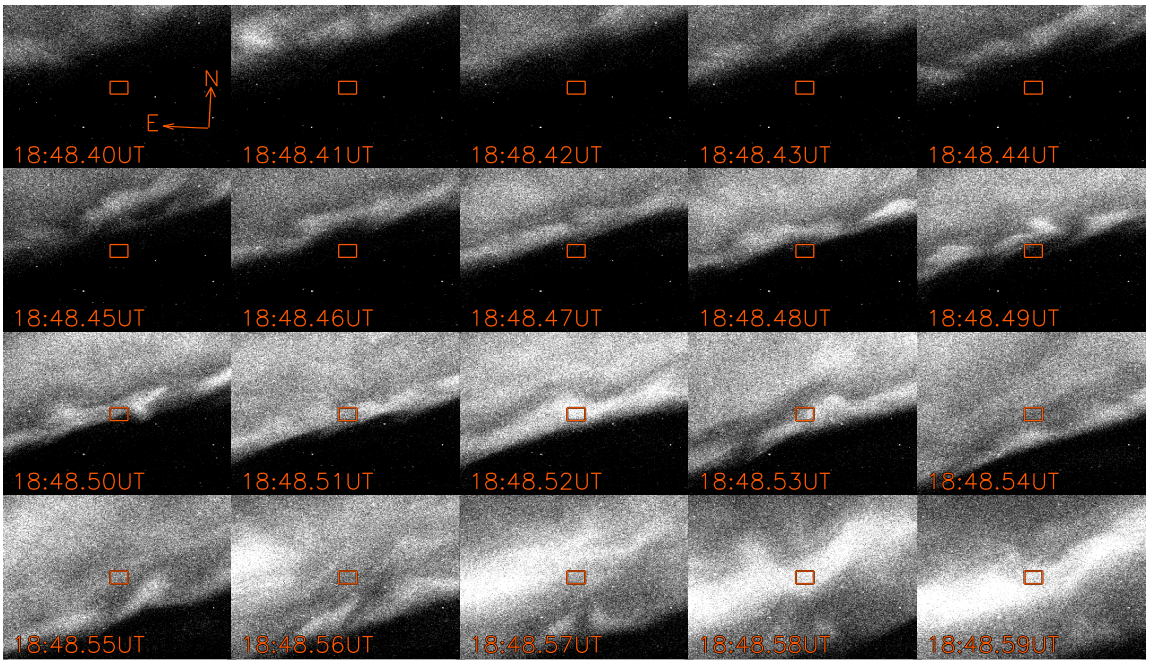

FIGURE 5.4: Images from the ASK1 camera at one second resolution between 18:48:40-18:48:59 UT. The orange box indicated 20x20 pixels surrounding magnetic zenith. In each image North is approximately to the top and East to the left.

Figure 5.4 shows images from the ASK instrument between 18:48:42-18:49:00 UT, when the arc passed over magnetic zenith. During this event, the ASK instrument was running

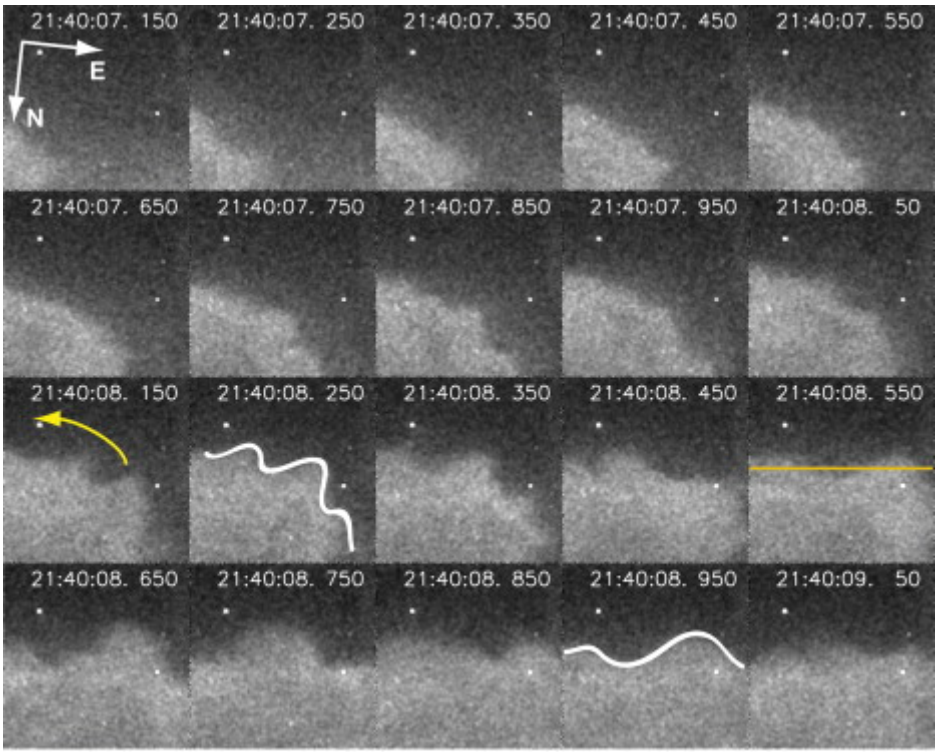

FIGURE 5.5: Figure taken from Dahlgren et al. [2010] showing observations of 'ruffs' on the edge of an auroral fold from the ASK instrument on 23rd November 2006 between approximately 21:40.07-21:40.09 UT. These 'ruffs' are outlined by white lines in two of the images and the motion is indicated by a yellow arrow. The horizontal yellow line is indicated for later analysis in the paper.

at 20 frames per second. These images are from the ASK1 camera which has a filter that is sensitive to a prompt emission caused by high energy precipitation (Section 2.1.1). The orange boxes in these images indicate the 20 $\times$ 20 pixels surrounding magnetic zenith which are used later for analysis. During this interval an auroral boundary-like form can be seen to sweep across the ASK field of view from a North-East direction, consistent with the direction of the arc seen in the all sky images (Fig. 5.3). Small scale structures can be seen on the edge of this 'boundary' which may be considered to be ruffs or even small-scale curls. An example of 'ruffs' observations from Dahlgren et al. [2010] is given in Fig. 5.5 for comparison; these observations are taken by ASK during the period it was located in Tromsø and hence likely to be observing aurora on the closed field lines of the main auroral oval. These 'ruffs' are not exactly what we have in Fig. 5.4 but small scale distortions of the edge of an auroral boundary can be seen in both.

These observations are quite different from the 'failed' transpolar arc presented in Chapter 3 (Fig. 3.6) which was more swirled and diffuse in nature (referred to by the

Southampton group as 'chocolate sauce' aurora). If we consider both arcs to be formed by the mechanism described in Milan et al. [2005] (Section 1.5.2.2), the differences in the structure could be due to the arcs being in different stages of formation, i.e. the 'failed' transpolar arc had not protruded across the entire polar cap and therefore could be considered to be at the beginning of the formation mechanism, whereas the arc presented here is more developed. However, as each observation only shows the auroral emissions over a brief period, it is possible that these differences are due to the variable nature of small scale structures, which can be seen in Fig. 5.4 to be changing on timescales of less than 2 seconds. In both cases, the highly structured dynamic auroral observations are consistent with previous ASK observations taken when ASK was situated in Tromsø under the main auroral oval (for example, Lanchester et al. [2009], Dahlgren et al. [2010, 2011, 2016]) and are hence consistent with formation on closed field lines.

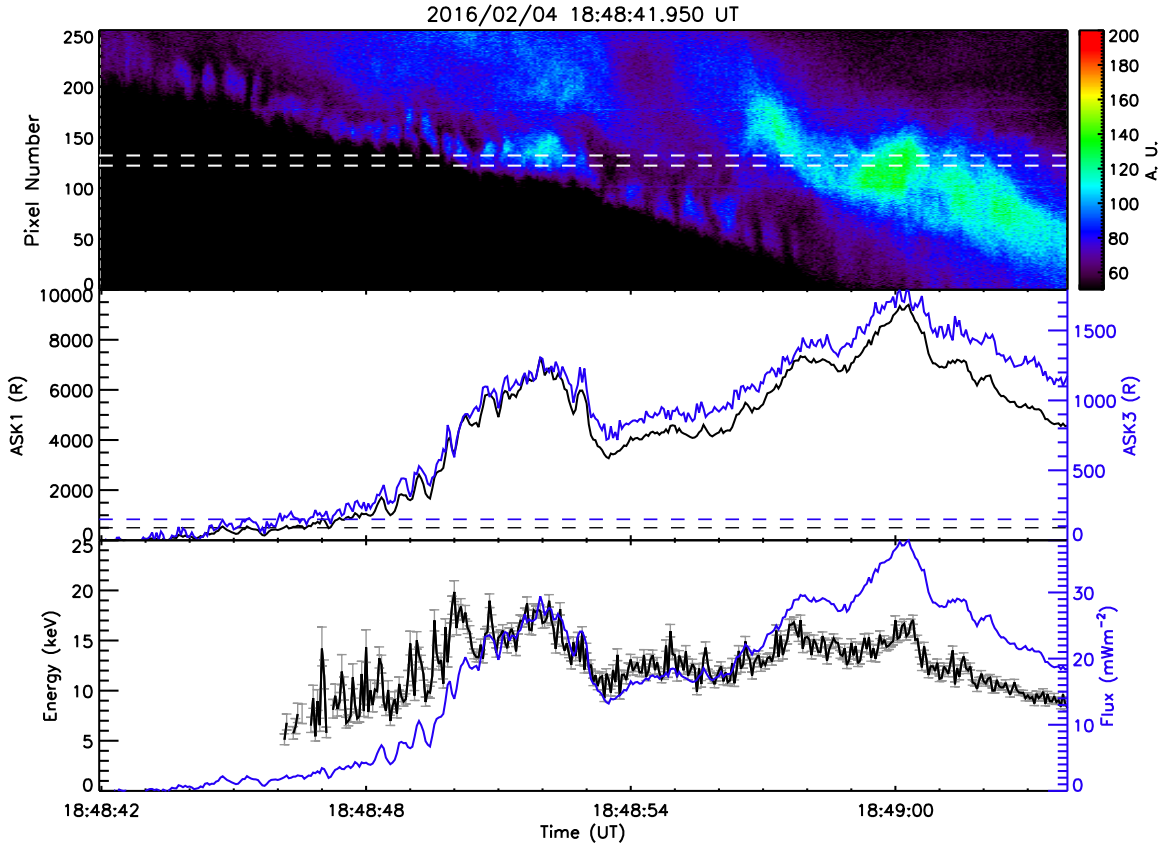

FIGURE 5.6: ASK data from a period when the polar cap arc passes through magnetic zenith over Svalbard. The top panel shows a keogram of images from the ASK1 camera in arbitrary units. The second panel shows the intensities measured by ASK1 and ASK3 in black and blue respectively. The estimates of energies (black) and flux (blue) are shown in the bottom panel. The error on the energy estimation is shown by grey energy bars.

Figure 5.6 shows the ASK observations during our period of interest in a more quantitative way. The top panel shows a keogram of the ASK1 observations between 18:48:42-18:49:04 UT. The colour scale is in arbitrary units. This keogram clearly shows the repetitive structures on the boundary of the arc discussed above. The second panel of Fig. 5.6 shows the intensities measured by the ASK1 (black) and ASK3 (blue) cameras in the 20 × 20 pixels around magnetic zenith indicated by the boxes in Fig. 5.4 and the white dashed lines in the above keogram. These intensities are similar in magnitude to those found in the case for the 'failed' TPA (Fig. 3.6). Panel 3 shows the energy (black) and energy flux (blue) estimated by comparing the ratio of the measured intensities from ASK1 and 3 to the Southampton Ionospheric model (Section 2.1.1.1). The energies are only estimated when the intensities are above a background level indicated by a horizontal dashed lines in panel 2. The error on the energy is shown by grey error bars; these errors are propagated from the initial counts measured by the ASK1 and ASK3 cameras. The errors on the intensities and flux are not shown because they are so small, each with a percentage error less than 1%. The estimated energies are varying between approximately 5 and 20 keV during this interval, with a mean value of 12.6 ± 0.9 keV; this is higher than the mean energy estimated for the 'failed' transpolar arc which was found to be 5 keV. Around 18:49:00 UT, a brightening in the keogram (panel 1) and a corresponding increase in the intensities (panel 2) can be observed. Panel 3 shows that at this time the energy remained approximately constant but the energy flux has increased and hence this indicates that this brightening was caused by an increase in the flux rather than the energy of the precipitation. These estimates will be further investigated in Section 5.4 but for now we note that, due to the high values of the estimated energy and energy flux and the structure of the auroral forms seen in Fig. 5.4, this observation appears to be consistent with formation on closed field lines and is hence referred to as the 'closed' event for the remainder of this chapter.

Figure 5.7 shows the spectra measured by the H-α panel of the HiTIES instrument, which has been averaged between 18:48:48-18:36:10 UT during this event. The contributions from OH, N_2, N^+ and O_2^+ emissions (but not H-alpha) have been fitted in this spectra using methods outlined in Chadney and Whiter [2018] and Price et al. [2019]. The overall fit, excluding the H-α emission at 6563 Å, is shown in red. These observations will be discussed in more detail in Section 5.3 but for now we note the presence of a peak at 6563 Åindicates H-α emission, and that the peak appears to be broader towards

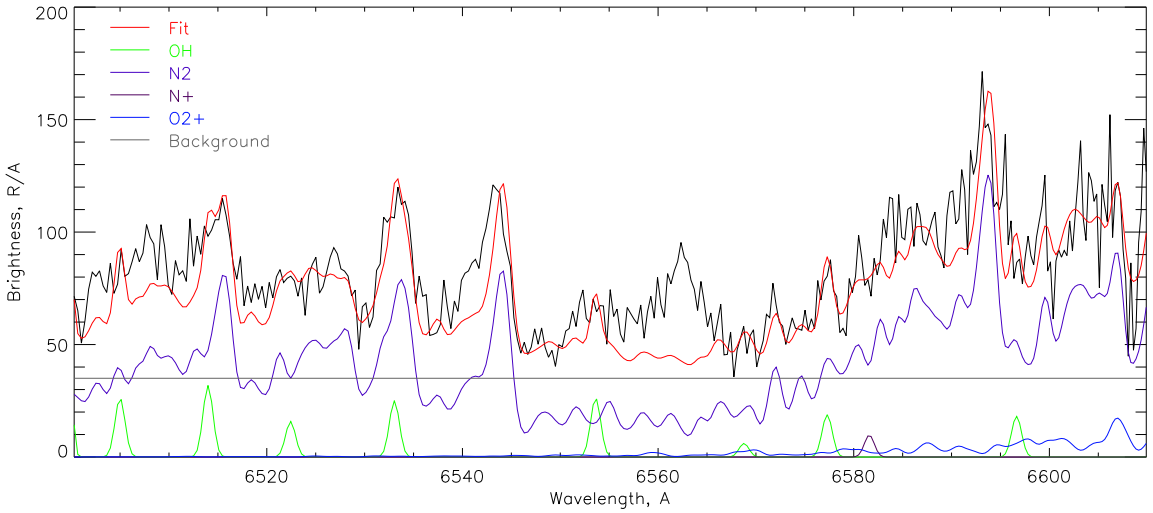

FIGURE 5.7: Spectra from the HITIES instrument between 6500-6610 Å (where 1 Å= 0.1 nm) for the 'closed' event.

shorter wavelengths ('blue wing'), which is indicative of accelerated protons.

5.2.2 Open field line observation

Figure 5.8 (presented in the same format as Fig. 5.1) shows the auroral and IMF conditions for a polar cap arc event occurring on 15th December 2015. This event was included in the Reidy et al. [2018] survey (Chapter 4) and was classified as an event containing arcs consistent with both open and closed field lines, consistent with Reidy et al. [2017] (Chapter 3) who first showed that the different magnetic topologies could occur simultaneously. This chapter is concerned with the arc occurring on the duskside of the northern hemisphere over Svalbard (shown in Fig. 5.8a), indicated by orange lines. The corresponding DMSP particle data show that this arc is associated with electron-only precipitation, consistent with accelerated polar rain on open field lines [Newell et al., 2009, Carlson and Cowley, 2005]. This event is hence termed the 'open' event. The arcs associated with ion and electron signatures observed in both hemispheres (indicated by red lines) are not further discussed in this thesis.

Fig. 5.8c shows the IMF conditions for this event. Throughout this interval, the IMF was predominately northward with weakly positive B_x and negative B_y components. Similar to Fig. 5.1, the times of northern hemisphere SSUSI images where the electron-only polar cap arc was identified are indicated by boxes. These SSUSI images can be

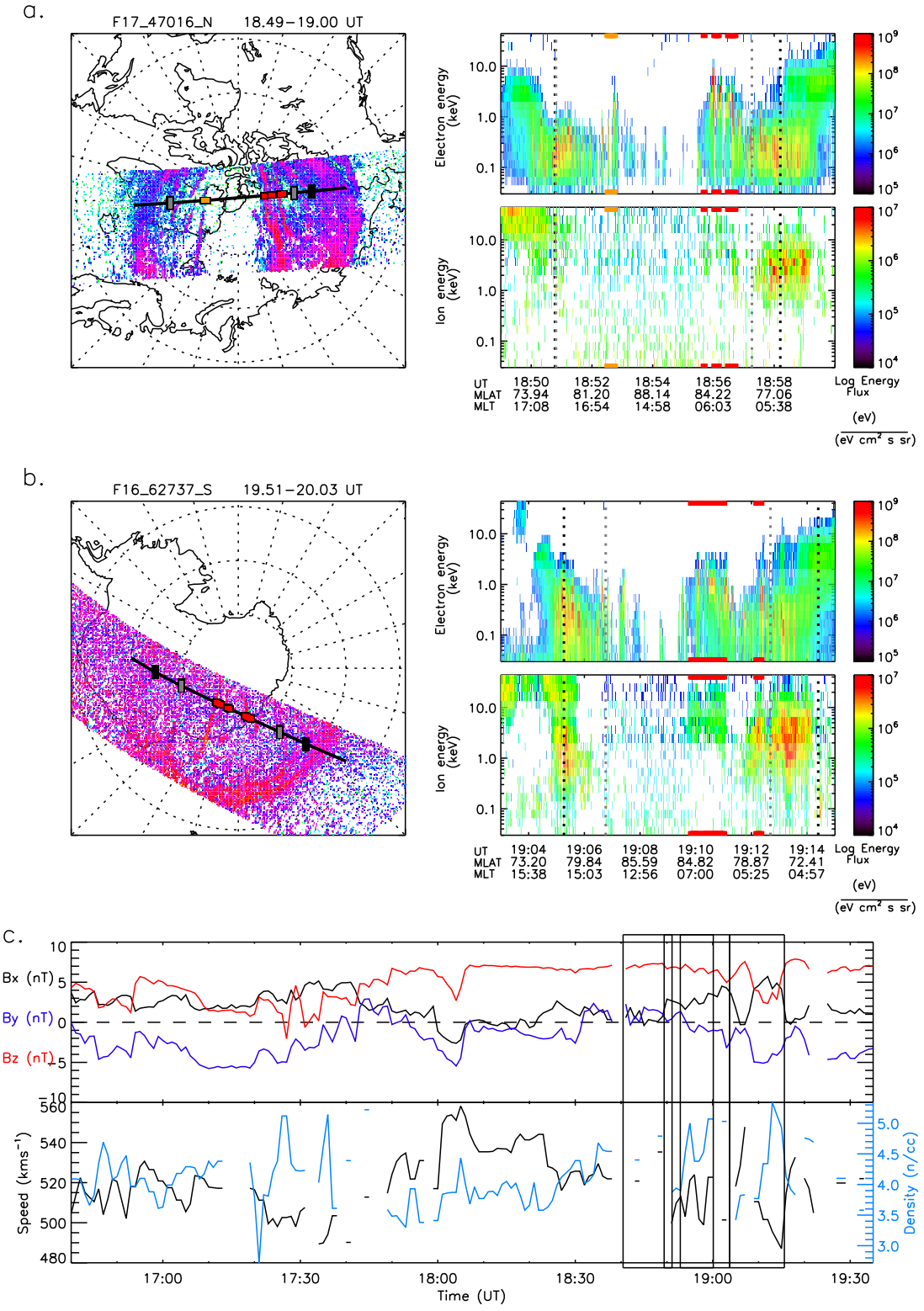

FIGURE 5.8: Similar to Fig. 5.1, the SSUSI and corresponding SSJ/5 data are shown for the northern hemisphere (a) and southern hemisphere (b) during a polar cap arc event. (c) the magnetic IMF components of the IMF are given in the top panel, the solar wind speed and density in the bottom panel. Times of the SSUSI observations are indicated by boxes.

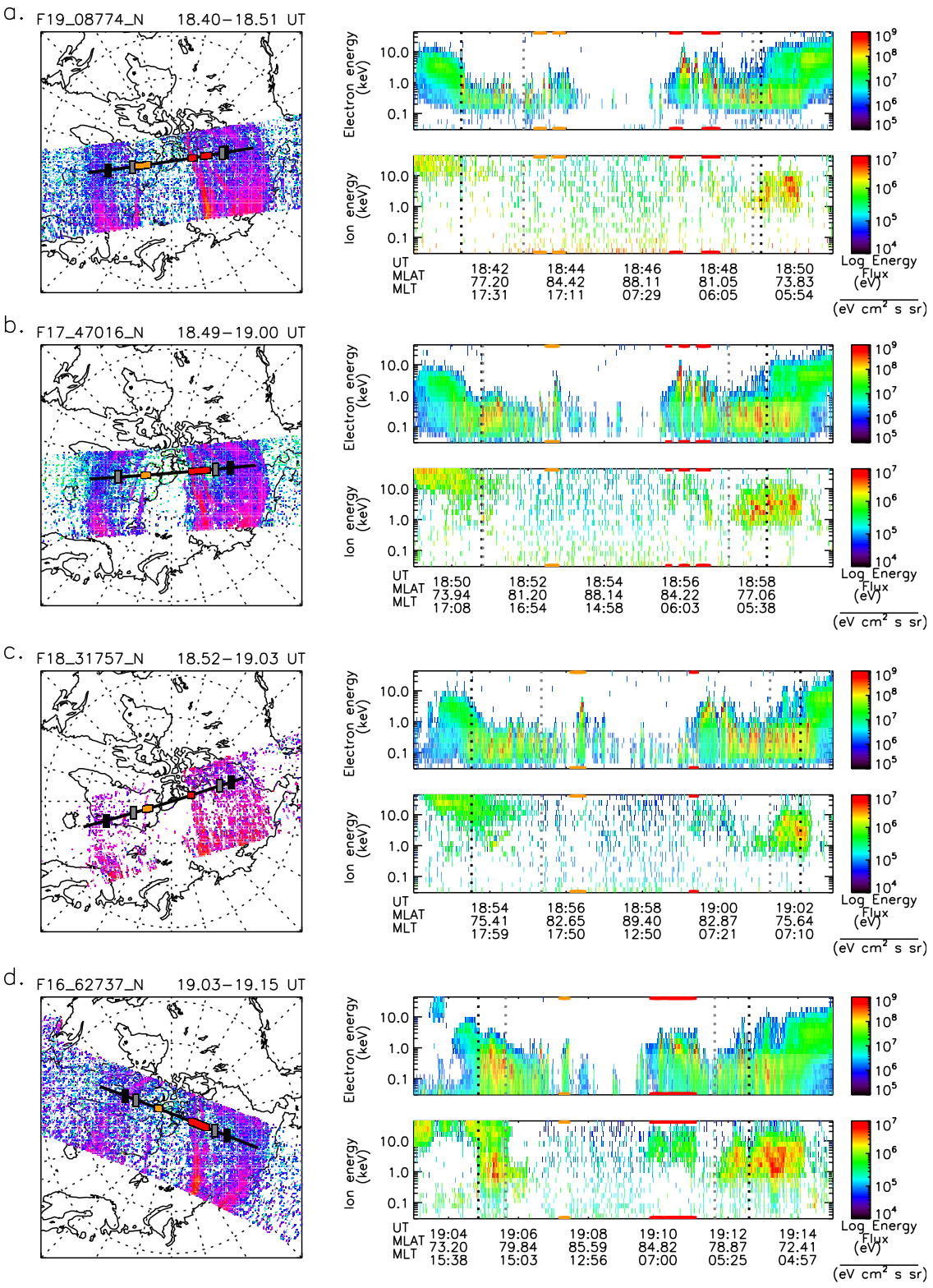

FIGURE 5.9: a-d: The auroral and corresponding particle measurements from each DMSP satellite when the duskside arc was observed in time order.

used to infer a minimum event duration of 35 minutes (between 18:40-19:15 UT), when the arc was observed, and a maximum event duration of 3 hours from the images before and after this time, when the arc was not observed. A more accurate event duration cannot be obtained due to the limited SSUSI observations in the northern hemisphere but either way we note that this 'open' event is shorter in duration than the 'closed' event presented in Section 5.2.1..

Fig. 5.9 presents the observations of the electron-only arc on the duskside of the northern hemisphere from all four SSUSI and SSJ/5 instruments on board the different DMSP spacecraft. The arc is clearest in the SSUSI DMSP F19 and F17 images (Fig. 5.9a and b) and is hardest to distinguish in the SSUSI DMSP F18 images (Fig. 5.9c), similar to the observations for the 'closed' event. An electron-only signature (orange) is observed by all four SSJ/5 instruments in association with the duskside arc. These observations are consistent with those presented in previous chapters for polar cap arc formation on open field lines, generated by accelerated polar rain [Reidy et al., 2017, Reidy et al., 2018].

The SSUSI DMSP F19 observations between 18:40-18:51 UT are replotted in Figure 5.10a, with images from the Sony all sky camera in 2 minute intervals between around 18:28-18:40 UT (Figs. 5.10b-i). This is the interval in which a roughly north-south aligned arc passed through the ASK field of view, indicated by yellow boxes on each of the all sky images (same as Fig. 5.3). Fig. 5.10f shows the time when an arc was seen by ASK, around 18:35 UT. At first sight, the brightest arc appears to cross ASK's field of view between Figs. 5.10b and c, however, no clear structure could be distinguished in the ASK instrument at this time. This is potentially because the aurora may have been diffuse in the small field of view of ASK during this interval. An all sky image at 18:41:06 UT has been projected onto the SSUSI DMSP F19 image in Fig. 5.10a as this image was closest to the time when the polar cap arc was observed by the SSUSI instrument. This projection demonstrates that the approximately north-south arc passing through the field of view of ASK is aligned with the polar cap arc seen in the SSUSI images.

Figure 5.11 shows stills from the ASK 3 camera between 18:35:20-18:35:48 UT; this is during the period shown by Fig. 5.10f. This ASK3 camera has a filter which is sensitive to prompt auroral emission that is caused by a mixture of low and high energy precipitation.

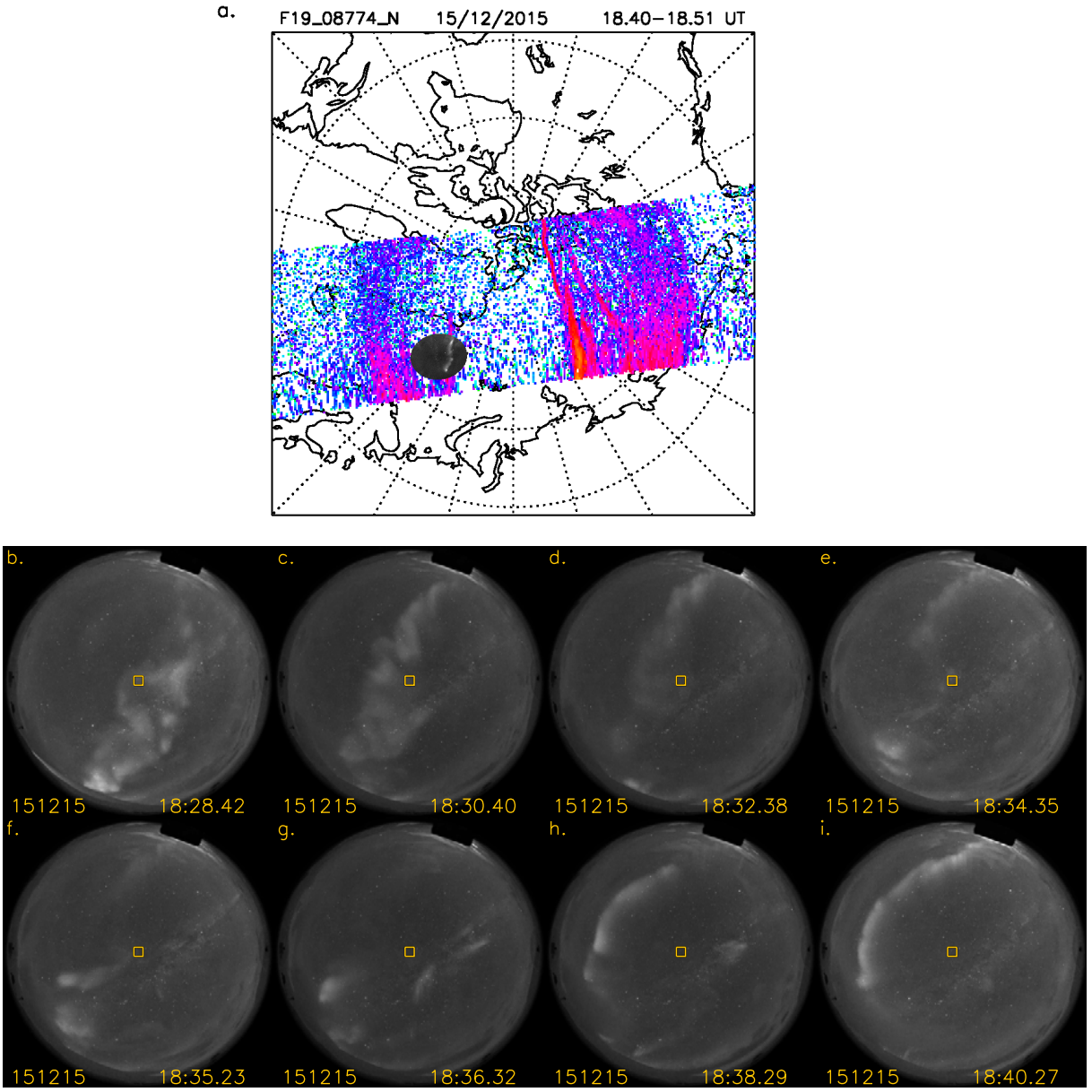

FIGURE 5.10: a. A SSUSI image from DMSP F19 between 18:40-18:51 UT with an all sky image at 18:41 UT projected onto the same MLT grid. b-i: images from the Sony all sky camera between 18:28-18:40UT.

As for the 'closed' event, these images are produced at 20 frames per second. However in this case, we have used mean images, which are averaged over 2 seconds, because this arc is much lower in intensity compared to the 'closed' field line observation presented in Fig. 5.4 and hence averaging was required to discern any structure in this event. As well as being much fainter than the 'closed' event, the structure of the 'open' arc is much less continuous. We can start to pick out some structure at the top of the arc passing from the north-west direction (around 18:35:32 UT). It is possible that some of

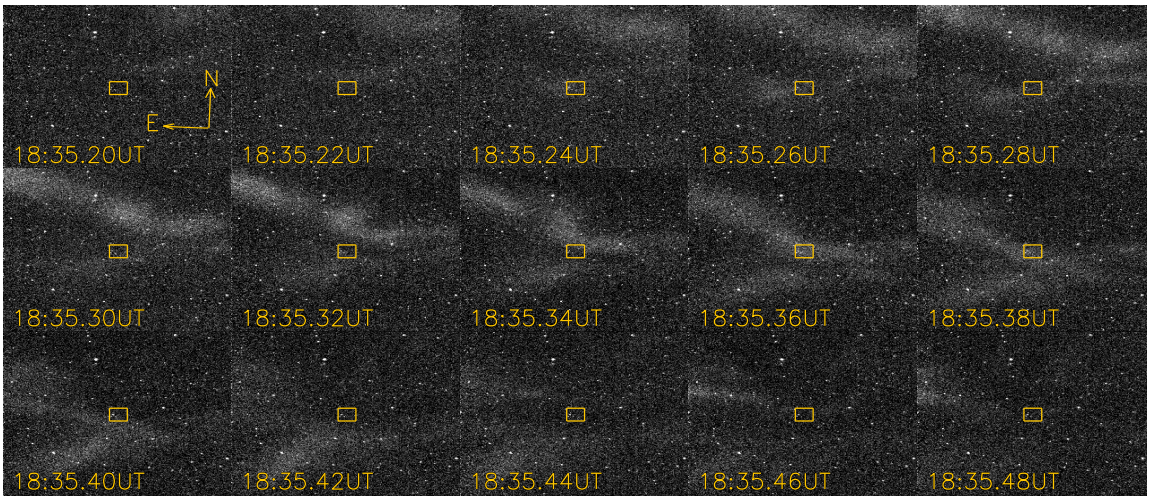

FIGURE 5.11: Stills from the ASK3 camera between 18:35.20-18:35:48 UT when the 'open' field line arc passed through magnetic zenith.

the auroral structure during this interval has been lost due to the averaging, which is comparable to the timescales of the structure seen in the closed event (i.e. less that 2 seconds). Although a more detailed description of this 'open' structure cannot be given due to the weakness of the emission, it is clearly very different from the dynamic 'closed' event presented in Section 5.2 and the 'failed' transpolar arc from Chapter 3.

Figure. 5.12 (similar to Fig. 5.6) shows the ASK data in keogram format, along with the intensities at magnetic zenith and, the energies and energy fluxes estimates from these intensities; as before, the errors on the energy are shown by grey error bars. The pixels averaged over magnetic zenith are shown by red dashed lines on the keogram. As for the 'closed' case, the energies are only estimated above a background level which is indicated by dashed lines in panel 2. However, as the intensities of the emissions are significantly lower in this case, the intensities are above the background for a shorter portion of the event. The arc can be seen to pass through magnetic zenith around 18:35.35 UT with a mean energy of approximately 3.4 $\pm$ 0.1 keV. As is evident from the ASK 3 stills in Fig. 5.11 and from panel 2 of Fig. 5.12, this event is of much lower intensity than the 'closed' event (Fig. 5.6). A more detailed comparison of these two different events will be given in the discussion section but for now we note that the lower flux and intensities associated with this 'open' arc are consistent with the low plasma density of the magnetotail lobes.

Figure 5.13, similar to Fig. 5.7, gives the HiTIES spectra measured by the H-α panel during the 'open' event, averaged between 18:35:00 UT and 18:36:10 UT. As before, a fit

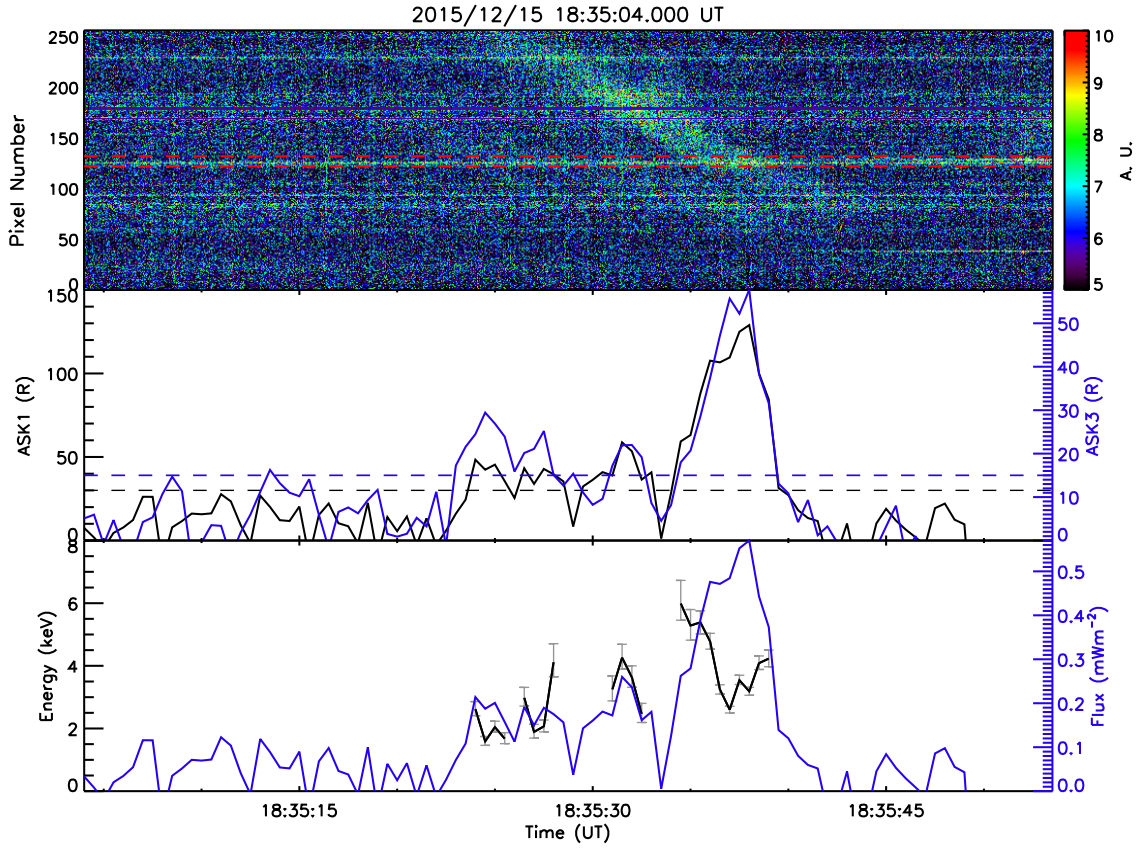

FIGURE 5.12: ASK data from a period when the polar cap arc consistent with open field lines passes through magnetic zenith over Svalbard. In the same format as Fig. 5.6

for the spectra (excluding H-α) has been obtained using methods outlined in Chadney and Whiter [2018] and Price et al. [2019]. Similarly to the 'closed' event, H-α emission is present, at 6563 Å, but here the emission is much narrower in its wavelength extent. A more detailed comparison of the two HiTIES observations will be given in the discussion section.

Figure 5.14 shows a series of SuperDARN map potential plots between 18:10-18:50 UT overlaid on the SSUSI DMSP F19 image between 18:40-18:51 UT. Evidence of lobe reconnection can be seen in all of the images with the merging gap (the footprint of the reconnection site, identified by a region of sunward flow) slightly dawnward of noon, around 80° magnetic latitude. On the dawnside more ionospheric scatter can be seen near the (closed field line) dawnside polar cap arc, with anti-sunward flow seen between the arc and the oval. Duskward of the dawnside arc, scatter is only observed at the sunward tipof the arc, but here we see the flows are sunward and hence the arc is aligned with the sunward flow channel into the merging gap. The clockwise motion of this dawnside lobe convection cell is consistent with upward field aligned current and

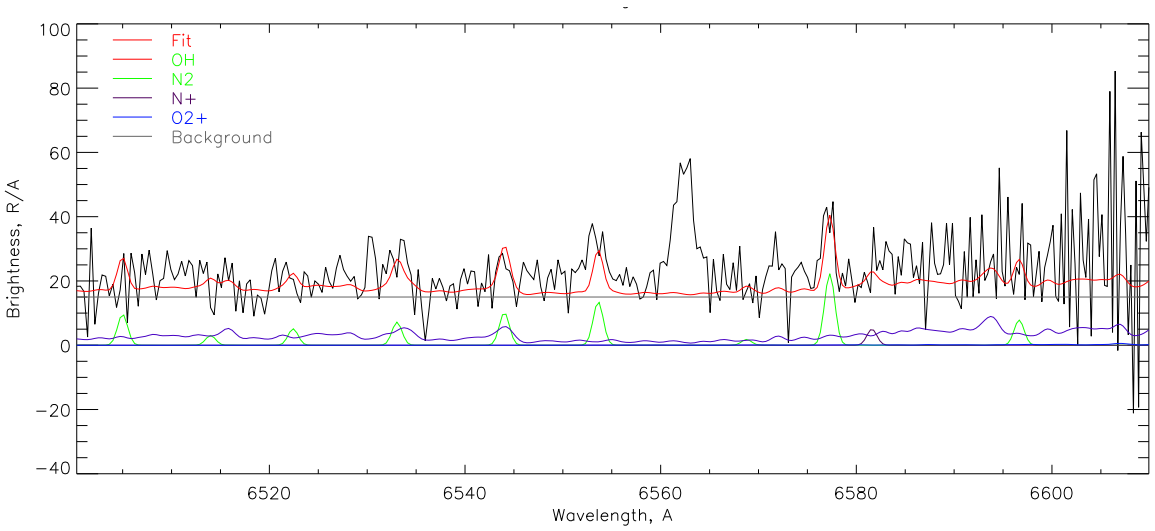

FIGURE 5.13: Spectra from the HITIES instrument between 6500-6610 Å for the 'open' event.

hence downward electron precipitation (e.g. Chiu et al. [1985]). However, in the Chiu et al. [1985] model, they predict the arc to be located in the center of the flow cell whereas around 18:40 UT (Fig. 5.14f), at the time of the SSUSI image, observations show the tip of the arc to be aligned with the sunward flow. This is consistent with Fear et al. [2015] who argued that a polar cap arc should be drawn towards the sunward flow channel by the flows themselves.

On the duskside, there is not so much scatter around the 'open' polar cap arc of interest to this study, particularly on the nightside. In Figs 5.14a, b, c, d and e the lobe convection cell appears to be sunward of the 'open' arc. In Figs. 5.14f, g and h, the sunward tip of the arc is approximately aligned with the duskward edge of the sunward flow channel; this is again potentially consistent with Fear et al. [2015] but inconsistent with a direct application of the arguments of Chiu et al. [1985], as the arc does not seem to be centred on what we can see of the dusk convection cell; even if it were, the sense of the rotation of the flow would suggest a downward current and hence upward-moving electrons. In the absence of more extensive scatter coincident with the duskside open arc, we cannot comment conclusively on the cause of this arc. However, we speculate from our knowledge of the sunward extent of the flow pattern that if the duskside arc is caused by a shear flow, this shear is more likely to arise from a gradient in the strength of the sunward flow excited by lobe reconnection, rather than by the opposite flows on either side of the convection cell as envisaged by Chiu et al. [1985].

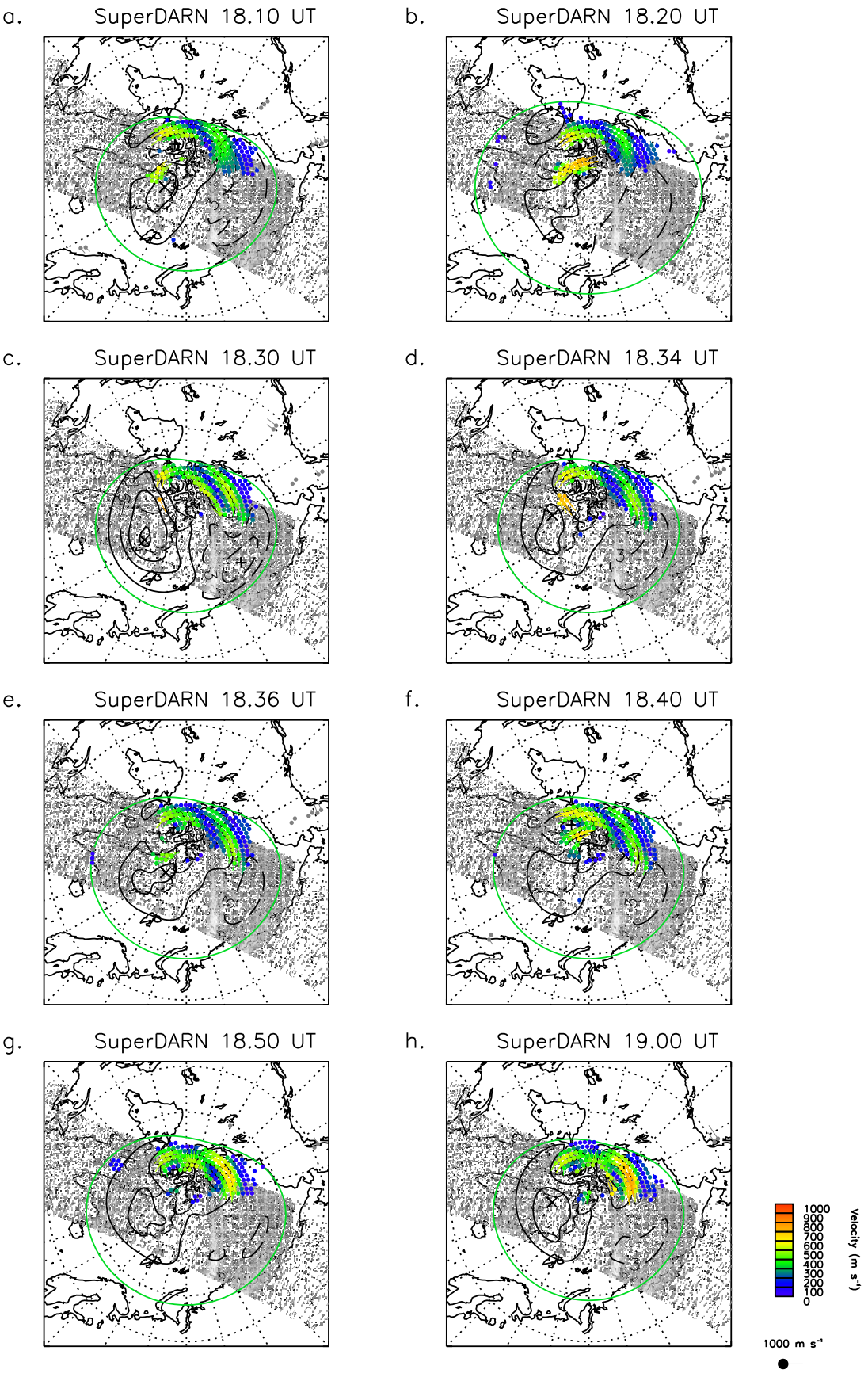

FIGURE 5.14: SuperDARN map potential plots between 18:10-19:00 UT overplotted on a SSUSI image at 18:49-19:00 UT.

5.3 Discussion

In this chapter we have shown two different observations of polar cap arcs occurring over Svalbard. The two events were consistent with formation on different magnetic field line topologies, termed the 'closed' and 'open' events. The small scale structure of these events was investigated using the Auroral Structure and Kinetic (ASK) instrument. These observations were then combined with an ionospheric model to estimate the energy and energy flux of the auroral precipitation.

The aurora observed by ASK for the 'closed' event (Figs. 5.4 and 5.6) was seen to be much brighter than for the 'open' event (Figs. 5.11 and 5.12). The intensities observed in ASK1 and hence the estimated flux (which depends on this parameter) were seen to be approximately 60 times greater for the 'closed' event compared to the 'open' event. These lower fluxes are consistent with the open field line theory as much less plasma is expected on open field lines. The energies of the two events are comparable, with mean values of 12.6 $\pm$ 0.9 keV estimated for the 'closed' case and 3.4 $\pm$ 0.1 keV estimated for the 'open' case. Carlson and Cowley [2005] state that any mechanism which drives shear flow across open field lines can accelerate polar rain and hence generate aurora on open field lines in the polar cap. They also estimate, for three sub-visual polar cap arcs (which refer to arcs lower than 1 kR, consistent with our 'open' observation), energies between 100-1000 eV which they state are consistent with Shinohara and Kokubun [1996] and Hardy [1984]. Therefore our mean value for the energy of the 'open' event from the ASK analysis is larger than previous reports. This will be further discussed below when we compare the ASK analysis to the DMSP particle data observations.

The structure of the arcs as they pass through ASK's small (6°) field of view during intervals from each event appeared to be quite different; the aurora in the 'closed' event (Fig. 5.4) was highly dynamic with lots of structure (especially on the edges of the arc), similar to structure observed within the main auroral oval (e.g. Dahlgren et al. [2010]). However, in the 'open' case it was hard to distinguish any clear features; this is may be due to the flux being so low that we had to use the averaged images and therefore any time-dependent features would be difficult to resolve.

Figures 5.15a and b show one minute of data from the SSJ/5 instrument when the DMSP spacecraft intersected the polar cap arcs for the 'closed' and 'open' events respectively;

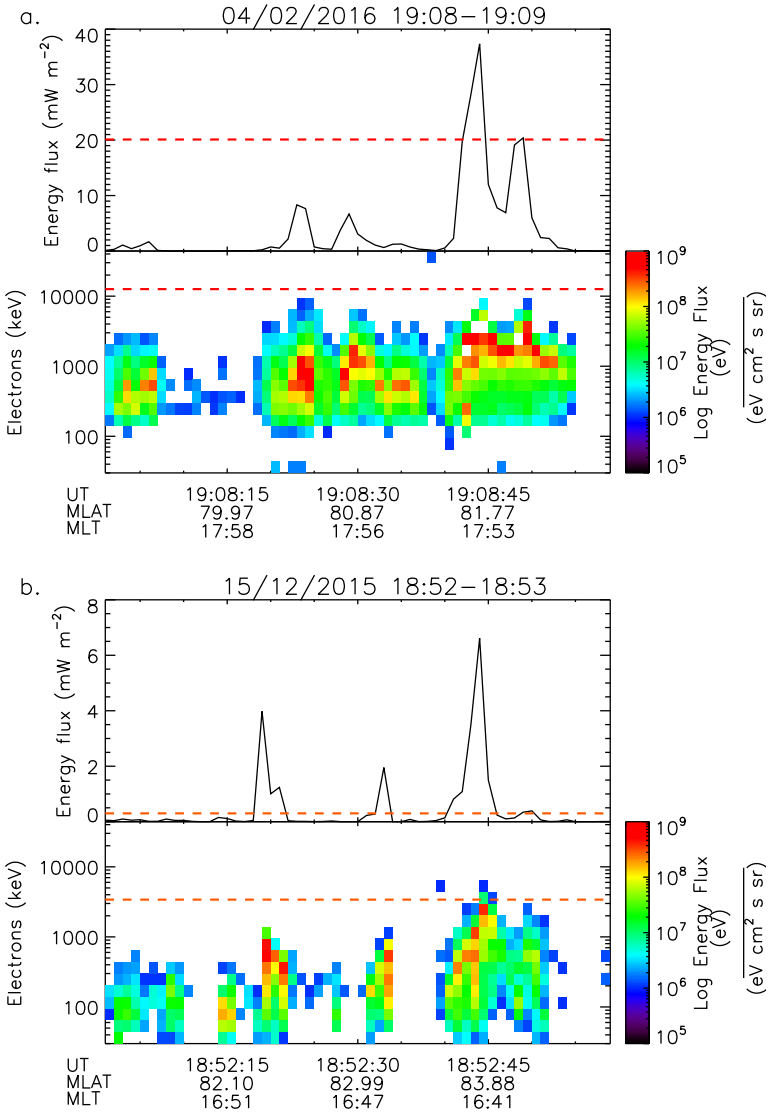

FIGURE 5.15: The summed energy flux (top panel) and corresponding electron spectrograms (bottom panel) for the 'closed' (a) and 'open' (b) events over one minute as the DMSP F19 and F17 spacecraft intersected the arcs respectively. The red and orange lines show the approximate energy flux and energy estimated using ground based techniques.

the top panel gives the integrated energy flux and the bottom panel shows the electron spectrogram. The red and orange lines plotted in the top and bottom panels of Fig. 5.15a and Fig. 5.15b give the mean energy flux and the mean energy estimated from the ASK instrument (Figs. 5.6 and 5.12) for the 'closed' and 'open' events respectively. It can be seen in the top panel of Fig. 5.15a, for the 'closed' event, that the mean energy flux estimated by ASK (20.1 mW m^{-2}) agrees well with the energy flux recorded by the DMSP spacecraft, despite the two values being determined at different times and locations in the polar cap (DMSP F19 is crossing the arc around 19:24 UT and the ASK

measurements are approximately at 18:49 UT; the DMSP spacecraft are orbiting closer to the dayside than Svalbard during this interval). In the top panel of Fig. 5.15b, for the 'open' event, it can be see than the energy flux measured by the DMSP spacecraft is approximately a factor of 10 greater than the mean energy flux estimated from the ASK analysis (0.3 mW m^{-2}). As discussed above these measurements are occurring at different times and hence there will be some discrepancies in the values; the DMSP satellite is passing over the arc at approximately 18:53:30 UT whereas the ASK observations are from 18:35:30 UT. However, the difference in energies can also be understood in terms of the spatial separation between the two observation points. The DMSP pass occurs on the dayside of the polar cap whereas Svalbard is located on the nightside during this interval; therefore a physical reason for the discrepancy in the observations could be due the noon-midnight gradient in the polar rain flux. This was first explicitly shown by Newell et al. [2009] and is due to the the kink in the open field lines as they cross the polar cap and enter the magnetotail. As discussed in Section 1.4.5, for particles to enter the ionosphere via these open field lines they have to have thermal speeds greater than the bulk plasma velocity, which is approximately the kink speed of the magnetic field lines. Fewer particles are able to enter the ionosphere as the field lines travel further downtail, which leads to a drop off in the polar rain flux across the polar cap. This gradient is consistent with our observations and could therefore explain the discrepancies between the DMSP and ASK observations for the 'open' event.

The energies plotted in the bottom panels of Figs. 5.6 and 5.12 represent the characteristic energy of the precipitation from a Gaussian distribution. The SSJ/5 spectrograms show the energy distributed over a log scale. It can be seen that the estimated energy for the 'open field line' event (Fig. 5.15b), despite being larger than previous estimates for polar rain arcs as discussed above, agrees well with the DMSP particle data. In the case of the 'closed field line' event (Fig. 5.15a) the energy estimate from the ground-based techniques is slightly larger than measurements from DMSP. This could be explained by considering the closed field line formation mechanism described in Milan et al. [2005]. As previously discussed, this mechanism is based on open field lines undergoing nightside reconnection during northward IMF and getting 'stuck' in the magnetotail. The DMSP observations are further sunward when considering the ionospheric footprint of the field line than the ASK observations (shown in Fig. 5.1), and hence we may expect the electrons to be on field lines which are more contracted than their counterpart footprints

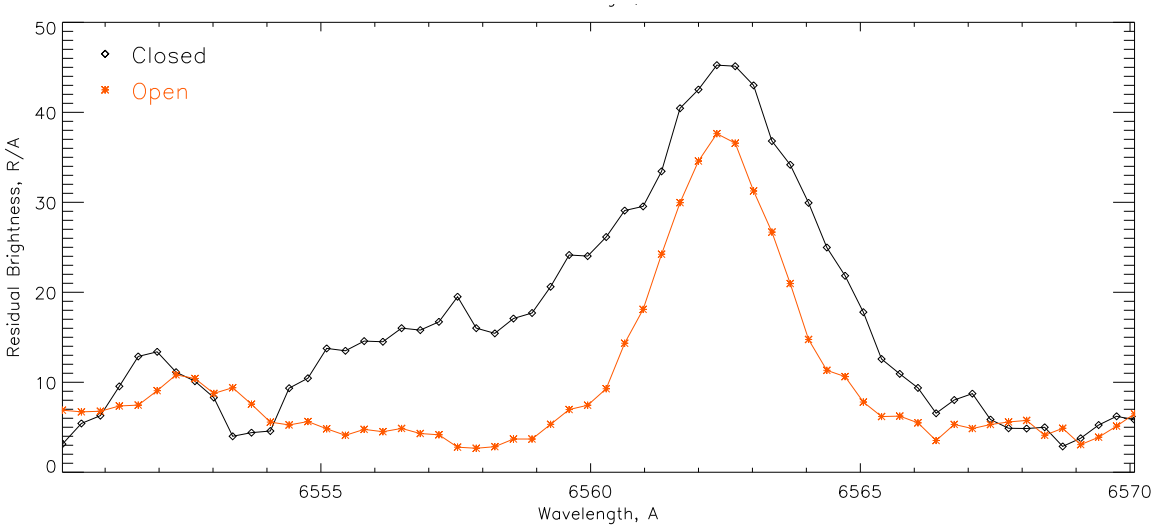

FIGURE 5.16: Residuals from the HITIES fit for the 'closed' (black) and 'open' (red) events.

closer to noon and hence have undergone more acceleration than electrons on field lines further sunwards. Hence this interpretation is consistent with our observations of higher energies estimated by ASK than DMSP for the 'closed' case.

Figure 5.16 shows the residual fit from the H-α panel of the HiTIES instrument, between 6550-6570 Å, from the data presented in Fig 5.7 and 5.13 for the 'closed' (black) and 'open' (red) events respectively. Here we have removed the non-H-α emissions to the best of our ability (using methods from Chadney and Whiter [2018] and Price et al. [2019]), and so what remains is our estimate for H-α. The H-α emission (at 656.3 nm) can be seen in both cases but the emission peak is clearly much wider in the closed case. Furthermore in the closed case, there is more broadening towards shorter wavelength, this indicative of a Doppler shifted blue wing generated by precipitating protons (e.g. Eather [1967]). The emission peak in the 'open' case does not exhibit this blue wing and hence we suggest that this emission is caused by dayglow (e.g. Weller et al. [1971]). These observations are consistent with the DMSP observations and hence show that the difference in the auroral precipitation used to identify the topology of the field lines on which the polar cap arcs are formed, can be verified using ground-based instrumentation.

SuperDARN map potential plots were shown in context with SSUSI observations during the 'open' event (Fig. 5.14); evidence of lobe reconnection was seen throughout the event. These data were initially investigated to try to find evidence of shear flows which could be accelerating polar rain and hence generating this arc. However, the ionospheric flows

associated with the lobe reconnection cell on the duskside were anti-clockwise which is not consistent with upward field aligned current or precipitating electrons [Chiu et al., 1985]. Furthermore, we note that scatter confirming the presence of this convection cell was only present sunward of the 'open' arc, and hence we have insufficient information on the presence or absence of shear flows at the location of the arc. We speculate that, if a shear flow does exist, rather than it being generated by opposing flow shears, as envisaged by Chiu et al. [1985], it is more likely to be excited by the gradient in the strength on the sunward flow generated by the lobe reconnection, due to the location of the sunward flow. We also noted that the sunward tips of both of the arcs observed in this event (the 'open' arc on the duskside discussed in this paper and the arc consistent with closed field lines on the dawnside), were aligned with the sunward flow channels generated with lobe reconnection, in agreement with Fear et al. [2015], as opposed to being centered between the opposing flow channels as suggested by Chiu et al. [1985].

5.3.1 Instrument contribution

In this study we have used data from multiple instruments that have different scale sizes, temporal resolution and taken the measurements from different locations.

As we have seen throughout this thesis, there is a big difference between the sensitivity of ground-based and space-craft auroral images. The polar cap arcs observed by the SSUSI instruments during both events presented here appear fairly similar in nature, whereas the ground-based observations from the Sony all sky camera and the ASK instrument are vastly different. The caveat to the ASK observations, as discussed above, is that the lack of structure observed for the 'open' event may be due to averaging of the weak emissions recorded.

Similar to Chapter 3, the multi-spectral ASK data is used to estimate the energy and energy flux of the precipitation during both events. As in Chapter 3, there was no ESR data available during these events with which to independently compare these estimates. We have therefore compared them to measurements from the SSJ/5 instrument on board the DMSP spacecraft. As stated above, these observations are coming from different positions in space (the DMSP spacecraft are crossing the polar cap further to the day-side, between 18-06 MLT, whereas ASK is situated on the nightside, around 21-22 MLT)

and at different times. The temporal resolution is also very different between the instrumentation with ASK measurements every 0.05 s, as opposed to to every minute from the SSJ/5 instrument. Despite these differences, as shown above, the ground-based and space-craft instrumentation show good agreement and any discrepancies can be explained by considering the nature of the magnetic field lines associated with each measurement.

SuperDARN data has been presented to investigate the possible source of shear flow in generating the 'open' event. Despite the lack of scatter around the polar cap arc itself, we suggest based on scatter that was recorded near the dayside tip of the arc, that there may be a gradient in the ionospheric flow which could provide the required downward current to generate the arc. However, contrary to the nightside polar cap flows presented in Chapter 3, the SuperDARN data originated from multiple radars with overlapping fields of view. Therefore, although the derived flow patterns are constrained by an empirical model, we have confidence that they reproduce the major aspects of the large-scale flow

HiTIES data was used to determine the presence (or lack) of proton precipitation from the ground. This analysis relies on the fitting of the H-alpha panel as described in Chadney and Whiter [2018] and Price et al. [2019] and is it possible that there are emissions missing from this fitting which then might contribute to the residuals presented in Fig. 5.16. However, from this figure a clear difference in the emissions between the two events can be seen, whereby a signature for proton precipitation is present in the data for the 'closed' event which is not seen in the 'open' event.

5.4 Conclusion

Two events containing polar cap arcs occurring over Svalbard have been investigated using both ground based and spacecraft instrumentation. Using the same criteria as discussed in Chapter 4, one event contains an arc occurring over Svalbard which is consistent with closed field lines (i.e. arcs associated with ion and electron precipitation were seen in both hemispheres); the other event contains an arc occurring over Svalbard which is consistent with formation on open field lines (i.e. the arc was associated with

electron-only precipitation). These arcs were analysed using ground based instrumentation including an all sky imager and a high resolution multi-spectral imager (ASK). The all sky images showed arcs passing through the field of view of ASK that were approximately aligned with the polar cap arcs seen by the UV imager on board DMSP (SSUSI).

The observations from ASK were combined with the Southampton Ionospheric model to gain estimates for the energy and the energy flux of the precipitation. These estimates were then compared with DMSP particle measurements. For the 'closed' event the ASK estimate of the energy flux (20.1 mW m^{-2}) agreed well with the DMSP measurements, although the energy estimate (12.6 $\pm$ 0.9 keV) was slightly higher. We explain this potential discrepancy by considering the formation of the plasma sheet such that field lines which are more contracted accelerate particles to higher energies. During this event, the DMSP observations are further sunward when considering the ionospheric footprint of the field lines than the field lines over Svalbard and hence we may expect higher energy precipitation above Svalbard. For the 'open' case, the energy estimates from ASK (mean value of 3.4 $\pm$ 0.1 keV) agreed well with the DMSP measurements but the energy flux estimate (0.3 mW m^{-2}) was less than that from DMSP by a factor of 10. We suggest that, assuming the source region of these arcs to be accelerated polar rain, the noon-midnight gradient of polar rain could explain these observations, such that higher fluxes would be expected further sunward (which is consistent with what we see). Furthermore, we have shown by comparing observations of the H-α emission for both events, that during the 'open' event the lack of ion precipitation can be measured from the ground.

These observations further the work presented in Chapters 3 and 4 by investigating polar cap arcs consistent with different magnetic topologies using ground-based observations. We found the fine-scale structure associated with these topologies to be very different, with the 'closed' event containing much more dynamic and structured aurora compared with the 'open' event. The differences in the fine-scale structure were consistent with expectations from the different topologies and could be linked to different formation mechanisms (for example, the tail reconnection mechanism suggested by Milan et al. [2005] and accelerated polar rain [Carlson and Cowley, 2005]) by comparing with spacecraft observations.

Key points:

- This chapter expands the knowledge of polar cap arcs by presenting the first observations of polar cap arcs on very small spatial scales (of the order of meters) and temporal resolution (millisecond) using the ASK instrument.
- The structure associated with arcs generated by different formation mechanisms is found to be very different and fits with expectations for the different magnetic field topologies, i.e. polar cap arcs on closed field lines are associated with dynamic structured aurora whereas arcs formed on open field lines were found to be associated with much lower fluxes and less structure.
- The criteria for identifying polar cap arcs occurring on different magnetic field topologies are tested using ground-based spectrograph data from the HiTIES instrument. During the event containing arcs consistent with closed field lines, a signature of proton precipitation was observed which was not present in the data during the 'open' event.
- The formation mechanisms of polar cap arcs occurring on open field line arcs have been investigated using measurements of the ionospheric flows associated with lobe reconnection using SuperDARN. A gradient in these flows is suggested to be a possible source of the shear flow which could result in downward current and acceleration of polar rain.

Chapter 6

Conclusion and further work

6.1 Conclusion

This thesis has investigated the formation of discrete aurora at high latitudes, inside the polar cap region. These arcs are known to be correlated with northward IMF and are generally sun-aligned in nature. As outlined in Section 1.5, there is some controversy in the formation mechanism of polar cap arcs, with some observations suggesting these arcs occur on open magnetic field lines, whilst others suggest that they form on closed field lines. It has been argued that more than one formation mechanism is needed to explain all the contrasting observations (e.g. Newell et al. [2009], discussed in Section 1.5.3.1). This idea has been investigated in this thesis using a multitude of ground-based and spacecraft instrumentation, which were introduced in Chapter 2.

In Chapter 3, we presented the first observations of polar cap arcs consistent with different topologies occurring at the same time. An event containing different auroral features on opposite sides of the northern hemisphere polar cap was identified using UV images from a low altitude spacecraft (SSUSI). An auroral protrusion to approximately 80° magnetic latitude was seen on the duskside of the northern hemisphere, occurring over Svalbard. A similar feature around the same magnetic local time was also seen in the southern hemisphere. The northern hemisphere feature was investigated using multiple ground-based instrumentation on Svalbard (including the ASK instrument and the ESR) and was found to be consistent with closed field lines. Furthermore, using SuperDARN data, this feature (termed a 'failed' transpolar arc, as it did not cross the entire polar

cap), was found to be associated with ionospheric flows consistent with nightside reconnection. It was hence suggested that this arc was formed by the mechanisms described by Milan et al. [2005] and that it 'failed' due to a southward turning of the IMF. On the dawnside of the northern hemisphere during this event, an arc with no clear counter part in the southern hemisphere was observed. This arc intersected the footprint of the DMSP spacecraft and the in-situ particle measurements showed it to be consistent with accelerated polar rain, formed on open field lines. This argument was strengthen by the IMF conditions which were favourable for polar rain on the dawnside of the northern hemisphere (polar rain preferences were discussed in section 1.4.5).

In Chapter 4, we continued to investigate polar cap arcs using data from low altitude DMSP spacecraft. We surveyed one month of data (December 2015) and found further examples of 'open' and 'closed' arcs, as well as some arcs that were not clearly consistent with either topology, including an example of a non-conjugate theta aurora. The in-situ particle measurements from the SSJ/5 instrument and the hemispheric nature determined from the SSUSI images were used to identify the topology of the arcs. Arcs associated with ion and electron precipitation, which were seen in both hemispheres, are considered to be consistent with formation on closed field lines. Arcs associated with electron-only signatures are consistent with formation on open field lines. Furthermore, we also looked into polar cap arc occurrence, finding that they were present in the SSUSI images at least 20% of the time. This value is between the 10% occurrence rate found using high altitude UV images [Kullen et al., 2002] and the 40% occurrence rate found using ground-based instrumentation [Valladares et al., 1994], suggesting that the SSUSI instruments are somewhat of an intermediary between the two.

The different formation mechanisms of polar cap arcs were further investigated in Chapter 5 using ground-based observations at high temporal and spatial resolution. We found polar cap arcs that are consistent with formation on closed field lines are highly dynamic and have complex structure (similar to the aurora seen on within the main auroral oval) whilst a polar cap arc consistent with open field lines was significantly lower in intensity and far less structure could be discerned.

Overall, we have contributed to the study of polar cap arcs by explicitly showing polar cap arcs consistent with different topologies exist, and that these mechanisms can occur simultaneously. This is something which has not previously been possible using the same

data set. Furthermore, we have presented the first small scale observations of polar cap arcs using the Auroral Structure and Kinetics instrument located on Svalbard. These observations offer a new perspective in polar cap arc study with observations with spatial scales of meters and temporal scales of 0.05 seconds.

6.2 Further work

There are several possible avenues to continue this work, for example there are still many open questions surrounding the 'non-conjugate' theta aurora and the arcs which form on open field lines. By finding more examples of these types of phenomena, plus further examples of closed field lines structures, we can start to build up a better idea of the configuration of the Earth's magnetosphere during northward IMF (which could eventually be fed into large scale MHD models). One avenue which could be explored, is to develop machine learning algorithms to automatically detect polar cap events in SSUSI images; this idea will be discussed in Section 6.2.1. Another area where more work could be done, as is evident from Appendix A, is to develop a more automatic method to identify the poleward boundary of the auroral oval during northward IMF; this will be discussed in Section 6.2.2. Lastly, there is more to do with the ASK instrument, in particular using its abilities to estimate the small scale electric fields associated with polar cap arcs, this will be outlined in Section 6.2.3.

6.2.1 Using machine learning to identify polar cap arcs

This thesis found polar cap arcs occur almost every day and are hence a regular feature of the polar cap rather than a rare phenomenon. These arcs are key to understanding the configuration of the magnetosphere during northward IMF (which occurs approximately half the time). As previously discussed, the SSUSI instruments on board the DMSP spacecraft have many strengths which are advantageous in polar cap arc studies. We have shown in this thesis that they are capable of imaging the fine-scale structure of polar cap arcs, which has perhaps been missed by the high latitude UV imagers (e.g. Section 4.4). The SSUSI images also offer more global coverage of the auroral oval than ground based imagers and they do not have clouds to contend with. Furthermore, the SSUSI instruments are on board DMSP spacecraft which have a relatively short orbital

period of around 90 minutes, plus there are multiple SSUSI instruments on board different DMSP spacecraft, providing an excellent opportunity for inter-hemispheric study; this is something which has previously been difficult to do. Additionally, the DMSP spacecraft provide in-situ particle measurements, through the SSJ/5 instruments, which have been shown to be invaluable in determining the characteristics of the particle precipitation.

Over approximately the last 15 years, the four SSUSI instruments have produced over 300,000 low-altitude UV images of the auroral region, which are waiting to be exploited. Assuming the occurrence rate found in Chapter 4 to be representative of all years, one could expect to find tens of thousands of images containing polar cap arcs. Therefore, given more time, a machine learning algorithm could be developed to automatically find these polar cap arcs in the SSUSI images. A reasonable starting point to this process would be adapting the 'off the shelf' method outlined in Clausen and Nickisch [2018], who used these algorithms to identify aurora in ground based images. The survey presented in Chapter 4, where approximately 1000 images containing polar cap arcs were visually identified out of approximately 10 000 SSUSI images, would provide a perfect training set. Once an automated detection method has been optimized, a large data base of polar cap arc events can be produced which will unlock the potential for multiple different case studies (which can be combined with a multitude of ground based and spacecraft instrumentation, such as ASK) and more statistical studies.

6.2.2 Developing automated auroral boundary detection during northward IMF conditions

As previously discussed, Newell et al. [1996a] developed an automated system for identifying the different regions of the auroral oval using particle data from the SSJ/4 spectrometers on board DMSP spacecraft; however these classifications do not work well during northward IMF. In Appendix A, an initial technique for using SSJ/5 data to find the poleward boundary of the auroral oval during northward IMF, based on similar methods as Newell et al. [1996a] and Milan et al. [2003], was outlined. However, the algorithm used in this method is only semi-automatic; it is constrained by the amount of variation in northward IMF auroral features and requires user intervention to be

effective. Therefore, improvements of this method are necessary and would provide interesting future work. It is important to be able to classify the poleward edge of the auroral oval as this leads to an estimate of the size of the polar cap and hence how much open flux is in the system. Tracking the amount of flux is one way of keeping track of the energy and flows which govern the configuration of the Earths magnetosphere during all periods of IMF.

Using SSUSI images in conjunction with the DMSP SSJ/5 particle data would be an excellent way to improve the identification of the poleward boundary of the auroral oval. Auroral boundary identification using a combination of near-simultaneous and near-continuous observations from UV images and particle data is something which is yet to be exploited.

6.2.3 Investigating electric fields surrounding different types of polar cap arcs using ASK

Another future work area that would be interesting would be to use the ASK instrument to quantify the electric field structures associated with the polar cap arcs formed on different magnetic field topologies. One of the things the ASK instrument was designed for was to trace plasma flows, which in turn can be used to estimate the electric field strength and direction to very good spacial and temporal resolution [Dahlgren et al., 2016]. The filter on the ASK2 camera is sensitive to emission from the $O^+(^2P)$ ion at 732.0 nm. This ion has a metastable life time of up to 5 seconds and hence the by tracking the after glow, an estimate of the flow velocity can be obtained. The emissions from ASK1 and ASK3 can be used to separate the motion of the source from the plasma motion. In the F-region, where $O^+(^2P)$ dominates, the neutral collision frequency is considered negligible and hence the bulk plasma velocity can be determined by the $E \times B$ drift. Therefore, by determining the plasma velocity, an estimate of the electric field can be made. Dahlgren et al. [2009] presented a study where they optically traced the motion after glow using the auroral brightness from the ASK cameras. From this, and using the International Geomagnetic reference field model to obtain a value for the magnetic field, they were able to estimate the electric fields associated with 4 different events. Another method, outlined by Tuttle et al. [2014], uses modelled images of the

O^+ to extract the flow velocity by finding the velocity which minimizes the difference between the modelled and observed images.

Once a list of polar cap arc events have been identified as detailed above, finding suitable events for such a study will be easy, not to mention exploring the events already outlined in this thesis.

Appendix A

Identification of the poleward boundary of the auroral oval

This appendix, which was published as supplementary material to Reidy et al. [2018], presents the method used to identify the poleward boundary of the auroral oval used in chapter 4. All figures presented here show the DMSP SSJ/5 particle data corresponding to the data given for each event in the paper and are all of the same format. For each event we plot four panels (numbered 1-4 from top to bottom). The electron and ion spectrograms are given as before (panels 1 and 3 respectively) with the summed fluxes of the electrons and ions given underneath (panels 2 and 4 respectively). The flux summed above 3 keV, used to define the poleward boundary of the auroral oval, is shown in black. The flux summed above 1 keV, used to identify the particle signatures of the polar cap arcs, is shown in blue.

A.1 Identification of poleward edge of auroral oval

The poleward edge of the auroral oval is conceptually defined to be where the precipitating particles drop by a factor of 4 over a short distance [Newell et al., 1996a]. Milan et al. [2003] a similar method stating that they search for a significant drop in the energy flux of high energy (>keV) particles. We have used a similar method during this study to identify the poleward boundary in a semi-automatic way. The energy fluxes of both the ions and electrons are summed above 3 keV to evaluate the high energy

component of the precipitation (black line on panels 2 and 4 of all figures). The dashed lines mark the maximum flux on each side of the auroral oval (black for electrons, grey for ions), which is a point within the auroral oval. For some events this could not be done automatically as the polar cap arc was brighter than the auroral oval and hence an additional criterion was used to limit the search to fluxes below a certain magnetic latitude, i.e. equatorward of the polar cap arc signature. The poleward edges of the oval are then found to be where this summed flux drops by a significant level.

For most of the events a drop of a factor of 1.5 was required, but this value was adapted in some cases based on comparison with the SSUSI images and hence this method is only semi-automatic. 14 out of the 21 events required a different level for the significant drop, detailed in Table A1. No obvious dependence on the spacecraft, hemisphere or side of the polar cap can be discerned to explain these amendments but in all cases a significant drop in the high energy flux is found with reasonable correspondence to the SSUSI images. The poleward edges of the auroral oval identified by this method are indicated by black solid lines for electrons and grey solid lines for ions on all the figures.

A.2 Identification of ion/electron signatures of polar cap arcs

The high energy electron and ion signatures of the polar cap arcs discussed in the paper were identified using the energy flux summed above 1keV, shown by the blue lines in panels 2 and 4 of the figures. Ion signatures were identified by clear peaks in both the electrons and ions above a certain threshold and hence, although we refer to arcs with an ion signature we technically mean an ion and electron signature. We require an electron and an ion signature to avoid classifying cusp precipitation as polar cap arcs, which may contain lower energy precipitating ions. In some cases this requirement results in a thinner ion signature detection than may be apparent from the summed ion fluxes in panel 4 as the ion and electron fluxes are not always exactly co-located. For example in the northern hemisphere of Event 3 (Figure A.1), around 23:37 UT, the ion and electron signatures only overlap for a short period making the detected ion signature appear thinner than the width of the ion flux above the threshold. Despite this requirement, in most cases, the ion and electron signatures are well aligned with the polar cap arcs in

the SSUSI images. The electron-only signatures were similarly defined to be where the electron flux went above a certain threshold but in this case we required the summed ion flux to be below a certain threshold. Furthermore, both the ion (and electron) and the electron-only signatures were only searched for within the polar cap region defined by the poleward boundary of the ions using the method described above. To account for some error in the estimation of this boundary, plasma signatures detected had to be at least 1° in magnetic latitude away from these boundaries.

Thresholds of 1x10^6 eV (eV cm^2 s sr)$^{-1}$ for ions and 1x10^7 eV (eV cm^2 s sr)$^{-1}$ for electrons were used in most cases. In five of the events, detailed in Table S1, these thresholds were adapted based on comparison with the SSUSI images, the particle spectrograms and the summed particle fluxes. In all five of these events the ion threshold was lowered to 5 x10^5 eV (eV cm^2 s sr)$^{-1}$ and in two of the events the electron boundary was lowered to either 1x10^6 eV (eV cm^2 s sr)$^{-1}$ or 5x10^6 eV (eV cm^2 s sr)$^{-1}$. These lower thresholds could not be applied to all other events without identifying noisy features that did not correspond to polar cap arcs. In the supplementary figures presented below, a red line is used to indicate the threshold of both the electrons and ions in panels 2 and 4, between the two grey lines which identify the poleward edge of the auroral oval ion precipitation.

TABLE A.1: Summary of the changes made to the default thresholds detailed in sections A.1 and A.2. This table indicates the values of the drop in electron and ion fluxes used to identify the poleward boundary of the auroral oval, the threshold used to identify the ion and electron signatures in the DMSP SSJ/5 particle data for each event discussed in the paper and the magnetic latitude threshold used in some cases to identify the auroral oval when the polar cap arc was brighter than the oval

Event number	Amendments
4	A drop of 1.3 in the ion flux is used to define the poleward edge of the dawnside oval in the southern hemisphere and the duskside oval in the northern hemisphere.
6	An ion threshold of 5x10^5 eV (eV cm^2 s sr)$^{-1}$ is used. A drop of 1.3 in the electron flux is used to define the poleward edge of the auroral oval on both sides of the polar cap in the southern hemisphere.
11	A drop of 2.5 in the electron flux and a drop of 1.2 in the ion flux is used to define the poleward edge of the auroral oval in the northern hemisphere on the dusk and dawn respectively.
12	A drop of 1.4 in the ions is used to define the poleward boundary on the dawnside of the northern hemisphere.
14	An ion threshold of 5x10^5 eV (eV cm^2 s sr)$^{-1}$ is used. A drop of 1.4 in the ions is used to define poleward boundary on the duskside of the northern hemisphere.
15	A drop of 1.4 in the ion flux is used to define the poleward boundary on the duskside of the northern and southern hemisphere.
23	A drop of 1.3 in the electron flux is used to define the poleward boundary on the dawnside of the northern hemisphere.
24	A drop of 1.4 in the electron flux was used to define the poleward boundary of the duskside in the northern and southern hemispheres. An ion drop of 1.3 was used for the dawnside of the southern hemisphere.
26	An ion threshold of 5 x10^5 eV (eV cm^2 s sr)$^{-1}$ was used. A drop of 1.4 and 1.3 in the ion flux was used to define the poleward boundary on the dawn and duskside of the southern hemisphere respectively.
30	A drop of 1.3 and 1.2 in the electron flux was used to define the poleward boundary on the dawnside of the southern and northern hemispheres respectively.
31	A drop of 1.2 in the ions was used to define the poleward boundary on the duskside of the southern hemisphere.
35	An ion threshold of 5 x10^5 eV (eV cm^2 s sr)$^{-1}$ and an electron threshold of 1x10^6 eV (eV cm^2 s sr)$^{-1}$ was used. A drop of 2.5 in the electron flux was used to define the poleward boundary on the dawnside of the southern hemisphere.
38	A drop of 1.1 and 1.3 in the ion flux was used to define the poleward boundary on the duskside of the northern and southern hemispheres respectively.
40	An ion threshold of 5 x10^5 eV (eV cm^2 s sr)$^{-1}$ an electron threshold of 5 x10^6 eV (eV cm^2 s sr)$^{-1}$ was used.
43	A drop of 1.3 and 1.4 in the ion flux was used to define the poleward edge on the duskside of the northern and southern hemispheres respectively. A further drop of 1.4 in the electron flux was used to define the poleward edge on the dawnside of the northern hemisphere.

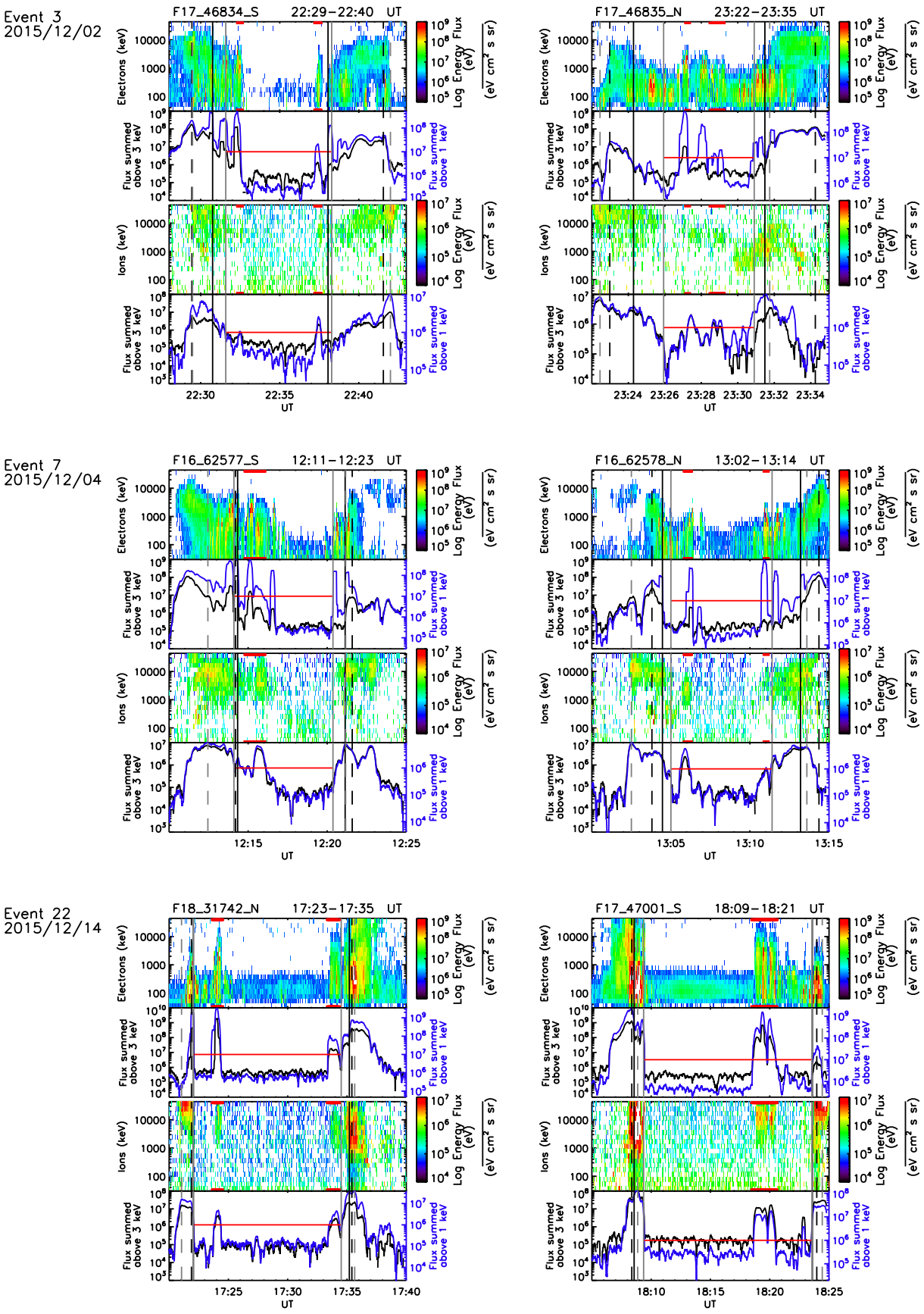

FIGURE A.1: DMSP SSJ/5 particle data for events containing a polar cap arc associated with ion precipitation in both hemisphere (corresponding to Figure 4.2). Dotted lines give the approx position of the auroral oval (highest flux on each side of polar cap), solid lines is estimated poleward boundary of the auroral oval, both lines are black for electrons grey for ions. Ion signatures are indicated in red, electron-only signatures in orange. Continued Overleaf.

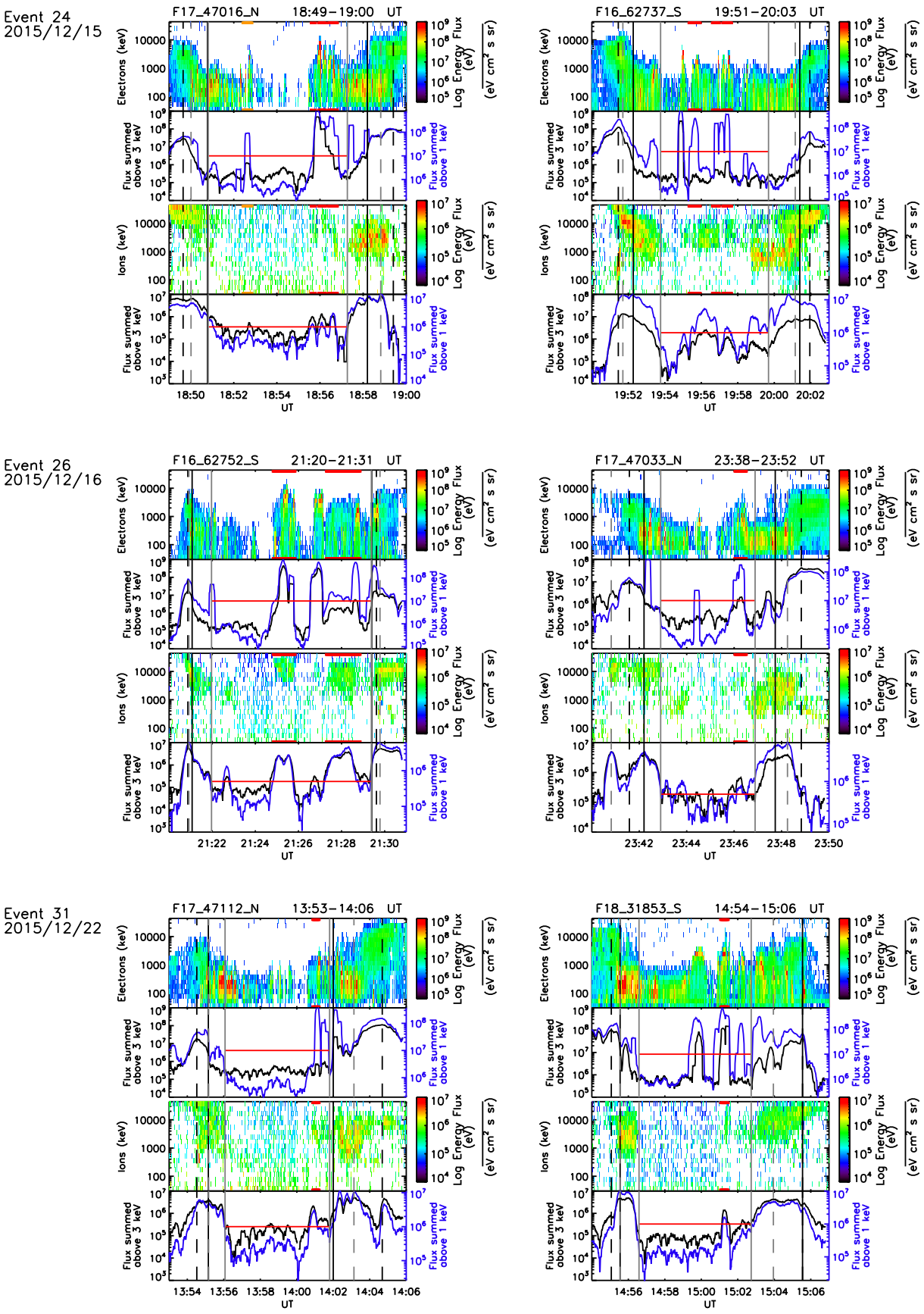

FIGURE A.1: Continued.

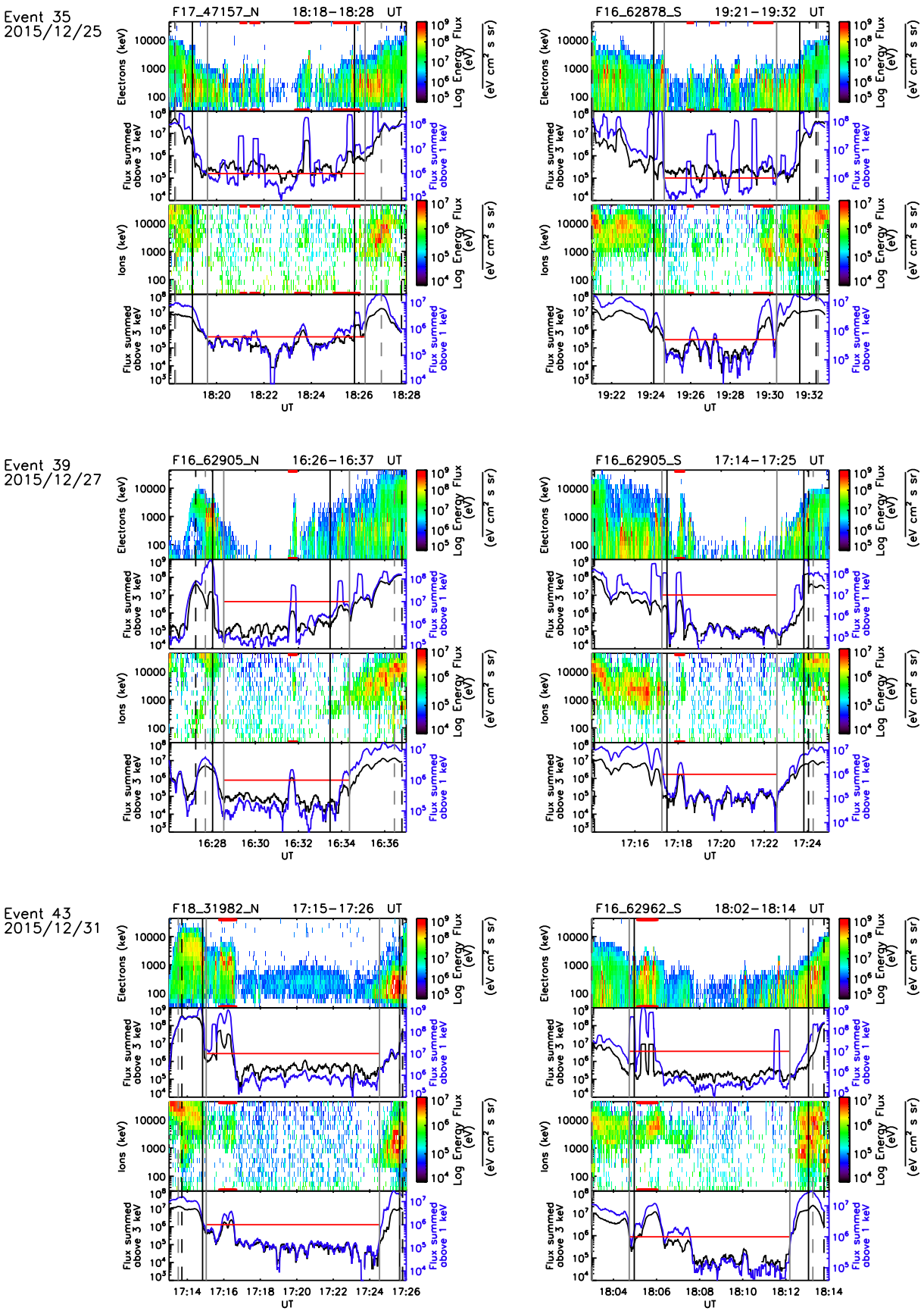

FIGURE A.1: Continued.

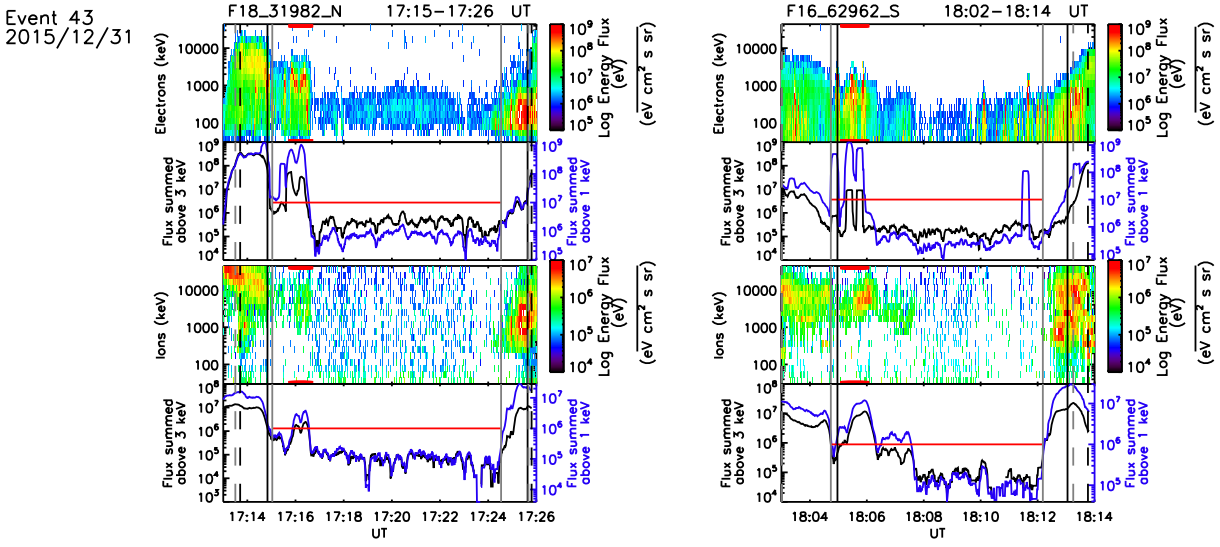

FIGURE A.2: DMSP SSJ/5 particle data for the northern hemisphere pass of Event 43. The F18 data is shown again for completeness (corresponding to Figure 4.3)

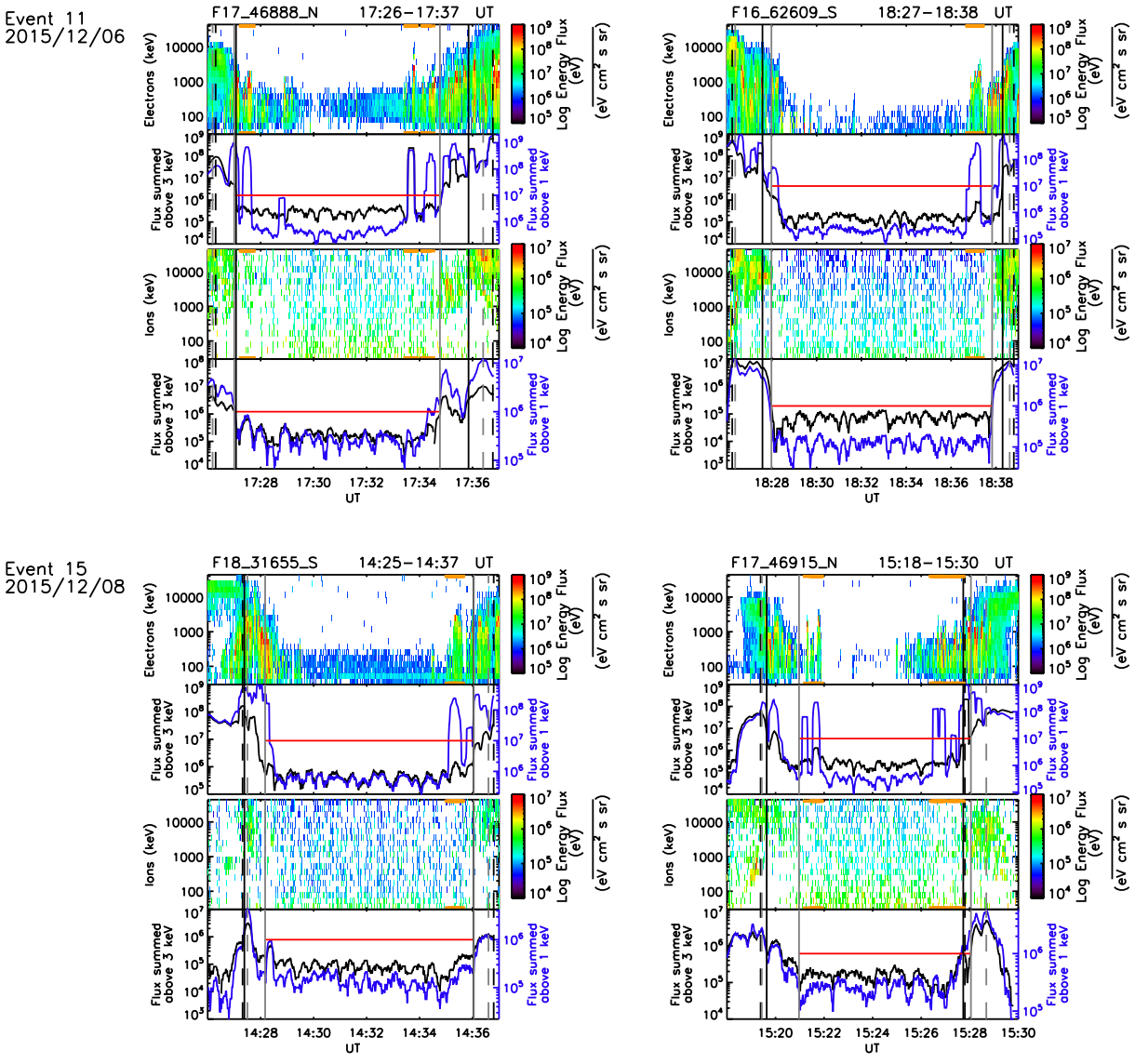

FIGURE A.3: DMSP SSJ/5 particle data corresponding to events identified as having an electron-only arc in both hemispheres (corresponding to Figure 4.6).

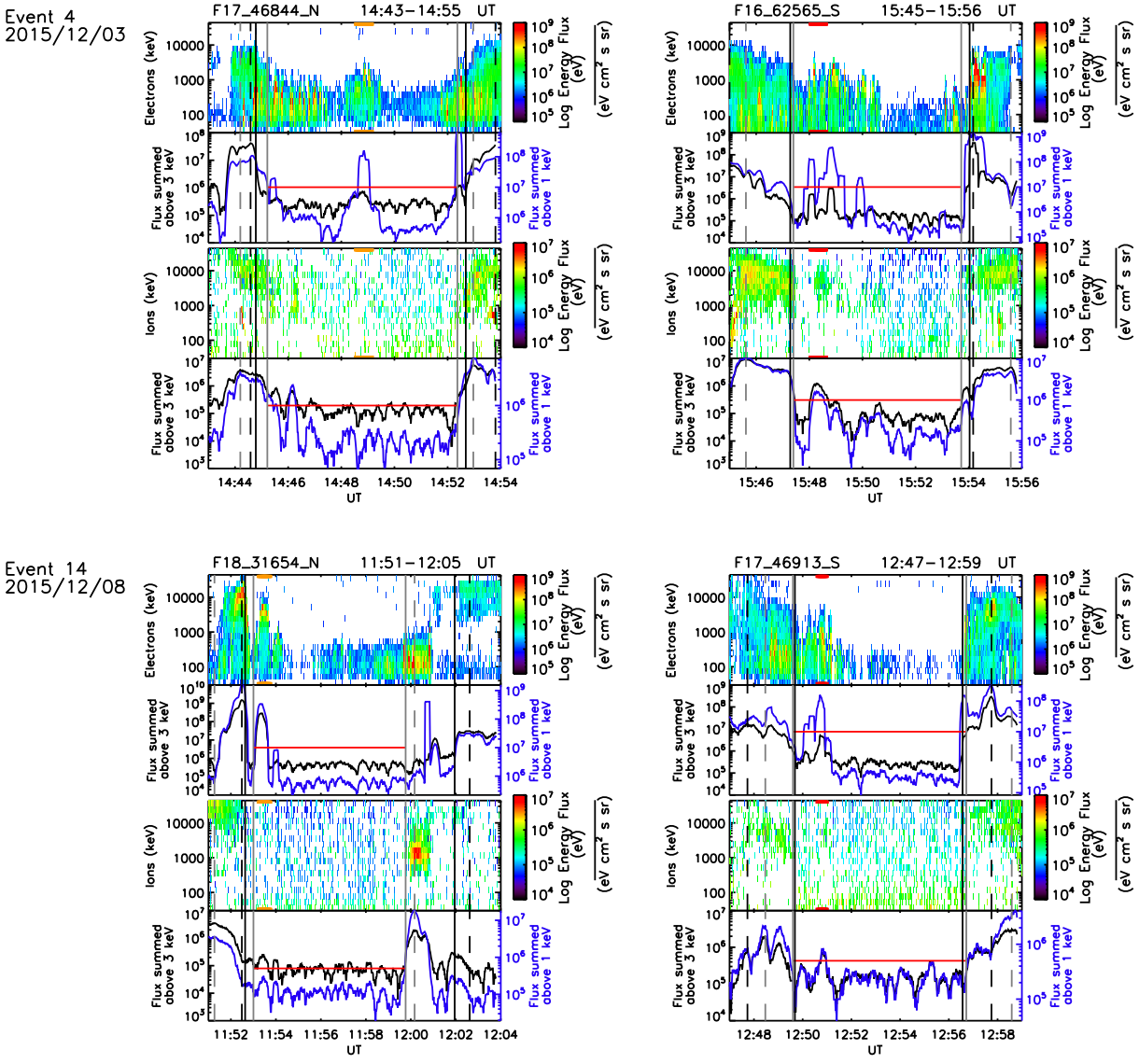

FIGURE A.4: DMSP SSJ/5 data for polar arcs with different plasma signatures in each hemisphere (corresponding to Figure 4.8).

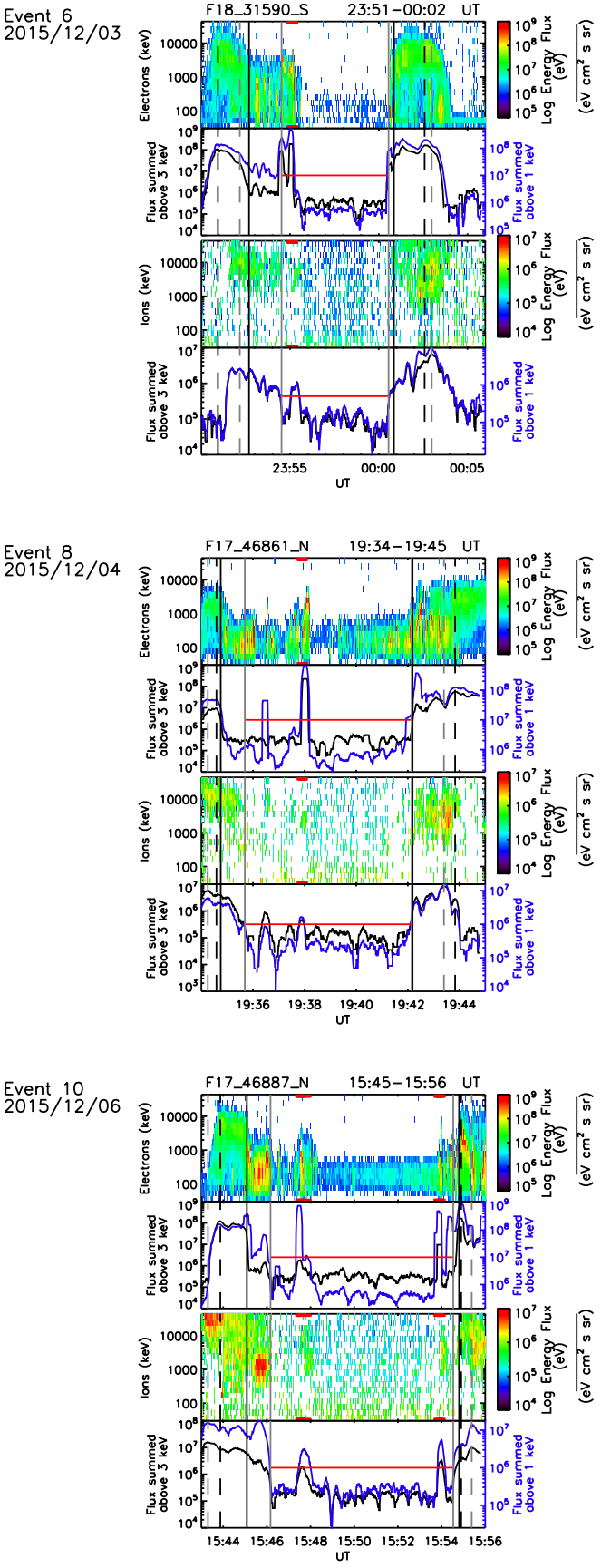

FIGURE A.5: DMSP SSJ/5 data for the polar cap arcs in one hemisphere, where no particle data were available from the other hemisphere as the DMSP spacecraft did not intersect the arc (corresponding to Figure 4.10). Continued overleaf.

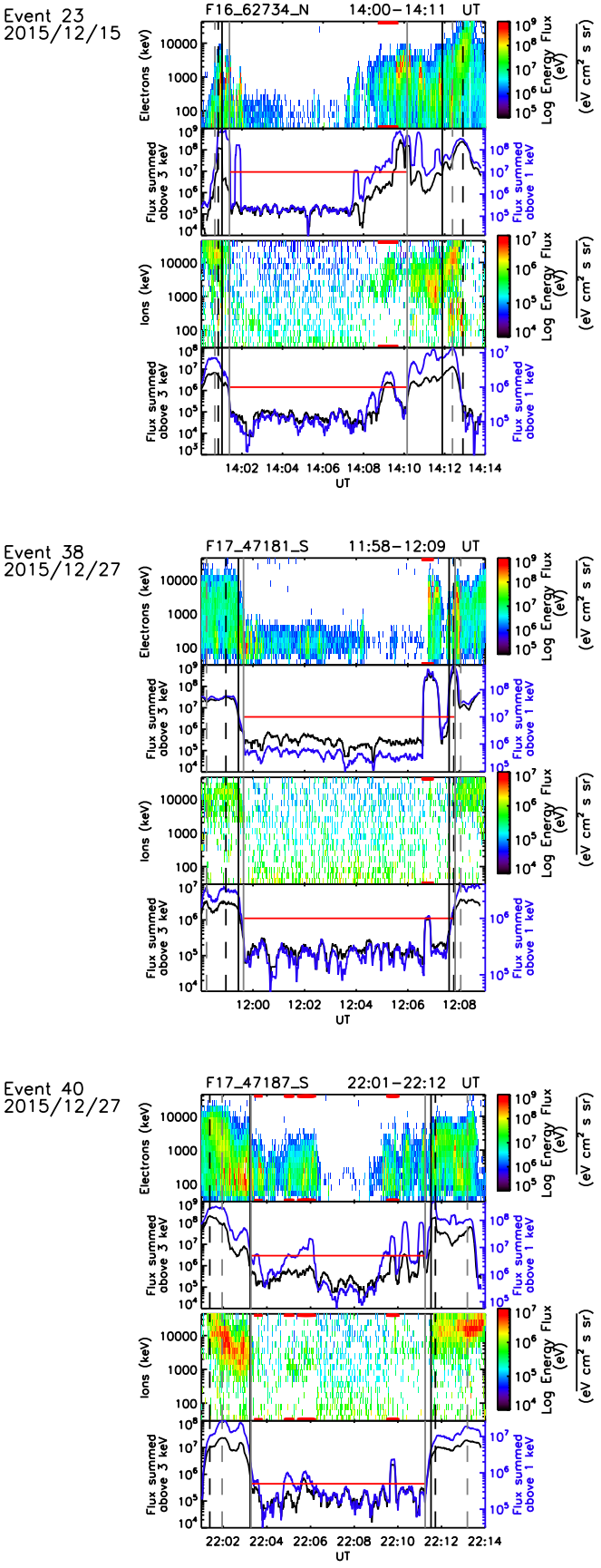

FIGURE A.5: Continued.

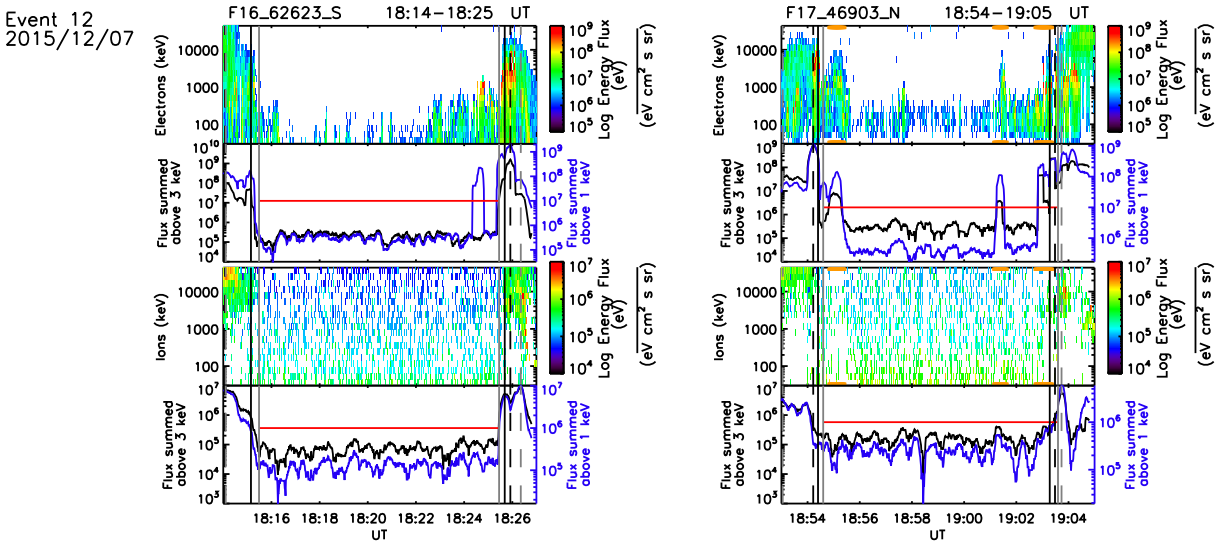

FIGURE A.6: DMSP SSJ/5 particle data for an event with a polar cap arc occurring in one hemisphere, associated with an electron-only plasma signature (corresponding to Figure 4.12).

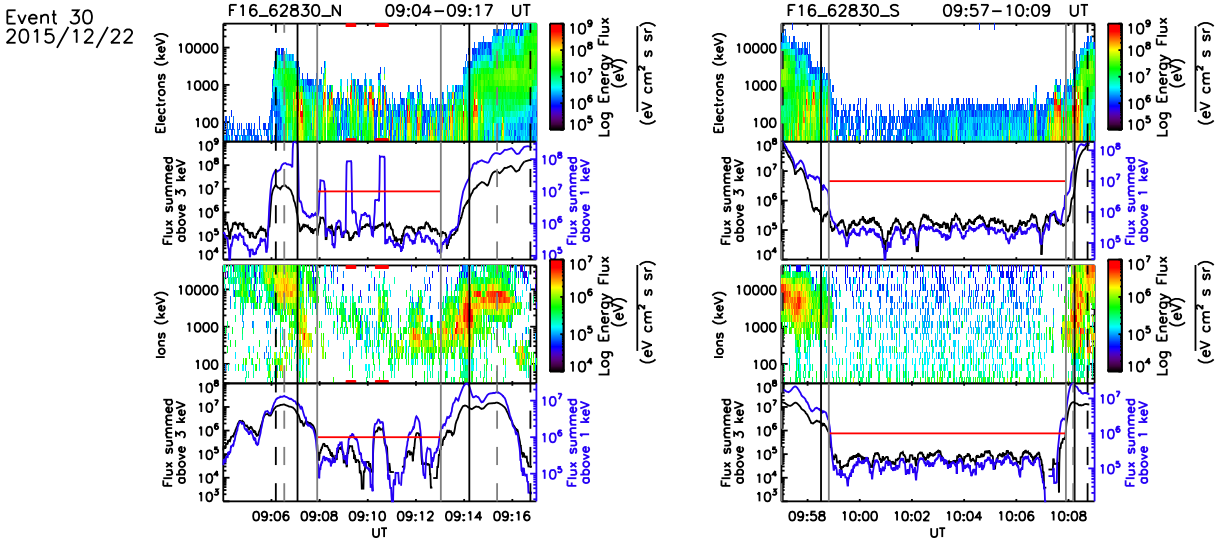

FIGURE A.7: DMSP SSJ/5 particle data for an event with a polar cap arc occurring in one hemisphere, associated with both an ion and electron signature (corresponding to Figure 4.14).

Bibliography

A. T. Aikio, T. Pitkänen, A. Kozlovsky, and O. Amm. Method to locate the polar cap boundary in the nightside ionosphere and application to a substorm event. *Annales Geophysicae*, 24:1905–1917, 2006. doi: 10.5194/angeo-24-1905-2006.

S.-I. Akasofu. The development of the auroral substorm. *Planet Space Scicence*, 12: 273–282, 1964. doi: 10.1016/0032-0633(64)90151-5.

S.-I. Akasofu. The Aurora and the magnetosphere: The Chapman memorial lecture. *Planetary Space Science*, 22:885–923, 1974. doi: 10.1016/0032-0633(74)90161-5.

Akasofu, S.-I. Physics of magnetospheric substorms. In *Astrophysics and Space Science Library*, volume 47, 1977. doi: 10.1007/978-94-010-1164-8.

B. J. Anderson, K. Takahashi, and B. A. Toth. Sensing global Birkeland currents with Iridium engineering magnetometer data. *Geophysical Research Letters*, 27(24):4045–4048, 2000. ISSN 1944-8007. doi: 10.1029/2000GL000094.

B. J. Anderson, H. Korth, C. L. Waters, D. L. Green, V. G. Merkin, R. J. Barnes, and L. P. Dyrud. Development of large-scale Birkeland currents determined from the Active Magnetosphere and Planetary Electrodynamics Response Experiment. *Geophysical Research Letters*, 41(9):3017–3025, 2014. ISSN 1944-8007. doi: 10.1002/2014GL059941.

V. Angelopoulos, J. P. McFadden, D. Larson, C. W. Carlson, S. B. Mende, H. Frey, T. Phan, D. G. Sibeck, K. Glassmeier, U. Auster, E. Donovan, I. R. Mann, I. J Rae, C. T. Russell, A. Runov, X. Zhou, and L. Kepko. Tail reconnection triggering substorm onset. *Science*, 321(5891):931–935, 2008. doi: 10.1126/science.1160495.

M. Ashrafi. ASK: Auroral Structure and Kinetics in action. *Astronomy and Geophysics*, 48(4):4.35–4.37, 2007. doi: 10.1111/j.1468-4004.2007.48435.x.

M. Ashrafi, B. S. Lanchester, D Lummerzheim, N. Ivchenko, and O. Jokiaho. Modelling of $N_2$1P emission rates in aurora using various cross sections for excitation. *Annales Geophysicae*, 27:25452553, 2009.

H. U. Auster, K. H. Glassmeier, W. Magnes, O. Aydogar, W. Baumjohann, D. Constantinescu, D. Fischer, K. H. Fornacon, E. Georgescu, P. Harvey, O. Hillenmaier, R. Kroth, M. Ludlam, Y. Narita, R. Nakamura, K. Okrafka, F. Plaschke, I. Richter, H. Schwarzl, B. Stoll, A. Valavanoglou, and M. Wiedemann. The THEMIS Fluxgate Magnetometer. *Space Science Reviews*, 141:235–264, 2008. doi: 10.1007/s11214-008-9365-9.

D. N. Baker, S. J. Bame, W. C. Feldman, J. T. Gosling, R. D. Zwickl, J. A. Slavin, and E. J. Smith. Strong electron bidirectional anisotropies in the distant tail - ISEE 3 observations of polar rain. *Journal of Geophysical Research*, 91:5637–5662, 1986. doi: 10.1029/JA091iA05p05637.

A. Balogh, C. M. Carr, M. H. Acuña, M. W. Dunlop, T. J. Beek, P. Brown, K.-H. Fornaçon, E. Georgescu, K.-H. Glassmeier, J. Harris, G. Musmann, T. Oddy, and K. Schwingenschuh. The Cluster Magnetic Field Investigation: overview of in-flight performance and initial results. *Annales Geophysicae*, 19:1207–1217, 2001. doi: 10.5194/angeo-19-1207-2001.

C. N. Banwell. *Fundamentals of Molecular & Spectroscopy.* McGraw-Hill Education (India) Pvt Limited, 1994. ISBN 9780074620250.

W. Baumjohann and R. A. Treumann. *Basic space plasma physics.* London: Imperial College Press, —c1996, 1996. doi: 10.1142/p015.

F. T. Berkey, L. L. Cogger, S. Ismail, and Y. Kamide. Evidence for a correlation between sun-aligned arcs and the interplanetary magnetic field direction. *Geophysical Research Letters*, 3:145–147, 1976. doi: 10.1029/GL003i003p00145.

K. Birkeland. volume 1. H. Aschelhoug & Co., Christiania, Norway, 1908.

K. Birkeland. volume 2. H. Aschelhoug & Co., Christiania, Norway, 1913.

S. D. Browett, R. C. Fear, A. Grocott, and S. E. Milan. Timescales for the penetration of IMF B_Y into the Earth's magnetotail. *Journal of Geophysical Research*, 2016. doi: 10.1002/2016JA023198.

J. L. Burch, R. B. Torbert, T. D. Phan, L.-J. Chen, T. E. Moore, R. E. Ergun, J. P. Eastwood, D. J. Gershman, P. A. Cassak, M. R. Argall, S. Wang, M. Hesse, C. J. Pollock, B. L. Giles, R. Nakamura, B. H. Mauk, S. A. Fuselier, C. T. Russell, R. J. Strangeway, J. F. Drake, M. A. Shay, Y. V. Khotyaintsev, P.-A. Lindqvist, G. Marklund, F. D. Wilder, D. T. Young, K. Torkar, J. Goldstein, J. C. Dorelli, L. A. Avanov, M. Oka, D. N. Baker, A. N. Jaynes, K. A. Goodrich, I. J. Cohen, D. L. Turner, J. F. Fennell, J. B. Blake, J. Clemmons, M. Goldman, D. Newman, S. M. Petrinec, K. J. Trattner, B. Lavraud, P. H. Reiff, W. Baumjohann, W. Magnes, M. Steller, W. Lewis, Y. Saito, V. Coffey, and M. Chandler. Electron-scale measurements of magnetic reconnection in space. *Science*, 352:aaf2939, 2016. doi: 10.1126/science.aaf2939.

H. C. Carlson and S. W. H. Cowley. Accelerated polar rain electrons as the source of Sun-aligned arcs in the polar cap during northward interplanetary magnetic field conditions. *Journal of Geophysical Research*, 110:A05302, 2005. doi: 10.1029/2004JA010669.

H. C. Carlson, R. A. Heelis, E. J. Weber, and J. R. Sharber. Coherent mesoscale convection patterns during northward interplanetary magnetic field. *Journal of Geophysical Research*, 93:14501–14514, 1988. doi: 10.1029/JA093iA12p14501.

J. A. Carter, S. E. Milan, R. C. Fear, A. Kullen, and M. R. Hairston. Dayside reconnection under interplanetary magnetic field B_y-dominated conditions: The formation and movement of bending arcs. *Journal of Geophysical Research*, 120:2967–2978, 2015. doi: 10.1002/2014JA020809.

J. A. Carter, S. E. Milan, R. C. Fear, M.-T. Walach, Z. A. Harrison, L. J. Paxton, and B. Hubert. Transpolar arcs observed simultaneously in both hemispheres. *Journal of Geophysical Research*, 122(6):6107–6120, 2017. doi: 10.1002/2016JA023830. 2016JA023830.

N. A. Case and J. A. Wild. A statistical comparison of solar wind propagation delays derived from multispacecraft techniques. *Journal of Geophysical Research (Space Physics)*, 117:A02101, 2012. doi: 10.1029/2011JA016946.

J. M. Chadney and D. K. Whiter. Neutral temperature and atmospheric water vapour retrieval from spectral fitting of auroral and airglow emissions. *Geoscientific Instrumentation, Methods and Data Systems*, 7(4):317–329, 2018. doi: 10.5194/gi-7-317-2018.

S. Chakrabarti, D. Pallamraju, J. Baumgardner, and J. Vaillancourt. HiTIES: A high throughput imaging echelle spectrograph for ground-based visible airglow and auroral studies. *Journal of Geophysical Research*, 106:30337–30348, 2001. doi: 10.1029/2001JA001105.

S.-W. Chang, J. D. Scudder, J. B. Sigwarth, L. A. Frank, N. C. Maynard, W. J. Burke, W. K. Peterson, E. G. Shelley, R. Friedel, J. B. Blake, R. A. Greenwald, R. P. Lepping, G. J. Sofko, J.-P. Villain, and M. Lester. A comparison of a model for the theta aurora with observations from Polar, Wind, and SuperDARN. *Journal of Geophysical Research*, 103:17367–17390, 1998. doi: 10.1029/97JA02255.

S. Chapman and V. C. A. Ferraro. A New Theory of Magnetic Storms. *Nature*, 126: 129–130, 1930. doi: 10.1038/126129a0.

C. C. Chaston, L. M. Peticolas, J. W. Bonnell, C. W. Carlson, R. E. Ergun, J. P. McFadden, and R. J. Strangeway. Width and brightness of auroral arcs driven by inertial Alfven waves. *Journal of Geophysical Research (Space Physics)*, 108:1091, 2003. doi: 10.1029/2001JA007537.

C. C. Chaston, C. W. Carlson, J. P. McFadden, R. E. Ergun, and R. J. Strangeway. How important are dispersive Alfvén waves for auroral particle acceleration? *Geophysical Research Letters*, 34:L07101, 2007. doi: 10.1029/2006GL029144.

G. Chisham, M. Lester, S. E. Milan, M. P. Freeman, W. A. Bristow, A. Grocott, K. A. McWilliams, J. M. Ruohoniemi, T. K. Yeoman, P. L. Dyson, R. A. Greenwald, T. Kikuchi, M. Pinnock, J. P. S. Rash, N. Sato, G. J. Sofko, J.-P. Villain, and A. D. M. Walker. A decade of the Super Dual Auroral Radar Network (SuperDARN): scientific achievements, new techniques and future directions. *Surveys in Geophysics*, 28:33–109, 2007. doi: 10.1007/s10712-007-9017-8.

Y. T. Chiu, N. U. Crooker, and D. J. Gorney. Model of oval and polar cap arc configurations. *Journal of Geophysical Research*, 90:5153–5157, 1985. doi: 10.1029/JA090iA06p05153.

A. B. Christensen, L. J. Paxton, S. Avery, J. Craven, G. Crowley, D. C. Humm, H. Kil, R. R. Meier, C.-I. Meng, D. Morrison, B. S. Ogorzalek, P. Straus, D. J. Strickland, R. M. Swenson, R. L. Walterscheid, B. Wolven, and Y. Zhang. Initial observations with

the Global Ultraviolet Imager (GUVI) in the NASA TIMED satellite mission. *Journal of Geophysical Research (Space Physics)*, 108:1451, 2003. doi: 10.1029/2003JA009918.

L. B. N. Clausen and H. Nickisch. Automatic Classification of Auroral Images From the Oslo Auroral THEMIS (OATH) Data Set Using Machine Learning. *Journal of Geophysical Research (Space Physics)*, 123:5640–5647, 2018. doi: 10.1029/2018JA025274.

L. B. N. Clausen, J. B. H. Baker, J. M. Ruohoniemi, S. E. Milan, and B. J. Anderson. Dynamics of the region 1 Birkeland current oval derived from the Active Magnetosphere and Planetary Electrodynamics Response Experiment (AMPERE). *Journal of Geophysical Research (Space Physics)*, 117:A06233, 2012. doi: 10.1029/2012JA017666.

S. W. H. Cowley. Magnetospheric and ionospheric flow and the interplanetary magnetic field. In *AGARD The Phys. Basis of the Ionosphere in the Solar-Terrest. System 14 p (SEE N81-23507 14-42)*. Cowley, S. W. H., 1981.

S. W. H. Cowley. Magnetosphere-Ionosphere Interactions: A Tutorial Review. *Washington DC American Geophysical Union Geophysical Monograph Series*, 118:91, 2000. doi: 10.1029/GM118p0091.

S. W. H. Cowley and M. Lockwood. Excitation and decay of solar wind-driven flows in the magnetosphere-ionosphere system. *Annales Geophysicae*, 10:103–115, 1992.

J. C. Coxon, S. E. Milan, L. B. N. Clausen, B. J. Anderson, and H. Korth. The magnitudes of the regions 1 and 2 Birkeland currents observed by AMPERE and their role in solar wind-magnetosphere-ionosphere coupling. *Journal of Geophysical Research (Space Physics)*, 119:9804–9815, 2014a. doi: 10.1002/2014JA020138.

J. C. Coxon, S. E. Milan, L. B. N. Clausen, B. J. Anderson, and H. Korth. A superposed epoch analysis of the regions 1 and 2 Birkeland currents observed by AMPERE during substorms. *Journal of Geophysical Research (Space Physics)*, 119:9834–9846, 2014b. doi: 10.1002/2014JA020500.

J. C. Coxon, S. E. Milan, J. A. Carter, L. B. N. Clausen, B. J. Anderson, and H. Korth. Seasonal and diurnal variations in AMPERE observations of the Birkeland currents compared to modeled results. *Journal of Geophysical Research (Space Physics)*, 121: 4027–4040, 2016. doi: 10.1002/2015JA022050.

J. C. Coxon, S. E Milan, and B. J. Anderson. A Review of Birkeland Current Research Using AMPERE. In *Electric Currents in Geospace and Beyond*, Geophysical Monograph. America Geophysical Union, 2018. doi: 10.1002/9781119324522.ch16.

J. D. Craven, J. S. Murphree, L. L. Cogger, and L. A. Frank. Simultaneous optical observations of transpolar arcs in the two polar caps. *Geophysical Research Letters*, 18:2297–2300, 1991. doi: 10.1029/91GL02308.

J. A. Cumnock. High-latitude aurora during steady northward interplanetary magnetic field and changing IMF B_y. *Journal of Geophysical Research (Space Physics)*, 110: A02304, 2005. doi: 10.1029/2004JA010867.

J. A. Cumnock, L. G. Blomberg, A. Kullen, T. Karlsson, and K. Â. T. Sundberg. Small-scale characteristics of extremely high latitude aurora. *Annales Geophysicae*, 27:3335–3347, 2009. doi: 10.5194/angeo-27-3335-2009.

H. Dahlgren, N. Ivchenko, B. S. Lanchester, M. Ashrafi, D. Whiter, G. Marklund, and J. Sullivan. First direct optical observations of plasma flows using afterglow of O in discrete aurora. *Journal of Atmospheric and Solar-Terrestrial Physics*, 71:228–238, 2009. doi: 10.1016/j.jastp.2008.11.015.

H. Dahlgren, A. Aikio, K. Kaila, N. Ivchenko, B. S. Lanchester, D. K. Whiter, and G. T. Marklund. Simultaneous observations of small multi-scale structures in an auroral arc. *Journal of Atmospheric and Solar-Terrestrial Physics*, 72:633–637, 2010. doi: 10.1016/j.jastp.2010.01.014.

H. Dahlgren, B. Gustavsson, B. S. Lanchester, N. Ivchenko, U. Brändström, D. K. Whiter, T. Sergienko, I. Sandahl, and G. Marklund. Energy and flux variations across thin auroral arcs. *Annales Geophysicae*, 29:1699–1712, 2011. doi: 10.5194/angeo-29-1699-2011.

H. Dahlgren, B. S. Lanchester, N. Ivchenko, and D. K. Whiter. Electrodynamics and energy characteristics of aurora at high resolution by optical methods. *Journal of Geophysical Research*, 121:5966–5974, 2016. doi: 10.1002/2016JA022446.

I. Dandouras, A. Barthe, E. Penou, S. Brunato, H. Rème, L. M. Kistler, M. B. Bavassano-Cattaneo, and A. Blagau. Cluster Ion Spectrometry (CIS) Data in the Cluster Active Archive (CAA). *Astrophysics and Space Science Proceedings*, 11:51–72, 2010. doi: 10.1007/978-90-481-3499-1_3.

T. N. Davis. The Morphology of the Polar Aurora. *Journal of Geophysical Research*, 65:3497, 1960. doi: 10.1029/JZ065i010p03497.

T. N. Davis. The Morphology of the Auroral Displays of 1957-1958, 2, Detail Analyses of Alaska Data and Analyses of High-Latitude Data. *Journal of Geophysical Research*, 67:75–110, 1962. doi: 10.1029/JZ067i001p00075.

T. N. Davis. Negative Correlation between Polar-Cap Visual Aurora and Magnetic Activity. *Journal of Geophysical Research*, 68:4447, 1963.

T. N. Davis. Observed characteristics of auroral forms. *Space Science Review*, 22:77–113, 1978. doi: 10.1007/BF00215814.

J. W. Dungey. Interplanetary Magnetic Field and the Auroral Zones. *Physical Review Letters*, 6:47–48, 1961. doi: 10.1103/PhysRevLett.6.47.

J. W. Dungey. Interactions of solar plasma with the geomagnetic field. *Planetary and Space Science*, 10:233–237, 1963. doi: 10.1016/0032-0633(63)90020-5.

J. W. Dungey. The Length of the Magnetospheric Tail. *Journal of Geophysical Research*, 70:1753–1753, 1965. doi: 10.1029/JZ070i007p01753.

R. H. Eather. Auroral proton precipitation and hydrogen emissions. *Reviews of Geophysics*, 5(3):207–285, 1967. doi: 10.1029/RG005i003p00207.

S. Eriksson, J. B. H. Baker, S. M. Petrinec, H. Wang, F. J. Rich, M. Kuznetsova, M. W. Dunlop, H. Rème, R. A. Greenwald, H. U. Frey, H. Lühr, R. E. Ergun, A. Balogh, and C. W. Carlson. On the generation of enhanced sunward convection and transpolar aurora in the high-latitude ionosphere by magnetic merging. *Journal of Geophysical Research*, 110:A11218, 2005. doi: 10.1029/2005JA011149.

D. H. Fairfield and J. D. Scudder. Polar rain - Solar coronal electrons in the Earth's magnetosphere. *Journal of Geophysical Research*, 90:4055–4068, 1985. doi: 10.1029/JA090iA05p04055.

G. J. Fasel. Dayside poleward moving auroral forms: A statistical study. *Journal of Geophysical Research*, 100:11, 1995. doi: 10.1029/95JA00854.

R. C. Fear. The northward IMF magnetosphere in Magnetospheres in the Solar System. In H. Hasegawa R. Maggiolo, N. André and D. Welling, editors, *AGU Centennial monograph*. Wiley, in press, 2019.

R. C. Fear and S. E. Milan. The IMF dependence of the local time of transpolar arcs: Implications for formation mechanism. *Journal of Geophysical Research*, 117:A03213, 2012a. doi: 10.1029/2011JA017209.

R. C. Fear and S. E. Milan. Ionospheric flows relating to transpolar arc formation. *Journal of Geophysical Research*, 117:A09230, 2012b. doi: 10.1029/2012JA017830.

R. C. Fear, S. E. Milan, R. Maggiolo, A. N. Fazakerley, I. Dandouras, and S. B. Mende. Direct observation of closed magnetic flux trapped in the high-latitude magnetosphere. *Science*, 346:1506–1510, 2014. doi: 10.1126/science.1257377.

R. C. Fear, S. E. Milan, J. A. Carter, and R. Maggiolo. The interaction between transpolar arcs and cusp spots. *Geophysical Research Letters*, 42:9685–9693, 2015. doi: 10.1002/2015GL066194.

L. A. Frank and J. D. Craven. Imaging results from Dynamics Explorer 1. *Reviews of Geophysics*, 26:249–283, 1988. doi: 10.1029/RG026i002p00249.

L. A. Frank, J. D. Craven, J. L. Burch, and J. D. Winningham. Polar views of the Earth's aurora with Dynamics Explorer. *Geophysical Research Letters*, 9:1001–1004, 1982. doi: 10.1029/GL009i009p01001.

L. A. Frank, J. D. Craven, and R. L. Rairden. Images of the Earth's aurora and geocorona from the Dynamics Explorer mission. *Advances in Space Research*, 5:53–68, 1985. doi: 10.1016/0273-1177(85)90116-4.

L. A. Frank, J. D. Craven, D. A. Gurnett, S. D. Shawhan, J. L. Burch, J. D. Winningham, C. R. Chappell, J. H. Waite, N. C. Maynard, and M. Sugiura. The theta aurora. *Journal of Geophysical Research*, 91:3177–3224, 1986. doi: 10.1029/JA091iA03p03177.

A. C. Fraser-Smith. Spectrum of the geomagnetic activity index Ap. *Journal of Geophysical Research*, 77:4209, 1972. doi: 10.1029/JA077i022p04209.

H. U. Frey, S. B. Mende, S. A. Fuselier, T. J. Immel, and N. Østgaard. Proton aurora in the cusp during southward IMF. *Journal of Geophysical Research (Space Physics)*, 108:1277, 2003. doi: 10.1029/2003JA009861.

M. Galand, J. Baumgardner, D. Pallamraju, S. Chakrabarti, U. P. Løvhaug, D. Lummerzheim, B. S. Lanchester, and M. H. Rees. Spectral imaging of proton aurora and

twilight at Tromsø, Norway. *Journal of Geophysical Research (Space Physics)*, 109: A07305, 2004. doi: 10.1029/2003JA010033.

J. M. Gloag, E. A. Lucek, L.-N. Alconcel, A. Balogh, P. Brown, C. M. Carr, C. N. Dunford, T. Oddy, and J. Soucek. FGM Data Products in the CAA. *Astrophysics and Space Science Proceedings*, 11:109–128, 2010. doi: 10.1007/978-90-481-3499-1_7.

A. Goudarzi, M. Lester, S. E. Milan, and H. U. Frey. Multi-instrumentation observations of a transpolar arc in the northern hemisphere. *Annales Geophysicae*, 26:201–210, 2008. doi: 10.5194/angeo-26-201-2008.

R. A. Greenwald, K. B. Baker, J. R. Dudeney, M. Pinnock, T. B. Jones, E. C. Thomas, J.-P. Villain, J.-C. Cerisier, C. Senior, C. Hanuise, R. D. Hunsucker, G. Sofko, J. Koehler, E. Nielsen, R. Pellinen, A. D. M. Walker, N. Sato, and H. Yamagishi. Darn/Superdarn: A Global View of the Dynamics of High-Latitude Convection. *Space Science Review*, 71:761–796, 1995. doi: 10.1007/BF00751350.

A. Grocott. Dawn-dusk asymmetries in planetary plasma environment. In *Time-dependence of dawn-dusk asymmetries in the terrestrial ionospheric convection pattern*, Geophysical Monograph. American Geophysical Union, 2017. doi: 10.1002/9781119216346.

A. Grocott, S. W. H. Cowley, and J. B. Sigwarth. Ionospheric flow during extended intervals of northward but B_y -dominated IMF. *Annales Geophysicae*, 21:509–538, 2003. doi: 10.5194/angeo-21-509-2003.

A. Grocott, T. K. Yeoman, S. E. Milan, O. Amm, H. U. Frey, L. Juusola, R. Nakamura, C. J. Owen, H. Rème, and T. Takada. Multi-scale observations of magnetotail flux transport during IMF-northward non-substorm intervals. *Annales Geophysicae*, 25: 1709–1720, 2007. doi: 10.5194/angeo-25-1709-2007.

M. G. Gusev and O. A. Troshichev. Hook-shaped arcs in dayside polar cap and their relation of the IMF. *Planetary Space Science*, 34:489–496, 1986. doi: 10.1016/0032-0633(86)90087-5.

M. S. Gussenhoven. Extremely high latitude auroras. *Journal of Geophysical Research*, 87:2401–2412, 1982. doi: 10.1029/JA087iA04p02401.

M. S. Gussenhoven and E. G. Mullen. Simultaneous relativistic electron and auroral particle access to the polar caps during interplanetary magnetic field B(z) northward - A scenario for an open field line source of auroral particles. *Journal of Geophysical Research*, 94:17121–17132, 1989. doi: 10.1029/JA094iA12p17121.

M. S. Gussenhoven, D. A. Hardy, N. Heinemann, and R. K. Burkhardt. Morphology of the polar rain. *Journal of Geophysical Research*, 89:9785–9800, 1984. doi: 10.1029/JA089iA11p09785.

G. Gustafsson. On the orientation of auroral arcs. *Planetary Space Science*, 15:277–294, 1967. doi: 10.1016/0032-0633(67)90195-X.

T. J. Hallinan and T. N. Davis. Small-scale auroral arc distortions. *Planetary Space Science*, 18:1735, 1970. doi: 10.1016/0032-0633(70)90007-3.

D. A. Hardy. Intense fluxes of low energy electrons at geomagnetic latitudes above 85. *Journal of Geophysical Research*, 89:3883–3892, 1984. doi: 10.1029/JA089iA06p03883.

D. A. Hardy, W. J. Burke, and M. S. Gussenhoven. DMSP optical and electron measurements in the vicinity of polar cap arcs. *Journal of Geophysical Research*, 87: 2413–2430, 1982. doi: 10.1029/JA087iA04p02413.

D. A. Hardy, M. S. Gussenhoven, K. Riehl, R. Burkhardt, and N. Heinemann. The characteristics of polar cap precipitation and their dependence on the interplanetary magnetic field and the solar wind. In Y. Kamide and J. A. Slavin, editors, *Solar Wind Magnetosphere Coupling*, volume 126 of *Astrophysics and Space Science Library*, pages 575–604, 1986. doi: 10.1007/978-90-277-2303-1_40.

D. A. Hardy, D. M. Walton, A. D. Johnstone, M. F. Smith, M. P. Gough, A. Huber, J. Pantazis, and R. Burkhardt. Low energy plasma analyzer. *IEEE Transactions on Nuclear Science*, 40(2):246–251, 1993. ISSN 0018-9499. doi: 10.1109/23.212349.

D. A. Hardy, E. G. Holeman, W. J. Burke, L. C. Gentile, and K. H. Bounar. Probability distributions of electron precipitation at high magnetic latitudes. *Journal of Geophysical Research (Space Physics)*, 113:A06305, 2008. doi: 10.1029/2007JA012746.

J. H. Hecht, A. B. Christensen, and J. B. Pranke. High-resolution auroral observations of the OI(7774) and OI(8446) multiplets. *Geophysical Research Letters*, 12:605–608, 1985. doi: 10.1029/GL012i009p00605.

A. E. Hedin. Extension of the MSIS thermosphere model into the middle and lower atmosphere. *Journal of Geophysical Research*, 96:1159–1172, 1991. doi: 10.1029/90JA02125.

R. A. Hoffman, R. A. Heelis, and J. S. Prasad. A sun-aligned arc observed by DMSP and AE-C. *Journal of Geophysical Research*, 90:9697–9710, 1985. doi: 10.1029/JA090iA10p09697.

K. Hosokawa, J. I. Moen, K. Shiokawa, and Y. Otsuka. Motion of polar cap arcs. *Journal of Geophysical Research*, 116:A01305, 2011. doi: 10.1029/2010JA015906.

C. Y. Huang, L. A. Frank, W. K. Peterson, W. Lennartsson, D. J. Williams, D. G. Mitchell, R. C. Elphic, and C. T. Russell. Filamentary structures in the magnetotail lobes. *Journal of Geophysical Research*, 92:2349–2363, 1987. doi: 10.1029/JA092iA03p02349.

C. Y. Huang, J. D. Craven, and L. A. Frank. Simultaneous observations of a theta aurora and associated magnetotail plasmas. *Journal of Geophysical Research*, 94:10137–10143, 1989. doi: 10.1029/JA094iA08p10137.

D. C. Humm, L. J. Paxton, A. B. Christensen, B. S. Ogorzalek, C. T. Pardoe, C.-I. Meng, D. Morrison, D. J. Strickland, J. S. Evans, M. B. Weiss, W. Crain, P. H. Lew, D. J. Mabry, J. O. Goldsten, S. A. Gary, K. Peacock, D. F. Persons, M. J. Harold, E. B. Alvarez, and C. J. Ercol. Design and performance of the Global Ultraviolet Imager (GUVI). In O. H. Siegmund and M. A. Gummin, editors, *EUV, X-Ray, and Gamma-Ray Instrumentation for Astronomy IX*, volume 3445, pages 2–12, 1998. doi: 10.1117/12.330325.

T. Iijima and T. A. Potemra. The amplitude distribution of field-aligned currents at northern high latitudes observed by Triad. *Journal of Geophysical Research*, 81:2165–2174, 1976a. doi: 10.1029/JA081i013p02165.

T. Iijima and T. A. Potemra. Field-aligned currents in the dayside cusp observed by Triad. *Journal of Geophysical Research*, 81:5971–5979, 1976b. doi: 10.1029/JA081i034p05971.

T. Iijima and T. A. Potemra. Large-scale characteristics of field-aligned currents associated with substorms. *Journal of Geophysical Research*, 83:599–615, 1978. doi: 10.1029/JA083iA02p00599.

S. M. Imber, S. E. Milan, and B. Hubert. The auroral and ionospheric flow signatures of dual lobe reconnection. *Annales Geophysicae*, 24(11):3115–3129, 2006. doi: 10.5194/angeo-24-3115-2006.

S. Ismail, D. D. Wallis, and L. L. Cogger. Characteristics of polar cap sun-aligned arcs. *Journal of Geophysical Research*, 82:4741–4749, 1977. doi: 10.1029/JA082i029p04741.

A. V. Jones. *Aurora*. D. Reidel Pub. Co Dordrecht, Holland, 1974. ISBN 9027702721 902770273.

N. M. E. Kalmoni, I. J. Rae, K. R. Murphy, C. E. J. Watt, C. Forsyth, M. Samara, R. G Michell, and G. Grubbs. A direct diagnosis of the plasma waves responsible for the explosive energy release of substorm onset. *Nature Communications*, 2018. doi: 10.1038/s41467-018-07086-0.

J. H. King and N. E. Papitashvili. Solar wind spatial scales in and comparisons of hourly Wind and ACE plasma and magnetic field data. *Journal of Geophysical Research*, 110: A02104, 2005. doi: 10.1029/2004JA010649.

M. G. Kivelson and C. T. Russell. *Introduction to Space Physics*. Cambridge University Press, 1995. ISBN 0521451043.

D. J. Knudsen, E. F. Donovan, L. L. Cogger, B. Jackel, and W. D. Shaw. Width and structure of mesoscale optical auroral arcs. *Geophysical Research Letters*, 28(4): 705–708, 2001. doi: 10.1029/2000GL011969.

A. Kullen. The connection between transpolar arcs and magnetotail rotation. *Geophysical Research Letters*, 27:73–76, 2000. doi: 10.1029/1999GL010675.

A. Kullen and P. Janhunen. Relation of polar auroral arcs to magnetotail twisting and imf rotation: a systematic mhd simulation study. *Annales Geophysicae*, 22(3): 951–970, 2004. doi: 10.5194/angeo-22-951-2004.

A. Kullen, M. Brittnacher, J. A. Cumnock, and L. G. Blomberg. Solar wind dependence of the occurrence and motion of polar auroral arcs: A statistical study. *Journal of Geophysical Research*, 107:1362, 2002. doi: 10.1029/2002JA009245.

A. Kullen, R. C. Fear, S. E. Milan, J. A. Carter, and T. Karlsson. The statistical difference between bending arcs and regular polar arcs. *Journal of Geophysical Research*, 120(12):10,443–10,465, 2015. doi: 10.1002/2015JA021298.

B. S. Lanchester, K. Kailá, and I. W. McCrea. Relationship between large horizontal electric fields and auroral arc elements. *Journal of Geophysical Research*, 101:5075–5084, 1996. doi: 10.1029/95JA02055.

B. S. Lanchester, M. H. Rees, K. J. F. Sedgemore, J. R. Palmer, H. U. Frey, and K. U. Kaila. Ionospheric response to variable electric fields in small-scale auroral structures. *Annales Geophysicae*, 16:1343–1354, 1998. doi: 10.1007/s00585-998-1343-8.

B. S. Lanchester, M. H. Rees, D. Lummerzheim, A. Otto, K. J. F. Sedgemore-Schulthess, H. Zhu, and I. W. McCrea. Ohmic heating as evidence for strong field-aligned currents in filamentary aurora. *Journal of Geophysical Research*, 106:1785–1794, 2001. doi: 10.1029/1999JA000292.

B. S. Lanchester, M. Ashrafi, and N. Ivchenko. Simultaneous imaging of aurora on small scale in OI (777.4 nm) and $N_2$1P to estimate energy and flux of precipitation. *Annales Geophysicae*, 27:2881–2891, 2009. doi: 10.5194/angeo-27-2881-2009.

K. Lassen and C. Danielsen. Quiet time pattern of auroral arcs for different directions of the interplanetary magnetic field in the Y-Z plane. *Journal of Geophysical Research*, 83:5277–5284, 1978. doi: 10.1029/JA083iA11p05277.

B. Lavraud, M. F. Thomsen, M. G. G. T. Taylor, Y. L. Wang, T. D. Phan, S. J. Schwartz, R. C. Elphic, A. Fazakerley, H. Rème, and A. Balogh. Characteristics of the magnetosheath electron boundary layer under northward interplanetary magnetic field: Implications for high-latitude reconnection. *Journal of Geophysical Research (Space Physics)*, 110:A06209, 2005. doi: 10.1029/2004JA010808.

B. Lavraud, M. F. Thomsen, B. Lefebvre, S. J. Schwartz, K. Seki, T. D. Phan, Y. L. Wang, A. Fazakerley, H. Rme, and A. Balogh. Evidence for newly closed magnetosheath field lines at the dayside magnetopause under northward IMF. *Journal of Geophysical Research: Space Physics*, 111(A5), 2006. doi: 10.1029/2005JA011266.

M. Lester. Ionospheric convection and its relevance for space weather. *Advances in Space Research*, 31:941–950, 2003. doi: 10.1016/S0273-1177(02)00790-1.

M. Lester, P. Chapman, S. Cowley, S. Crooks, J. Davies, P. Hamadyk, K. McWilliams, S. Milan, M. Parsons, D. Payne, E. Thomas, J. Thornhill, N. Wade, T. Yeoman, and R. Barnes. Stereo CUTLASS - A new capability for the SuperDARN HF radars. *Annales Geophysicae*, 22:459–473, 2004. doi: 10.5194/angeo-22-459-2004.

K. Liou, P. T. Newell, C.-I. Meng, M. Brittnacher, and G. Parks. Synoptic auroral distribution: A survey using Polar ultraviolet imagery. *Journal of Geophysical Research*, 102:27197–27206, 1997. doi: 10.1029/97JA02638.

M. Lockwood. Identifying the Open-Closed Field Line Boundary. In J. Moen, A. Egeland, and M. Lockwood, editors, *Polar Cap Boundary Phenomena*, page 73, 1998.

H. Lühr, A. Aylward, S. C. Bucher, A. Pajunpää, K. Pajunpää, T. Holmboe, and S. M. Zalewski. Westward moving dynamic substorm features observed with the IMAGE magnetometer network and other ground-based instruments. *Annales Geophysicae*, 16:425–440, 1998. doi: 10.1007/s00585-998-0425-y.

A. T. Y. Lui. Comment on "Tail Reconnection Triggering Substorm Onset". *Science*, 324(5933):1391–1391, 2009. ISSN 0036-8075. doi: 10.1126/science.1167726.

D. Lummerzheim. *Electron transport and optical emissions in the aurora.* PhD thesis, Alaska Univ., Fairbanks., 1987.

L. R. Lyons, T. Nagai, G. T. Blanchard, J. C. Samson, T. Yamamoto, T. Mukai, A. Nishida, and S. Kokobun. Association between Geotail plasma flows and auroral poleward boundary intensifications observed by CANOPUS photometers. *Journal of Geophysical Research*, 104:4485–4500, 1999. doi: 10.1029/1998JA900140.

J. E. Maggs and T. N. Davis. Measurements of the thicknesses of auroral structures. *Planet Space Science*, 16:205, 1968. doi: 10.1016/0032-0633(68)90069-X.

B. Mailyan, Q. Q. Shi, A. Kullen, R. Maggiolo, Y. Zhang, R. C. Fear, Q.-G. Zong, S. Y. Fu, X. C. Gou, X. Cao, Z. H. Yao, W. J. Sun, Y. Wei, and Z. Y. Pu. Transpolar arc observation after solar wind entry into the high-latitude magnetosphere. *Journal of Geophysical Research*, 120:3525–3534, 2015. doi: 10.1002/2014JA020912.

K. Makita and C.-I. Meng. Long-period polar rain variations, solar wind and hemispherically symmetric polar rain. *Journal of Geophysical Research*, 92:7381–7393, 1987. doi: 10.1029/JA092iA07p07381.

K. Makita, C.-I. Meng, and S.-I. Akasofu. Transpolar auroras, their particle precipitation, and IMF B_y component. *Journal of Geophysical Research*, 96:14, 1991. doi: 10.1029/90JA02323.

D Mawson. Auroral observations at the Cape Royds station, Antarctica. *Trans. Proc. R. Soc. S. Aust., XL*, 151, 1916.

D. Mawson. Records of the Aurora Polaris. *Australasian Antarctic Expedition 1911-14, Scientific Reports Series B*, 1925. URL http://data.aad.gov.au/aadc/pubs/pubs_list.cfm?pub_list=AAE.

R. L. McPherron. Growth phase of magnetospheric substorms. *Journal of Geophysical Research*, 75(28):5592, 1970. doi: 10.1029/JA075i028p05592.

C.-I. Meng. Polar cap arcs and the plasma sheet. *Geophysical Research Letters*, 8: 273–276, 1981a. doi: 10.1029/GL008i003p00273.

C.-I. Meng. The auroral electron precipitation during extremely quiet geomagnetic conditions. *Journal of Geophysical Research*, 86:4607–4627, 1981b. doi: 10.1029/JA086iA06p04607.

C.-I. Meng and S.-I. Akasofu. The relation between the polar cap auroral arc and the auroral oval arc. *Journal of Geophysical Research*, 81:4004–4006, 1976. doi: 10.1029/JA081i022p04004.

C.-I. Meng and H. W. Kroehl. Intense uniform precipitation of low-energy electrons over the polar cap. *Journal of Geophysical Research*, 82:2305–2313, 1977. doi: 10.1029/JA082i016p02305.

J. D. Menietti and J. L. Burch. DE 1 observations of theta aurora plasma source regions and Birkeland current charge carriers. *Journal of Geophysical Research*, 92:7503–7518, 1987. doi: 10.1029/JA092iA07p07503.

S. E. Milan, M. Lester, S. W. H. Cowley, and M. Brittnacher. Dayside convection and auroral morphology during an interval of northward interplanetary magnetic field. *Annales Geophysicae*, 18:436–444, 2000a. doi: 10.1007/s00585-000-0436-9.

S. E. Milan, M. Lester, S. W. H. Cowley, and M. Brittnacher. Convection and auroral response to a southward turning of the IMF: Polar UVI, CUTLASS, and IMAGE signatures of transient magnetic flux transfer at the magnetopause. *Journal of Geophysical Research*, 105:15741–15756, 2000b. doi: 10.1029/2000JA900022.

S. E. Milan, M. Lester, S. W. H. Cowley, K. Oksavik, M. Brittnacher, R. A. Greenwald, G. Sofko, and J.-P. Villain. Variations in the polar cap area during two substorm cycles. *Annales Geophysicae*, 21:1121–1140, 2003. doi: 10.5194/angeo-21-1121-2003.

S. E. Milan, B. Hubert, and A. Grocott. Formation and motion of a transpolar arc in response to dayside and nightside reconnection. *Journal of Geophysical Research*, 110: A01212, 2005. doi: 10.1029/2004JA010835.

S. E. Milan, P. D. Boakes, and B. Hubert. Response of the expanding/contracting polar cap to weak and strong solar wind driving: Implications for substorm onset. *Journal of Geophysical Research (Space Physics)*, 113:A09215, 2008. doi: 10.1029/2008JA013340.

P. F. Mizera, D. J. Gorney, and D. S. Evans. On the conjugacy of the aurora - High and low latitudes. *Geophysical Research Letters*, 14:190–193, 1987. doi: 10.1029/GL014i003p00190.

S. M. Naehr and F. R. Toffoletto. Quantitative modeling of the magnetic field configuration associated with the theta aurora. *Journal of Geophysical Research (Space Physics)*, 109:A07202, 2004. doi: 10.1029/2003JA010191.

T. A. Nagy. Documentation for the Machine-readable Version of Lynds' Catalogue of Dark Nebula. Technical report, 1979.

P. T. Newell, Y. I. Feldstein, Y. I. Galperin, and C.-I. Meng. Morphology of nightside precipitation. *Journal of Geophysical Research*, 101:10737–10748, 1996a. doi: 10.1029/95JA03516.

P. T. Newell, C.-I. Meng, and K. M. Lyons. Suppression of discrete aurorae by sunlight. *Nature*, 381:766–767, 1996b. doi: 10.1038/381766a0.

P. T. Newell, K. Liou, and G. R. Wilson. Polar cap particle precipitation and aurora: Review and commentary. *Journal of Atmospheric and Solar-Terrestrial Physics*, 71: 199–215, 2009. doi: 10.1016/j.jastp.2008.11.004.

B. Ni, R. M. Thorne, Y.Y. Shprits, and J. Bortnik. Resonant scattering of plasma sheet electrons by whistler-mode chorus: Contribution to diffuse auroral precipitation. *Geophysical Research Letters*, 35(11), 2008. doi: 10.1029/2008GL034032.

Y. Nishimura, J. Bortnik, W. Li, R. M. Thorne, L. R. Lyons, V. Angelopoulos, S. B. Mende, J. W. Bonnell, O. Le Contel, C. Cully, R. Ergun, and U. Auster. Identifying

the driver of pulsating aurora. *Science*, 330(6000):81–84, 2010. doi: 10.1126/science.1193186.

T. Obara, M. Kitayama, T. Mukai, N. Kaya, J. S. Murphree, and L. L. Cogger. Simultaneous observations of sun-aligned polar CAP arcs in both hemispheres by EXOS-C and Viking. *Geophysical Research Letters*, 15:713–716, 1988. doi: 10.1029/GL015i007p00713.

H. J. Opgenoorth, I. Haggstrom, P. J. S. Williams, and G. O. L. Jones. Regions of strongly enhanced perpendicular electric fields adjacent to auroral arcs. *Journal of Atmospheric and Terrestrial Physics*, 52:449–458, 1990. doi: 10.1016/0021-9169(90)90044-N.

N. Østgaard, S. B. Mende, H. U. Frey, L. A. Frank, and J. B. Sigwarth. Observations of non-conjugate theta aurora. *Geophysical Research Letters*, 30:2125, 2003. doi: 10.1029/2003GL017914.

N. Østgaard, S. B. Mende, H. U. Frey, J. B. Sigwarth, A. Åsnes, and J. M. Weygand. Auroral conjugacy studies based on global imaging. *Journal of Atmospheric and Solar-Terrestrial Physics*, 69:249–255, 2007. doi: 10.1016/j.jastp.2006.05.026.

E. N. Parker. Dynamics of the Interplanetary Gas and Magnetic Fields. *Astrophysical Journal*, 128:664, 1958. doi: 10.1086/146579.

E. N. Parker. *Interplanetary dynamical processes.* Interscience Publishers, 1963.

N. Partamies, M. Syrjäsuo, E. Donovan, M. Connors, D. Charrois, D. Knudsen, and Z. Kryzanowsky. Observations of the auroral width spectrum at kilometre-scale size. *Annales Geophysicae*, 28:711–718, 2010. doi: 10.5194/angeo-28-711-2010.

L. J. Paxton, C.-I. Meng, G. H. Fountain, B. S. Ogorzalek, E. H. Darlington, S. A. Gary, J. O. Goldsten, D. Y. Kusnierkiewicz, S. C. Lee, L. A. Linstrom, J. J. Maynard, K. Peacock, D. F. Persons, and B. E. Smith. Special Sensor Ultraviolet Spectrographic Imager (SSUSI) - an instrument description. In S. Chakrabarti and A. B. Christensen, editors, *Instrumentation for Planetary and Terrestrial Atmospheric Remote Sensing*, volume 1745 of *SPIE*, pages 2–15, 1992. doi: 10.1117/12.60595.

L. J. Paxton, D. Morrison, Y. Zhang, H. Kil, B. Wolven, B. S. Ogorzalek, D. C. Humm, and C.-I. Meng. Validation of remote sensing products produced by the Special Sensor

Ultraviolet Scanning Imager (SSUSI): a far UV-imaging spectrograph on DMSP F-16. In A. M. Larar and M. G. Mlynczak, editors, *Optical Spectroscopic Techniques, Remote Sensing, and Instrumentation for Atmospheric and Space Research IV*, volume 4485 of *Proc. SPIE 4485*, pages 338–348, 2002. doi: 10.1117/12.454268.

G. W. Perry, H. Dahlgren, M. J. Nicolls, M. Zettergren, J.-P. St.-Maurice, J. L. Semeter, T. Sundberg, K. Hosokawa, K. Shiokawa, and S. Chen. Spatiotemporally resolved electrodynamic properties of a Sun-aligned arc over Resolute Bay. *Journal of Geophysical Research*, 120:9977–9987, 2015. doi: 10.1002/2015JA021790.

W. K. Peterson and E. G. Shelley. Origin of the plasma in a cross-polar cap auroral feature (theta aurora). *Journal of Geophysical Research*, 89:6729–6736, 1984. doi: 10.1029/JA089iA08p06729.

D. J. Price, J. M. Chadney, and D. K. Whiter. Observations of Joule heating associated with an auroral arc above Svalbard. *in prep*, 2019.

R. J. Redmon, W. F. Denig, L. M. Kilcommons, and D. J. Knipp. New DMSP database of precipitating auroral electrons and ions. *Journal of Geophysical Research (Space Physics)*, 122:9056–9067, 2017. doi: 10.1002/2016JA023339.

M. H. Rees. Auroral ionization and excitation by incident energetic electrons. *Planetary Space Science*, 11:1209–1218, 1963. doi: 10.1016/0032-0633(63)90252-6.

M. H. Rees. *Physics and Chemistry of the Upper Atmosphere*. Cambridge Atmospheric and Space Science Series. Cambridge University Press, 1989. doi: 10.1017/CBO9780511573118.

M. H. Rees and D. Luckey. Auroral electron energy derived from ratio of spectroscopic emissions 1. model computations. *Journal of Geophysical Research*, 79(34):5181–5186, 1974. doi: 10.1029/JA079i034p05181.

J. A. Reidy, R. C. Fear, D. K. Whiter, B. S. Lanchester, A. J. Kavanagh, L. J. Paxton, Y. Zhang, and M. Lester. Multi-instrument observation of simultaneous polar cap auroras on open and closed magnetic field lines. *Journal of Geophysical Research (Space Physics)*, 122:4367–4386, 2017. doi: 10.1002/2016JA023718.

J. A. Reidy, R. C. Fear, D. K. Whiter, B. Lanchester, A. J. Kavanagh, S. E. Milan, J. A. Carter, L. J. Paxton, and Y. Zhang. Interhemispheric survey of polar cap

aurora. *Journal of Geophysical Research: Space Physics*, 123(9):7283–7306, 2018. doi: 10.1029/2017JA025153.

P. H. Reiff and J. L. Burch. IMF B_y-dependent plasma flow and Birkeland currents in the dayside magnetosphere: 2. A global model for northward and southward IMF. *Journal of Geophysical Research: Space Physics*, 90(A2):1595–1609, 1985. doi: 10.1029/JA090iA02p01595.

J. P. Reistad, N. Østgaard, P. Tenfjord, K. M. Laundal, K. Snekvik, S. Haaland, S. E. Milan, K. Oksavik, H. U. Frey, and A. Grocott. Dynamic effects of restoring footpoint symmetry on closed magnetic field lines. *Journal of Geophysical Research (Space Physics)*, 121:3963–3977, 2016. doi: 10.1002/2015JA022058.

H. Rème, C. Aoustin, J. M. Bosqued, I. Dandouras, B. Lavraud, J. A. Sauvaud, A. Barthe, J. Bouyssou, T. Camus, O. Coeur-Joly, A. Cros, J. Cuvilo, F. Ducay, Y. Garbarowitz, J. L. Medale, E. Penou, H. Perrier, D. Romefort, J. Rouzaud, C. Vallat, D. Alcaydé, C. Jacquey, C. Mazelle, C. D'Uston, E. Möbius, L. M. Kistler, K. Crocker, M. Granoff, C. Mouikis, M. Popecki, M. Vosbury, B. Klecker, D. Hovestadt, H. Kucharek, E. Kuenneth, G. Paschmann, M. Scholer, N. Sckopke, E. Seidenschwang, C. W. Carlson, D. W. Curtis, C. Ingraham, R. P. Lin, J. P. McFadden, G. K. Parks, T. Phan, V. Formisano, E. Amata, M. B. Bavassano-Cattaneo, P. Baldetti, R. Bruno, G. Chionchio, A. di Lellis, M. F. Marcucci, G. Pallocchia, A. Korth, P. W. Daly, B. Graeve, H. Rosenbauer, V. Vasyliunas, M. McCarthy, M. Wilber, L. Eliasson, R. Lundin, S. Olsen, E. G. Shelley, S. Fuselier, A. G. Ghielmetti, W. Lennartsson, C. P. Escoubet, H. Balsiger, R. Friedel, J.-B. Cao, R. A. Kovrazhkin, I. Papamastorakis, R. Pellat, J. Scudder, and B. Sonnerup. First multispacecraft ion measurements in and near the Earth's magnetosphere with the identical Cluster Ion Spectrometry (CIS) experiment. *Annales Geophysicae*, 19:1303–1354, 2001. doi: 10.5194/angeo-19-1303-2001.

B. V. Rezhenov:. A possible mechanism for θ aurora formation. *Annales Geophysicae*, 13:698–703, 1995. doi: 10.1007/s00585-995-0698-3.

J. M. Ruohoniemi and K. B. Baker. Large-scale imaging of high-latitude convection with Super Dual Auroral Radar Network HF radar observations. *Journal of Geophysical Research*, 103:20797–20811, 1998. doi: 10.1029/98JA01288.

H. N. Russell and F. A. Saunders. New Regularities in the Spectra of the Alkaline Earths. *Astrophysical Journal*, 61:38, 1925. doi: 10.1086/142872.

P. E. Sandholt and C. J. Farrugia. Poleward moving auroral forms (PMAFs) revisited: responses of aurorae, plasma convection and Birkeland currents in the pre- and post-noon sectors under positive and negative IMF B_y conditions. *Annales Geophysicae*, 25:1629–1652, 2007. doi: 10.5194/angeo-25-1629-2007.

P. E. Sandholt, C. J. Farrugia, M. Øieroset, P. Stauning, and S. W. H. Cowley. Auroral signature of lobe reconnection. *Journal of Geophysical Research*, 23:1725–1728, 1996. doi: 10.1029/96GL01846.

J. Semeter. Critical comparison of OII(732-733 nm), OI(630 nm), and N_2(1PG) emissions in auroral rays. *Geophysical Research Letters*, 30:1225, 2003. doi: 10.1029/2002GL015828.

I. Shinohara and S. Kokubun. Statistical properties of particle precipitation in the polar cap during intervals of northward interplanetary magnetic field. *Journal of Geophysical Research*, 101:69–82, 1996. doi: 10.1029/95JA01848.

J.-H. Shue, P. T. Newell, K. Liou, and C.-I. Meng. The quantitative relationship between auroral brightness and solar EUV pedersen conductance. *Journal of Geophysical Research*, 106:5883–5894, 2001. doi: 10.1029/2000JA003002.

G. L. Siscoe and T. S. Huang. Polar cap inflation and deflation. *Journal of Geophysical Research*, 90:543–547, 1985. doi: 10.1029/JA090iA01p00543.

C. W. Smith, J. L'Heureux, N. F. Ness, M. H. Acuña, L. F. Burlaga, and J. Scheifele. The ACE Magnetic Fields Experiment. *Space Science Review*, 86:613–632, 1998. doi: 10.1023/A:1005092216668.

G.C. Southworth. *Microwave Radiation from the Sun.* Springer, Dordrecht, 1945. doi: https://doi.org/10.1007/978-94-009-7752-5_17.

K. Stasiewicz, P. Bellan, C. Chaston, C. Kletzing, R. Lysak, J. Maggs, O. Pokhotelov, C. Seyler, P. Shukla, L. Stenflo, A. Streltsov, and J.-E. Wahlund. Small Scale Alfvénic Structure in the Aurora. *Space Science Review*, 92:423–533, 2000.

E. C. Stone, A. M. Frandsen, R. A. Mewaldt, E. R. Christian, D. Margolies, J. F. Ormes, and F. Snow. The Advanced Composition Explorer. *Space Science Review*, 86:1–22, 1998. doi: 10.1023/A:1005082526237.

E. I. Tanskanen. A comprehensive high-throughput analysis of substorms observed by IMAGE magnetometer network: Years 1993-2003 examined. *Journal of Geophysical Research*, 114:A05204, 2009. doi: 10.1029/2008JA013682.

K Tapping. The 10.7 cm solar radio flux (f10.7). *Space Weather*, 11:394–406, 2013. doi: 10.1002/swe.20064.

P. Tenfjord, N. Østgaard, K. Snekvik, K. M. Laundal, J. P. Reistad, S. Haaland, and S. E. Milan. How the IMF B_y induces a B_y component in the closed magnetosphere and how it leads to asymmetric currents and convection patterns in the two hemispheres. *Journal of Geophysical Research*, 120:9368–9384, 2015. doi: 10.1002/2015JA021579.

R. B. Torbert, C. A. Cattell, F. S. Mozer, and C.-I. Meng. The boundary of the polar cap and its relation to electric fields, field-aligned currents, and auroral particle precipitation. In S.-I. Akasofu and J. R. Kan, editors, *Physics of Auroral Arc Formation*, pages 143–153, 1981.

T. S. Trondsen and L. L. Cogger. A survey of small-scale spatially periodic distortions of auroral forms. *Journal of Geophysical Research*, 103:9405–9416, 1998. doi: 10.1029/98JA00619.

S. Tuttle, B. Gustavsson, and B. Lanchester. Temporal and spatial evolution of auroral electron energy spectra in a region surrounding the magnetic zenith. *Journal of Geophysical Research (Space Physics)*, 119:2318–2327, 2014. doi: 10.1002/2013JA019627.

C. Twitty, T. D. Phan, G. Paschmann, B. Lavraud, H. Rème, and M. Dunlop. Cluster survey of cusp reconnection and its IMF dependence. *Geophysical Research Letters*, 31:L19808, 2004. doi: 10.1029/2004GL020646.

C. E. Valladares, H. C. Carlson, Jr., and K. Fukui. Interplanetary magnetic field dependency of stable Sun-aligned polar cap arcs. *Journal of Geophysical Research*, 99:6247–6272, 1994. doi: 10.1029/93JA03255.

J. Vogt, H. U. Frey, G. Haerendel, H. Höfner, and J. L. Semeter. Shear velocity profiles associated with auroral curls. *Journal of Geophysical Research*, 104:17277–17288, 1999. doi: 10.1029/1999JA900148.

A. P. Walsh, A. N. Fazakerley, C. Forsyth, C. J. Owen, M. G. G. T. Taylor, and I. J. Rae. Sources of electron pitch angle anisotropy in the magnetotail plasma sheet. *Journal of Geophysical Research (Space Physics)*, 118:6042–6054, 2013. doi: 10.1002/jgra.50553.

M. Walt. *Introduction to Geomagnetically Trapped Radiation*. Cambridge University Press, 2005. ISBN 0521616115. doi: 10.1017/CBO9780511524981.

G. Wannberg, I. Wolf, L.-G. Vanhainen, K. Koskenniemi, J. Röttger, M. Postila, J. Markkanen, R. Jacobsen, A. Stenberg, R. Larsen, S. Eliassen, S. Heck, and A. Huuskonen. The EISCAT Svalbard radar: A case study in modern incoherent scatter radar system design. *Radio Science*, 32:2283–2307, 1997. doi: 10.1029/97RS01803.

C. L. Waters, B. J. Anderson, and K. Liou. Estimation of global field-aligned currents using the Iridium System magnetometer data. *Geophysical Research Letters*, 28(11): 2165–2168, 2001. ISSN 1944-8007. doi: 10.1029/2000GL012725.

D. R. Weimer, D. M. Ober, N. C. Maynard, M. R. Collier, D. J. McComas, N. F. Ness, C. W. Smith, and J. Watermann. Predicting interplanetary magnetic field (IMF) propagation delay times using the minimum variance technique. *Journal of Geophysical Research (Space Physics)*, 108:1026, 2003. doi: 10.1029/2002JA009405.

C. S. Weller, R. R. Meier, and B. A. Tinsley. Simultaneous measurements of the hydrogen airglow emissions of Lyman alpha, Lyman beta, and Balmer alpha. *Journal of Geophysical Research*, 76:7734, 1971. doi: 10.1029/JA076i031p07734.

D. K. Whiter, B. S. Lanchester, B. Gustavsson, N. Ivchenko, and H. Dahlgren. Using multispectral optical observations to identify the acceleration mechanism responsible for flickering aurora. *Journal of Geophysical Research*, 115:A12315, 2010. doi: 10.1029/2010JA015805.

D. K. Whiter, B. Gustavsson, N. Partamies, and L. Sangalli. A new automatic method for estimating the peak auroral emission height from all-sky camera images. *Geoscientific Instrumentation, Methods and Data Systems*, 2:131–144, 2013. doi: 10.5194/gi-2-131-2013.

J. D. Winningham and W. J. Heikkila. Polar cap auroral electron fluxes observed with Isis 1. *Journal of Geophysical Research*, 79:949, 1974. doi: 10.1029/JA079i007p00949.

Q. Wu, T. J. Rosenberg, F. T. Berkey, and R. H. Eather. Intensification and fading of auroral arcs in the dusk-midnight sector of the polar cap. *Journal of Geophysical Research*, 96:7709–7719, 1991. doi: 10.1029/91JA00256.

Z. Xing, Q. Zhang, D. Han, Y. Zhang, N. Sato, S. Zhang, H. Zejun, Y. Wang, and Yuzhang Ma. Conjugate Observations of the Evolution of Polar Cap Arcs in Both Hemispheres. *Journal of Geophysical Research*, 123:1794–1805, 2018. doi: 10.1002/2017JA024272.

D. Y. Yeager and L. A. Frank. Low-energy electron intensities at large distances over the Earth's polar cap. *Journal of Geophysical Research*, 81:3966–3976, 1976. doi: 10.1029/JA081i022p03966.

Q.-H. Zhang, M. Lockwood, J. C. Foster, S.-R. Zhang, B.-C. Zhang, I. W. McCrea, J. Moen, M. Lester, and J. M. Ruohoniemi. Direct observations of the full Dungey convection cycle in the polar ionosphere for southward interplanetary magnetic field conditions. *Journal of Geophysical Research (Space Physics)*, 120:4519–4530, 2015. doi: 10.1002/2015JA021172.

L. Zhu, R. W. Schunk, and J. J. Sojka. Polar cap arcs: a review. *Journal of Atmospheric and Solar Terrestrial Physics*, 59:1087–1126, 1997. doi: 10.1016/S1364-6826(96)00113-7.